



Balkan Journal of Electrical & Computer Engineering

An International Peer Reviewed, Referred, Indexed and Open Access Journal

www.bajece.com

Vol : 7
No : 3
Year : 2019
ISSN : 2147 - 284X



It is abstracted and indexed in, Index Google Scholarship, the PSCR, Cross ref, DOAJ, Research Bible, Indian Open Access Journals (OAJ), Institutional Repositories (IR), J-Gate (Informatics India), Ulrich's, International Society of Universal Research in Sciences, DRJI, EyeSource, Cosmos Impact Factor, Cite Factor, SIS SIS Scientific Indexing Service, IJIF, iifactor. ULAKBİM-TR Dizin.

General Publication Director & Editor-in-Chief
Musa Yılmaz, Batman University, Turkey.

Vice Editor
Hamidreza Nazaripouya, University of California Riverside, USA

Scientific Committee
Abhishek Shukla (India)
Abraham Lomi (Indonesia)
Aleksandar Georgiev (Bulgaria)
Arunas Lipnickas (Lithuania)
Audrius Senulis (Lithuania)
Belle R. Upadhyaya (USA)
Brijender Kahanwal (India)
Chandar Kumar Chanda (India)
Daniela Dzhonova-Atanasova (Bulgaria)
Deris Stiawan (Indonesia)
Emel Onal (Turkey)
Emine Ayaz (Turkey)
Enver Hatimi (Kosovo)
Ferhat Sahin (USA)
Gursel Alici (Australia)
Hakan Temeltaş (Turkey)
Ibrahim Akduman (Turkey)
Jan Izykowski (Poland)
Javier Bilbao Landatxe (Spain)
Jelena Dikun (Lithuania)
Karol Kyslan (Slovakia)
Kunihiko Nabeshima (Japan)
Lambros Ekonomou (Greece)
Lazhar Rahmani (Algerie)
Marcel Istrate (Romania)
Marija Eidukeviciute (Lithuania)
Milena Lazarova (Bulgaria)
Muhammad Hadi (Australia)
Muhamed Turkanović (Slovenia)
Mourad Houabes (Algerie)
Murari Mohan Saha (Sweden)
Nick Papanikolaou (Greece)
Okyay Kaynak (Turkey)
Osman Nuri Ucan (Turkey)
Ozgun E. Mustecaplioglu (Turkey)
Padmanaban Sanjeevikumar (India)
Ramazan Caglar (Turkey)
Rumen Popov (Bulgaria)
Tarek Bouktir (Algeria)
Sead Berberovic (Croatia)
Seta Bogosyan (USA)
Savvas G. Vassiliadis (Greece)
Suwarno (Indonesia)
Tulay Adali (USA)
Yogeshwarsing Calleecharan (Mauritius)
YangQuan Chen (USA)
Youcef Soufi (Algeria)

Aim & Scope

The journal publishes original papers in the extensive field of Electrical-Electronics and Computer engineering. It accepts contributions which are fundamental for the development of electrical engineering, computer engineering and its applications, including overlaps to physics. Manuscripts on both theoretical and experimental work are welcome. Review articles and letters to the editors are also included.

Application areas include (but are not limited to): Electrical & Electronics Engineering, Computer Engineering, Software Engineering, Biomedical Engineering, Electrical Power Engineering, Control Engineering, Signal and Image Processing, Communications & Networking, Sensors, Actuators, Remote Sensing, Consumer Electronics, Fiber-Optics, Radar and Sonar Systems, Artificial Intelligence and its applications, Expert Systems, Medical Imaging, Biomedical Analysis and its applications, Computer Vision, Pattern Recognition, Robotics, Industrial Automation.



ISSN: 2147- 284X
Vol: 7
No : 3
Year: July 2019

CONTENTS

- S. Turkdogan;** Design and Implementation of a Cost Effective Quartz Crystal Microbalance System for Monitoring Small Changes**213-217**
- E. Yanmaz Adam;** Leveraging Connectivity for Coverage in Drone Networks for Target Detection,**218-225**
- O. Yaman and Y. Bicen;**An Internet of Things (IoT) based Monitoring System for Oil-immersed Transformers,.....**226-234**
- M. U. Khan;** Mobile Robot Navigation Using Reinforcement Learning in Unknown Environments,**235-244**
- M. Cansiz;** Radio Frequency Energy Harvesting with Different Antennas and Output Powers,**245-249**
- M. S. Cengiz;** Effects of Luminaire Angle on Illumination Performance in Tunnel Lighting,**250-256**
- L. A. Ajao, J. Agajo, O. M. Olaniyi, I. Z. Jibril, A. E. Sebiotimo;** Design of a Secure Tracking Automobile System for Oil and Gas,**257-268**
- M.E. Başoğlu;** Analyzes of Flyback DC-DC Converter for Submodule Level Maximum Power Point Tracking in Off-grid Photovoltaic,.,**269-275**
- B. B. Alagoz, G. Kavuran, A. Ates, C. Yeroglu and H. Aliso;** Multi-loop Model Reference Adaptive PID Control for Fault-Tolerance,**276-285**
- B. Reis, S.B. Kaya, and O.K. Sahingoz;** A Clustering Approach for Intrusion Detection with Big Data Processing on Parallel Comp.,**286-293**
- Y. Kaya, D. Avcı and M. Gedikpinar;** Comparing of K-Means, K-Medoidis and Fuzzy C Means Cluster Method for Analog Mod,....**294-299**
- M. R. Çorapsız, H. Kahveci and M. F. Çorapsız;** Analysis and Suppressing Speed Fluctuations in Brushless DC Motors,**300-310**
- T. Tuncer, Y.Sönmez;** A Novel Data Hiding Method based on Edge Detection and 2k Correction with High Payload and High Visual,**311-318**
- M.R. Tur;** The Impact of Emerging Renewable Energy on Capacity Mechanisms in Power Systems and Expert Opinion,**319-325**
- O. Çiçek and S. Kurnaz;** LabVIEW Based a Software System: Quantitative Determination of Main Electronic Parameters for S,**326-331**
- A. Karafil and H. Ozbay;** Power Control of Single Phase Activ. **332-336**
- M.A.Arserim, C.Haydaroğlu, H.Acar, A.Uçar;** Forming and Co-simulation of Square and Triangular Waveforms by Using Sys,....**337-341**
- V. Ozduran;** Physical Layer Security of Multi-user Half/Full-Duplex Wireless Two-Way Relaying Network,**342-354**
- Z. Omaç;** Design and Analysis of a Water Pumping System with Photovoltaic Source and Switched Reluctance Motor,**355-361**
- M. B. Yelten;** Cryogenic DC Characteristics of Low Threshold Voltage (VTH) n-channel MOSFETs,.....**362-365**

BALKAN

JOURNAL OF

ELECTRICAL & COMPUTER ENGINEERING

(An International Peer Reviewed, Indexed and Open Access Journal)

Contact

Batman University
Department of Electrical-Electronics Engineering
Bati Raman Campus Batman-Turkey

Web: <http://dergipark.gov.tr/bajece>
<https://www.bajece.com>
e-mail: bajece@hotmail.com

Design and Implementation of a Cost Effective Quartz Crystal Microbalance System for Monitoring Small Changes on any Surface

S. TURKDOGAN


Abstract— Quartz crystal microbalance systems are widely used in different fields from biology to electronic. Those devices are very sensitive to mass changes on the piezoelectric crystal surface in nano gram scale and therefore can be used to detect even a single virus on surface of any substance. Although they are very practical and versatile, they are sold with very high prices and thus hindering the usage for someone with tight research budget. In this work, we try to find a cost effective solution and bring this device into the price range on two to three orders of magnitude lower than the commercial counterparts. For that purpose, we develop a cost effective quartz crystal microbalance system using a cost effective microcontroller and a typical oscillator circuit and the final product can be used in different fields to detect the mass change on any surface caused by different reactions or effects.

Index Terms— Piezoelectric, QCM (Quartz Crystal Microbalance), Sensors, Transducers, Thickness/Gas Monitor.

I. INTRODUCTION

PIEZOELECTRIC EFFECT produced by piezoelectric crystals sandwiched between two metal electrodes is an essential phenomena used in electronic applications. When we compress a piezoelectric material such as Quartz it produces an electric charge. However, it works in other way as well and when the electric current is flown it changes the shape slightly and creates a mechanical vibration [1]. In electronics, we utilize the first effect, but latter effect can also be utilized in some applications. Besides producing clock pulses for electronic circuits, piezoelectric crystal can also be used as a mass sensor that is known as Quartz Crystal Microbalance (QCM) [2-7]. They are of great interest for a wide variety of measurements in many fields as they are able to work in different operating conditions in gas or liquid mediums [1-9]. In addition, they offer high sensitivity, high stability, low power consumption and easy operation at room temperature.

SUNAY TURKDOGAN, is with Department of Electrical and Electronics Engineering University of Yalova, Yalova, Turkey, (e-mail: sunayturkdogan@hotmail.com).

 <https://orcid.org/0000-0002-9690-325X>

Manuscript received February 22, 2019; accepted May 10, 2019.
DOI: [10.17694/bajece.530796](https://doi.org/10.17694/bajece.530796)

QCM sensors are well-suited for the sensor arrays used in environmental, biomedical and chemical applications. For example, in a recent study [10] QCM was utilized to detect the water vapor adsorption level (humid) by nanomaterials in different morphologies. As the morphology changes from thin film to nanowire the surface area significantly increase and therefore more water molecules in gas form can adsorb on their surface which eventually casue to shift resonance frequency of QCM crystal more due to the mass uptake. Other studies also utilize QCM to detect any other gas molecules. In addition to those, QCM can be also used for the following applications. We can measure the real time addition of molecular layers, swelling and desorption rates, rigidity, thickness and water contents, binding events, induced changes in viscoelasticity and thickness, and cellular attachments in parallel with microscopy on any surface.

Our main purpose of this study is to bring such a versatile QCM device into the life with substantially low cost and comparable device performance and make everyone utilize it. This work would be a good reference for someone in a tight budget because the developed system will be on par with the commercial counterparts except with a massive lower cost.

II. WORKING PRINCIPLE OF QCM

QCM is a widely used acoustic wave sensor to figure out the mass change on any surface of a substance as a function of the change on the quartz crystal's resonance frequency. We can calculate the mass change on thin and uniform films using Sauerbrey equation [10]:

$$\Delta m = - \frac{A\sqrt{\mu\rho}}{2f_0^2} \Delta f \quad (1)$$

where A is the active electrode layer area on the crystal, μ the shear modulus of quartz, ρ density of the crystal, f_0 resonance frequency of the crystal, and Δf frequency shift from its fundamental resonance frequency.

Our QCM device utilizes an AT-cut quartz crystal with resonance frequency of 5MHz. AT-cut crystals widely used by the industry are made from Y bar at 35° rotation (lower right of Fig. 1) and those provide a stable performance over a wide temperature range (-55°C - 125°C). In our device, the Shear Modulus (μ) and density (ρ) of the crystal are 2.947x10¹¹ g/cm.s² and 2.684 g/cm³, respectively. According to Sauerbrey equation (1), the change of ± 1 Hz of the resonance frequency corresponds to 5.02ng of materials desorbed/adsorbed on the 0.282735 cm² active crystal surface. It is important to note that

a QCM sensor with low resonance frequency should be heavy in order to eliminate the vibrational effects caused by the environment. However, we will utilize a crystal oscillating in a frequency greater than 5MHz and will automatically prevent the occurrence of the aforementioned problem because in nature there is no such vibrations. This will make our QCM system very lightweight.

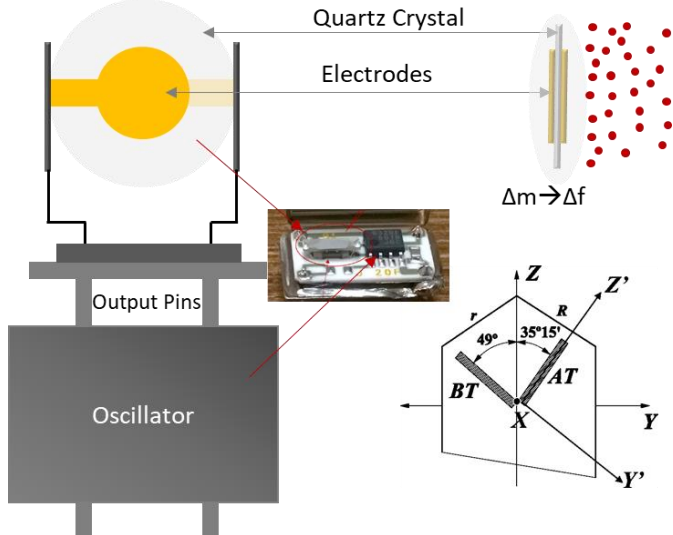


Fig.1. Schematic view of the quartz crystal from side and cross sectional views. Lower right is the demonstration of AT-cut crystal orientation.

III. RESULTS AND DISCUSSION

A. Design and simulation of a QCM

The idea behind a QCM circuitry is very simple and as follows. The circuit basically consists of a crystal oscillator and the signal produced by this oscillator is detected by a microcontroller and measures the oscillation frequency of the corresponding signal. As previously mentioned this signal is proportional to the mass change over the active electrodes of the piezoelectric crystal. When the crystal adsorbs some species, negative frequency shift occurs in the oscillation frequency while this turns to be opposite in case of the mass desorption. Various crystal oscillator circuits can be designed, but for the sake of easiness, we can exploit a cost effective crystal oscillator in a single package with potentially different fundamental oscillation frequencies. It is important to note that 1 Hz frequency shift corresponds to a lower mass change as the fundamental oscillation frequency (f_0) gets higher because in Eq.(1), mass change is inversely proportional to the square of f_0 . It means that as f_0 increases we get more sensitive measurements. In this research, we utilized TCO-711A oscillator, which can be used between 0.25MHz and 100MHz [12]. This oscillator has hermetically sealed package to prevent any effect caused by the environment; however, we cut the package in order to reach two pins of the crystal connections (see Figure 3b) and those connections could be extended for our convenience in the measurement procedure. Figure 1 shows the cut package and crystal can be clearly seen. This crystal can be replaced by any other crystal operating in the aforementioned frequency range and this determines the oscillation frequency of the system. By changing the crystal pointed in Fig.1 we can use the oscillator

in the indicated range. This circuit uses the second harmonic of the crystals meaning that whatever rated crystal we use we can get half of the rated oscillation frequency. For example, if we replace the crystal with 10MHz crystal we can get 5MHz signal out of TCO-711A. Since we are able to replace the quartz crystal, it gives a chance to do disposable tests. It is recommended that only crystals rather than TCO-711A oscillator (top left component seen in Figure 3b) can be bought and by cutting the package quartz crystals can be taken and face to the environment with a much lower price.

By replacing the original crystal in TCO-711A with HEC 10MHz crystal we test our oscillator and the signal produced by the modified oscillator was analyzed using two channel oscilloscope. Figure 3a shows the signal oscillating around 5Mhz. We will design a circuit to detect this signal and project the result in any serial monitor.

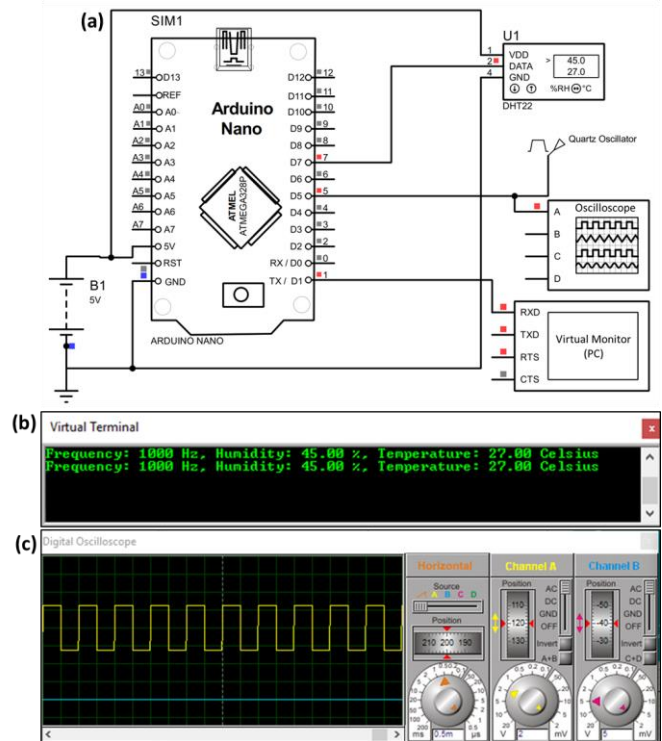


Fig.2. (a) Circuit diagram of the designed QCM system. (b) Simulation results obtained from the virtual terminal. (c) Oscilloscope view of the signal used in simulation to test our QCM device.

Before implementing the designed circuit, a simulation using Proteus 8.0 was done for the system seen in Fig. 2a. In this simulation, a square wave signal with 50% duty cycle was used as the signal produced by crystal oscillator and a model of DHT22 was used to replicate the humidity/temperature sensor. Arduino Nano microcontroller working 16MHz clock speed was utilized to evaluate the data gathered by sensors and oscillator and project the results on a virtual terminal used as a serial monitor. It is important to note that test signal was 1kHz as seen in Fig.2c. The reason for that the signal is disturbed as we increase the frequency to MHz ranges; however, the real device is tested under 5MHz as we will see later. The program we compiled to make this circuit operational was written in Arduino IDE and seen in Appendix section. In the simulation,

we get the temperature, humidity and frequency values and monitored those in virtual terminal as seen in Fig. 2b.

B. Prototype circuit and experimental results

After a successful operation of our device in Proteus we implemented our circuit on a breadboard as seen in Fig. 3b. Before testing, the capability of frequency range that our device can run, 50% duty cycle signals with a wide range of frequency from 1kHz to 10MHz was tested. Since our microcontroller work with 16MHz clock speed and we are limited with the frequency up to 8MHz (half of clock speed) by using “FreqCount” command which can be found in [13]. By employing more advanced microcontrollers such as Teensy 3.0, Teensy 3.5 etc. working with high clock speed we can measure the oscillation frequency greater than 8MHz. After testing the capability of frequency read, we build up our system on the breadboard and read the detected values on the PC screen. Although our aim is to measure the oscillating frequency of the crystal, we embedded a temperature and humidity sensor because correlation of humid, temperature and frequency shift is required to make a meaningful comment in many applications.

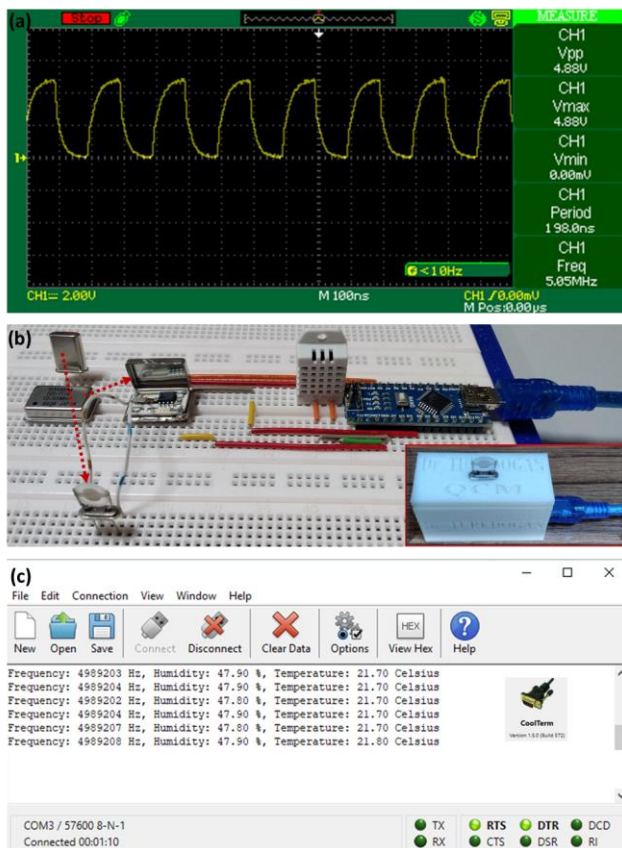


Fig.3. (a) Real oscillating signal captured by 2 channel oscilloscope showing 5MHz oscillation frequency. (b) Real color image of the system built on a breadboard. Inset: 3D printed casing for the circuit to make our device more compact. (c) Data on the screen was sent by the QCM device and projected on the “CoolTerm” screen via USB connection between PC and circuit.

As seen in Fig.3c, the received data is projected on a free program called “CoolTerm”. Our microcontroller sends the

data with 57600 baud rate and the program is set to that value (lower left of Fig.3c) to capture them. The reason we used this program is because the data seen on the screen can simultaneously be saved into the PC and the saved data can be later used for data processing. In other words, we can utilize this program as a cost effective data logger. By 3D printing a case for our system as seen in Fig. 3c, we can make everything compact and implement tests in different environments easily.

As a proof of concept, we test our device in a hermetically sealed humidity test chamber and the results are shown in Fig. 4. The data was obtained in about twelve minutes and with some intervals humidity was altered by flowing a humid air into the chamber. The result shows that the oscillation frequency shifts to lower values as we increase the humidity and the oscillation frequency increases as the humidity gets to the original ambient value. This is as we expected because when the water molecules adsorbed by the electrodes of the crystal, mass increases and this shifts the oscillation to lower frequency values. In addition, the frequency increases as the adsorbed molecules starts to desorb from the surface. It is worth to note that the frequency change is not very high in this case because the electrode surface is very smooth and there is no enough surface area to be adsorbed on. If we coat the electrodes with some nanomaterials having very high surface area, the change in the oscillation frequency becomes more intense. By this way, we can utilize a QCM to detect any phenomenon occurring in gasses or liquid environments.

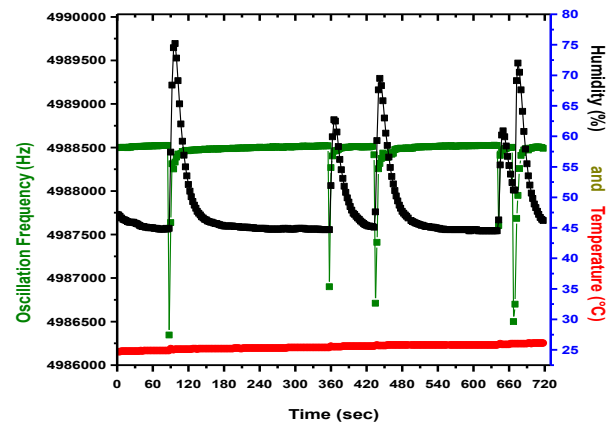


Fig.4. A graph showing the experimental data gathered via our device in a given time.

IV. CONCLUSION AND FUTURE WORK

In conclusion, we have developed, simulated and implemented a simple but versatile QCM device employing cost effective components and integrated circuits. The results show that it works very satisfactorily. Although our design is very easy to implement it can substitute a very expensive and more complex QCM device and realize the sensitive analysis in different fields with low-cost. This design is believed to be widely speeded all over the world and will be utilized for sensing variety of gases, depositions, desorption and etc. and contribute the development of science. As a future work, we are planning to integrate an OLED/LCD display, real time

clock and SD card writer/reader and by this way, we can carry a complete QCM test system in our pocket. This circuit will show the frequency shift, mass change, temperature and humidity information as a function of time on the OLED/LCD screen and can save all these data into a micro SD card to be used in data processing.

Yalova, Turkey and his research mainly focuses on nanotechnology, nanophotonics, nanomaterial growth and characterization, optical devices, sensors, solar cells and photovoltaic systems.

ACKNOWLEDGMENT

This work was supported by the Scientific Research Fund of Yalova University under the project number 2017/AP/140.

REFERENCES

- [1] A. Alassi, M. Benammar, D. Brett, "Quartz crystal microbalance electronic interfacing systems: A review." *Sensors*, Vol.17, 12, (2017), pp. 2799.
- [2] K.N. Chappanda, O. Shekhah, O. Yassine, S.P. Patole, M. Eddaoudi, K.N. Salama, "The quest for highly sensitive QCM humidity sensors: The coating of CNT/MOF composite sensing films as case study" *Sensors and Actuators B: Chemical*, Vol.257, (2018), pp.609-619.
- [3] X. Cha, F. Yu, Y. Fan, J. Chen, L. Wang, Q. Xiang, J. Xu, "Superhydrophilic ZnO nanoneedle array: Controllable in situ growth on QCM transducer and enhanced humidity sensing properties and mechanism" *Sensors and Actuators B: Chemical*, Vol.263, (2018), pp.436-444.
- [4] A. Erol, S. Okur, N. Yağmırcukardeş, M.Ç. Arıkan, "Humidity-sensing properties of a ZnO nanowire film as measured with a QCM" *Sensors and Actuators B: Chemical*, Vol.152, (2011), pp.115-120.
- [5] F. Pascal-Delannoy, B. Sorli, A. Boyer, "Quartz crystal microbalance (QCM) used as humidity sensor" *Sensors and Actuators A: Physical*, Vol.84, (2000), pp.285-291.
- [6] B. Ding, J. Kim, Y. Miyazaki, S. Shiratori, "Electrospun nanofibrous membranes coated quartz crystal microbalance as gas sensor for NH₃ detection" *Sensors and Actuators B: Chemical*, Vol.101, 3, (2004), pp.373-380.
- [7] I. A. Koshets, Z. I. Kazantseva, Y. M. Shirshov, S. A. Cherenok, V. I. Kalchenko, "Calixarene films as sensitive coatings for QCM-based gas sensors" *Sensors and Actuators B: Chemical*, Vol.106, 1, (2005), pp.177-181.
- [8] M. M. Kamel, M. K. El Nimr, S. T. Assar, A. S. Atlam, "Design of a Simple Low-Cost Quartz Crystal Microbalance System" *Instrumentation Science & Technology*, Vol.41, 5, (2013), pp.473-489.
- [9] E. S. Muckley, C. Anazagasty, C. B. Jacobs, T. Hianik, I. N. Ivanov, "Low-cost scalable quartz crystal microbalance array for environmental sensing" *In Organic Sensors and Bioelectronics IX International Society for Optics and Photonics*, Vol.9944, (2016), pp.99440Y.
- [10] G. Sauerbrey, "The use of quartz crystal oscillators for weighing thin layers and for microweighing applications" *Zeitschrift für Physik*, Vol.155, 3, (1959), pp.206-222.
- [11] Turkdogan, S. *J Mater Sci: Mater Electron* (2019). <https://doi.org/10.1007/s10854-019-01384-z>
- [12] "Crystal Oscillator." TOYOCOM. Accessed February 21, 2019. http://eshop-bg.com/PDFs/CrystalOscillators/TOYOCOM_TCO-711A.pdf
- [13] "FreqCount Library." PJRC. Accessed February 21, 2019. https://www.pjrc.com/teensy/td_libs_FreqCount.html

BIOGRAPHY



SUNAY TURKDOGAN received his B.Sc. degree in Electronic Engineering from Uludag University, Turkey in 2007 and he got both his M.S. and Ph.D. degrees in Electrical Engineering from Arizona State University, US in 2012 and 2015, respectively. Currently, he is an Associate Professor in the Department of Electrical and Electronics Engineering at University of

APPENDIX

```
//Libraries
#include <DHT.h>
#include <FreqCount.h>

//Constants
#define DHTPIN 2 // What pin we're connected to
#define DHTTYPE DHT22 // DHT 22 type of sensor is used
DHT dht(DHTPIN, DHTTYPE); /// Initialize DHT22 sensor

//Variables
float hum; //Stores humidity value
float temp; //Stores temperature value

void setup()
{
  Serial.begin(57600);
  FreqCount.begin(1000);
  dht.begin();
}

void loop()
{
  if (FreqCount.available()) {
    unsigned long count = FreqCount.read();
    //Print frequency value to serial monitor
    Serial.print("Frequency: ");
    Serial.print(count);
    Serial.print(" Hz, Humidity: ");
  }
  //Read data and store it to variables hum and temp
  hum = dht.readHumidity();
  temp= dht.readTemperature();
  //Print temp and humidity values to serial monitor
  Serial.print(hum);
  Serial.print(" %, Temperature: ");
  Serial.print(temp);
  Serial.println(" Celsius");
  delay(2000); //Delay 2 sec. Sampling rate of DHT22 0.5 Hz
}
```

Leveraging Connectivity for Coverage in Drone Networks for Target Detection

E. YANMAZ ADAM

Abstract— Target or event detection is one of the main applications of drone networks. Several cooperative search algorithms have been proposed for teams of unmanned aerial vehicles (UAVs), where the goal is to minimize search time or maximize detection probability. In these works, connectivity often is considered a constraint in enabling cooperation. In this paper, we approach the target detection problem in drone networks from both detection and connectivity viewpoints. Our goal is not only to find a stationary target but also to inform the ground personnel (e.g., a rescue team) about the status of the target over a multi-hop communication chain. We analyze the performance of our coverage-based and connectivity-based path planning algorithms in terms of probability and time of detection as well as notification. We show that there is a trade-off between coverage and connectivity and with limited number of drones both aspects need to be considered for successful mission completion.

Index Terms— drones, monitoring, networking, swarms, target detection.

I. INTRODUCTION

DRONE networks are being deployed for environmental monitoring, surveillance, infrastructure inspection, delivery systems, search and rescue to name a few [1]–[4]. For applications such as wildfire tracking, glacier or volcano monitoring, liveliness detection, the area to be monitored can be physically inaccessible or dangerous for humans to enter or the emergency personnel might need to cover the area of interest with high efficiency to be able to respond to the detected event in a timely manner. In such cases, use of drone networks can be extremely beneficial.


In this work, we consider a team of small UAVs (e.g., multi-rotors) equipped with sensors (e.g., cameras, GPS), network interface (e.g., WiFi), and computation power. The aim of this network is to search a certain area and detect and monitor a target. Only the boundaries of the area the UAV network needs to search is known. We consider two main challenges: i) achieving spatial coverage in an efficient manner (for target

detection) and ii) establishing and maintaining communication links between UAVs and the ground station (for target monitoring). In our previous work, we have shown that there is a trade-off between area coverage and connectivity [5], [6]. For a given number of UAVs, an area of interest can be observed faster if the trajectories of the drones minimally overlap. On the other hand, the farther the drones fly from each other the more difficult it will be to stay connected and exchange observations. In this work, we analyze two path planning models based on potential fields for a team of UAVs, where each UAV autonomously decides its path, taking into account their own observations and position of their immediate neighboring teammates. In particular, the UAVs adapt their directions maintaining either efficient coverage [7] or connectivity [5].

We compare the performance of the coverage- and connectivity-based path models for a UAV network toward a target detection mission. We make no assumptions regarding the sensors onboard the UAVs that will be used for detection, except that the target will be detected with probability 1 if it is within the coverage of at least one UAV; i.e., the detection sensors are considered to be error-free. The mission is considered successful if a time-limited target is found and the ground station is informed about it before the target disappears. We numerically investigate several scenarios, where communication links between the UAVs and the ground station can be formed over a multi-hop network. We analyze the performance in terms of probability of detection and notification as well as mission times. In this work, probability of detection is affected by target duration and not sensing quality. The latter will be analyzed in our future work. Our results show that with the right combination of resources (e.g., number of drones, transmission power) equivalent performances can be achieved from the coverage- and connectivity-based schemes. This indicates that both connectivity and coverage requirements need to be taken into account while planning the paths of UAV networks that are deployed for search applications.

The remainder of the paper is organized as follows. In Section II, related work on networking and path planning in drone networks is provided. The analyzed coverage- and connectivity-based path planning strategies are presented in Section III. Results are given in Section IV and the paper is concluded in Section V.

EVŞEN YANMAZ ADAM, Department of Electrical and Electronics Engineering, Faculty of Engineering, Ozyegin University, Istanbul, Turkey, (e-mail: evsen.yanmaz@ozyegin.edu.tr).

 <https://orcid.org/0000-0003-2983-1978>

Manuscript received December 27, 2018; accepted June 11, 2019.
DOI: [10.17694/bajece.503818](https://doi.org/10.17694/bajece.503818)

II. RELATED WORK

A. Wireless Networking with UAVs

From a networking viewpoint, the multi-UAV system or drone network is classified as flying ad hoc network (FANET) in [8] and differentiated from mobile ad hoc networks (MANET) and vehicular ad hoc networks (VANET) in terms of node mobility and density, frequency of topology change, radio propagation, power consumption, computation power, and localization. A FANET is usually deployed toward a mission, and hence has some common traits with a wireless sensor network as well (see [9], [10], [11]). For instance, sensor node activating strategies are considered in static wireless networks such that coverage time is minimized or detection probability of a target is maximized, or event coverage and connectivity are integrated [9]. Mobile sensor networks have been shown to improve the network capacity and coverage [12], [13]. Mobile robots with swarming capability that operate cooperatively and aim to achieve a global goal have also been considered (see [14], [15], [16]). Meshed communication architecture (multihop) is shown to offer flexibility, performance, and reliability [17]. However, mobility leading to sparsely connected nodes and fast changing network topology is still a key issue to be addressed.

B. Path planning

From robotic network viewpoint, the team of drones need to be coordinated and we interpret coordination within the scope of our network as multi-uav path planning. Several planning strategies exist for ground robots [18], delivery systems, or mobile sensor networks [14]. Some strategies use prior information with exact or partial decomposition of the areas, whereas others use sensor-based information to make navigation decisions. Path planning and swarming algorithms that rely on network connectivity between drones are also being investigated [5], [19]–[21].

Basic path planning approaches are based on cell decomposition, roadmaps, and potential fields [22], [23]. Cell decomposition methods (exact or approximate) partition the configuration space into a finite number of regions, marking the obstacles on the grid. Roadmaps (such as visibility graphs and Voronoi diagrams) pre-compute a graph such that obstacles can be avoided by staying on the “roads”. Approaches based on potential fields on the other hand utilize attractive forces toward the goal and repulsive forces from the obstacles. The use of UAVs has been proposed for target detection applications (see [4] and references therein), where search algorithms have been used for path planning. The target detection algorithms aim to either provide fast area coverage [24], or maximize probability of target detection [25]. Path planning for search usually utilizes communication for information merging to improve the target detection probability [4]. In [7], the transmission ranges are used to create potential fields to repel the mobile nodes in the network to maximize area coverage. However, the successful completion of such missions depend both on locating the target and informing the BS about the target location.

III. COVERAGE AND CONNECTIVITY BASED PATH PLANNING

In our recent work, we have proposed two path planning models for fast area coverage [7] and for connectivity [5]. Both models make use of the local physical topology information and rely on artificial potential fields to determine the next action of each UAV in a UAV swarm in a distributed manner. The performance of the algorithms will be tested for target detection later in the paper.

A. System Model

We assume that there is no prior knowledge of the search area except for its boundaries. The UAVs can have different capabilities, they can enter and leave the system at will. The area of interest can also be dynamic and the proposed algorithms can adapt to it. The UAV team consists of N_m drones, each with a sensing range of r and a transmission range of r_c (with a disc coverage). The drones fly with speeds uniformly distributed in $[0; V_m]$. In this work, we assume the drones all fly at the same altitude (h). The extension of the work for movement in three-dimensional air space is beyond the scope of the paper.

The UAVs know their own positions (e.g., from onboard GPS). They are equipped with sensors (e.g., cameras) that can detect a target as soon as the target is within their coverage. There are no further assumptions regarding the type of detection sensors and the processing time of the sensed information. As a rule, each UAV senses its neighbors every t_s seconds and depending on its location at the end of next timestep given its current heading it decides if it needs to change direction. The UAVs exchange only their current location and/or direction. Same algorithm is run on all UAVs and the directions are updated accordingly. If, at the time of direction change, a UAV does not have any neighbors, the direction is not changed. Note that the step length (t_s) is a design parameter and depends on the system parameters such as N_m and r among others.

In the following, we briefly explain how coverage- and connectivity-based path planning strategies work. For a detailed analysis of both schemes for area coverage, readers are referred to [5], [7].

B. Coverage-based distributed path planning

The objective of this path planning strategy is to search a given geographical area by a drone network. Since the goal is fast coverage, the overlap between the covered areas by the limited number of drones need to be minimal. As explained above, there is no centralized controller that optimizes the trajectories of each drone jointly. We assume that each drone decides its own path using the coverage-based path planning algorithm, which changes the direction of the drones at the end of each time step, if necessary. Such a distributed approach is advantageous especially in the case of sparse connectivity between drones and the ground control.

The coverage-based path planning algorithm, which is run on each UAV, is illustrated in Fig. 1. On each UAV i , the algorithm takes as input the area of interest (\mathbf{A}), sensing period (t_s), transmission range (r), current direction and position of node i (θ_i^c, P_i), and position of neighboring drones ($\{N_i\}$). It returns the next direction (θ_i^+).

The main direction decision depends on a drone's current position and direction relative to the position of its neighboring teammates and it happens every t_s sec (update time). Timer starts at zero and is increased at increments much smaller than t_s . At each time increment t_i , the direction of a drone can change if the drone notices it would leave the search area \mathbf{A} , based on its estimated position (P_i^+) given its current direction. In that case, the drone chooses a random direction (θ_i^+) toward \mathbf{A} . Once the total time increment reaches t_s , each drone computes the resultant force (\vec{R}_v) acting on it and the timer is set to zero. In particular, each drone pushes its neighboring drones with a force (\vec{F}_{ji}) that is inversely proportional to the distance between the nodes. An attraction force (\vec{F}_{ii}) which is inversely proportional to the drone's sensing range (i.e., r) is also applied to avoid backtracking. Each drone, then, moves in the direction of the resultant vector, which is the sum of all applied forces on the drone of interest. The calculation of the applied forces and the resultant force is shown in Fig. 1, where Θ_i^c and Θ_{ij} are the unit vectors with angles θ_i^c and θ_{ij} , respectively.

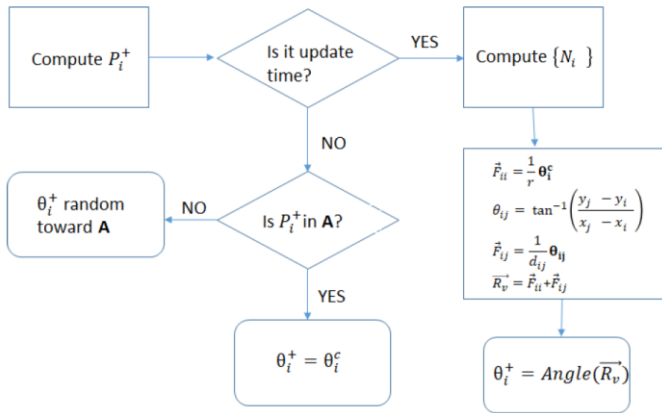


Fig.1. Coverage-based path planning algorithm

C. Connectivity-based distributed path planning

This path planning strategy takes communication requirements into account. The goal of the drone network is to search a given area, while the drones maintain connectivity to the BS (sink node) and/or their neighbors. Due to the probabilistic nature of the algorithm, disconnections from the BS can occur, but likelihood of isolated drones is low. The parameters used in the algorithm running on each UAV are defined in Table I and the algorithm is illustrated in Fig. 2. We denote the UAV of interest as UAV i .

As with the previous strategy, connectivity-based path planning is also distributed and every t_s seconds, each UAV computes their next direction. Similarly, at each time increment t_i during a timestep of t_s , the drones ensure they do not leave \mathbf{A} .

TABLE I
ALGORITHM PARAMETERS

Parameter	Definition
t_s	sensing period
t_i	time increment
r_c	transmission range
\mathbf{A}	search area
A_s	coverage area of BS
θ_i^c	current direction of drone i
θ_i^+	next direction of drone i
P_i	current position of drone i given by (x_i, y_i, h)
P_i^+	position of drone i given by (x_i^+, y_i^+, h) after t_i sec
P_i^{next}	position of drone i given by $(x_i^{next}, y_i^{next}, h)$ after t_s sec
$\{N_i\}$	current positions of set of neighbors of drone i given by $(x_j, y_j, h)_i$
$\{N_i^+\}$	positions of current neighbors of drone i after t_i sec given by $(x_j^+, y_j^+, h)_i$
$\{N_i^{next}\}$	positions of current neighbors of drone i after t_s sec given by $(x_j^{next}, y_j^{next}, h)_i$
R^+	network routing table for a given $P_i^+, \{N_i^+\}$
R^{next}	network routing table for a given $P_i^{next}, \{N_i^{next}\}$

Different than coverage-based algorithm, at each increment drone i computes its routing table at the end of t_i and t_s , assuming there would be no direction change. Using these routing table estimates, drone i checks whether it would be connected to the BS at the end of t_s . If yes, it continues with its current direction θ_i^c .

If not, the drone i aims to avoid being isolated by staying connected to the BS or one of its neighbors which we will denote by drone j . First, each drone checks whether the BS is an immediate neighbor. If it is, the drone chooses a random direction toward the BS coverage area (A_s) to ensure connectivity. If the next hop in the route is not the BS, we have two cases. Algorithm checks R^+ to see if the UAV i has a route to the BS at the end of a time increment even if it doesn't have a route at the end of t_s . If it has a route, then j is set to be the next hop neighbor of i in the multi-hop route to BS. If it is not connected to the BS after t_i either, drone i calls the function *max_contact_id*. This function estimates the contact time to each neighbor (i.e., the time UAV i would be connected to a given neighbor if all neighbor UAVs in $\{N_i^+\}$ keep their current heading) and chooses the neighbor with longest estimated contact time. Parameter j in this case is set to the ID of this neighboring node. All of these steps are taken to keep the network connected while avoiding frequent direction changes.

Once the node j , to which the UAV i decides to stay connected, is determined, we again use artificial potential fields to determine the next direction θ_i^+ . The forces that apply on drone i are 1) a force that pulls the UAV in its current direction (\vec{F}_{ii}) with unit magnitude and 2) a force that pulls the UAV toward the last contact point with neighbor j , should both UAVs keep their direction (\vec{F}_{ij} , again with unit magnitude). This way UAV i is gradually pulled toward neighbor j while keeping the overlap between coverages still small. Recall that the goal is to search an area to find targets as fast as possible. As such, we want to keep the drones as far from each other as possible, while still being connected. Exact

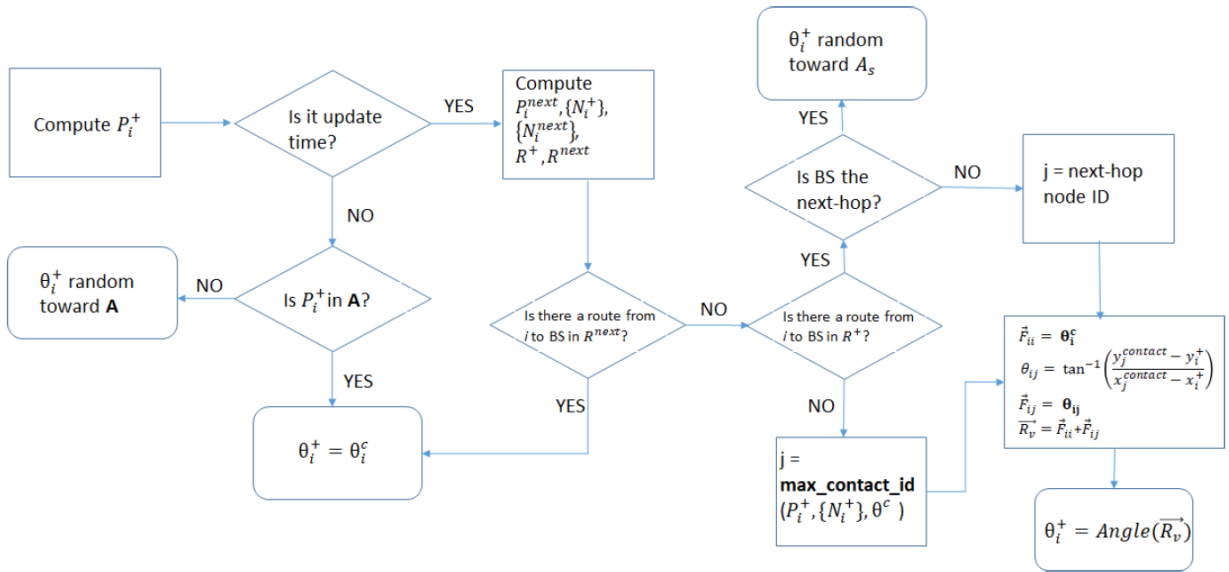


Fig. 2. Connectivity-based path planning algorithm.

calculation of the applied forces and resultant force is given in Fig. 2.

If a UAV nevertheless becomes isolated (i.e., because t_s is too long, the transmission range of the sink is too short, or the UAV speed is too high), it does not change its direction until it reaches the boundary or it meets another UAV.

IV. RESULTS AND DISCUSSION

In this section, we compare the target detection and BS notification performance of the coverage and connectivity-based path planning strategies via Monte Carlo simulations. Each data point is computed over 2000 different runs. The simulation area is square-shaped with a length of 4000m. The UAVs start their mission above the ground station, which is placed at center of the search area. The travel time of the UAVs is assumed to be 2500 s and their velocity is fixed to 5 m/s. The sensing range, r , of the UAVs is set to 500m and the sensing period for direction change is 2s. We study a multi-hop system, where the UAVs are connected to the ground station via a shortest-hop network route. The number of hops in the routes between the UAVs and the ground station depend on the transmission range r_c of the nodes.

We assume that a single event occurs at a random location within the simulation area and lasts for a duration of t_d seconds. N_m drones search the area. Assuming a target is detected without error as soon as it is within sensing range of a UAV, the performance metrics of interest are: i) probability of detection within t_d ; ii) time to detect; iii) probability of immediate notification (at the time of detection); iv) probability of later notification (within t_d); v) time to notify; and v) total mission time, where the mission is over once the BS is notified (i.e., includes search time and notification time).

We also provide the detection probability of an ideal mobile network, where there is minimal to no overlap between drone trajectories. In [7], we have shown that the percentage of covered area by at least one node in $[0; t]$ is:

$$P_{cm} = 1 - e^{-N_m(\pi r^2 + 2rE[V]t)/A} \quad (1)$$

where r is the disc sensing range of the drones, N_m is the number of drones, V is the uniformly distributed velocity within $[0; V_m]$, and A is the total area to be covered.

A. Detection performance

First, we study the impact of target duration and number of drones on the probability of detection performance of coverage- and connectivity-based path models. Fig. 3 shows the probability of detection versus target duration, when $N_m = \{6, 26\}$ and $r_c = \{500, 1000, 2000\}$ m. Analytical results for mobile and static random network are obtained using Equation(1). Observe that coverage-based paths perform as well as the ideal mobile network if t_d is long enough for both N_m values. The need for static nodes can be very high, illustrating that mobility improves coverage. The probability of detection for both schemes increase with increasing t_d , eventually becoming 1. The performance of connectivity-based mobility model depends on the transmission range. If r_c is large enough the drones can freely spread in the search area, bringing the performance of connectivity-based scheme closer to that of coverage-based scheme. If there are enough number of nodes, the performance of the two schemes become equivalent, since the drone network eventually becomes connected due to increased spatial node density.

Fig. 4 shows the probability of detection versus N_m , when target duration is $\{300, 2400\}$ s. Similar to the previous case, coverage-based mobility model performs better if r_c is not large enough. While for short target durations, the two schemes perform worse than an ideal mobile network, the benefit of mobility over static network can be observed even with short target durations, when the number of drones is low. If the target duration is short, adding more drones into the

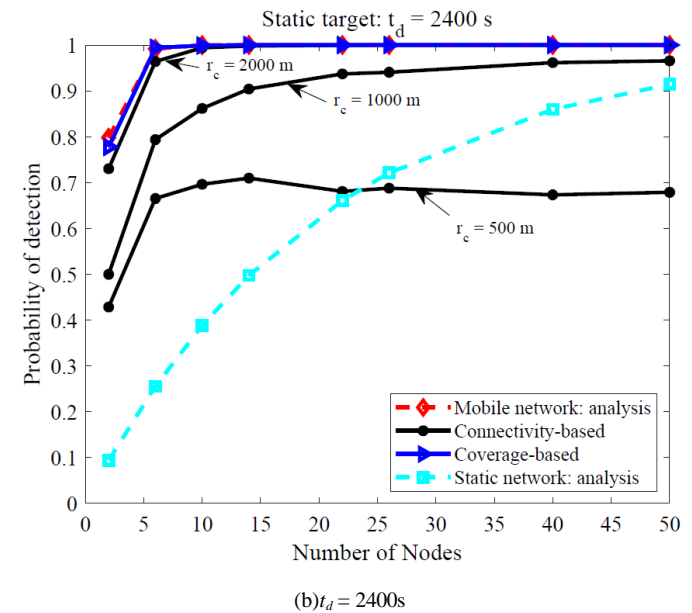
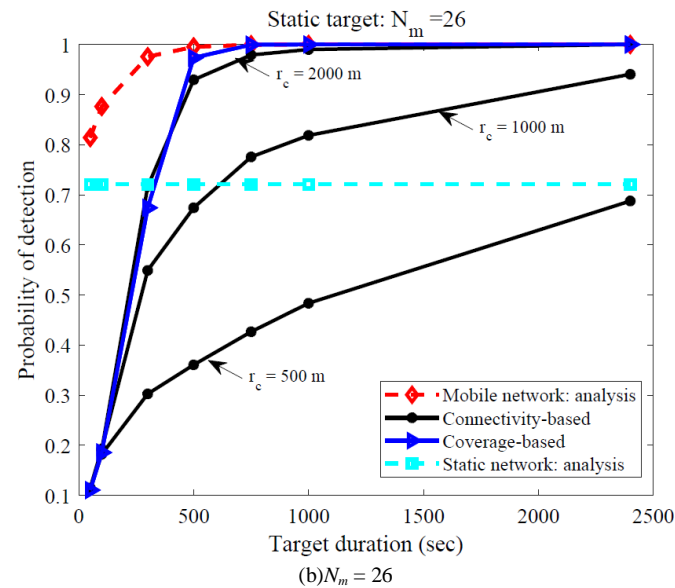
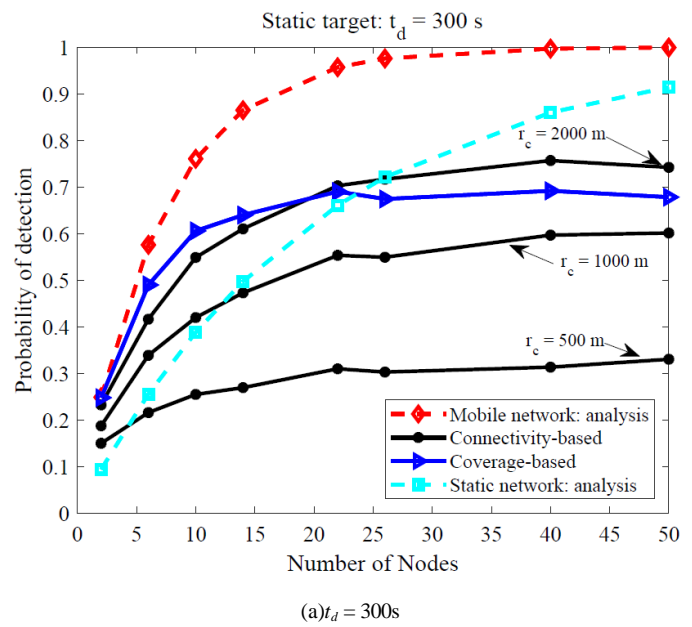
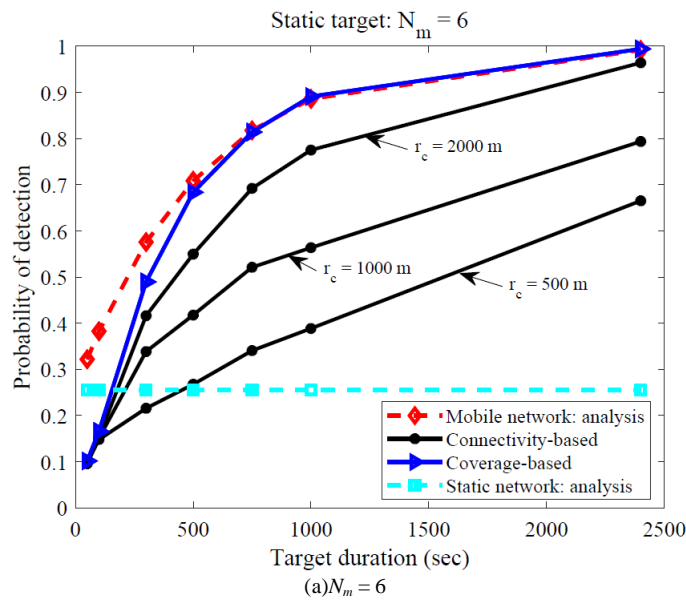


Fig. 3. Probability of detection versus target duration

Fig. 4. Probability of detection versus number of nodes.

network does not improve the performance, since all nodes depart from a single ground station. If the target duration is long, on the other hand, even with a low number of drones the target can be detected as expected. If the transmission range is low (e.g., $r_c = 500\text{m}$), the performance of the connectivity-based scheme is limited and a much higher number of drones would be required to achieve an acceptable performance.

B. Notification performance

In the previous section, we have seen that the detection performance of the connectivity-based path model is limited by the transmission range. In the following, we will illustrate that conversely the notification performance of the coverage-based model is limited by the transmission range. The probability of notification is conditioned on detection. Fig. 5

shows the probability of notification performance versus N_m , when target duration is 2400s. We analyze the immediate notification probability (a) as well as notification probability before the target disappears (b). Fig. 5 (c) shows the total notification probability. We also provide the simulation results for a random static network, where the total notification probability is the same as the immediate notification probability. We observe that since the connectivity-based scheme takes into account the transmission range of the drones when determining the drone movements, the drones stay connected throughout the mission with a high probability. Therefore, the likelihood that the BS will immediately be notified is very high and when r_c becomes high enough (1000m in the figure), the likelihood becomes one even with low number of nodes. Even for low transmission ranges, the

performance of connectivity-based scheme is more than twice of the coverage-based scheme when N_m is low. When r_c is 1000 m, coverage-based scheme needs 40 drones for an immediate notification probability of 1, whereas connectivity-based scheme needs around 15. Furthermore, with 15 drones coverage-based scheme could detect the target with probability 1 (Fig. 4), whereas connectivity-based scheme would detect with a probability of 0.9. Therefore, the gain in immediate notification probability for connectivity-based model is more prominent than the gain in detection probability for coverage-based model.

Conversely, probability of later notification is much higher for coverage-based model. If the eventual notification of the BS within the target duration is sufficient, immediate notification might not be essential. Observe from Fig. 5 (c) that the total notification performance of the two schemes is very similar if the number of drones is high enough.

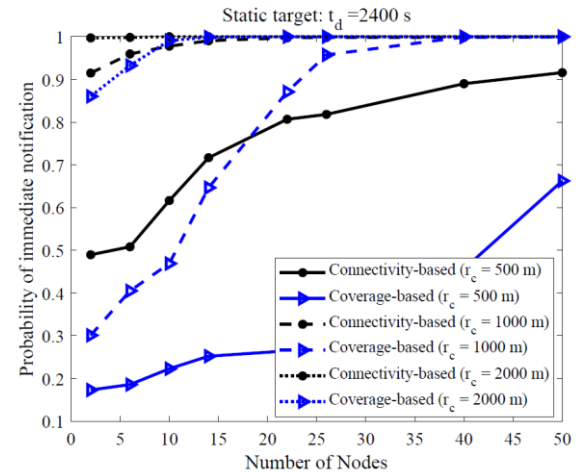
C. Mission time performance

So far, we have looked on the detection and notification performance in terms of probabilities. It is important to determine relative times for different parts of the mission and also how late is “later notification”. Fig. 6 shows the time required to detect the target (a) and notify the BS (b), as well as the total mission time that includes both the detection and notification phases. As expected, the time to detect is shorter for coverage-based scheme and the time to notify is shorter for the connectivity-based scheme. The difference reduces as the transmission range and the number of drones (i.e., the spatial node density) increases. In terms of the total mission time, the connectivity-based scheme outperforms the coverage-based scheme even with low transmission ranges, when t_d is high. This, however, should be considered together with the fact the mission success probability can be less for connectivity-based schemes when the target duration is low (recall the probability of detection when $t_d = 300$ s), especially when r_c is low.

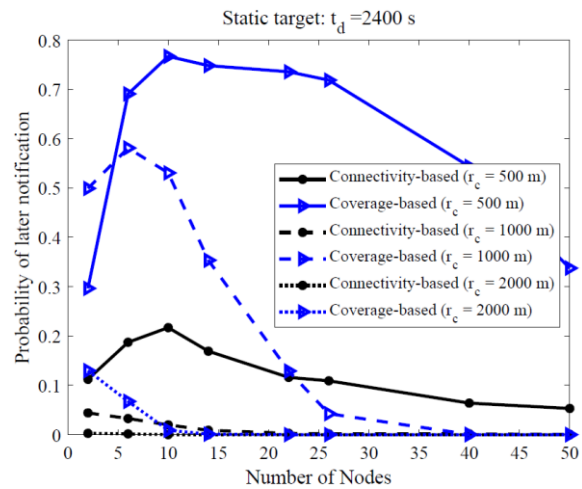
V. CONCLUSIONS

In this work, local, cooperative distributed path planning methods for a UAV team are analyzed for a target detection application in terms of detection and connectivity performance. We analyze two of our models: coverage-based and connectivity-based. As expected, the path decisions of the UAVs for the two schemes have conflicting goals. Whereas the coverage-based model aim to spread the UAVs as much and fast as possible, the connectivity-based model aims to keep the team together so that information on the target can immediately be exchanged. The performance of the models in terms of detection and notification reflects this conflict. When the number or the transmission range of drones increase the performance difference between the two schemes reduce. However, the available resources depend on the cost and goal of a mission. Therefore, we conclude that the choice of the path planning model depends on the needs of the mission. With the right combination of resources (e.g., number of drones, transmission power) equivalent performances can be achieved. A potential approach could utilize the coverage and connectivity benefits of the two schemes and adapt to the

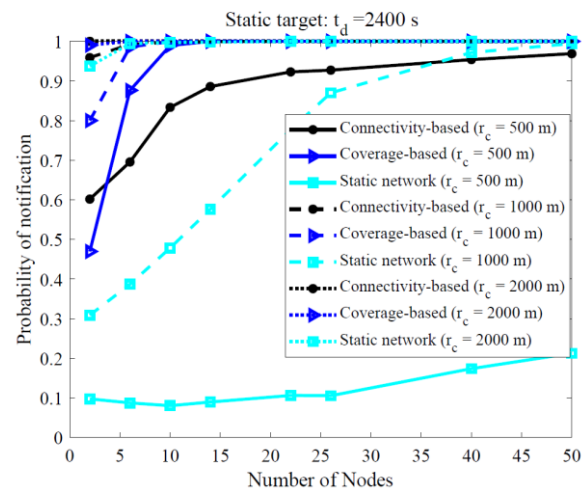
mission needs. A weighted approach that combine the two schemes is currently under investigation.



(a)Probability of immediate notification

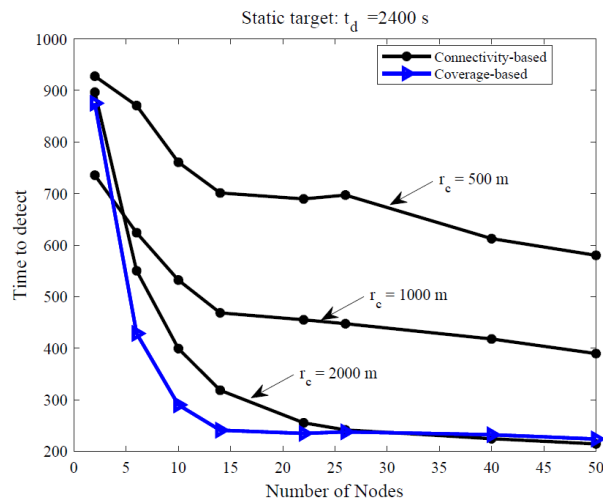


(b)Probability of later notification

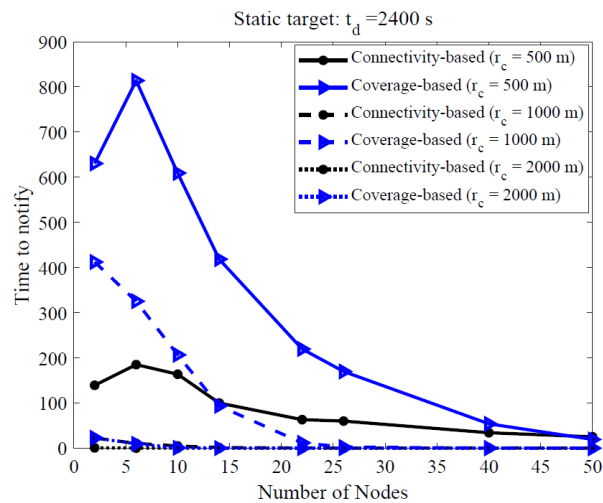


(c)Probability of notification

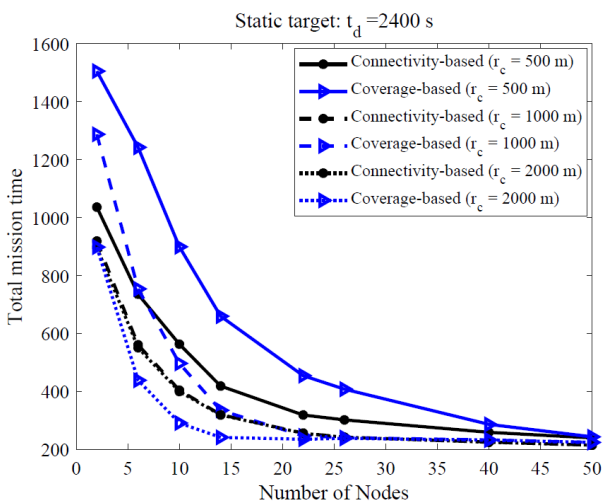
Fig. 5. Probability of notification versus number of nodes when $t_d = 2400$ s.



(a) Detection time



(b) Notification time



(c) Total mission time

Fig. 6. Mission phase times versus number of nodes when $t_d = 2400$ s.

REFERENCES

- [1] D. Cole, A. Goktogan, P. Thompson, and S. Sukkarieh, "Mapping and tracking," *IEEE Robotics Automation Magazine*, vol. 16, no. 2, pp. 22–34, June 2009.
- [2] S. Hayat, E. Yanmaz, and R. Muzaffar, "Survey on unmanned aerial vehicle networks for civil applications: A communications viewpoint," *IEEE Communications Surveys Tutorials*, vol. 18, no. 4, pp. 2624–2661, Fourthquarter 2016.
- [3] M. Erdelj, E. Natalizio, K. R. Chowdhury, and I. F. Akyildiz, "Help from the sky: Leveraging UAVs for disaster management," *IEEE Pervasive Computing*, vol. 16, no. 1, pp. 24–32, Jan 2017.
- [4] A. Khan, E. Yanmaz, and B. Rinner, "Information Exchange and Decision Making in Micro Aerial Vehicle Networks for Cooperative Search," *IEEE Transactions on Control of Network Systems*, vol. 2, no. 4, pp. 335–347, 2015.
- [5] E. Yanmaz, "Connectivity versus area coverage in unmanned aerial vehicle networks," in *Proc. IEEE Int. Conf. on Communications (ICC)*, 2012.
- [6] S. Hayat, E. Yanmaz, T. Brown, and C. Bettstetter, "Multi-objective UAV path planning for search and rescue," in *Proc. Intl. Conf. Robotics and Automation*, ser. ICRA '17, 2017.
- [7] E. Yanmaz and H. Guclu, "Stationary and mobile target detection using mobile wireless sensor networks," in *Proc. IEEE Conf. on Computer Communications (INFOCOM)*, Mar. 2010, pp. 1–5.
- [8] I. Bekmezci, O. K. Sahingoz, and C. Temel, "Flying Ad-Hoc Networks (FANETs): A Survey," *Ad Hoc Networks*, vol. 11, no. 3, pp. 1254–1270, May. 2013.
- [9] X. Wang, G. Xing, Y. Zhang, C. Lu, R. Pless, and C. Gill, "Integrated coverage and connectivity configuration in wireless sensor networks," in *Proc. Int's. Conf. Emb. Net. Sens. Sys. (SenSys'03)*, 2003, pp. 28–39.
- [10] B. Liu and D. Towsley, "A study of the coverage of large-scale sensor networks," in *Proc. IEEE Int'l. Conf. Mob. Ad hoc Sens. Sys. (IEEE MASS'04)*, Oct. 2004, pp. 475–483.
- [11] S. Megerian, F. Koushanfar, M. Potkonjak, and M. B. Srivastava, "Worst and best-case coverage in sensor networks," *IEEE Trans. Mob. Comp.*, vol. 4, no. 1, pp. 84–92, Jan./Feb. 2005.
- [12] M. Grossglauser and D. N. C. Tse, "Mobility increases the capacity of ad hoc wireless networks," *IEEE/ACM Trans. Networking*, vol. 10, no. 4, pp. 477–486, Aug. 2002.
- [13] B. Liu, P. Brass, O. Dousse, P. Nain, and D. Towsley, "Mobility improves coverage of sensor networks," in *Proc. ACM Intl. Symp. Mobile Ad hoc Networking and Computing (MobiHoc '05)*, 2005, pp. 300–308.
- [14] S. Poduri and G. S. Sukhatme, "Constrained coverage for mobile sensor networks," in *Proc. IEEE Intl. Conf. on Robotics and Automation*, 2004, pp. 165–172.
- [15] P. Vincent and I. Rubin, "A framework and analysis for cooperative search using UAV swarms," in *Proc. ACM Symp. Applied Computing*, 2004, pp. 79–86.
- [16] Y. Jin, Y. Liao, M. M. Polycarpou, and A. A. Minai, "Balancing search and target response in cooperative unmanned vehicle teams," *IEEE Trans. on Sys., Man and Cybernetics*, vol. 36, pp. 571–587, 2006.
- [17] E. W. Frew and T. X. Brown, "Airborne communication networks for small unmanned aircraft systems," *Proc. of the IEEE*, vol. 96, no. 12, 2008.
- [18] H. Choset, "Coverage for robotics – a survey of recent results," *Annals of Math. and Artificial Intel.*, vol. 31, no. 1-4, pp. 113–126, 2001.
- [19] S. Hauer, S. Leven, J.-C. Zufferey, and D. Floreano, "Communication-based swarming for flying robots," in *Proc. Intl. Conf. Robotics and Automation Workshop on Network Science and Systems*, 2010.
- [20] Y. Mostofi, "Communication-aware motion planning in fading environments," in *Proc. Intl. Conf. Robotics and Automation*, 2008, pp. 3169–3174.
- [21] E. F. Flushing, M. Kudelski, L. M. Gambardella, and G. A. D. Caro, "Connectivity-aware planning of search and rescue missions," in *Proc. IEEE International Symposium on Safety, Security, and Rescue Robotics (SSRR)*, Oct 2013, pp. 1–8.
- [22] E. Frazzoli, M. Dahleh, and E. Feron, "Real-time motion planning for agile autonomous vehicles," *Journal of Guidance, Control, and Dynamics*, vol. 25, pp. 116–129, 2002.
- [23] J.-C. Latombe, *Robot Motion Planning*. Kluwer, 1991.
- [24] S. Waharte and N. Trigoni, "Supporting search and rescue operations with UAVs," in *Proc. International Conference on Emerging Security Technologies (EST)*, October 2010, pp. 142–147.

[25] L. Lin and M. A. Goodrich, "UAV intelligent path planning for wilderness search and rescue," in Proc. IEEE/RSJ International Conference on Intelligent Robots and Systems (IROS), Oct 2009, pp. 709–714.

BIOGRAPHIES



EVSEN YANMAZ received the BS degree in electrical and electronics engineering from Bogazici University in 2000, the MS degree in electrical engineering from SUNY at Buffalo in 2002, and the PhD degree in electrical and computer engineering from Carnegie Mellon University, in 2005. She is an assistant professor at Ozyegin University.

Previously, she held positions as a senior researcher and project leader at Lakeside Labs, Klagenfurt, as a senior researcher at the NES Institute at the University of Klagenfurt, as a postdoctoral researcher at the Los Alamos National Laboratory, and as a researcher at Carnegie Mellon University. Her research interests include drone networks, self-organizing networks, cooperative networks, and coordination of airborne and ground sensor networks. She published more than 50 peer-reviewed works focusing on the fields of telecommunications, networking, self-organization, and path planning.

An Internet of Things (IoT) based Monitoring System for Oil-immersed Transformers

O. YAMAN and Y. BICEN

Abstract—While the electricity power industry in the world continues to grow, it also becomes more traceable and smart with the developing technology. Naturally, the integration of these technologies into the electrical power systems brings with an additional cost. Most of the time producers and consumers struggle under the pressure of these additional costs and try new products that will reduce the cost. In this sense, competitive products in the market must be advantageous in terms of cost. In this study, an original IoT based transformer monitoring system has been developed by using open source software, modular and low cost components as an alternative to studies in literature. Arduino Mega 2560 microcontroller has been used as the main component in the system. The system can acquire data from a wide variety of sensors using internal and external transducers. And this data can be saved to the cloud system synchronously with the memory card on the monitoring system. The developed monitoring system has been utilized free and reliable platforms such as the ThingSpeak web interface and PushingBox Notification application. The all test process of the developed monitoring system has been carried out in the laboratory environment on a prototype transformer.

Index Terms— Internet of Things, IOT, Lifetime, Monitoring, Transformer

I. INTRODUCTION

THE CONTINUOUS increase in the world population leads to an increase in energy demand. That means an additional capacity increase for those existing in electrical power systems. One of the most important parts of the energy transmission and distribution ring is oil filled transformer and affected by these capacity increase [1-3]. For this reason, it is very important to monitor the load conditions and operational performance of the transformers [4,5]. Also, demand for smart grid applications is increasing all over the world with the technological development [6-8]. Since the monitoring technologies are a sector with high R&D investments, the costs of the technologies produced are quite high [9-12]. In addition, many different companies develop different

monitoring systems in their own area of expertise [13-14]. When several monitoring systems are used together, costs can be very high. Although low-cost applications are limited in the literature, they have become popular. These applications are generally focused on monitoring technologies. It is very limited in terms of intervention, diagnostics or recognition. In a similar application, the current, voltage parameters for the distribution transformers were monitored by the ThingSpeak web interface [15]. In another study, the data were monitored using the low cost ESP8266 wireless module and Arduino Uno microcontroller [16]


In this study, it is aimed to develop a low cost and open source monitoring system that can be an alternative to high cost monitoring systems in the literature. The main advantage of using the open source software of the monitoring system is that it allows the user to modify and improve the system software. Developed system is based on Internet of Things (IoT) and is intended to perform the tasks defined in the electronic card. The open source Arduino Mega 2560 microcontroller developed by Atmel has been used in the transformer monitoring system. The Arduino development environment (IDE) is based on "Processing" and the Arduino programming language is based on "Wiring". The data received from the sensors on the transformer can be stored in the monitoring system and/or can be sent to the cloud system. Also, this data can be monitored via user-defined computers, tablets and phones. The monitoring system gives warning and informs the operator when the safe operating limit values are exceeded. These limit values, which are defined as default in accordance with the standard, can be easily updated on software in accordance with the information and approval of the operator. There are input modules for sensors on the board as well as output modules that can perform different tasks.

In this paper, the components of transformer monitoring system have been defined at section 2; the ThingSpeak web interface integration has been introduced used for the monitoring system at section 3, the PushingBox Notification application has been described at section 4, The details of the aging and lifecycle monitoring have been presented at section 5, and the final section contains the conclusions and recommendations, respectively.


II. TRANSFORMER MONITORING SYSTEM DESIGN

While designing the monitoring system, it has been aimed to be fulfilling five key functions. Firstly, it should be possible to get the data from the sensors with different input parameters

YUNUS BICEN, is with Department of Electrical-Electronics Engineering, University of Duzce, Duzce, Turkey, (e-mail: yunusbicen@duzce.edu.tr).

 <https://orcid.org/0000-0001-8712-2286>

OKAN YAMAN, is with Institute of Science and Technology, University of Duzce, Duzce, Turkey, (e-mail: yaman41okan@gmail.com).

 <https://orcid.org/0000-0002-4074-4050>

Manuscript received February 9, 2019; accepted June 11, 2019.
DOI: [10.17694/bajece.524921](https://doi.org/10.17694/bajece.524921)

and to perform instant monitoring. Secondly, it should be possible to save this data both on its own system and on the cloud system. Thirdly, it should be ensured that analytical procedures can be performed on the system and the limit values related to the measured quantities are identifiable. Fourthly, in case of exceeding the limit values specified by the operator, he / she must fulfil the warning / information tasks and activate the pre-defined output relays. Finally, it has been

expected to show the aging condition and the remaining service life estimation in accordance with the IEEE standard.

In this context, monitoring system components that can perform the specified functions have been determined and a general concept scheme has been created as shown in Fig. 1. Then, the flow chart of the monitoring system has been composed as shown in Fig. 2.

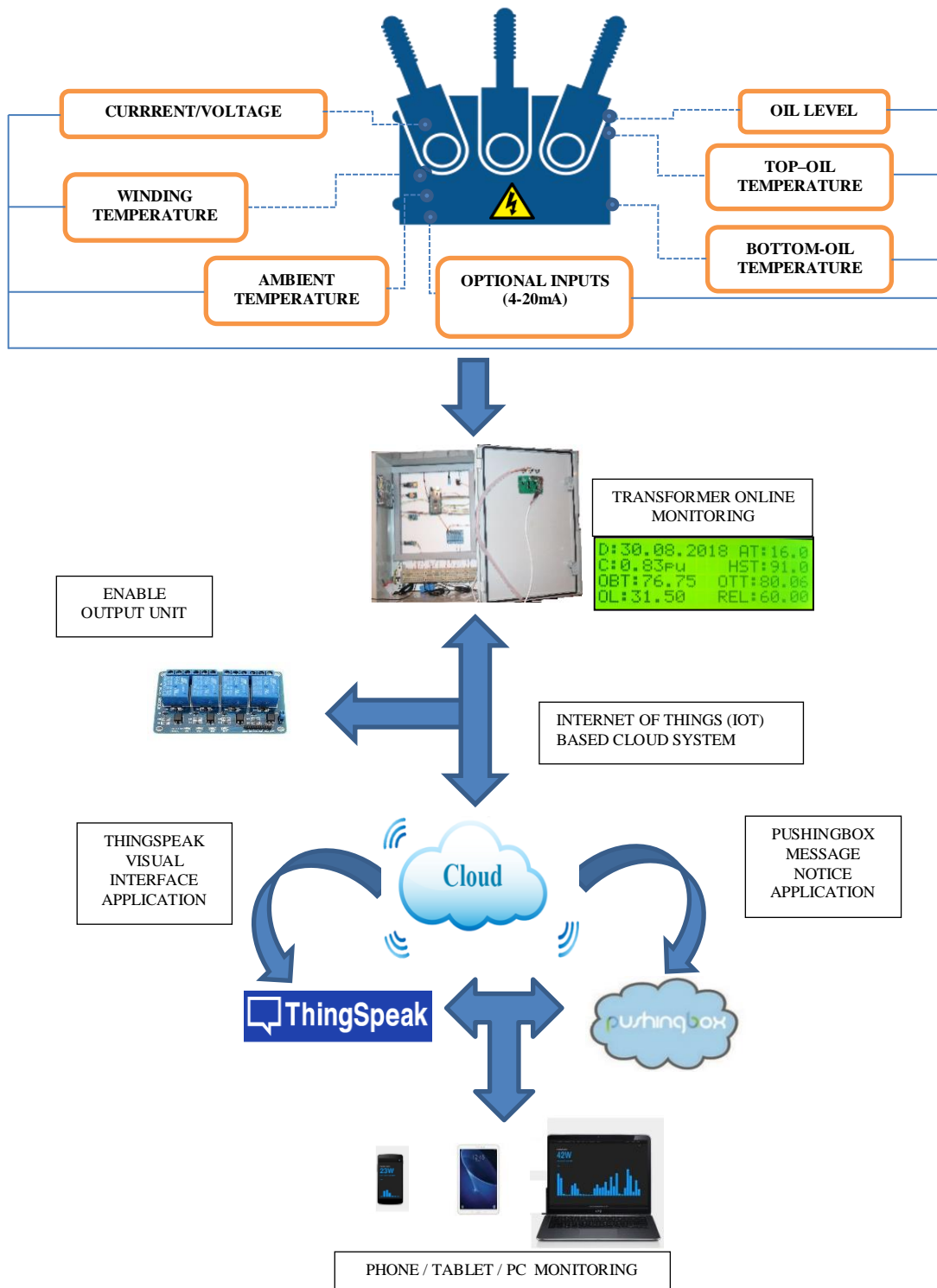


Fig. 1. Block diagram of transformer monitoring system

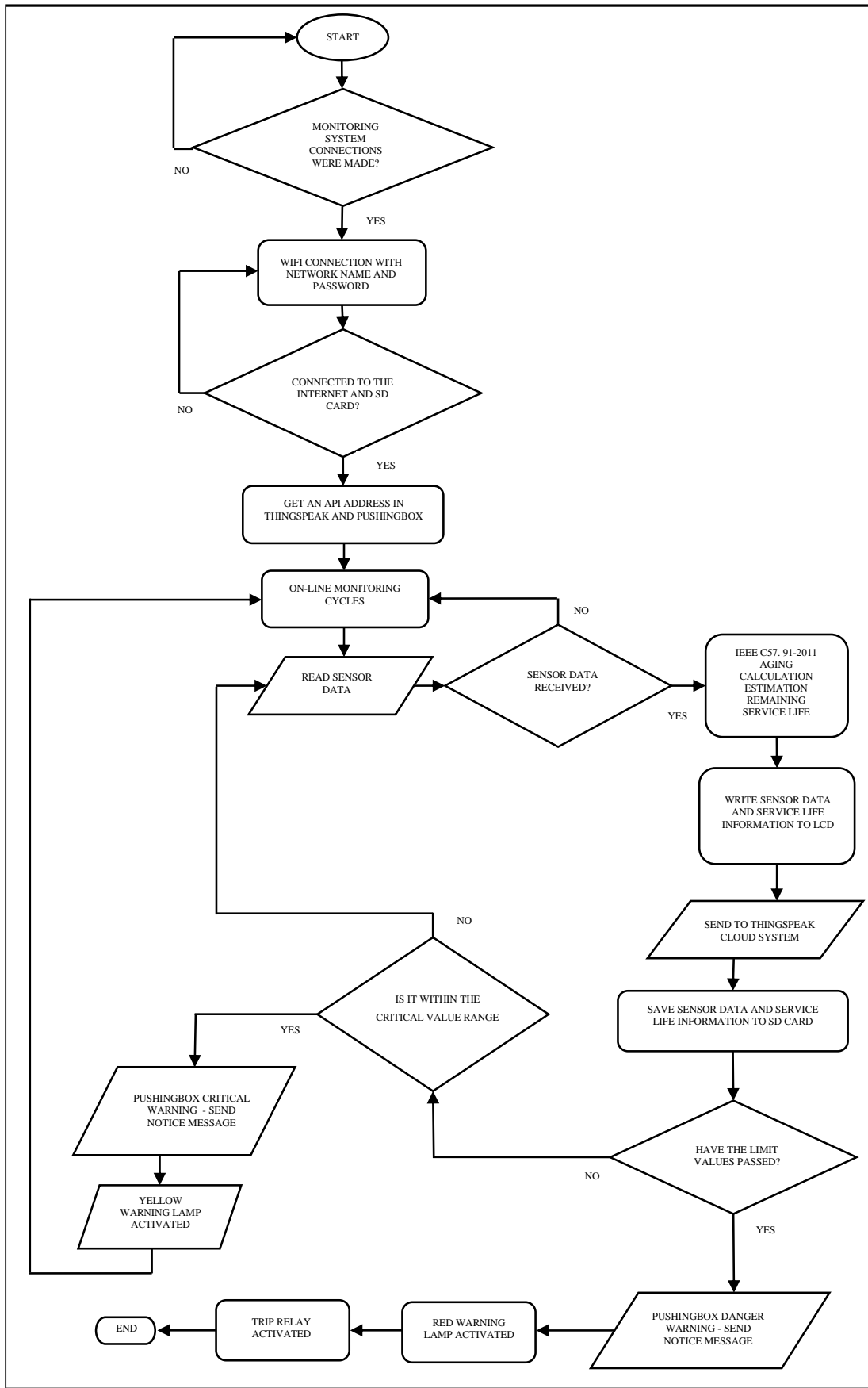


Fig. 2. Transformer monitoring system flow-chart

The analogue signals accrued from different sensors installed on the transformer have been scaled between 0-5V using transducer modules. Many parameters with standard sensor signals such as temperature (ambient, oil and hot-spot), current / voltage, insulation fluid level and so on can be defined as input. In this study, the temperature values at different points have been obtained by different sensors. The best measurement for hot-spot is done with fiber-optic sensors [18,19]. However, it is still a disadvantaged option considering the cost-benefit relationship [20]. Therefore, K type thermocouple with a precision of 0.25 degrees Celsius and rapid response time has been preferred for acquiring the temperature data from hot-spot. The digital temperature sensor DS18B20, manufactured by Dallas, has been used for oil and oil. This sensor is a very good option for its compatibility with the microcontroller, its ease of use and its resolution of up to

12 bits. The DHT11 digital sensor is used to measure the ambient temperature. This sensor which is capable of measuring with a resolution of 8 bits by 2% error margin between 0-50 degrees Celsius has been preferred because of its low cost and it can also receive the ambient humidity data optionally. A magnetic float level sensor has been used to measure the oil level. It has been made of heat-resistant stainless steel that producing an analogue output of 0-5V. As the current sensor, the non-invasive AC SCT-013 model, which was developed by YHDC, has been preferred. This sensor output is between 0-50 mA and can be used to measure AC currents up to a maximum of 100 A. In addition to being compatible with microcontroller, it provides ease of use thanks to its clamp structure. A simple RC filter has been added to the sensor output in order to provide accurate values for the measurement results against external interference [21].

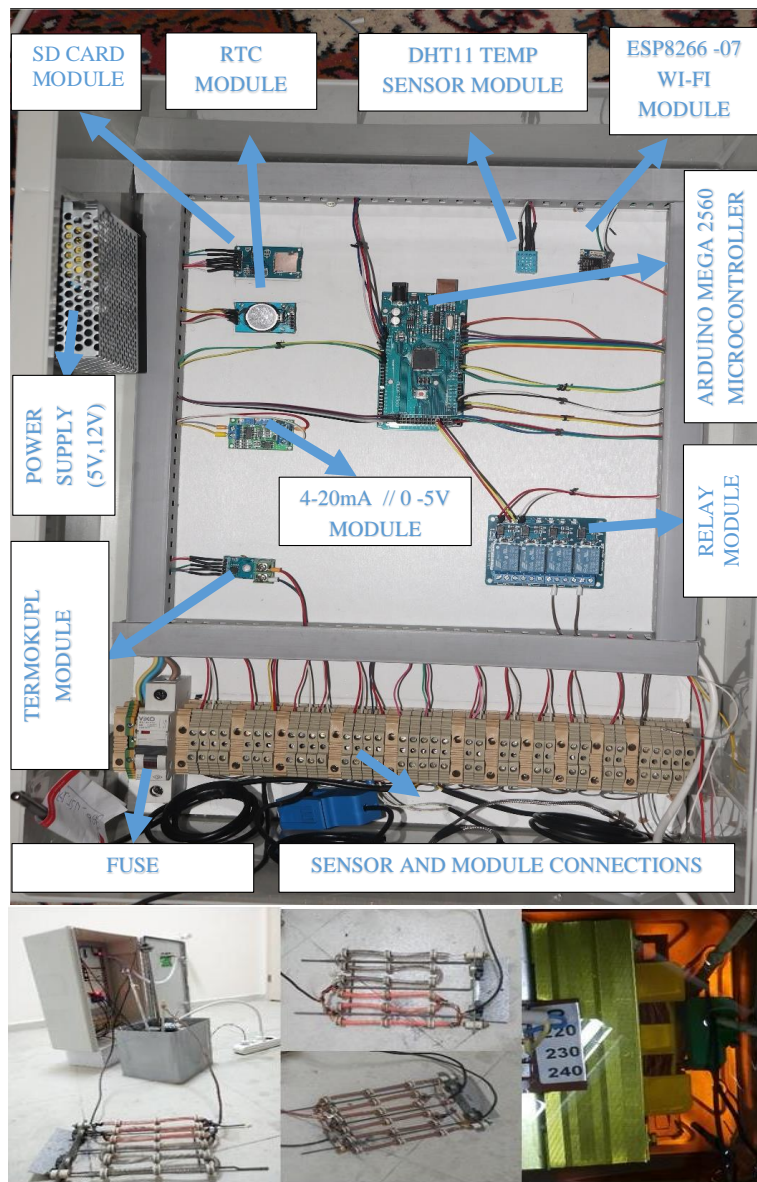


Fig. 3. Transformer monitoring system and test equipment

Different parameters which cannot be taken as data in this study can be included with expansion modules in the following periods. In order to integrate sensors with a 4-20mA output to the monitoring system, an analogue transducer module from 0 to 5V has been used.

The mini SD card module has been used with the RTC-DS3231 module in order to store the data received from the transformer with date and time information. The RTC-DS3231 module supports the I2C communication protocol. The ESP8266-07 series has been chosen as a Wi-Fi module for wireless transmission of sensor data to the cloud. This module has low power consumption and low cost. It also has a built-in antenna and supports the TCP / IP protocol. With this module that supports the Internet of Things (IOT), the data received from the sensors have been easily transferred to the ThingSpeak web interface. Also, the measured parameters of the transformer can be monitored on the panel of the system with the 20x4 LCD display. Yellow and red led, which are activated in early warning and emergency situations, have been used on the panel. In similar emergency situations, the output relays on the panel are also activated in order to perform the functions previously defined by the operator according to the limit values. In the monitoring system, 50W switching power supply with 5V and 12V output and a fuse for system safety have been used. The inside of the completed panel of the monitoring system has been shown in the Fig. 3.

III. THE THINGSPEAK WEB INTERFACE

In recent two decades, with the rapid development of internet technology, it has become possible to design different

monitoring and control systems. One of these technologies is the Internet of Things (IoT). This structure is based on the idea of collecting, analyzing, making decisions and managing the data of the environment in which the objects are located on a common platform [22,23]. ThingSpeak is an open IOT platform using for real-time monitoring of the data and the data accrued from the sensors can be monitored by means of a user-defined IP address and ThingSpeak API key [24]. Any other user can see or download the data by using ThingSpeak at any location, if the system operator uses the public IP address. The user can also add location information.

In this study, 2 API addresses have been defined in ThingSpeak interface as shown in Fig. 4. These have been used for transformer online monitoring system Fig. 5. The transformer online monitoring system interface shows real-time winding (hot-spot) temperature, oil bottom, top-oil and ambient temperatures, oil level and current data from the sensors. It is observed that the ambient temperature is constant in the test environment. When the transformer load is increased in a controlled manner, it is seen that the winding temperature increases with the current. Increased winding temperature increases the aging factor. The aging condition and the remaining service life estimation have been calculated by reference to the hot spot temperature. At the oil level, there was no change during the test. The data accrued from the sensors and then calculated parameter changes have been shown in the ThingSpeak Graphical Interface. Fig. 6 shows that the same data can also be accessed via the mobile device. In this way, the system is constantly under the control of the operator.

The screenshot displays the ThingSpeak web interface. At the top, there is a navigation bar with 'ThingSpeak™' logo and menu items: 'Channels', 'Apps', 'Community', and 'Support'. Below this, the main heading is 'My Channels'. There is a 'New Channel' button and a search bar labeled 'Search by tag'. A table lists two channels:

Name	Created	Updated
Transformer Online Monitoring	2018-08-10	2018-12-17 17:39
Transformer Estimate The Remaining Life	2018-08-30	2018-12-17 17:41

Each channel entry has buttons for 'Private', 'Public', 'Settings', 'Sharing', 'API Keys', and 'Data Import / Export'. Below the table, there is a detailed view of the 'Transformer Online Monitoring' channel, showing its ID (557459), author (okanyaman1), and access level (Private). It also includes options for 'Private View', 'Public View', 'Channel Settings', 'Sharing', 'API Keys', and 'Data Import / Export'. There are buttons for 'Add Visualizations', 'Add Widgets', and 'Export recent data'. A 'Channel Location' map is shown on the right, with a red pin indicating the location in Turkey. At the bottom, 'Channel Stats' are displayed: Created: 3 months 2 weeks, Last entry: 3 days 2 weeks, Entries: 3117.

Fig. 4. ThingSpeak web interface

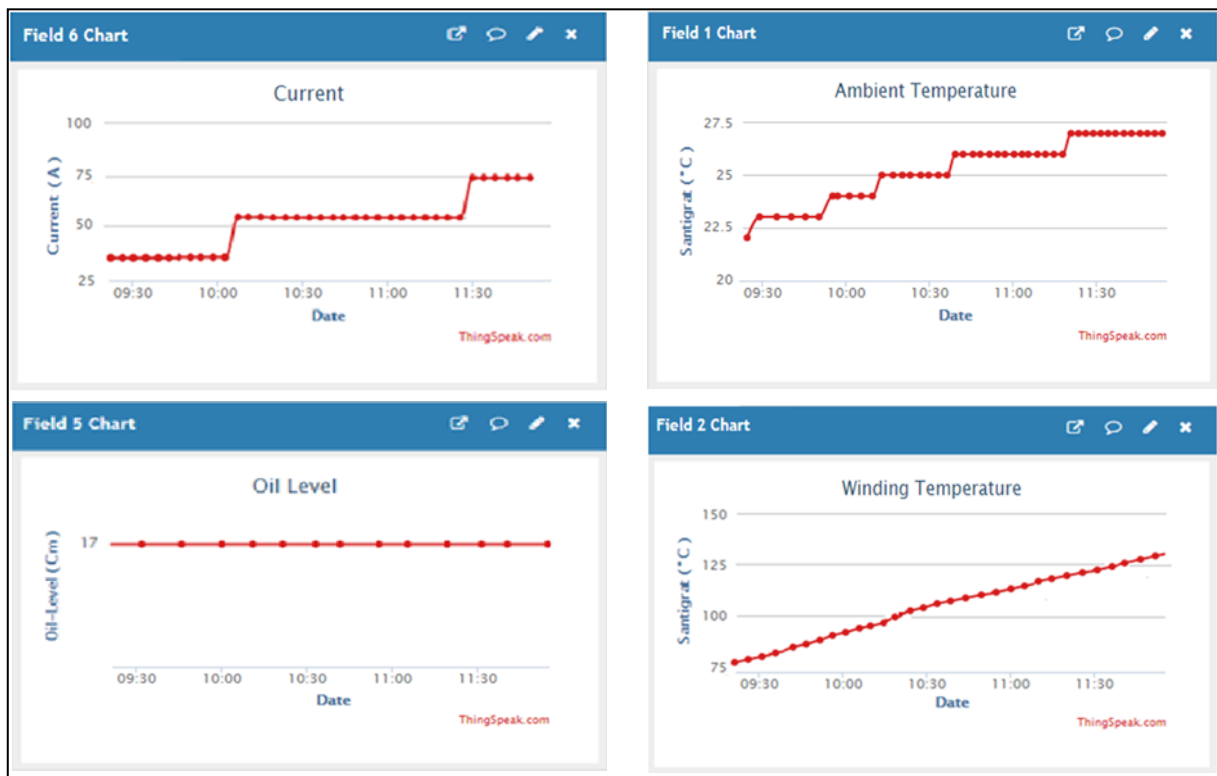


Fig. 5. ThingSpeak sensor data graphical interfaces

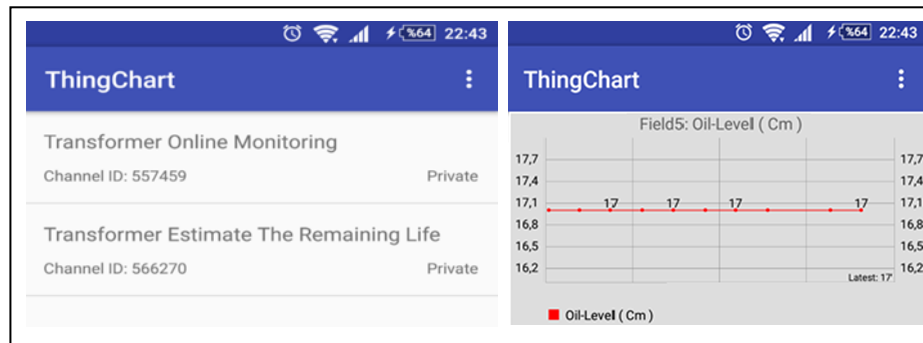


Fig. 6. ThingSpeak mobile interface

IV. PUSHINGBOX NOTIFICATION SERVICE

PushingBox is defined as a cloud that runs with the Internet of Things (IoT) and can send many real time notifications like e-mail, tweet based on API calls [25, 26]. This free platform supports working with the ESP8266 Wi-Fi module. In this way, if any data received from the sensors exceed the critical values, the notification message can be sent to the computer and/or android device with this application. The warning notifications have been tested by deliberately exceeding the limit values, within the scope of this study. For this purpose, an API address has been defined in order to receive notification from PushingBox. Then different notification scenarios have been created with this API address. Fig. 7 show images of PushingBox interfaces.

V. THE REMAINING SERVICE LIFE ESTIMATION DISCUSSIONS

The loss of life calculation and the remaining service life estimation require analytical processing in the monitoring system. According to IEEE-C57.91-2011 standards, the loss of life calculations has been performed with reference to the hot-spot temperature in windings [27]. According to the relevant standards, the service life of the transformer in the case of nominal operation is 20.55 years [28,29]. However, it is known that the service life of transformers varies with changing load conditions [30,31]. The main reason is that the temperature values in the windings are variable due to the heat loss according to the loading conditions. Since the loading information and the temperature parameters can be received via the monitoring system, it can be performed aging calculations at high resolution as shown in Fig.8. In the meanwhile, the remaining service life of the transformer can also be estimated using the linear approach.

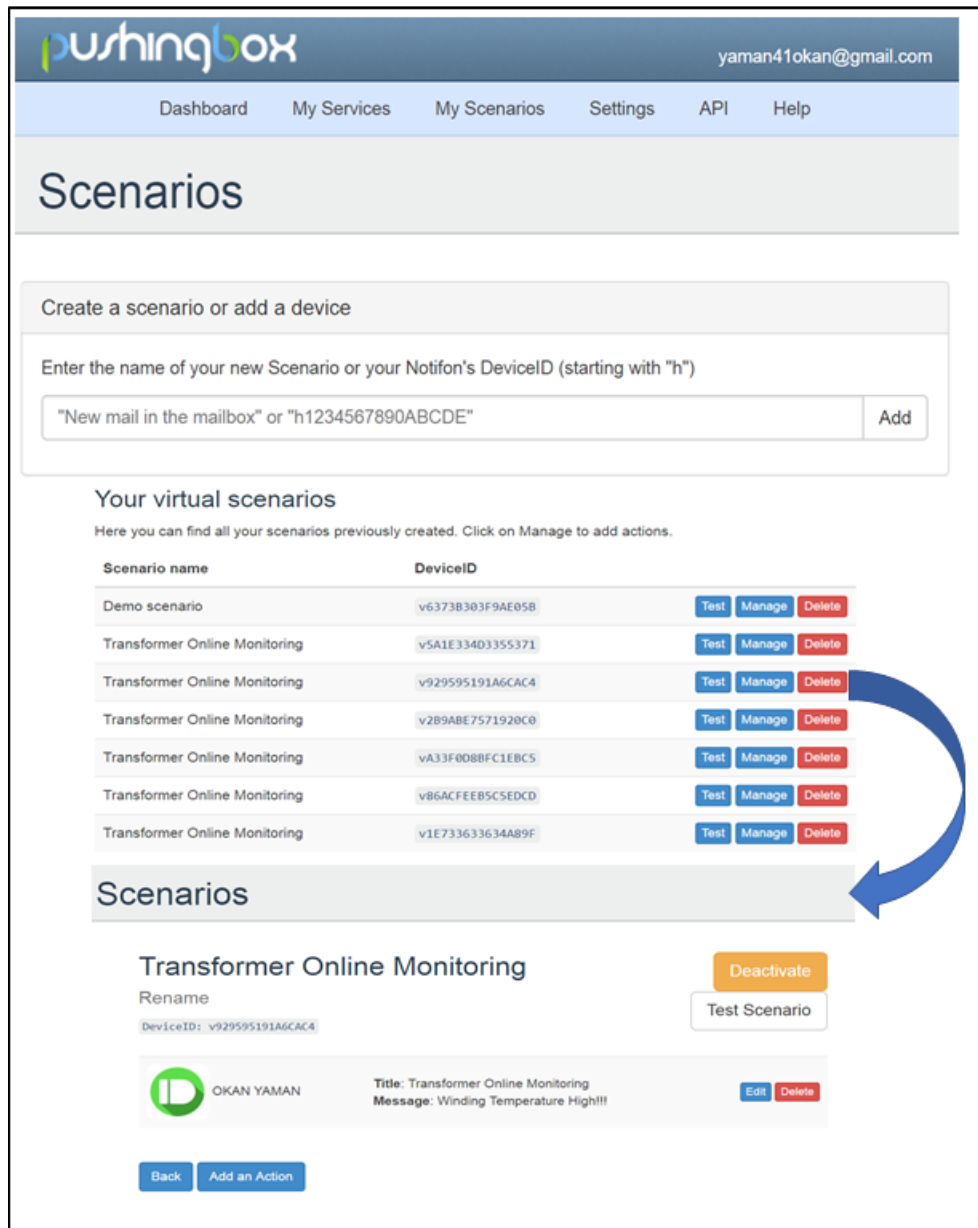


Fig. 7. PushingBox API addresses

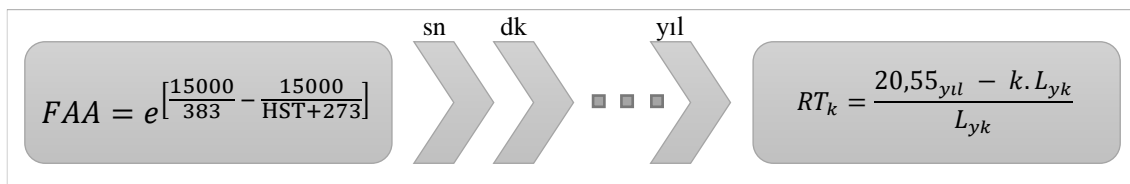


Fig. 8. Remaining service life estimation process

Where, FAA refers to the loss of life at a certain temperature and HST refers to the hot spot temperature. RT_k is remaining service life value, k is year index, L_{yk} is refers to the total loss of life coefficient up to k year. The average of the total data obtained from the second period is taken as a single value to the period of minutes. Likewise, the average of the sum of the data obtained from the minute period is shifted to the hourly period. In this way, the loss of life calculated in seconds can be calculated by adding the loss of life in the

annual period. In this way, the loss of life calculated in seconds is carried in high resolution up to years. The instant aging acceleration factor, the total loss of life and the remaining service life estimation values can be shown on the LCD display with monitoring system. Similar information can also be displayed as graphical form within the ThingSpeak interface like in Fig. 9.

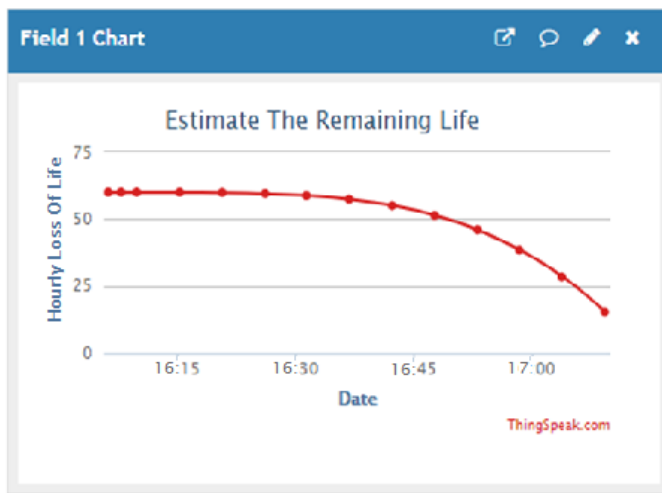


Fig. 9. ThingSpeak service life monitoring

VI. CONCLUSION

In this study, an original IoT based monitoring system has been developed by using open source software, modular and low cost components. With this system, data can be acquired from different sensors and can be monitored in various environments such as LCD display, computer, mobile phones, and tablets continuously. For this purpose, the ThingSpeak platform free web interface supporting the Internet of Things (IoT) technology has been integrated into the system. In addition, the PushingBox application, which supports IoT technology, can send warning messages without additional hardware and cost. The developed system is capable of performing service life monitoring by using aging equations given in IEEE-C57.91-2011 standards according to change of HST point depending on the loading conditions of transformer. Although the developed system has been designed to monitor a transformer, it is possible to monitor the units in a number of different locations at the same time as replicating similar monitoring platforms. The developed system has been tested on a prototype transformer. It was observed that the data collection, calculation operations and output signals according to the limit values, service life management, recording operations and warning systems were working without error. As a result, this system provides a low-cost alternative to high-cost professional monitoring systems.

REFERENCES

- [1] Su, Yu, et al. "Optimal Planning Method of On-load Capacity Regulating Distribution Transformers in Urban Distribution Networks after Electric Energy Replacement Considering Uncertainties." *Energies* 11.6 (2018): 1457.
- [2] Biçen, Yunus, and Faruk Aras. "Loadability of power transformer under regional climate conditions: the case of Turkey." *Electrical Engineering* 96.4 (2014): 347-358.
- [3] Humayun, Muhammad, et al. "Demand response for operational life extension and efficient capacity utilization of power transformers during contingencies." *IEEE Transactions on Power Systems* 30.4 (2015): 2160-2169.
- [4] Osztermayer, J., et al. "Asset management based on improved online monitoring systems applied to a 110/380 kV substation." *Power Tech Conference Proceedings, 2003 IEEE Bologna. Vol. 4. IEEE, 2003.*
- [5] Tenbohlen, Stefan, et al. "Diagnostic measurements for power transformers." *Energies* 9.5 (2016): 347.
- [6] Kun, Wang. "A survey on energy Internet: architecture, approach, and emerging technologies." *IEEE Syst J* (2017).
- [7] Abiri-Jahromi, Amir, et al. "A two-stage framework for power transformer asset maintenance management—Part II: Validation results." *IEEE Transactions on Power Systems* 28.2 (2013): 1404-1414.
- [8] Ma, Hui, et al. "Smart transformer for smart grid—intelligent framework and techniques for power transformer asset management." *IEEE Transactions on Smart Grid* 6.2 (2015): 1026-1034.
- [9] Velasquez-Contreras, Juan L., Miguel A. Sanz-Bobi, and Samuel Galceran Arellano. "General asset management model in the context of an electric utility: application to power transformers." *Electric Power Systems Research* 81.11 (2011): 2015-2037.
- [10] Mariño, Perfecto, et al. "Development of condition monitoring instrumentation for sensing power transformers." *INTERNATIONAL CONFERENCE ON SENSING TECHNOLOGY. Vol. 1. 2005.*
- [11] Islam, Md Mominul, Gareth Lee, and Sujeeva Nilendra Hettiwatte. "A review of condition monitoring techniques and diagnostic tests for lifetime estimation of power transformers." *Electrical Engineering* 100.2 (2018): 581-605.
- [12] Abu-Elanien, Ahmed EB, and M. M. A. Salama. "Asset management techniques for transformers." *Electric power systems research* 80.4 (2010): 456-464.
- [13] Murugan, Raji, and Raju Ramasamy. "Failure analysis of power transformer for effective maintenance planning in electric utilities." *Engineering Failure Analysis* 55 (2015): 182-192.
- [14] Wagle, Anant M., et al. "Real time web based condition monitoring system for power transformers-Case study." *Condition Monitoring and Diagnosis, 2008. CMD 2008. International Conference on. IEEE, 2008.*
- [15] M. Poongothai, P. M. Subramanian, and A. Rajeswari, "Design and implementation of IoT based smart laboratory," 2018 5th Int. Conf. Ind. Eng. Appl. ICIEA 2018, pp. 169–173, 2018.
- [16] H. Jamal, M. F. Nadeem Khan, A. Anjum, and M. K. Janjua, "Thermal Monitoring and Protection for Distribution Transformer Under Residential Loading Using Internet of Things," 2018 IEEE Glob. Conf. Internet Things, no. January, pp. 1–6, 2019.
- [17] Tenbohlen, S., and F. Figel. "On-line condition monitoring of power transformers." *Power Engineering Society Winter Meeting, 2000. IEEE. Vol. 3. IEEE, 2000.*
- [18] Arabul, Ahmet Yigit, Fatma Keskin Arabul, and Ibrahim Senol. "Experimental thermal investigation of an ONAN distribution transformer by fiber optic sensors." *Electric Power Systems Research* 155 (2018): 320-330.
- [19] Deng, Jian- Gang, et al. "Hot- spot temperature and temperature decay rate measurement in the oil immersed power transformer through FBG based quasi- distributed sensing system." *Microwave and Optical Technology Letters* 59.2 (2017): 472-475.
- [20] Bengtsson, C. "Status and trends in transformer monitoring." *IEEE Transactions on Power delivery* 11.3 (1996): 1379-1384.
- [21] OpenEnergyMonitor, (2019, 6 Mart). [Online]. Erişim: <https://learn.openenergymonitor.org/electricity-monitoring/ct-sensors>
- [22] Bagheri, Mehdi, Amin Zollanvari, and Svyatoslav Nezhipenko. "Transformer Fault Condition Prognosis Using Vibration Signals Over Cloud Environment." *IEEE Access* 6 (2018): 9862-9874.
- [23] Mohamad, Aday AH, Yaqeen S. Mezaal, and Seevan F. Abdulkareem. "Computerized power transformer monitoring based on internet of things." *International Journal of Engineering & Technology* 7.4 (2018): 2773-2778.
- [24] Meana-Llorián, Daniel, et al. "IoFClima: The fuzzy logic and the Internet of Things to control indoor temperature regarding the outdoor ambient conditions." *Future Generation Computer Systems* 76 (2017): 275-284.
- [25] Fioccola, Giovanni B., et al. "Polluino: An efficient cloud-based management of IoT devices for air quality monitoring." *Research and Technologies for Society and Industry Leveraging a better tomorrow (RTSI), 2016 IEEE 2nd International Forum on. IEEE, 2016.*
- [26] Joshi, Shreedhar A., et al. "Home automation system using wireless network." *Communication and Electronics Systems (ICCES), 2017 2nd International Conference on. IEEE, 2017.*
- [27] IEEE Guide for Loading Mineral-Oil-Immersed Transformers, IEEE C57.91-1995.
- [28] Biçen, Yunus, et al. "Aging of Paper Insulation in Natural Ester & Mineral Oil." *Electrical and Electronic Engineering* 2.3 (2012): 141-146.

- [29] Agah, SM Mousavi, and H. Askarian Abyaneh. "Quantification of the distribution transformer life extension value of distributed generation." *IEEE Transactions on Power Delivery* 26.3 (2011): 1820-1828.
- [30] Vaidya, Chinmay V., et al. "Evaluation of High Temperature Operation of Natural Ester Filled Distribution Transformers." 2018 North American Power Symposium (NAPS). IEEE, 2018.
- [31] Biçen, Yunus, Faruk Aras, and Hulya Kirkici. "Lifetime estimation and monitoring of power transformer considering annual load factors." *IEEE Transactions on Dielectrics and Electrical Insulation* 21.3 (2014): 1360-1367.

BIOGRAPHIES



OKAN YAMAN was born in Kocaeli, Turkey in 1995. He received the B.S. Electrical from the University of Tokat Gaziosmanpaşa, Tokat in 2017. He is currently an MSc student in Institute of Science and Technology at the University of Duzce. His research interests include automation systems, electronic circuit design and applications.



YUNUS BICEN was born in Kastamonu, Turkey in 1981. He received the BSc degree from Kocaeli University, Electrical Education Department, in 2004, the MSc and PhD degrees from Kocaeli University, Turkey in 2007 and 2012 respectively. He was with the University of Kocaeli between 2004 and 2008. Currently, he works as an Associate Professor at the Department of Electrical-Electronics Engineering - Duzce University. His research interests are in the area of power systems analysis, aging of power system equipment, fault diagnostics and development of computer aided programs.

Mobile Robot Navigation Using Reinforcement Learning in Unknown Environments

M. U. KHAN

Abstract— In mobile robotics, navigation is considered as one of the most primary tasks, which becomes more challenging during local navigation when the environment is unknown. Therefore, the robot has to explore utilizing the sensory information. Reinforcement learning (RL), a biologically-inspired learning paradigm, has caught the attention of many as it has the capability to learn autonomously in an unknown environment. However, the randomized behavior of exploration, common in RL, increases computation time and cost, hence making it less appealing for real-world scenarios. This paper proposes an informed-biased softmax regression (iBSR) learning process that introduce a heuristic-based cost function to ensure faster convergence. Here, the action-selection is not considered as a random process, rather, is based on the maximum probability function calculated using softmax regression. Through experimental simulation scenarios for navigation, the strength of the proposed approach is tested and, for comparison and analysis purposes, the iBSR learning process is evaluated against two benchmark algorithms.

Index Terms— Reinforcement learning, mobile robots, navigation, autonomous, unknown environment

I. INTRODUCTION

IN RECENT years, the impact of robots in our daily lives and in industry has increased by manifolds. According to the World Robotics Report 2018, the demand for robots increased by 31% in one year as compared to 2016. Whether it is an industrial robot, mobile robot or any other, if it has to interact with the environment, it should be able to navigate. The task of navigation can be further broken down into localization and path planning. In localization, the robot's pose, i.e. its orientation and translation needs to be determined with respect to the surroundings. Path-planning is a process in which a robot should be able to find out its collision-free, feasible path in an on-line or off-line fashion, from the start to the goal point.

The task of path-planning can be more challenging in the presence of obstacles and in unknown environments. The basic trait of the autonomous mobile robot is that it should be

able to traverse through the obstacles in a safe manner and attain the goal position. Navigation requires the robot to continuously update its information about the surroundings and plan its next action, accordingly. In general, such information is acquired by means of various sources, such as GPS [1], ultrasonic [2], and laser range finder [3]. This information about the robot's pose and obstacles' location is, then, utilized to control the movements of the robot through its actuators.

Over the last decade, many researchers have been continuously striving to solve the problem of path-planning in an effective manner. The most notable algorithms in this respect are A* [4], Dijkstra [5], PRM [6], and RRT [7]. More recently, researchers have shown their keen interest towards biologically-inspired algorithms, such as ANN [8], GA [9], PSO [10], and RL [11]. Among these, RL algorithms have received special attention due to their efficient problem solving in various fields such as control engineering, game theory, and even robotics.


The most renowned one of all RL algorithms is Q-learning [12], proposed in 1989, based upon the learning from delayed rewards and punishments. Since then, many researchers have quite effectively utilized Q-learning for mobile robot navigation and obstacle avoidance [13, 14]. The Q-learning has also been tested for solving mobile robots' path-planning problem in 3D environments [15]. Many authors have also proposed hybrid approaches by combining the un-supervised RL with Fuzzy Logic [16, 17], or Artificial Neural Network [18, 19].

The learning process, true online SARSA Q-biased softmax regression (TOSL-QBIASSR) [20], evolved from classical Q-learning, has attempted to tackle a wide variety of robotic tasks with minimal tuning required. A complimentary low-reward-loop evasion algorithm has been utilized to avoid local minima sequences. An open-source software framework is also developed with a large collection of various learning processes.

Recent research has attempted to integrate deep learning with RL as deep reinforcement learning (DRL) to deal with a wide variety of control problems. Although, deep learning enables an effective learning process for high-dimensional tasks, it also requires high computational costs both in terms of the number of used cores and computational time. This is a drawback which prevents such algorithms to be considered for real-time applications.

From the literature review, the conclusion can be drawn that there is a remarkable tendency among researchers to solve navigation problems using RL since, in most cases the

MUHAMMAD UMER, KHAN, is with Department of Mechatronics Engineering, Atılım University, Ankara, Turkey, (e-mail: umer.khan@atilim.edu.tr).

 <https://orcid.org/0000-0002-9195-3477>

Manuscript received February 26, 2019; accepted June 10, 2019.

DOI: [10.17694/bajece.532746](https://doi.org/10.17694/bajece.532746)

environment is unknown and involves a great degree of uncertainty. The bench marking Q-learning algorithm has been tested for many scenarios and is found to be effective as it can deal with unknown non-deterministic Markovian systems. The more recent TOSL-QBIASSR learning tested for multiple tasks is claimed to be effective. Therefore, for comparison and analysis, Q-learning with softmax regression (Q-SR) and TOSL-QBIASSR has been chosen as the test bench.

In this paper, using simulation, it is shown that the proposed approach outperforms the Q-SR and TOSL-QBIASSR. In detail, the main focus of this research is to perform 2D navigation in an unknown environment by combining the recent TOSL-QBIASSR learning process with a more informed action-selection technique. The contributions of this paper are three-fold:

- The true online SARSA informed-Biased Softmax Regression (TOSL-iBSR) is proposed which introduce a heuristic-based cost function to TOSL-QBIASSR to ensure faster convergence;
- An optimum action-selection is proposed based upon the maximum probability function value of the state instead of randomly picking the action; and
- A learning process based upon the Boltzmann distribution does not use a constant thermodynamic temperature; rather, an annealing schedule is introduced to ascertain the global maximum by moving towards narrower and narrower regions from wider ones in the start.

The paper is structured as follows: In section II, a brief summary of RL is presented together with a problem statement. The proposed approach based upon the existing QBIASSR algorithm is detailed in Section III. Section IV addresses the environment setup and implementation issues. Section V includes simulation results, analysis and discussion. Finally, section VI summarizes the conclusion and future work.

II. BACKGROUND

In this section, a brief summary of the related RL algorithms is provided, followed by the problem statement.

Assumption:

The differential drive robot considered is from the broad class of Wheeled Mobile Robots (WMRs). It is assumed that the moving frame is associated to the robot using which location of the robot (x, y) in 2D plane and heading angle θ can be updated and available at all times.

2.1 Markov Decision Process

The process of learning and improvement has always been considered as a built-in feature among humans. Based upon these characteristics, a well-known mathematician, Alan Turing, invented the Turing machine in 1936 [21]. This machine mechanically operated on discrete states, where the

state register stored the state of the machine. It was also featured with decision-making so as to select suitable actions. Markov generalized this idea for the situations, where the outcomes are partly random and partly under the control of a decision-maker [22]. The process, formally named after Markov as Markov Decision Process (MDP), is extensively applied in many disciplines, such as robotics and automatic control to name a few. An MDP is defined as a 5-tuple

$(\mathcal{S}, \mathcal{A}, \mathcal{P}_a(s'|s, a), \mathcal{R}(r|s), \mathcal{G})$, where

- \mathcal{S} is a finite set of states,
- \mathcal{A} is a finite set of actions,
- $\mathcal{P}_a(s'|s, a)$ is the transition probability to define the chances that the next state s' will be picked as a consequence of action a ,
- $\mathcal{R}(r|s)$ is the expected reward received due to action a while in state s' , r is a signed value used for the reward or punishment,
- \mathcal{G} are specific parameters for some RL algorithms' settings. This will be the discount factor $\gamma \in [0, 1]$ and learning rate $\alpha \in [0, 1]$ in our case.

The output of the process is dependent upon the selection of the policy $\pi : \mathcal{S} \rightarrow \mathcal{A}$, that specifies the action $\pi(s)$, chosen by the decision-maker while in state s . The goal of the Markov record process is to determine the state and reward sequence given that the policy $\pi(s)$ ensures a maximum cumulative reward. RL has proved itself to be an effective tool for closed-loop problems that satisfy the Markov property as to maximize numerical reward in an unknown environment [11], [23], [24].

2.2 Reinforcement Learning

Almost in all RL algorithms, the main focus of RL algorithms is upon maximizing policy value \mathcal{V} , which is a direct indicator of the long-term desirability of states considering the rewards available in those states.

Widely accepted, Q-learning is probably the most practical and effective algorithm that belongs to the Temporal Difference (TD) learning, a model-independent and fully-incremental algorithm. The state-value function V^π gives information about the desirability of that state for an agent under a policy π , and is defined as:

$$V_k^\pi(s) = \max_a Q_k(s, a) \quad (1)$$

The successful outcome of the Q-learning (Algorithm 1), as well as of most RL algorithms is heavily affected by the exploration and exploitation phenomena. The optimal choice between these two needs to be made because none of them can be pursued exclusively without failing at the task. The agent's behavior must be evaluated by repeatedly trying different combinations of parameters α and γ in order to define the balance between the two.

Algorithm 1: Q-Learning**Input:**

States $\mathcal{X} = \{1, \dots, n_x\}$
 Actions $\mathcal{A} = \{1, \dots, n_a\}$
 Reward function $\mathcal{R}: \mathcal{X} \times \mathcal{A} \rightarrow \square$
 Learning rate $\alpha \in [0, 1]$, typically α is set to be 0.1
 Discounting factor $\gamma \in [0, 1]$

Procedure:

Initialize $Q: \mathcal{X} \times \mathcal{A} \rightarrow \square$ arbitrarily
repeat
 Pick state $s \in \mathcal{X}$
repeat
 select new action a (based upon the exploration strategy)
 perform action a
 observe new state s' and attain reward \mathcal{R}
 update
 $Q(s, a) \leftarrow Q(s, a) + \alpha(\mathcal{R} + \gamma V(s') - Q(s, a))$
 $V(s) = \max_a Q(s, a)$
 update state $s \rightarrow s'$
until s is not a terminal state
until Q is not converged

Output:

Best action selection a'

An improved and practical modification to the Q-learning, State-Action-Reward-State-Action (SARSA) [25], performs the learning based upon the action performed by the current policy instead of the greedy policy.

$$Q(s, a) \leftarrow Q(s, a) + \alpha(\mathcal{R} + \gamma Q(s', a') - Q(s, a)) \quad (2)$$

Hence, a' , the action to be performed in the next step must also be evaluated before updating $Q(s, a)$. Another variant of SARSA, the true online SARSA(λ) algorithm (TOSL), proved to be a more efficient learning process [26].

The recently proposed mechanism, TOSL-QBIASSR, combines the advantages of both TOSL and softmax regression. The basic idea is to improve efficiency for the cases where agent experiences new states with strong resemblance to already explored ones. In this approach, softmax regression is performed over a scaled Q-value, defined as $Q(s)_{biased}$:

$$Q(s)_{biased} \leftarrow Q(s) + bias(s) \quad (3)$$

where, $bias(s)$ is a vector generated based upon the information gathered from other states of Q similar to s . At each step the bias is updated using averaged information from sets of states that share some structure with the current state s . The working of TOSL-QBIASSR is detailed in Algorithm 2 [20]:

Algorithm 2: TOSL Q-biased softmax regression (TOSL-QBIASSR)**Input:**

States $\mathcal{S} = \{s_1, s_2, \dots, s_m\}$
 Actions $\mathcal{A} = \{a_1, a_2, \dots, a_p\}$
 Input variables $\mathcal{X} = \{x_1, x_2, \dots, x_n\}$
 $Q(s) = [Q(s, a_1), Q(s, a_2), \dots, Q(s, a_p)]$
 $\mathcal{SQ}(s \in \mathcal{S}, x_i \in \mathcal{X}) = \text{subset of states } ss \in \mathcal{S} \text{ with}$
 $x_j(ss) = x_j(s) \forall j \in [1, 2, \dots, n] \neq i$
 Agent in state s must select action a' given Q

Procedure:

for all the $x_i \in \mathcal{X}$ **do**
 $bias(s, x_i) \leftarrow \text{avg}(\mathcal{SQ}(s, x_i)) \quad \forall ss \in \mathcal{SS}(s, x_i),$
 pick state $s \in \mathcal{X}$
end
 $bias(s) \rightarrow \frac{1}{n} \sum_{i=0}^n bias(s, x_i)$
 $Q(s)_{biased} \leftarrow Q(s) + bias(s)$
 $a' \leftarrow \text{softmax_selection}(Q_{biased}, Temperature)$

Output:

Best action selection a'

2.3 Problem Statement

Consider an agent, in our case a mobile robot, operating in a virtual environment in the presence of obstacles. Given the initial state s_0 and ending goal state g , the robot has to determine its path using RL. The path is a sequence of adjacent traversable cells, $(s, next(s), next(s), \dots, g)$; and $next(x)$ stands for the successor of cell x and, for this paper, it will be the neighboring (adjacent) cell.

III. LEARNING PHASE OF THE AGENT

In mobile robotics, navigation and wandering are considered as the foremost scenarios for operating with the former regarded as more complex. In robotics navigation, the task is to enroute through the obstacles safely and approach the target. In most RL algorithms, the mobile robot observes the environment and updates its reward, which it intends to maximize. Usually, the agent drives itself based upon the acquisition of the highest award. Therefore, it is desired to induce information about the goal to accelerate the achievement of the highest reward, thus also ensuring that the agent approaches the solution in a finite time.

In TOSL-iBSR (Algorithm 3), an acceptance probability function $P(e, e', T)$, depending upon energies $e = E(s)$ and $e' = E(s')$ of the two states and a global time varying temperature T , is introduced in order to define the probability

Algorithm 3: TOSL informed-biased softmax regression (TOSL-iBSR)**Input:**

States $\mathcal{S} = \{s_1, s_2, \dots, s_m\}$
 Actions $\mathcal{A} = \{a_1, a_2, \dots, a_p\}$
 Input variables $\mathcal{X} = \{x_1, x_2, \dots, x_n\}$
 $Q(s) = [Q(s, a_1), Q(s, a_2), \dots, Q(s, a_p)]$
 Temperature $\mathcal{T} \leftarrow \mathcal{T}_{max}$
 $\mathcal{SQ}(s \in \mathcal{S}, x_i \in \mathcal{X}) = \text{subset of}$
 states $ss \in \mathcal{S}$ with $x_j(ss) = x_j(s) \forall j \in [1, 2, \dots, n] \neq i$
 Agent in state s must select action a' given Q

Procedure:

for all $x_i \in \mathcal{X}$
 if $ss \in \mathcal{SQ}(s, x_i)$
 pick state $s \in \mathcal{SS}$
 end
 generate biased state $bias(s) \rightarrow \frac{1}{n} \sum_{i=0}^n bias(s, x_i)$
 generate virtual vector $Q(s)_{biased} \leftarrow Q(s) + bias(s)$
 temperature update $\mathcal{T} \leftarrow g(\mathcal{T})$
 input feature for softmax
 regression $z^{(i)} \leftarrow \frac{Q(s)_{biased} + J(s')}{\mathcal{T}}$
 acceptance probability
 function $P(e, e', \mathcal{T}) \leftarrow \phi_{softmax}(z^{(i)})$
 select action $a' \leftarrow \text{argmax}_a P(e, e', \mathcal{T})$

Output:

Best action selection a'

of making the transition from the current state s to a candidate new state s' . The probability function P is bound to be non-negative in order to avoid local minimum.

In the proposed algorithm, when computing the input feature for softmax regression, the energy-based cost function is introduced by means of the cost function $J(s')$, which is calculated at each possible next state during the learning process. Many approaches can be used to define a suitable $J(s')$ as either: heuristic-based function such as the distance covered from the start, the remaining distance, or a combination of both. In this work, cost is introduced as the Euclidean norm of the remaining distance:

$$J(s') = \|s' - g\| \quad (4)$$

The evolution of the state s of the system is also affected by temperature \mathcal{T} . The evolution process is sensitive to coarser energy variations for a large \mathcal{T} ; whereas, for a small \mathcal{T} , it is sensitive to finer such variations. Considering this fact, the algorithm initializes with quite high temperature, \mathcal{T}_{max} , and

gradually approaches towards zero, $\mathcal{T} \approx 0$, following some annealing schedule $g(\mathcal{T})$.

$$\mathcal{T} \leftarrow g(\mathcal{T}) = \mathcal{T}(1 - \varepsilon) \quad (5)$$

where, ε is considered as a small number. Combining this with the built-in feature of RL as to search for the states with highest reward, the agent drifts towards low-energy regions that become narrower and narrower and, finally, moves downhill.

To assess the goodness of true online SARSA with informed-biased softmax regression (TOSL-iBSR), a comparison with two well-known approaches is made, namely, Q-learning with softmax regression (Q-SR), and true online SARSA with Q-biased softmax regression (TOSL-QBIASSR). In the context of this paper, 2D navigation scenario in Virtual Robot Experimentation Platform (V-REP) is considered. The setup and results are described in Section 4 and 5. This comparative study proves that TOSL-iBSR outperforms other learning processes, both in terms of the mean-average reward and the convergence rate.

IV. IMPLEMENTATION PRE-REQUISITES

In the first step, the virtual environments are developed in V-REP. The routines for the learning process and the robot movement's control were written in Python. The versatility of the scheme that makes it different from others is the use of a mobile robot with physical characteristics in a virtual environment. The whole learning process is executed in real-time where Remote API is used to control the robot's movement from within Python.

4.1 Physical characteristics of the mobile robot

The Pioneer 3dx mobile robot, shown in Fig. 1, is a differential drive robot developed by Adept. The 3D model of this robot is readily available in the V-REP library. The robot is equipped with 16 ultrasonic sensors, with related information as to the obstacles available in Python. It features 2 powered rear wheels and 1 castor wheel.



Fig. 1. Pioneer 3dx

4.2 Modeling of the work environment

The real-world environments are commonly filled with obstacles of different sizes. Figs. 2 and 3 represents the virtual scenes developed in V-REP. The elements that exist in the environments are:

Virtual Scenario 1

Workspace: The environment is a $4 \times 4m$ grid resembling a maze, which is fully confined from the outer end.

Obstacles: Three obstacles with size attribute of $(0.1,1.0,0.4)m$, and another bigger one as $(0.1,2.0,0.4)m$.

Virtual Scenario 2

Workspace: The environment is a $6 \times 6m$ grid fully confined from the outer end.

Obstacles: Five obstacles are placed in a disordered manner with size attributes of $(0.1,0.5,0.4)m$, and $(0.1,1.0,0.4)m$.

Target: The target is a bounding box.

Robot and sensors: The Pioneer robot viewable in the scene is equipped with 16 ultrasonic sensors covering all sides. The ultrasonic beam angle is defined as 30° and conically shaped with the range measurement defined as $1.0m$.

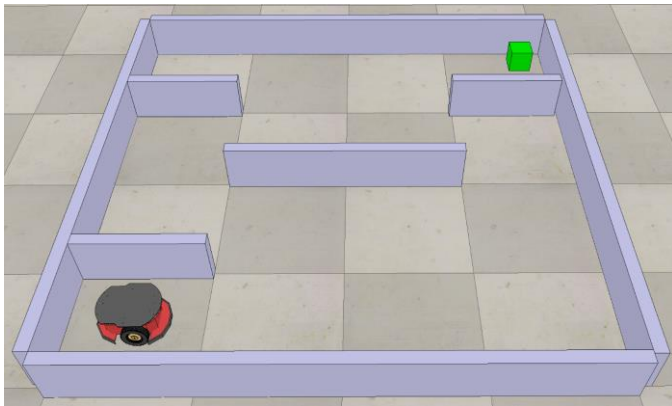


Fig. 2. Navigation scenario, $4 \times 4m$ with obstacles

4.3 Reward Function

The reward value is determined based upon the observation information of each state. Mostly, the reward value is updated based upon the distance from the obstacles and/or the target location. To define a simple yet effective reward function, the desired end-position of the task is defined as g ; each time the robot goes within the safe distance d , defined between obstacle O and the robot, a collision n_c is detected. The reward rules are defined as follows:

$$r = \begin{cases} R & , s = g \\ -0.2R & , s \in O \text{ and } n_c = 1 \\ -R & , s \in O \text{ and } n_c > 1 \end{cases} \quad (6)$$

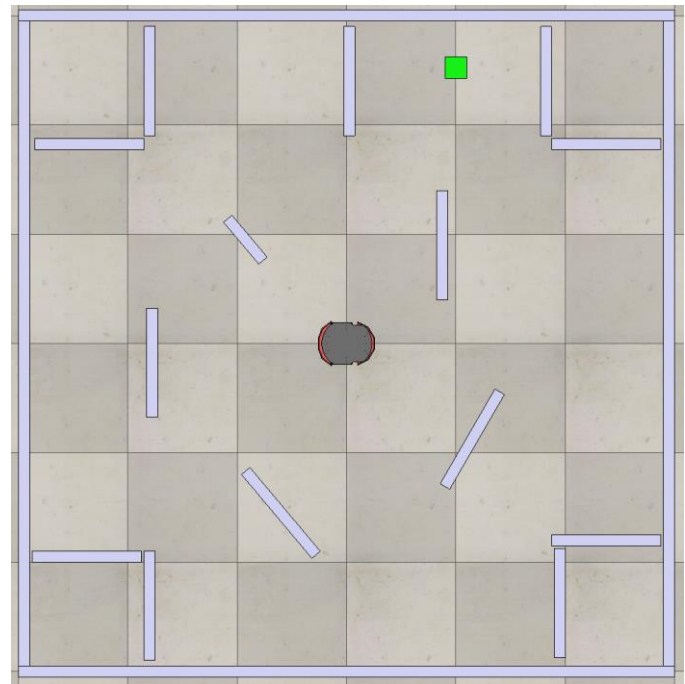


Fig. 3. Navigation scenario, $6 \times 6m$ with obstacles

4.4 Interfacing Python with V-REP

Fig. 4 illustrates the application architecture adapted for the implementation of the entire process. The architecture is system-independent; though, depending upon the operating system, the workspace configuration files need to be selected from within the V-REP installation folder. These configuration files consist of Remote API and Dynamic Link Libraries. The link to the V-REP server can be made through socket communication by specifying the IP address as well as a connection port. On the V-REP, Pioneer will perform the action chosen by Python. The sensory information is, then, forwarded to Python and is used for calculating the reward points and the next sequence state.

The task is considered completed once the robot reaches target g . The first time it comes in close contact with an obstacle, a small penalty is imposed.

V. SIMULATED EXPERIEMNTS AND DISCUSSIONS

For the experimental evaluation of 2D navigation, the V-REP scene is kept the same as in [20] for true comparison. The Pioneer 3dx is a differential drive robot with 2 DC motors and encoders. The kinematics for the differential drive robot under no-slippage is

$$\begin{bmatrix} \dot{x} \\ \dot{y} \\ \dot{\theta} \end{bmatrix} = \begin{bmatrix} \cos \theta & 0 \\ \sin \theta & 0 \\ 0 & 1 \end{bmatrix} \begin{bmatrix} v \\ \omega \end{bmatrix} \quad (7)$$

where, v is the robot translational velocity and ω is the robot rotational velocity defined with respect to the body frame. The linear and angular velocities of the robot are associated to the individual wheel's angular velocities as:

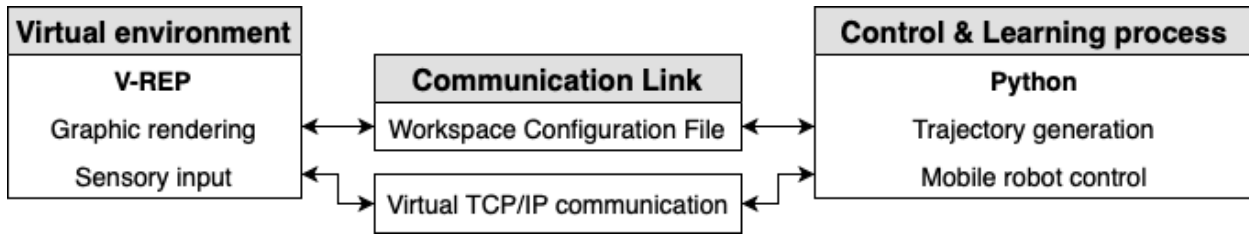


Fig. 4. Application architecture

$$v = \frac{(\omega_r + \omega_l)}{2} \tag{8}$$

$$\omega = \frac{(\omega_r - \omega_l)}{W}$$

where, ω_r and ω_l are the angular velocities of the right and the left wheels, and W is the distance between the two's centers. The control input is directly given to the wheels in terms of ω_r and ω_l .

For the defined task and scenarios, the agent has the freedom to choose between any of its immediate neighboring states $\in \{E, NE, N, NW, W, SW, S, SE, \phi\}$. The last state, i.e. the null state, refers to the case where the next state is the same as the current one; therefore, in total there will be 9 possible actions. Through preliminary tests, the tuning parameters α and γ are selected as 0.1 and 0.9. Three algorithms: Q-SR, TOSL-QBIASSR and TOSL-iBSR are evaluated in terms of the performance.

A. Scene 1: Maze grid 4x4m

The results of the learning process for the three algorithms are averaged for 6 episodes and plotted against 3600 times steps. From Fig. 5, it can be observed that the TOSL-iBSR outperforms both TOSL-QBIASSR and Q-SR. For episodic tasks, the mean-average reward is a true indicator as it gives us a clearer picture. At the start of the task, the mean-average reward is evaluated as negative. It can be witnessed that just after 500 steps with the learning process in place, the mean-average reward began to pull up. The QBIASSR shows steady behavior towards the end of the task as it creeps towards the iBSR curve; therefore, it will obviously require additional steps in order to reach it.

The learning curves for the three algorithms are also shown in Figs. 6-8. The average reward obtained using the Q-SR is acceptable, but still far from the maximum reward and, hence, it demands additional convergence time. For the QBIASSR, the difference between the learning curves is high compared to iBSR, thereby generating a low mean-average reward as witnessed in Fig. 5. On the other hand, the Q-SR is observed to yield much flatter learning process.

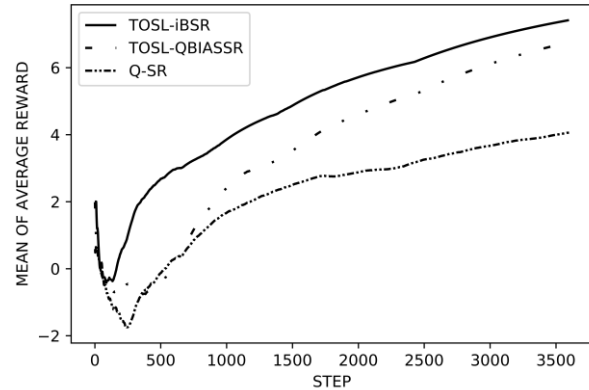


Fig. 5. Learning results for 6 episodes

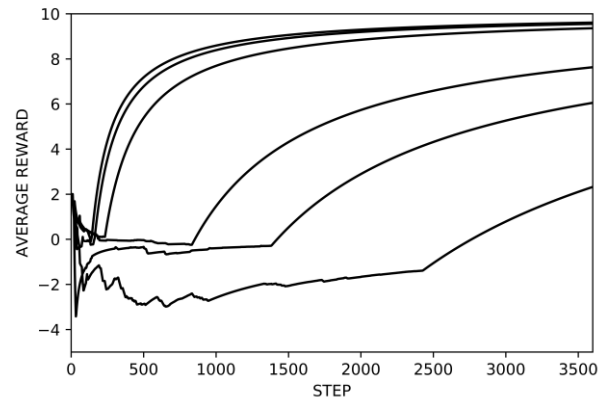


Fig. 6. Average reward for TOSL-iBSR for 6 episodes

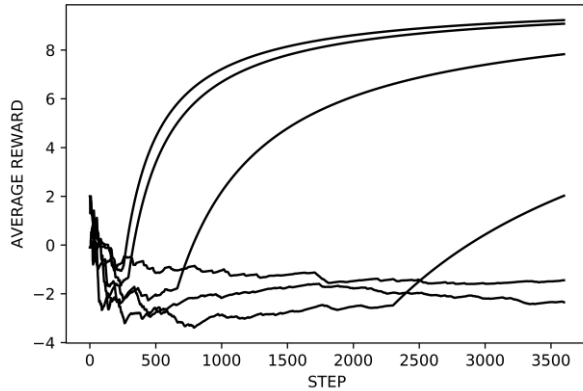


Fig. 7. Average reward for Q-SR for 6 episodes

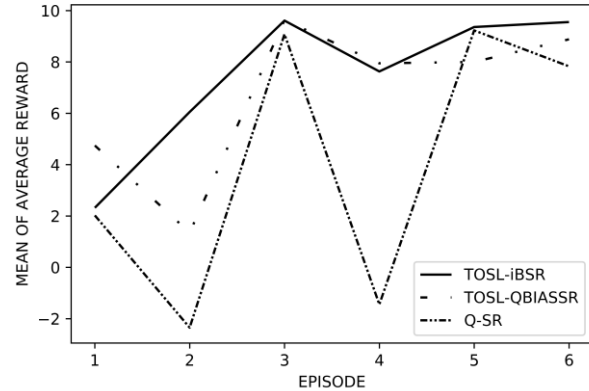


Fig. 9. Mean-average reward per 3600 steps

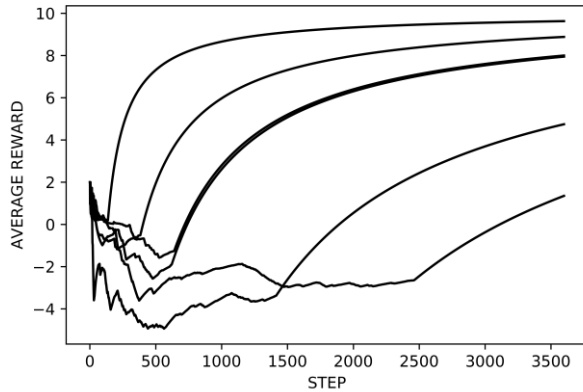


Fig. 8. Average reward for TOSL-QBIASSR for 6 episodes

Fig. 9 illustrates the mean-average reward for the three algorithms over 3600 steps and 6 episodes. This gives us a clear picture as to the performance of the three algorithms. As it can be seen, the Q-SR curve shows poor learning since, after 3 episodes, it is still unable to repeat its behavior which is indicative of a lack of learning, repeatability and consistency. It shall be stated that the task was not fully completed after episode 4. The learning curve of iBSR shows that the robot has learned to perform the task in an effective manner with continuous improvement; whereas, QBIASSR curve, albeit starting with a higher reward, remained unable to maintain its superiority. For implementation, Intel Core 2 Duo processor under Windows 64 bits has been utilized. To evaluate the computational cost, CPU time per step (s) is defined as a measure. The results in Table 1 shows that Q-SR is the second most effective learning process after TOSL-iBSR; whereas, TOSL-QBIASSR demanded more learning steps to complete the task. The same can be observed through Figs. 7 and 8.

B. Scene 1: Maze grid $6 \times 6m$

A more complex scenario (Fig. 3) for navigation is considered where obstacles are placed randomly. The learning process is repeated for 6 episodes; 3600 time steps per episode. The results shown in Fig. 10 highlight the performances of each learning process. It is worth mentioning that Q-SR has not been able to complete the task even for once within specified number of steps. TOSL-QBIASSR has been moderate in performance and is dominated by TOSL-iBSR for attaining highest reward. The QBIASSR learning process is very slow and sluggish as compare to the iBSR whose learning curve demonstrates notable continuous improvement.

The results of the learning experiments are individually shown in Figs. 11-13. The average reward obtained using Q-SR is always negative; therefore, completely fails in this scenario. For the QBIASSR, in only half of the episodes, the learning curve has been able to attain steady state value, thereby generating a low mean-average reward as compare with iBSR whose performance has been very much consistent throughout.

The mean-average reward for the three learning processes over 3600 steps and 6 episodes are shown in Fig. 14. The learning curve of Q-SR presents continuous attainment of negative reward; hence, it has not been able to accomplish the task even for once. The mean average reward obtained using iBSR exhibits that it started with higher positive value and is able to continuously improve as compared to QBIASSR that experiences many ups and down before attaining the steady state value after 4 episodes. The computational cost for scene 2, shown in Table 1, has been increased due to its complexity. The computational cost of TOSL with QBIASSR is higher in magnitude as compared to other two. The TOSL-iBSR found to be computationally efficient due to the reason that it requires much lesser number of steps to accomplish the task.

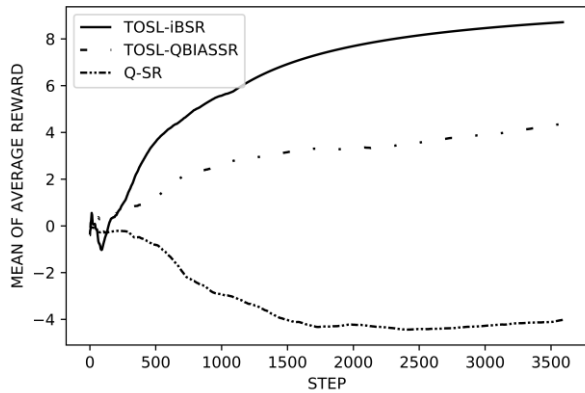


Fig. 10. Learning results for 6 episodes

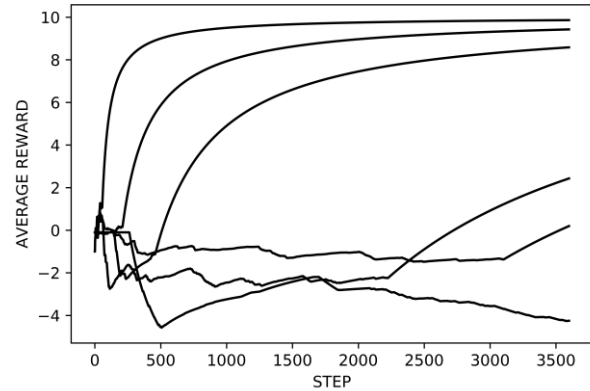


Fig. 13. Average reward for TOSL-QBIASSR for 6 episodes

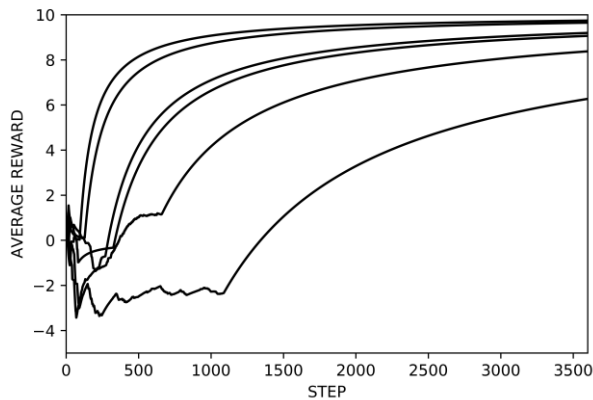


Fig. 11. Average reward for TOSL-iBSR for 6 episodes

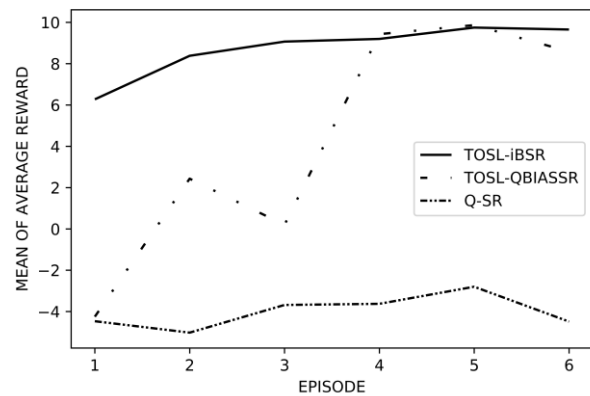


Fig. 14. Mean-average reward per 3600 steps

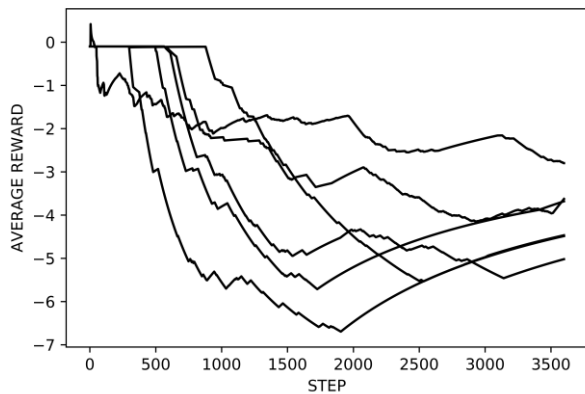


Fig. 12. Average reward for Q-SR for 6 episodes

Table I
COMPUTATIONAL COST

RL algorithm	CPU time / step (s)	
	Scene 1	Scene 2
Q-SR	0.203	0.350
TOSL-QBIASSR	0.352	0.481
TOSL-iBSR	0.040	0.068

VI. CONCLUSION

In this research, a new and improved learning process, named as, TOSL informed-biased softmax regression (TOSL-iBSR) is presented for mobile robot navigation. The novel exploration technique is equipped with the ability to pick the most suitable action in order to maximize the reward point and minimize the convergence rate. One of the notable contributions of the present study is to establish the framework between Python and the V-REP and to use an actual robot with all physical parameters, instead of merely using a point robot [27, 28, 29] as in most RL navigation-based research literature. A virtual scenario for 2D navigation is generated to test the efficiency of the proposed approach. The performance of the robot during navigation using the TOSL-

iBSR is, then, compared with the Q-SR and the TOSL-QBIASSR. Using the approach presented in this paper, the robot is found to complete the navigation task while attaining a higher positive reward and less computational cost. Despite this accomplishment, one of the minor drawbacks that reduces the generalization may be that the true pose of the robot is available at all time sequences and that the sensory information is noise-free, - which is certainly not the case in real workspaces. In such scenario, an effective approach can be the introduction of a robust estimation technique. As to the future work, it involves the extension and testing of the iBSR for multiple real tasks in actual real-world settings. In addition, the proposed algorithm can be extended for more practical high-dimensional tasks. Incorporating DRL into the proposed algorithm can also generate a promising learning process. Finally, we intend to test the proposed algorithm in a more complex environment, namely scattered, denser, and dynamic.

REFERENCES

- [1] S.-H. Kim, C.-W. Roh, S.-C. Kang and M.-Y. Park, "Outdoor navigation of a mobile robot using differential GPS and curb detection," in *Proceedings of IEEE international conference on Robotics and Automation*, 2007.
- [2] L. Moreno, J. M. Armingol, S. Garrido, A. D. L. Escalera and M. A. Salichs, "A genetic algorithm for mobile robot localization using ultrasonic sensors," *Journal of Intelligent and Robotic Systems*, vol. 34, no. 2, pp. 135-154, 2002.
- [3] A. Sinha and P. Papadakis, "Mind the gap: Detection and traversability analysis of terrain gaps using LIDAR for safe robot navigation," *Robotica*, vol. 31, no. 7, pp. 1085-1101, 2013.
- [4] S. J. Russell and P. Norvig, *Artificial intelligence: a modern approach*, Pearson Education Limited, 2016.
- [5] R. E. Korf, *Artificial intelligence search algorithms*, Chapman & Hall/CRC, 2010.
- [6] L. E. Kavradi, M. N. Kolountzakis and J.-C. Latombe, "Analysis of probabilistic roadmaps for path planning," in *Proceedings international conference on robotics and automation*, 1996.
- [7] N. A. Melchior and R. Simmons, "Particle RRT for path planning with uncertainty," in *Proceedings of IEEE international conference on robotics and automation*, 2007.
- [8] S. X. Yang and C. Luo, "A neural network approach to complete coverage path planning," *IEEE Transactions on Systems, Man, and Cybernetics, Part B (Cybernetics)*, vol. 34, no. 1, pp. 718-724, 2004.
- [9] M. Z. Malik, A. Eizad and M. U. Khan, *Path planning algorithms for mobile robots: a comprehensive comparative analysis*, LAP LAMBERT Academic Publishing, 2014.
- [10] M. S. Alam, M. U. Rafique and M. U. Khan, "Mobile robot path planning in static environments using particle swarm optimization," *International journal of computer science and electronics engineering*, vol. 3, no. 3, 2015.
- [11] R. S. Sutton and A. G. Barto, *Reinforcement Learning: An introduction*, MIT press, 2018.
- [12] C. J. C. H. Watkins, "Learning from delayed rewards," King's College, Cambridge, Ph.D. thesis, 1989.
- [13] K. L. Smart W, "Practical reinforcement learning in continuous spaces," in *Proceedings of the seventeenth international conference on machine learning*, 2000.
- [14] K. L. Smart W, "Effective reinforcement learning for mobile robots," in *Proceedings of the international conference on robotics and automation*, 2002.
- [15] D. Aranibar and P. Alsina, "Reinforcement learning-based-path planning for autonomous robots," ENRI: Encontrol Nacional de Robotica Inteligente, 2004.
- [16] H. Boem and H. Cho, "A sensor-based navigation for a mobile robot using fuzzy logic and reinforcement learning," *IEEE Transaction on System, Man, and Cybernetics*, vol. 25, pp. 464-477, 1995.
- [17] N. Yung and C. Ye, "Self-learning fuzzy navigation of mobile vehicle," in *Proceedings of the international conference on signal processing*, 1996.
- [18] G. Yang, E. Chen and C. An, "Mobile robot navigation using neural Q-learning," in *IEEE proceedings of the third international conference on machine learning and cybernetics*, 2004.
- [19] K. Macek, I. Petrovic and N. Peric, "A reinforcement learning approach to obstacle avoidance of mobile robots," in *7th international workshop on advanced motion control*, 2002.
- [20] A. Martínez-Tenor, J. A. Fernández-Madrigal, A. Cruz-Martín and J. González-Jiménez, "Towards a common implementation of reinforcement learning for multiple robotic tasks," *Expert Systems with Applications*, vol. 100, pp. 246-259, 2018.
- [21] H. Andrew, *Alan Turing: The Enigma*, Princeton University Press, 2012.
- [22] R. Bellman, "A Markovian decision process," *Journal of Mathematics and Mechanics*, pp. 679-684, 1957.
- [23] A. G. Barto, R. G. Sutton and C. W. Anderson, "Neuronlike elements that can solve difficult learning control problems," *IEEE Transactions on Systems, Man, and Cybernetics*, vol. 13, pp. 835-846, 1983.
- [24] A. G. Barto, R. S. Sutton and P. S. Brouwer, "Associative search network: A reinforcement learning associative memory," *Biological Cybernetics*, pp. 201-211, 1981.
- [25] G. A. Rummery and M. Niranjan, *On-line Q-learning using connectionist system*, vol. 37, Cambridge, England: University of Cambridge, Department of Engineering, 1994.
- [26] H. Van Seijen, M. A. R. P. M. Pilarski and M. M. C. a. S. R. S, "Ture online temporal-difference learning," *The Journal of Machine Learning Research*, vol. 17, no. 1, pp. 5057-5096, 2016.
- [27] R. Abiyev, D. Ibrahim and B. Erin, "Navigation of mobile robots in the presence of obstacles," *Advances in Engineering Software*, vol. 41, pp. 1179-1186, 2010.
- [28] A. I. Panov, K. S. Yakovlev and R. Suvorov, "Grid path planning with deep reinforcement learning: preliminary results," *Procedia Computer*

Science, vol. 123, pp. 347-353, 2018.

- [29] J. d. R. Millan, "Reinforcement learning of goal-directed obstacle-avoiding reaction strategies in an autonomous mobile robot," *Robotics and Autonomous Systems*, vol. 15, pp. 275-299, 1995.
- [30] R. Bellman, "The theory of dynamic programming," RAND Corp Sanata Monica CA, 1954.

BIOGRAPHIES



Muhammad Umer KHAN received the B.S. in computer science from the International Islamic University, Islamabad, in 2004, and the Ph.D. in electrical engineering from the Pakistan Institute of Engineering and Applied Sciences, Islamabad, in 2011.

From 2011 to 2017, he was serving as an Assistant Professor with the Department of Mechatronics Engineering, Air University. He was a post-doctoral fellow with the Department of Computing, Hong Kong Polytechnic University, Hong Kong, from 2014 to 2015. Since 2018, he has been with the Mechatronics Engineering Department, Atilim University, Turkey. His current research interests include robust control, linear matrix inequalities, reinforcement learning, vision-based control, and navigation.

Radio Frequency Energy Harvesting with Different Antennas and Output Powers

M. CANSIZ

Abstract— In this study, the effects of antenna types and output powers on charging times of RF energy harvesting circuit were measured and analyzed in detail. A measurement system which consisting of a signal generator, an RF energy harvesting circuit, antennas and other devices was installed for receiving the measurement samples. According to the measurement results, the shortest charging time was obtained as 0.58 s at a distance of 20 cm, when 6.1 dBi antenna was connected to the RF energy harvesting circuit and the output power of the signal generator was set to 17 dBm. In addition to that, the longest charging time was evaluated as 25.01 s at a distance of 60 cm, when 1 dBi antenna was connected to the RF energy harvesting circuit and the output power of the signal generator was adjusted to 14 dBm. As a result, it was determined that increasing of antenna gains and output powers and shortening of distances between signal generator and RF energy harvesting circuit decreased the charging times of the RF energy harvesting circuit in this study.

Index Terms— Radio frequency, Energy harvesting, Antenna, Output power.

I. INTRODUCTION

MANY KINDS of energy sources such as solar [1], mechanical vibrations [2], thermal gradients [3] and electromagnetic waves [4] exist in nature. Electromagnetic waves are energy source for Radio Frequency (RF) energy harvesting technology. Thanks to this technology, the energy required for operation of many low power devices can be provided wirelessly [5].

The harvested energy obtained by the RF energy harvesting technology depends on many parameters such as power levels of RF bands, antenna types, distance between transmitter and receiver, etc. In order to increase the harvested energy, the RF bands in the ambient environment should be measured [6]–[12] and then, the operating frequency of the RF energy harvesting circuit should be adjusted according to the most powerful RF band or bands. Furthermore, suitable antenna types and distances should be chosen for increasing the harvested energy.

Efficiency of an RF energy harvesting circuit is crucial and it directly affects the harvested energy. For that reason, the efficiency should be increased as much as possible when an

RF energy harvesting circuit is designed and implemented. The efficiency of the RF energy harvesting system can be improved by using RF power signals with various waveforms [13]–[17]. In addition to that, the efficiency can also be enhanced by optimizing circuit parts such as antenna, rectifier and voltage multiplier forming the RF energy harvesting circuit. All parameters that increase the efficiency of the RF energy harvesting lead to shorter charging times.

In [18], the battery recharging time was analyzed when multiple RF sources were available. A statistical distribution model was proposed for RF energy harvesting systems. Furthermore, it was determined that the theoretical results were consistent with the experimental results.

In this study, it was aimed to measure and analyze the effects of antenna types and output powers on the charging times of the RF energy harvesting. A measurement system was established for obtaining the measurement samples. The measurement results were evaluated and then, charging times versus distances were shown in tables.

II. MATERIALS AND METHOD


In this section, the charging times of the RF energy harvesting circuit were measured for different antennas and output powers. Measurement system and devices were described in detail. Moreover, the collection of measurement data was explained.

A. Measurement System and Devices

Universal Software Radio Peripheral (USRP)-2900 Software Defined Radio from National Instruments [19], PCB dipole antenna, PCB patch antenna [20], P2110 Powerharvester module from Powercast Company [21], WSN-Eval-01 Wireless Sensor Board, Microchip 16-bit XLP Development Board and PICTail Daughter Card were used as measuring devices. In Fig. 1, measurement system was illustrated.

NI USRP-2900 was used as a signal generator and it produced RF power signals at 915 MHz carrier frequency in continuous wave mode for 14 and 17 dBm output powers. Then, the generated RF power signals were harvested by the RF energy harvesting circuit with different antennas at distances from 20 cm to 60 cm at the interval of 5 cm. On the other hand, between 902 MHz and 928 MHz frequency band, P2110 Powerharvester module as an RF energy harvesting circuit can provide efficient energy harvesting. This module can obtain the received power level down to -11.5 dBm.

MUSTAFA CANSIZ, is with Department of Electrical and Electronics Engineering, Dicle University, Diyarbakır, Turkey, (e-mail: mustafa.cansiz@dicle.edu.tr).

 <https://orcid.org/0000-0003-2534-9770>

Manuscript received April 10, 2019; accepted June 11, 2019.
DOI: [10.17694/bajece.551790](https://doi.org/10.17694/bajece.551790)

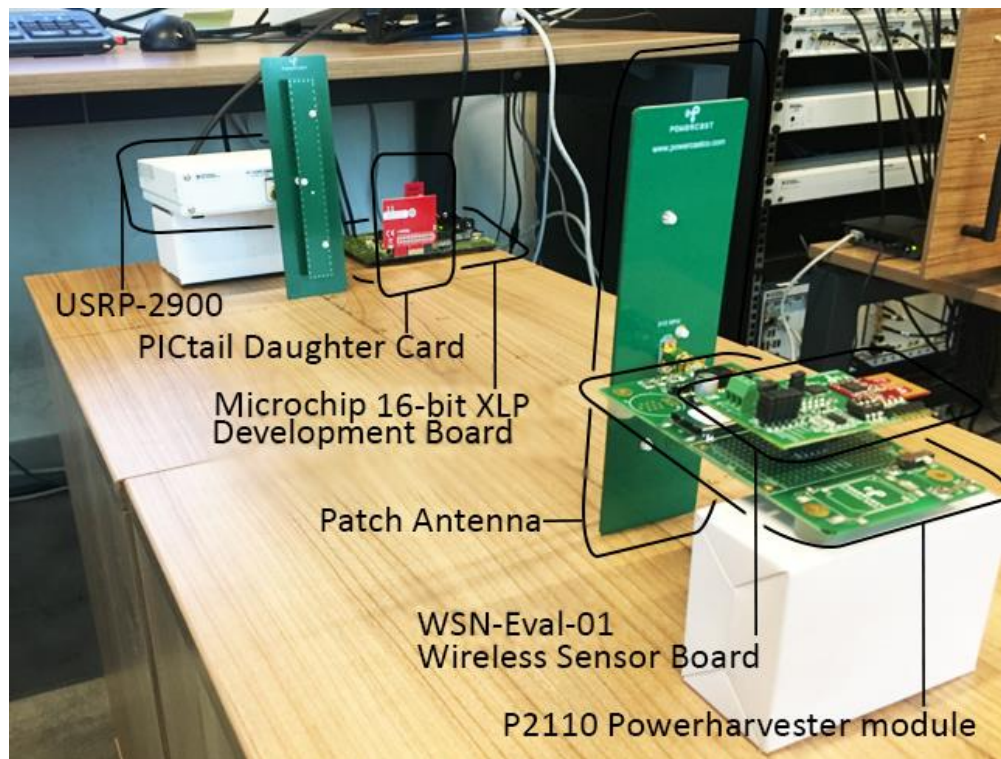


Fig. 1. Measurement system

As shown in Fig. 2, PCB dipole antenna and PCB patch antenna were connected to the RF energy harvesting circuit, respectively. Then, measurements were taken for each antenna at different distances. The PCB dipole antenna has 1.0 dBi antenna gain and it is vertically polarized and omni-directional antenna and it has 360° horizontal pattern [20]. The PCB patch

antenna has 6.1 dBi antenna gain and this antenna is vertically polarized and directional antenna. Furthermore, the PCB patch antenna has 122° horizontal and 68° vertical pattern [20]. During the measurements, only the PCB patch antenna was attached to the NI USRP-2900 which used as a signal generator.

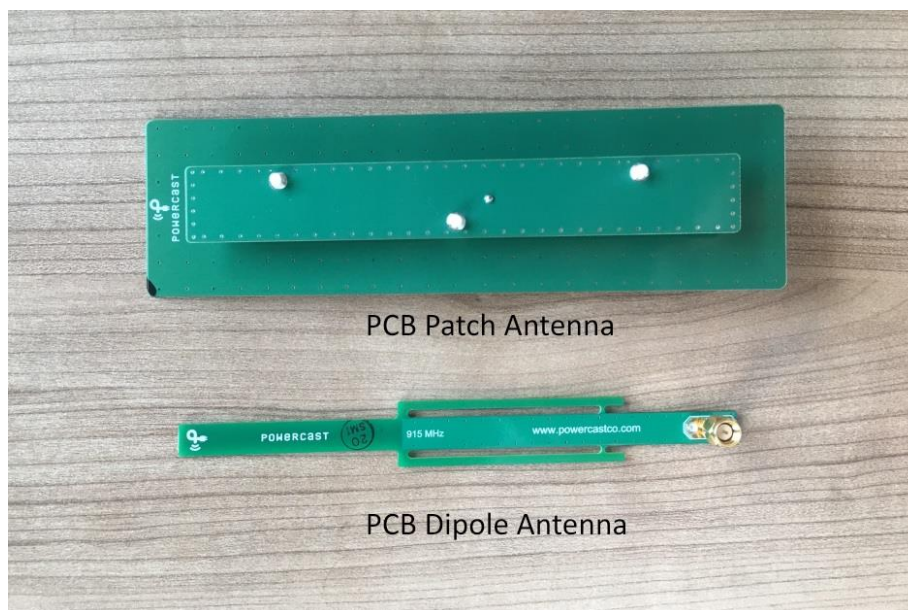


Fig. 2. PCB patch antenna and PCB dipole antenna

As shown in Fig. 1, the WSN-Eval-01 Wireless Sensor Board was plugged into the RF energy harvesting circuit (P2110 Powerharvester module) and this wireless sensor board can sense light, temperature and humidity. The WSN-Eval-01 Wireless Sensor Board transmits the measurement data such as light, temperature, humidity, Node ID, Transmitter (TX) ID and Received Signal Strength Indicator (RSSI) to the access point (PICtail Daughter Card) which is plugged into Microchip 16-bit XLP Development Board. The PICtail Daughter Card was used as an access point which has IEEE 802.15.4 radio module (2.4 GHz). Microchip 16-bit XLP Development Board can take data up to 8 Node IDs simultaneously and manage time counter for each Node ID. This development board has a Microchip's PIC24F micro controller unit.

B. Collection of Measurement Data

When the RF energy harvesting circuit charges the sufficient energy, it will feed the WSN-Eval-01 Wireless Sensor Board for transmitting the measurement data such as light, temperature, humidity, Node ID, TX ID and RSSI wirelessly to the PICtail Daughter Card (access point). Then, the Microchip 16-bit XLP Development Board calculates time and time difference (dT) and also receives packet numbers. Data from the access point and data from the wireless sensor board were shown in Fig. 3.

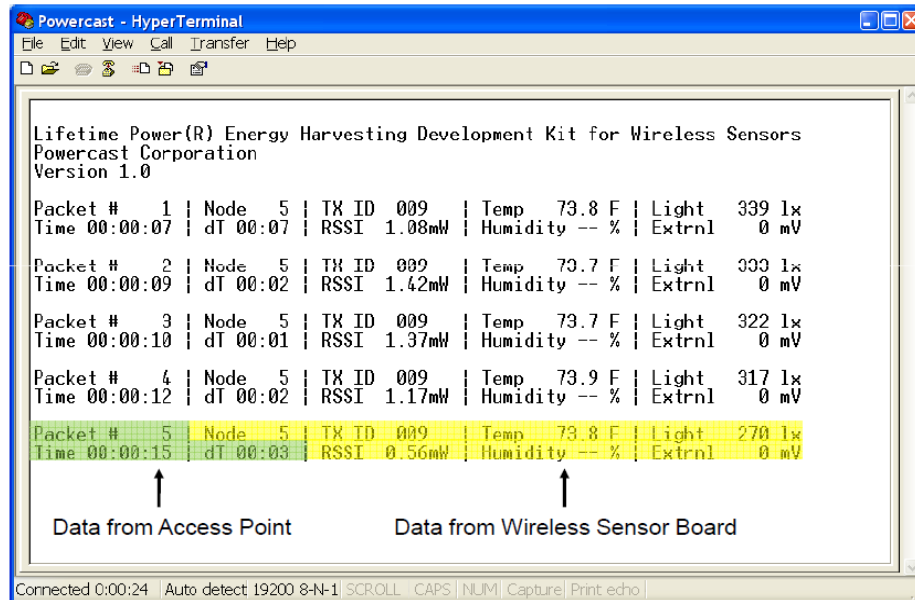


Fig. 3. Collection of measurement data via HyperTerminal [21]

In order to obtain the measurement data, the Microchip 16-bit XLP Development Board was connected to a computer with a cable. Then, the measurement data was shown via HyperTerminal as seen in Figure 3. HyperTerminal must be set as baud rate: 19200, flow control: hardware, parity: none stop bits: 1 bit and data bits: 8 bits for displaying the measurement data correctly. Finally, the measurement data was recorded on a computer via HyperTerminal.

III. RESULTS AND DISCUSSION

Charging times of an RF energy harvesting circuit depend on many parameters such as antenna type, distance and output power, etc. In this study, the charging time was defined as the time difference (dT in Fig. 3) between two consecutive packets. So, the shorter the time difference, the shorter the charging time. After the PCB dipole antenna was connected to the RF energy harvesting circuit and the output power of the signal generator was set to 14 dBm, 100 measurement samples were received for each distance from 20 cm to 60 cm at the interval of 5 cm and totally 900 measurement samples were taken for 14 dBm. In the same way, 900 measurement samples

were also taken for 17 dBm output power. On the other hand, after the PCB patch antenna was attached to the RF energy harvesting circuit, 900 measurement samples were obtained for 14 dBm and 17 dBm, respectively. The charging time for each distance was calculated as the average of the time differences for the consecutive 100 packets.

Table I indicates the charging times for PCB dipole antenna (1 dBi antenna gain) and PCB patch antenna (6.1 dBi antenna gain), respectively, while the output power is adjusted to 14 dBm. Units of charging time and distance are second (s) and centimeter (cm), respectively. According to the measurement results in Table I, the shortest charging time was determined as 2.61 s at a distance of 20 cm and the longest charging time was determined as 25.01 s at a distance of 60 cm for 1 dBi antenna gain. In addition to that, the shortest charging time was calculated as 0.93 s at a distance of 20 cm and the longest charging time was determined as 5.92 s at a distance of 60 cm for 6.1 dBi antenna gain.

TABLE I

CHARGING TIMES FOR PCB DIPOLE ANTENNA AND PCB PATCH ANTENNA AT 14 DBM OUTPUT POWER

Distance (cm)	14 dBm USRP	
	1 dBi antenna	6.1 dBi antenna
	Charging Time (s)	Charging Time (s)
20	2.61	0.93
25	4.09	1.38
30	5.63	1.82
35	8.92	2.35
40	11.10	3.18
45	11.43	3.86
50	12.38	4.23
55	18.11	5.00
60	25.01	5.92

TABLE II
CHARGING TIMES FOR PCB DIPOLE ANTENNA AND PCB PATCH ANTENNA AT 17 DBM OUTPUT POWER

Distance (cm)	17 dBm USRP	
	1 dBi antenna	6.1 dBi antenna
	Charging Time (s)	Charging Time (s)
20	1.27	0.58
25	1.77	0.72
30	3.06	0.94
35	3.73	1.28
40	4.94	1.59
45	7.51	1.84
50	7.81	2.17
55	9.09	2.46
60	11.20	2.75

Table II shows the charging times for PCB dipole antenna (1 dBi antenna gain) and PCB patch antenna (6.1 dBi antenna gain), respectively, while the output power is set to 17 dBm. In terms of the measurement results in Table II, the shortest charging time was determined as 1.27 s at a distance of 20 cm and the longest charging time was determined as 11.20 s at a distance of 60 cm for 1 dBi antenna gain. Moreover, the shortest charging time was calculated as 0.58 s at a distance of 20 cm and the longest charging time was calculated as 2.75 s at a distance of 60 cm for 6.1 dBi antenna gain.

The charging times according to the different antenna gains and output powers were clearly shown in Fig. 4. The shortest charging time was obtained for RF energy harvesting when 6.1 dBi antenna (PCB patch antenna) was connected to the circuit and the output power of the signal generator was set to 17 dBm. On the other hand, the longest charging time was determined for RF energy harvesting when 1 dBi antenna (PCB dipole antenna) was connected to the circuit and the output power of the signal generator was adjusted to 14 dBm as seen in Fig. 4.

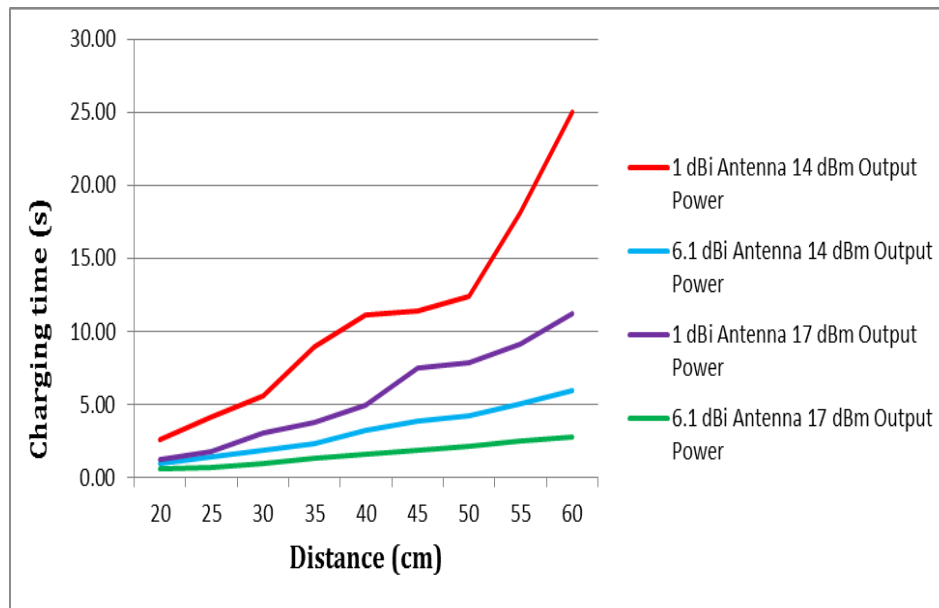


Fig. 4. Charging times versus distance for different antenna gains and output powers

IV. CONCLUSION

The harvested energy obtained by the RF energy harvesting technology is used as an alternative energy source for the operation of many low power devices. With this technology, it is estimated that the number of battery-free devices will increase.

An advanced measurement system was established for analyzing the effects of antenna types and output powers on the charging times of the RF energy harvesting circuit. This measurement system consisted of NI USRP-2900 as a signal generator, PCB dipole antenna, PCB patch antenna, P2110 Powerharvester module as an RF energy harvesting circuit, WSN-Eval-01 Wireless Sensor Board, Microchip 16-bit XLP

Development Board and PICtail Daughter Card as an access point.

When 6.1 dBi antenna was connected to the RF energy harvesting circuit and the output power of the signal generator was adjusted to 17 dBm, the shortest charging time was obtained at the distance of 20 cm. Furthermore, when 1 dBi antenna was connected to the RF energy harvesting circuit and the output power of the signal generator was set to 14 dBm, the longest charging time was received at the distance of 60 cm. As a result, it was determined that shortening of distances and increasing of antenna gains and output powers reduced the charging times of the RF energy harvesting circuit in this study.

ACKNOWLEDGMENT

The author would like to thank Güneş KARABULUT KURT and Wireless Communication Research Laboratory team of Istanbul Technical University for providing equipment support.

REFERENCES

- [1] M. A. Green, K. Emery, Y. Hishikawa, W. Warta, and E. D. Dunlop, "Solar cell efficiency tables (Version 38)," *Prog. Photovoltaics Res. Appl.*, vol. 19, no. 5, pp. 565–572, Aug. 2011.
- [2] A. C. Turkmen and C. Celik, "Energy harvesting with the piezoelectric material integrated shoe," *Energy*, vol. 150, pp. 556–564, May 2018.
- [3] A. R. M. Siddique, R. Rabari, S. Mahmud, and B. Van Heyst, "Thermal energy harvesting from the human body using flexible thermoelectric generator (FTEG) fabricated by a dispenser printing technique," *Energy*, vol. 115, pp. 1081–1091, Nov. 2016.
- [4] S. Keyrouz, H. Visser, and A. Tjhuis, "Multi-band simultaneous radio frequency energy harvesting," *Antennas Propag.*, no. Eucap, pp. 3058–3061, 2013.
- [5] J. Bito, S. Kim, M. Tentzeris, and S. Nikolaou, "Ambient Energy Harvesting from 2-way Talk-Radio Signals for 'Smart' Meter and Display Applications," in *2014 IEEE Antennas and Propagation Society International Symposium (APSURSI)*, 2014, pp. 1353–1354.
- [6] S. Kim, R. Vyas, J. Bito, K. Niotaki, A. Collado, A. Georgiadis, and M. M. Tentzeris, "Ambient RF Energy-Harvesting Technologies for Self-Sustainable Standalone Wireless Sensor Platforms," *Proc. IEEE*, vol. 102, no. 11, pp. 1649–1666, Nov. 2014.
- [7] N. Barroca, H. M. Saraiva, P. T. Gouveia, J. Tavares, L. M. Borges, F. J. Velez, C. Loss, R. Salvado, P. Pinho, R. Goncalves, N. Borges Carvalho, R. Chavez-Santiago, and I. Balasingham, "Antennas and circuits for ambient RF energy harvesting in wireless body area networks," in *2013 IEEE 24th Annual International Symposium on Personal, Indoor, and Mobile Radio Communications (PIMRC)*, 2013, pp. 532–537.
- [8] M. Cansiz, T. Abbasov, M. B. Kurt, and A. R. Celik, "Mobile measurement of radiofrequency electromagnetic field exposure level and statistical analysis," *Measurement*, vol. 86, pp. 159–164, May 2016.
- [9] P. Baltrėnas and R. Buckus, "Measurements and analysis of the electromagnetic fields of mobile communication antennas," *Measurement*, vol. 46, no. 10, pp. 3942–3949, Dec. 2013.
- [10] M. Pinuela, P. D. Mitcheson, and S. Lucyszyn, "Ambient RF Energy Harvesting in Urban and Semi-Urban Environments," *IEEE Trans. Microw. Theory Tech.*, vol. 61, no. 7, pp. 2715–2726, Jul. 2013.
- [11] M. Cansiz, T. Abbasov, M. B. Kurt, and A. R. Celik, "Mapping of radio frequency electromagnetic field exposure levels in outdoor environment and comparing with reference levels for general public health," *J. Expo. Sci. Environ. Epidemiol.*, vol. 28, no. 2, pp. 161–165, Nov. 2016.
- [12] F. T. Pachón-García, K. Fernández-Ortiz, and J. M. Paniagua-Sánchez, "Assessment of Wi-Fi radiation in indoor environments characterizing the time & space-varying electromagnetic fields," *Meas. J. Int. Meas. Confed.*, vol. 63, pp. 309–321, 2015.
- [13] A. Collado and A. Georgiadis, "Optimal Waveforms for Efficient Wireless Power Transmission," *IEEE Microw. Wirel. Components Lett.*, vol. 24, no. 5, pp. 354–356, May 2014.
- [14] M. S. Trotter, J. D. Griffin, and G. D. Durgin, "Power-optimized waveforms for improving the range and reliability of RFID systems," in *2009 IEEE International Conference on RFID*, 2009, pp. 80–87.
- [15] A. Collado and A. Georgiadis, "Improving wireless power transmission efficiency using chaotic waveforms," in *2012 IEEE/MTT-S International Microwave Symposium Digest*, 2012, pp. 1–3.
- [16] G. Andia Vera, D. Allane, A. Georgiadis, A. Collado, Y. Duroc, and S. Tedjini, "Cooperative Integration of Harvesting RF Sections for Passive RFID Communication," *IEEE Trans. Microw. Theory Tech.*, vol. 63, no. 12, pp. 4556–4566, Dec. 2015.
- [17] J. F. Ensworth, S. J. Thomas, S. Y. Shin, and M. S. Reynolds, "Waveform-aware ambient RF energy harvesting," in *2014 IEEE International Conference on RFID (IEEE RFID)*, 2014, pp. 67–73.
- [18] D. Altinel and G. Karabulut Kurt, "Energy Harvesting From Multiple RF Sources in Wireless Fading Channels," *IEEE Trans. Veh. Technol.*, vol. 65, no. 11, pp. 8854–8864, Nov. 2016.
- [19] National Instruments, "www.ni.com/en-us.html".
- [20] Powercast, "P2110-EVB Evaluation Board for P2110 Powerharvester datasheet."
- [21] Powercast Corporation, "www.powercastco.com".

BIOGRAPHY



Mustafa CANSIZ received the B.S. degree in electrical and electronics engineering in 2002 from Karadeniz Technical University, Trabzon, Turkey and the M.Sc. degree in electrical and electronics engineering in 2010 from Dicle University, Diyarbakır, Turkey. He received the Ph.D. degree in electrical and electronics engineering in 2016 from İnönü University, Malatya, Turkey.

Between 2005 and 2011, he worked in the electronics and telecommunication industry. Since 2011, he has been an instructor with Dicle University. His research areas include measurement of electromagnetic exposure and radio frequency energy harvesting systems.

Effects of Luminaire Angle on Illumination Performance in Tunnel Lighting

M. S. CENGİZ

Abstract— In this study, the effect of luminaire angle on the path parameters of tunnel lighting was investigated. Tunnel illumination was performed with a simulation program adapted to CIE 88-2004 standards. The lighting performance parameters were compared while the angle of the luminaire was 0°, 5°, 10° and 15°. According to the simulation results, the luminaire angle is 0° and the highest efficiency is reached. As the luminaire angle increased, the yield decreased in direct proportion to the angle. The highest lighting efficiency was observed at 0° and the lowest illumination efficiency was observed at 15°. This problem can be overcome by using a higher power lamp in angled lighting. As a result, it is revealed that angled lighting should be avoided in highway and tunnel lighting.


Index Terms—Illumination, luminance, road lighting, tunnel lighting.

I. INTRODUCTION

TUNNELS ARE underground road structures which are alternative to highways and railways. They are used to facilitate traffic flow. Tunnels, should ensure the visibility comfort, speed and safe traffic flow. If the tunnel lighting does not illuminate as much as necessary, a driver approaching the tunnel experiences a black hole effect. Therefore, intense lighting should be done at the entrance of the tunnel. Intensive lighting is not required in the interior of the tunnel [1-3].

In long tunnels, the tunnel interior area is an important part of tunnel lighting cost. Therefore, for the most appropriate tunnel illumination that provides economic but necessary vision conditions, the brightness level in the tunnel interior should be determined correctly. The driver using any vehicle on highways should have detailed visual information about the way in which he is driving. Especially at high speeds, the driver should be able to see the route easily, the driver should be able to perceive the position and movements of the vehicle he is driving, be able to monitor the movements of other vehicles, and easily be able to see the obstacles on the road [4-6].

MEHMET SAIT CENGİZ, is with Department of Technical Vocational School of Bitlis Eren University, Bitlis, Turkey, (e-mail: msaitcengiz@gmail.com).

 <https://orcid.org/0000-0003-3029-3388>

Manuscript received May 10, 2019; accepted June 10, 2019.
DOI: [10.17694/bajece.563021](https://doi.org/10.17694/bajece.563021)

CIE reports the results of 30 different studies, covering road lighting studies that improve vision conditions. In this report, according to the standards of road lighting: pedestrian accidents from 57% to 45%, fatal accidents from 65% to 48%, severe injuries from 30% to 24%, and the total number of accidents it decreased from 53% to 14% [7, 8]. Even if there is little traffic at night, the number of accidents that occur in roads or tunnels without illumination is about three times higher than in daylight hours. The reason for this is the lack of road lighting in accordance with the standards. Figure 1 shows traffic accidents in the tunnel.



Fig.1. Traffic accidents in the tunnel

Tunnel lighting design calculations performed in this study are based on the recommendations involved in the technical report “Guide for The Lighting of Road Tunnels and Underpasses” CIE-1990 dated 2004 No-88. Conducting appropriate road lighting to the CIE reduces the rate of crime committed in city roads. According to the studies in the literature, the number of forensic cases has decreased by 20% in urban roads thanks to the proper lighting. The severity of offenses has decreased by 40%. In the severity of crimes committed, it was seen that there was a 40% decrease [8-10].

II. TUNNEL VEHICLE TRANSITION ZONES

Tunnel lighting is examined by classifying different luminance zones in order to ensure adaptation and provide economic solutions. Figure 2 shows zones of the tunnel.

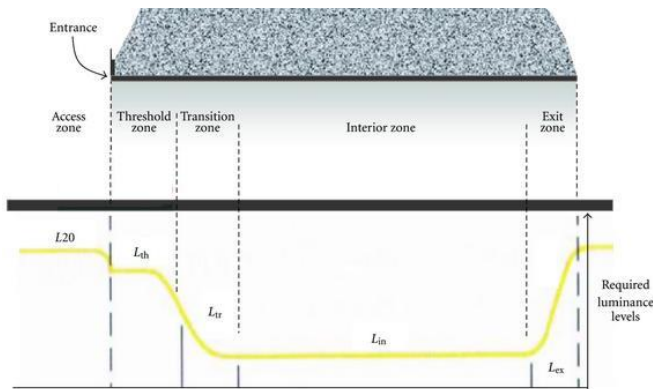


Fig.2. Zones of the tunnel

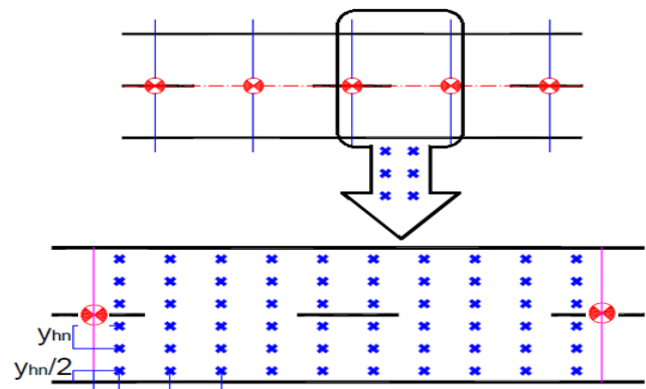


Fig.3. A sketch of a point lighting calculations

The **access zone** is the area starting before the tunnel entrance (100–200) m and ending at the tunnel entrance. There are two factors affecting the adaptation luminance:

- Around the tunnel entrance, “equivalent veiling luminance” (L_{seq}) formed by different luminance values;
- Luminance at the centre of the driver’s field of view. Equivalent veiling luminance is one of the most important factors in determining adaptation of the driver [1-2, 11-13].

Entrance zone is the place where adaptation accurately starts from the tunnel entrance and continues to the interior zone of the tunnel. It is examined in two different zones:

- **Threshold zone:** limits of the zone starting from the tunnel entrance are determined on the basis that a critical object that may be dangerous in that zone can be seen by the driver in the approach at least from a distance equal to the stopping distance;
- **Transition zone:** after the threshold zone, the transition zone is where the luminance in the threshold zone is reduced to a luminance level in the interior zone. The length of the zone varies by the initial and final luminance value and the allowed speed limit.
- **Interior Zone:** the constant luminance zone between entrance and exit zones of the tunnel.
- **Exit Zone:** the zone from the end of interior zone to the exit that makes the adaptation easier to the zone with high luminance at the exit [1-2, 11-13].

III. DETERMINATION OF THE ACCOUNT AREA FOR TUNNEL LIGHTING

In this study, Point Lighting Account Method is used on road surface. In this method, firstly the area to calculate the spot lighting is selected. The area between the two pole is determined as the account area. Starting from the first armature in the calculation area, point calculation is made according to the observer which is positioned 60 m backward and in the middle of each strip. The luminance level of a point on the road surface is equal to the sum of the light levels that come to a point [6, 14, 15]. Figure 3 shows a sketch of a point lighting calculations.

Calculations are based on a period for periodic and linear paths. If you have more than one periodic and linear path pieces on the road, you need to make a separate calculation for each part of the road. Radius greater than 300 m radius can be considered as linear path. The area between the two light sources on the single roads is considered the account area. On double roads (refugee), the area between two light sources is considered as the area of account, considering only one of the routes of departure or arrival. Only one side calculation is sufficient [16-23].

In this study, lighting calculations are made for tunnel inner zone. Tunnel inner region is the place where energy consumption is the highest in long tunnels.

The horizontal illumination of a point P on an illuminated path; This is the sum of the horizontal light levels that all the luminaires affecting the account area in the lighting installation formed at this point. Figure 4 shows the horizontal illumination level vector state [14, 15]. Equation 1 shows the correlation between horizontal illumination levels.

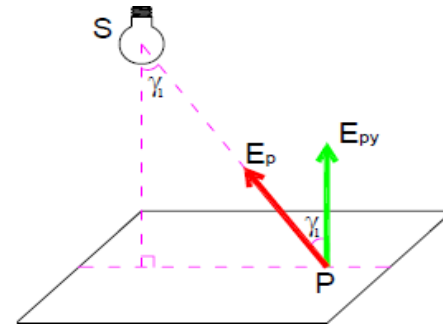


Fig.4. Horizontal illumination level vector state

$$E_{py} = \sum_{i=1}^a \frac{\Phi_L \cdot MF \cdot I(C, \gamma_2)}{1000 \cdot h^2} \tag{1}$$

$I(C, \gamma)$: is value of light intensity reaching from luminaire i to point P (cd),

γ : is angle of gleam falling within point P by the vertical line,

a : is amount of luminaires contributing to point P,

h : is ground clearance of luminaire photometric center (m)

C : is plane angle,

MF: Maintenance factor.

IV. TUNNEL LUMINANCE

The most important objective to design lighting systems is to obtain sufficient light without supplying excessive lighting and increasing energy cost [1, 2, 6]. Luminance is the most important dimension in terms of light effect on a road. Luminance is indicated by L and the unit is cd/m^2 . A smooth luminance distribution as much as possible on the road surface should be ensured for the good visibility of the objects and the driver's visual comfort. Today, road lighting is based on Luminance Method which is based on road surface glow. The horizontal illuminance of a point P on an illuminated road; It is the sum of the horizontal illuminance levels that all the light sources acting at point P have at this point [1, 2, 6, 14, 15]. In Equation 2, the relation between the variables to be used in the calculation of P point luminance is seen.

$$E_{p\gamma} = \sum_{i=1}^a \frac{\Phi_L \cdot MF \cdot I(C, \gamma_2)}{1000 \cdot h^2} \quad (2)$$

A fluorescent lamp has a glow of $5000\text{-}15000 \text{ cd}/\text{m}^2$, a full moon has a glow of $2500 \text{ cd}/\text{m}^2$ and a road surface under 30 lux of lighting has a glow of $2 \text{ cd}/\text{m}^2$. Since the glitter concept involves a specific point of the surface and observation direction, it is necessary to identify these conditions when glitter is mentioned. The glow of ideal reflective surfaces can be calculated by benefiting from the illumination level [1, 2]. When ρ is the reflection factor of the surface, the relation between glitter and illumination level is determined by Equation 3.

$$L = \rho \frac{E}{\pi} \quad (3)$$

The mean road level luminance (L_{th}) in any point of the threshold zone (it is the first extension at the tunnel entrance in Figure 5) is called the threshold zone luminance [3-5].

The rate of the threshold zone and access zone luminance's is $k = L_{th}/L_{20}$, where (L_{th}) is the mean road surface luminance at the beginning of the threshold zone and (L_{20}) is the luminance distance equal to the stopping distance in front of the tunnel. The mean value of the road surface luminance at any point of the transition zone is called the transition luminance (L_{tr}). The value of the mean road surface luminance in the interior zone is called the interior zone luminance (L_{in}) [1, 2, 6, 14, 15].

IV.1 Average road surface luminance

In the road lighting, the fund of objects is the road surface that forms the driver's field of vision. Therefore, a higher $L_{average}$ makes it easier to see by providing a higher background glow. The increase in $L_{average}$ increases the sensitivity of the driver's eye by increasing the luminosity of the objects in the road. Therefore, the most important parameter for detection is $L_{average}$. $L_{average}$ is calculated using the glitter values on the selected $m \times n$ pieces on the road. For $L_{average}$, the luminance values of all the light sources affecting the account area are calculated and collected as vector. In this

way, the glare value at each point is calculated. The average surface road luminance is calculated separately for each observer [1, 2, 6, 14, 15].

IV.2 Uniformity

Even though lighting systems provide a good mean road surface luminance, there may be zones with low luminance where contrast is weak and small obstacles cannot be detected. The difference between minimum and mean road surface luminance's into the field of view is expected to be lower than a certain value in order to obtain enough illumination at all points on the road. This obligation brings us to the overall uniformity and longitudinal uniformity values that are important secondary parameters.

There should be an equal distribution of luminance in the road (on the road surface) in order to provide a clear view for the driver. Two kinds of uniformity are considered important in tunnel lighting [7-10]:

1) Mean (resultant) uniformity (U_o): When traffic is on the right side, it is the rate of minimum luminance (L_{min}) to mean luminance of the road ($L_{average}$), which is determined by an observer at $1/4$ distance of the road width on the right side of the road. The lower sections of the walls should be considered as well as road surface [1, 2, 6, 14, 15]. Equation 4 presents the ratio suitable for the road surface and mean luminance uniformity of the walls up to 1.5 m from the ground according to CIE 140-2000 and CIE 88-2004 [24, 25].

$$U_o = \frac{L_{min}}{L_{average}} \geq 0.4 \quad (4)$$

Longitudinal uniformity (U_l): According to an observer on the center line of road lane, it is the rate of minimum luminance applied through the center line to maximum luminance. Equation 3 presents the rate suitable for longitudinal uniformity through the road. Equation 5 shows change of longitudinal uniformity factor.

$$U_l = \frac{L_{min}}{L_{max}} \geq 0.7 \quad (5)$$

IV.3 Surround rate

Light sources illuminate the emergency lane or pavement at a certain rate when illuminating the road surface. The parameter defined for this is the surround rate (SR).

IV.4 Light sources

High-pressure sodium vapor (HPS) lamps are preferred under conditions of higher luminance level, including under water tunnels, as HPS lamps have higher light flux and smaller dimensions than low-pressure lamps. As a result, less luminaries and area are required for lighting. The luminance efficiency is defined as the luminance level from the power required for the road (for 1 m^2). In this study, 50 W HPS lamp was used. The lamp is luminous flux 4000 .

V. DETERMINATION OF THE ACCOUNT AREA FOR TUNNEL LIGHTING

Road types are defined in international technical reports and an optimal solution range is presented technically for these road types. The required design calculations should be made through luminaries with known photometric values, and the number and type of the luminaries should be determined according to these calculations [8, 20, 26-31].

Related road, road lighting class is determined by the table in the CIE 115-2010 [8, 20, 27]. According to Table 1, road lighting class M2 was found. Road lighting class selection parameters are shown in Table 1. Road lighting quality parameters are shown in Table 2.

TABLE I
ROAD LIGHTING CLASS SELECTION PARAMETERS

Parameter	Options	Weight factor
Speed	High	0.5
Traffic jam	High	0.5
Traffic layout	Only motor vehicles	0
Middle median strip on the road	Yes	1
Intensity of intersection	High	1
Parked vehicle	No	0
Environmental lighting	High	1
Traffic control	Medium or good	0
Total of weight factors:		4

Road lighting class was found with equality 6, 7 and 8. Road lighting quality parameters are shown in table 4 [8, 20, 27].

$$MX = 6 - \text{Total weight factors} \quad (6)$$

$$MX = 6 - 4 = 2 \quad (7)$$

$$MX = M2 \quad (8)$$

TABLE II
ROAD LIGHTING QUALITY PARAMETERS

Lighting class	$L_{average}$	U_o	U_l	TI%	SR
M2	>1,5	>0,4	>0,7	<10	>0,5

V.1 Features of the tunnel lighting

The road pavement is asphalt, class R4. Additionally, $Q_o=0.08$, the wall coating is concrete, the reflectivity is 0.4, and the height of the luminary is 11 m. The maintenance factor of the luminary is 0.83 and all calculated luminance values are corrected. The ratio of the smallest luminance value to mean luminance value is greater than 0.4 in the calculations for road lighting, ensuring that the rate of the smallest luminance value to the largest at the latitude coordinate of the observer is greater than 0.7 ($U_l \geq 0.7$).

The luminance levels and uniformities of the tunnel walls are in accordance with relevant standards and they are very important for driving safety. All lighting luminaries were established in single line 2 m from the tunnel walkways to the axis of the road and at a height of 6 m. The lighting in the tunnel will be supplied by the luminaries with symmetric light distribution. The contrast revealing coefficient, which is the most important criterion in the application of symmetric light distribution, is less than 0.2. Table 3 illustrates the road and lighting parameters [20-22, 29, 30].

TABLE III
TUNNEL AND LIGHTING PARAMETERS

Tunnel lighting parameters			
Lighting pole type	Galvanized	Lighting class	M2
Number of road lanes	1	Console length (m)	-
Strip Width (m)	4	Console Angle	-
Road Width (m)	4	Armature Angle	0°/5°/10°/15°
Road Class	R4	Lamp type	HPS
Q_o	0.08	Lamp power(Watt)	50
Distance to illumination	0	Lamp luminous flux	4000
Illumination height from ground (m)	6	Maintenance factor (every 3 years)	0.83

V.2 Simulation study

A non-commercial simulation program was used for lighting in this study [1, 29, 30]. The main purpose of the new studies is to reach the most economical results that provide adequate conditions. In the new study's made about road lighting, classifications are taken into consideration in the various scenarios conditions. The most accurate reference to road-tunnel lighting are international standards. For this reason, simulation is adapted to CIE standards. According to CIE 140 - CIE 88, the luminance values, averaged luminance level, averaged and longitudinal uniformity values of all points were calculated for the observers [24, 25].

Luminaires to be used in road-tunnel lighting should be chosen by taking into account glare level, luminance level of the road, lighting uniformity and economy, and they should be determined in consequence of computer calculations according to the luminance method [30-37].

Various choices are available for the road parameters in the simulation program. For the road-tunnel parameters, the lighting system (mutual, cross, divided road, road with single luminary, road with two luminaries, etc.), road class (R1, R2, R3, R4, N1, N2, N3, N4, etc.), number of lanes, lane width, refuge width, and road lighting class (M1, M2, M3, M4, M5, M6, etc.) can be chosen. For the lighting parameters, features such as distance between the luminaries, height of the luminary, distance of the luminary from the road, console angle, IP protection class, pollution rate, cleaning period, and maintenance factor are chosen for post or hanger system lighting. For the luminary parameters, the name, angle of the luminary (angle relative to the road), power of the lamp used, lifetime, light flux, ballast power, and new lamps can be added into this simulation under the Database process at any time. As a result, it is possible to add any kind of lamp into the simulation [1, 2, 29, 30]. An easy and accurate calculation is achieved in the simulation results for the lighting system in which data is entered.

VI. APPLICATIONS OF TUNNEL LIGHTING

In this study, a problem encountered in tunnel lighting were investigated. These problem are about angled lighting. For this purpose, it has been proven with a simulation program that the angled lighting encountered almost everywhere in the road lighting is inaccurate [30-37]. It is proved that it is necessary to perform (0°) illumination parallel to the road surface instead of angled lighting. New solutions can be found in the simulation environment for roads with different strengths and

TABLE VI
LUMINANCE (LUMINAIRE ANGLE: 0°) FOR TUNNEL LIGHTING

$L_{average} = 1,51 \text{ cd/m}^2$ $U_o = 0,59$ $U_i = 0,77$ $TI = \%3,2$										Angle:0°
Observer location (m)	0,550	1,650	2,750	3,850	4,950	6,050	7,150	8,250	9,350	10,450
0,667	1,068	0,987	1,117	1,026	0,912	0,954	1,149	1,177	0,894	1,050
2,000	1,667	1,698	1,781	1,669	1,584	1,737	1,930	2,055	1,718	1,700
3,333	1,641	1,659	1,895	1,679	1,631	1,797	1,907	2,084	1,624	1,623

TABLE VII
LUMINANCE (LUMINAIRE ANGLE: 5°) FOR TUNNEL LIGHTING

$L_{average} = 1,36 \text{ cd/m}^2$ $U_o = 0,55$ $U_i = 0,83$ $TI = \%3,0$										Angle:5°
Observer location (m)	0,550	1,650	2,750	3,850	4,950	6,050	7,150	8,250	9,350	10,450
0,667	0,896	0,839	0,928	0,873	0,758	0,781	0,944	0,946	0,749	0,879
2,000	1,466	1,475	1,579	1,499	1,396	1,483	1,664	1,683	1,414	1,441
3,333	1,584	1,582	1,843	1,637	1,634	1,787	1,844	2,037	1,546	1,555

TABLE VIII
LUMINANCE (LUMINAIRE ANGLE: 10°) FOR TUNNEL LIGHTING

$L_{average} = 1,16 \text{ cd/m}^2$ $U_o = 0,53$ $U_i = 0,78$ $TI = \%3,0$										Angle:10°
Observer location (m)	0,550	1,650	2,750	3,850	4,950	6,050	7,150	8,250	9,350	10,450
0,667	0,714	0,696	0,734	0,708	0,627	0,642	0,723	0,702	0,614	0,695
2,000	1,293	1,180	1,320	1,258	1,160	1,224	1,360	1,381	1,081	1,260
3,333	1,447	1,432	1,643	1,470	1,463	1,595	1,643	1,799	1,410	1,411

TABLE IX
LUMINANCE (LUMINAIRE ANGLE: 15°) FOR TUNNEL LIGHTING

$L_{average} = 0,95 \text{ cd/m}^2$ $U_o = 0,52$ $U_i = 0,81$ $TI = \%3,1$										Angle:15°
Observer location (m)	0,550	1,650	2,750	3,850	4,950	6,050	7,150	8,250	9,350	10,450
0,667	0,577	0,567	0,597	0,602	0,544	0,554	0,603	0,554	0,499	0,558
2,000	1,083	0,982	1,080	1,040	0,942	0,976	1,093	1,102	0,894	1,051
3,333	1,243	1,172	1,345	1,247	1,198	1,319	1,372	1,433	1,131	1,195

VII. DISCUSSIONS

In this study, the effects of angled lighting in tunnel lighting were investigated. For this purpose, the parameters of a road used for single-lane military purposes (for underground arsenals) were processed into a lighting simulation. Firstly, the optimum distance was determined as 11 m when the angle of the luminaire was 0°. When the angle of the luminaire is 0° and the distance between the luminaires is 11 m, all values are suitable for CIE 88-2004 standard. If the luminaire angle is 5°, 10° and 15°, the distance between the poles falls below the average value of $L_{average}=1.50 \text{ cd/m}^2$. Luminaire angle 5° $L_{average}=1.36 \text{ cd/m}^2$; luminaire angle 10° $L_{average}=1.16 \text{ cd/m}^2$; luminaire angle 15° $L_{average}=0.95 \text{ cd/m}^2$; value falls. $L_{average}=1.50 \text{ cd/m}^2$ falling below does not comply with CIE standards. Accordingly, when the luminaire angle is 0°, the highest lighting efficiency is reached and the luminous efficiency decreases as the angle increases.

This work for the tunnel can be applied on all roads. Angled lighting is used in about 90% of the currently roads. As stated in this example, angled lighting (5°, 10° and 15°) with 70 W HPS lamp corresponds to tunnel lighting with 50 W HPS lamp (not angled, 0°). Using higher power lighting increases energy consumption. Increased energy consumption is undesirable in terms of efficiency.

VIII. CONCLUSION

The most accurate reference to road-tunnel lighting and lamp selection is the international standards. For this reason, simulation road lighting is adapted to CIE standards. According to CIE 88-2004 standard, luminance values, average luminance level, average and longitudinal uniformity

values of all scores were calculated for the observers. The data of the lamp used were processed in the simulation database and the results were analyzed.

The 50 W HPS lamp complies with the standards specified in the CIE 88-2004 The Lighting of Road Tunnels and Underpasses at the luminaire angle=0° optimum pole pitch (11m).

If the angle of the luminaire is 5°, 10° and 15°, the $L_{average}$ is less than 1.50 cd/m^2 . This doesn't fit the CIE standards. Inefficient and inadequate lighting was observed under the standards.

Such special solutions can be improved by lighting simulations. Therefore, as in this example, special solutions should be analyzed in road lighting in simulation environments.

REFERENCES

- [1] M.S. Cengiz, "A Simulation and Design Study for Interior Zone Luminance in Tunnel Lighting." Light & Engineering, vol. 27. 2, 2019, pp. 42-51.
- [2] M.S. Cengiz, "The Relationship Between Maintenance Factor and Lighting Level in Tunnel Lighting." Light & Engineering, vol. 27. 3, 2019.
- [3] M.S. Cengiz, Ç. Cengiz, "Numerical Analysis of Tunnel LED Lighting Maintenance Factor." IIUM Engineering Journal, vol. 19. 2, 2018, pp. 154-163.
- [4] S Onaygil, Ö Güler, E. Erkin, "Determination of the effects of structural properties on tunnel lighting with examples from Turkey." Tunnelling and underground space technology, vol. 18. 1, 2003, pp. 85-91.
- [5] S. Onaygil, "Parameters affecting the determination of the tunnel threshold-zone luminance." Turkish Journal of Engineering and Environmental Sciences, vol. 24. 2, 2000, pp. 119-126.
- [6] A. Ongun, "The Analysis of Optimum Solution Criteria for The Designing of Road Lighting Installations." M. Sc. Thesis, Gazi University Institute of Science and Technology, 2007. 174 pages. Ankara.

- [7] International Commission on Illumination, Road lightings as an Accident Countermeasure, CIE 93, Vienna-Austria, 92 (1992).
- [8] M.S. Cengiz, "Effects of Luminaire Angle and Illumination Topology on Illumination Parameters in Road Lighting." *Light & Engineering*, 2019.
- [9] K.A. Painter, D.P. Farrington, "Evaluating Situational Crime Prevention A Young People's Survey.", *The British Journal of Criminology*, London, vol. 41, 2, 2001, pp. 266-284.
- [10] Gan, F., Grabosky, P., *Improved street Lighting and Crime Reduction, The Promise of Crime Prevention*, 2nd ed. ISBN 0642241724, Canberra: Australian Institute of Criminology, Canberra, 1326-6004 (2000).
- [11] G. Gencer M. Eren, S. Yildirim. M. Kaynaklı. O. Palta, M.S. Cengiz, Ç. Cengiz, Numerical Approach to City Road Lighting Standards, Book of Abstracts, Imeset Int. Conf. Mult. Sci. Eng. Tech., October 27–29, 2017, Bitlis, Turkey.
- [12] M. Eren, M. Kaynaklı, I. Yapici, G. Gencer, Y. Yurci, M.S. Cengiz, Ç. Cengiz, Numerical Analysis of Maintenance Factor for Tunnel and Road In Solid State Lighting. International Conference on Multidisciplinary, Science, Engineering and Technology 2017, Bitlis, 2017, October 27-29, Turkey.
- [13] G. Leonid, S. Sergei, A. Feofanov, "Reconstruction of Illumination Devices at the Moscow Metro." *Light & Engineering*, vol. 27. 2, 2019, pp. 52-57.
- [14] W.V. Bommel, *Road Lighting: Fundamentals, Technology and Application*, Springer Int. Pub. Switzerland-2015, 333 pages, ISBN: 978-3-319-11465-1
- [15] M. Özkaya, "Aydınlatma Tekniği." Birsen Yayınevi, İstanbul-1994, 91.
- [16] E. Tetri, S.B. Chenani, R.S. Rasanen, "Advancement in Road Lighting." *Light & Engineering*, vol. 26. 1, 2018, pp. 99-109.
- [17] W.V. Bommel, G.V. DenBeld, M.V. Ooyen, "Industrial Light and Productivity." *Lighting & Engineering*, vol. 11. 1, 2003, pp. 14–21.
- [18] P. Barua, S. Mazumdar, S. Chakraborty, S. Bhattacharjee, "Road Classification Based Energy Efficient Design and its Validation for Indian Roads." *Light & Engineering*, vol. 26. 2, 2018, pp. 110-121.
- [19] G.I. Rossi, P. Soardo, "Energy Saving and Environmental Compatibility in Road Lighting." *Light & Engineering*, vol. 20. 4, 2012, pp. 55–63.
- [20] S. Onaygil, "Yol aydınlatma projelerinde yol sınıfının belirlenmesinin önemi." *Kaynak Elektrik Dergisi*, vol. 12, 1998, pp. 125-132.
- [21] Ö. Güler, S. Onaygil, "The effect of luminance uniformity on visibility level in road lighting." *Lighting Research & Technology*, vol. 35. 3, 2003, pp. 199-213.
- [22] B. Buyukkinaci, S. Onaygil, Ö. Guler, M.B. Yurtseven, "Determining minimum visibility levels in different road lighting scenarios, *Lighting Research & Technology* vol. 50. 7, 2018, pp. 1045-1056.
- [23] Gencer, G., Eren, M., Yildirim, S., Kaynaklı, M., Palta, O., Cengiz, M.S., Cengiz, Ç. 2017. Numerical Approach to City Road Lighting Standards, In: International Conference on Multidisciplinary, Science, Engineering and Technology 2017, Bitlis, October 27-29, Turkey
- [24] CIE Technical Report–88–2004. Guide for the Lighting of Road Tunnels and Underpasses [R], 2004.
- [25] CIE 140-2000 Road Lighting Calculations. CIE140, International Commission on Illumination, Road Lighting Calculations, Vienna-Austria, 33 (2000).
- [26] P. Thorns, "Review of the Current State and Future Development in Standardising Artificial Lighting." *Light & Engineering*, vol. 27. 2, 2019, pp. 4-22.
- [27] CIE 115-2010 CIE115, International Commission on Illumination, Recommendations far the Lighting of Roads for Motor and Pedestrian Traffic, Vienna-Austria, 1995, 25.
- [28] CIE 136-2000, Guide to the lighting of urban areas, 3 August 2000.
- [29] S. Onaygil, TEDAŞ Genel Müdürlüğü Meslek İçi Eğitim Semineri, TEDAŞ Basımevi, Ankara, 2005. pp. 1–70.
- [30] S. Onaygil, TEDAŞ Genel Müdürlüğü Meslek İçi Eğitim Semineri-Gölbaşı Eğitim Tesisleri, Yol aydınlatma Semineri 23–24 Ocak 2007
- [31] CIE 194-2011 On site measurement of the photometric properties of road and tunnel lighting, 2011.
- [32] S.B. Efe, "Dinamik güç sistemleri için Jakoben yöntemi tabanlı birleşik güç akış kontrolörü tasarımı." *DÜMF Mühendislik Dergisi*, vol.9. 2, 2018, pp. 601-607.
- [33] S.B. Efe, "UPFC Based Real-Time Optimization of Power Systems for Dynamic Voltage Regulation." vol.116. 3, 2018, pp.391-406.
- [34] M.S. Cengiz, "Smart meter and cost experiment." *Przeglad Elektrotechniczny*, vol. 89. 11, 2013, pp. 206-209.
- [35] M.S. Cengiz, M.S. Mamiş, "Endüstriyel tesislerde verimlilik ve güneş enerjisi kullanımı." VI. Enerji Verimliliği Kalitesi Sempozyunu ve Sergisi, 21-25. 4-6 Haziran 2015, Sakarya, Türkiye
- [36] M.S. Cengiz, M.S. Mamiş, "Solution Offers For Efficiency and Savings in Industrial Plants." *Bitlis Eren University Journal of Science and Technology*, vol. 5. 1, 2015, pp. 24-28.
- [37] M. Çıbuk, "Tek Atlı Kablo Algilayıcı Ağlarda Yeni Bir Hızlı Ağa Katılım Algoritması." *Bitlis Eren Üniversitesi Fen Bilimleri Dergisi*." Vol. 7. 1, 2018, pp. 72-83.
- [38] Ö.F. Ertuğrul, "Forecasting electricity load by a novel recurrent extreme learning machines approach." *International Journal of Electrical Power & Energy Systems*, vol. 78. 7, 2016, pp. 429-435.
- [39] M.S. Cengiz, "Evaluation of Smart Grids and Turkey." *Global Advanced Research Journal of Engineering Technology and Innovation*, vol. 3. 7, 2014, pp. 149-153.
- [40] B. Turan, H.I. Eskikurt, M.S. Can, "Dizüstü Bilgisayar Ekranında Bakılan Nokta Koordinatlarının Yapay Sinir Ağı ile Tahmin Edilmesi." 2014 IEEE 22nd Signal Processing and Communications Applications Conference (SIU 2014), Yayın No:1294070.
- [41] M.S. Can, B.Turan, Y.S. Ari (2013). Evler Ve Soğuk Hava Depoları İçin Sms ve Mikrodenetleyici Tabanlı Buzdolabi Soğutucu Arıza Uyarı Sistemi. Otomatik Kontrol Ulusal Toplantısı, TOK 2013.
- [42] D. Arı, M. Çıbuk, F. Ağgün, "Effect of Relay Priority Mechanism on Multi hop Wireless Sensor Networks." *Bitlis Eren University Journal of Science and Technology*, vol. 7. 2, 2017, pp. 145–153.

BIOGRAPHIES



MEHMET SAIT CENGİZ is the Director of Research and Development 2000-2010 years in Turkey Electricity Distribution Company. In 2011, he completed his master degree in the field of Electrical and Electronics Engineering. In 2016, he completed his doctorate degree in Inonu University, Institute of Science and Technology, Electrical and Electronics Engineering. Works in the field of applied lighting. He is currently working at Bitlis Eren University.

A Secure Tracking Automobile System for Oil and Gas Distribution using Telematics and Blockchain Techniques

L. A. AJAO, J. AGAJO, O. M. OLANIYI, I. Z. JIBRIL, A. E. SEBIOTIMO

Abstract— Crude oil is the major sources of income to most of the developed and developing countries. It is high significance as this natural resource contributed to the development countries wealthy, and cannot be over-emphasized. The distribution of oil and gas products in the developing ecosystem is mostly conveyed through the road networks, by engaging trucks and similar type of automobiles in the goods delivery. This approach of fuel distribution is susceptible to illegal diversion, tampering, vehicles hijacking and many others on-transit route. In this paper, we present the development of a secure tracking automobile system for oil and gas distribution using telematics and blockchain technology. This system helps in tracking the geo-location of automobile route and monitoring the volume of products loaded in automobile using telematics. The hash algorithm based blockchain technology approach helps to secure the system database and accomplished monitoring of the fuel volume records conveyed from agent tampering, diversion and hijacking. It prevents an individual concerned from remote database information altering or unscrupulous parties' intrusion. Also, it manages the archives and linking of the subsequent records through the developed secure distributed database system (blockchain). The secure in-vehicle tracking system uses a GPS (Tx and Rx) for the geo-location tracking, ultrasonic sensor (HCR05), SIM800 and ATmega328 microcontroller unit. This system was tested and evaluated in terms of accuracy and precision of the GPS receiver coordinates with a report of circular error probability radius of 15 meters and precision of 1.24 meters.

Index Terms— Automobiles, Blockchain, Database, Global Positioning System (GPS), Telematics.

L. A. AJAO is with Department of Computer Engineering, Federal University of Technology, Minna, Nigeria, (e-mail: ajao.wale@futminna.edu.ng).

 <https://orcid.org/0000-0003-1255-752X>

J. AGAJO is with Department of Computer Engineering, Federal University of Technology, Minna, Nigeria, (e-mail: james.agajo@futminna.edu.ng).

 <https://orcid.org/0000-0002-2306-6008>

O. M. OLANIYI is with Department of Computer Engineering, Federal University of Technology, Minna, Nigeria, (e-mail: mikail.olaniyi@futminna.edu.ng).

 <https://orcid.org/0000-0002-2294-5545>

I. Z. JIBRIL is with Department of Computer Engineering, Federal University of Technology, Minna Nigeria, (e-mail: danjumanupe@gmail.com).

A. E. SEBIOTIMO is with Department of Computer Engineering, Federal University of Technology, Minna Nigeria, (e-mail: sebiotimo.adedimeji@st.futminna.edu.ng).

Manuscript received February 1, 2019; accepted June 16, 2019.

DOI: [10.17694/bajece.520979](https://doi.org/10.17694/bajece.520979)

I. INTRODUCTION

OVER THE YEARS, aside agriculture and other related occupations in Nigeria, Oil and Gas has been the most source of nation revenue generation and as major dependent economy-driven. This has been the situation since the discovery, exploration and mining of crude oil in the country. Petroleum products in this context refer to the fuel components like premium motor spirit, domestic pure kerosene, and automotive gas oil [1]. The transportation of this products (petroleum) is structured from refineries to the depot through piping networks [2], and to the individual marketers using automobile through road networks. These activities require adequate coordination, monitoring and effective control. Crude oil as a raw materials product mining in large quantities faces terrible challenges of distribution that usually emanate to the fuel scarcity and price inflation. Also, inefficient distribution networks and lack of database record management outcome causes greater percentage of this product being flared off [3].

The Global Positioning System (GPS) is the satellite-based navigation maintained and operated by the government of the United States of America. It provides global geo-location and time services to GPS receivers within line of sight [4]. The origin of GPS started in the sputnik era where scientists determined satellites location by analyzing the doppler effect on the radio signals. Later, the US Navy was able to determine the location of submarines with six satellites orbiting from the north to south poles. This precedent approach helps the US Department of defense's Navigation System with Timing and Ranging (NAVSTAR) in direction finding which became fully implemented in 1993 with 24 satellites [5, 6].

Therefore, the satellites are made to orbit at an altitude of 20,200 km, it revolves round the earth twice every day and is divided into 6 orbital planes, and inclined at 55° to the equator. The GPS satellites transmit information using radio waves at frequency (1 – 2) GHz and wavelength ranging from (15 – 30) cm L-band [7, 8].

The terms telematics was defined in [9, 10] as a French acronym Telecommunication and Informatics. This practice in wireless network applications is responsible for an active role such as Wireless for the Vehicular Environment (WAVE) or Intelligent Transportation System (ITS) and computational system. Telematics approach is used as the broadcast or sending a remote information through telecommunications

devices [11].

This technology utilized a GPS-based artificial satellite and onboard diagnostics system (database) to record geographic information on a computerized map. Telematics is also called black box, an intelligent in-vehicle computer that recorded information based on geographic location and its environs in the On-Board Diagnostics System (OBD) [12]. Telematics techniques can be used to acquire large information remotely by integrating wireless sensors, multimedia devices and other connected hardware components.

A full-functional of telematics system can be built with, GPS transmitter and receiver, GSM module with SIM card, accelerometer sensor, ultrasonic sensor, buzzer, intelligent microchips input/output interface (port) and many others. The in-vehicle telematics system covered a wide area of application as in salts and sands spreader tracker, driving cameras, electronic logging displays (ELDs) and weather forecasting alert [13].

Blockchain is newly emerged and notable bitcoin technology for adequate security of distributed ledger in the database. It offers advanced platform of both decentralized and transparent transaction mechanism for all industries and businesses. This characteristics of the blockchain security is adapted in the developed system to improve trust and remote monitoring through the transparency and traceability of transaction of data resources carried out. Despite the initial doubts about this technology, governments and large corporations have recently investigated and improving on this technology in the applications domain like finance, social and legal industries, manufacturing and supply chain networks [14].

Blockchain technology makes it possible to store data in such a way that multiple peers can view, copy and update records in a real time. It is very difficult to make changes on the data secure with blockchain technology illegally or individually which helps to strengthens trust in a blockchain's content [15]. A standout amongst the most important parts of utilizations based on blockchains is that empower business to be directed with untrusted and obscure clients.

The outstanding parts of this article are organized into five sections. The reviewed of the existing related works are presented in section II. Methods and materials involved in this research are details outline in section III. While section IV discussed results, and research is finally concluded and recommended for further research in section V.

II. RELATED WORKS

A number of related works exist in literature. A GPS-based vehicle location tracking system using smartphone application interfaced with the google maps API for the location display and other related information was developed in [16]. An in-vehicle tracking system using GPS and GSM modem was developed by [17]. This system transmits information in form of SMS to a mobile phone with encoded format.

An embedded Bluetooth technology system was developed to acquired information about the proof of network location with security measure using blockchain in [18]. This system is

used to determine the location of devices in a peer to peer network. The proofs of locations are essential for the proper functioning of location-based services which are dependent on the accuracy of the reported locations. The system functioning with the concept of mutual location verification between peers in the same geographical location through a short-range wireless communication device.

A telematics-based multiple vehicle monitoring was proposed in [19-21] using GPS, cell phone and network facilities for the in-vehicle application. This system renders a remote service communication through the wireless networks connectivity and the satellite positioning.

The dominant distributed networks of the petroleum products in Nigeria are conveyed through the roads and pipelines network. Unfortunately, these distribution networks are associated with various challenges such as pipeline vandalism, automobile fuel hijacking, tampering, robbery and diversion. [2, 22-23].

Our contribution in this research focus on the development of an embedded system-based in-vehicle tracking gadget prototype using GPS (Telematics approach) for automobile fuel hijacking as discussed in sub-section IIIA. This technique helps to monitor the oil and gas volume of an automobile conveyance, tracking the vehicle route and also taking into consideration the geo-location of automobile direction. The implementation of secure hash blockchain techniques is to managing the transaction record in the database, to ensure the cooperative agreement and unanimous consensus of the participant in the chain as discussed in sub-section IIIB. Also, adequate management of dynamic information received, stored, updated, deletion in the database. The section IV illustrates the results and discussion of proposed methods using telematics and SHA-1 based blockchain algorithm.

III. METHODS AND MATERIALS

The methods adopted in this research are in two folds. These are hardware system design and secured software coding using synergistic combination of telematics approach and secure hash blockchain database management system. The hardware-based telematics component includes GPS module (NEO-6M), GSM module (850-EGSM), Arduino Uno board (ATmega 328), Ultrasonic sensor (HC-SR04), printed circuit board and jumper connectors. The software used for coding are C-language for hardware programming in Arduino IDE, Python language for secure hash algorithm, HTML and manipulation query language for secured distributed ledger database development (Blockchain). The complete developed system architecture is illustrated in "Fig. 1" which help to monitor, tracking and transmit the geo-location information to the database in a real time, as well as the information about petroleum volume level in the automobile. This acquired information is transfer to the remote server (secure database) through the telematics system in a real-time.

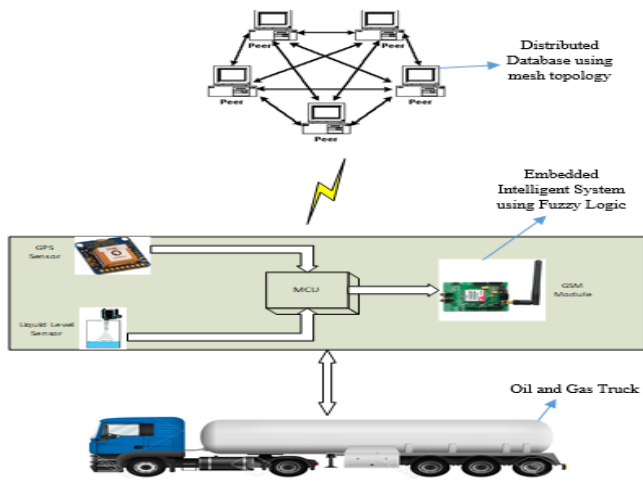


Fig. 1. In-vehicle based telematics and blockchain architecture

A. Hardware System Design

The hardware system consists of the controller unit, sensor unit, power supply unit, and the communication unit, all are integrated to function as telematic system. The system circuit sketch was designed and simulated in proteus virtual simulation model (PVSM) as demonstrated in “Fig. 2”.

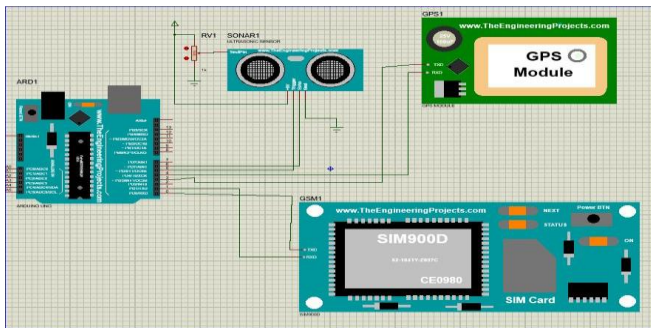


Fig.2. System circuit simulation in Proteus VSM

The sensing and communication unit comprises of the GPS (Ublox Neo 6M) transmitter-receiver (Tx/Rx), GSM and ultrasonic sensor. The GPS Tx/Rx used to obtain the latitude and longitude of geo-location, while the ultrasonic sensor used to determine the level of the liquid volume and measure distance to itself. This result obtained are sent to the microcontroller via transistor-transistor logic (TTL), and the controller transmit it to the server database periodically through the GSM module which utilize short messaging service (SMS).

The configuration of this GSM module with microcontroller is achieved through serial pins or communication port (UART) as illustrated in “Fig. 3”. This SIM800L communication module supports TCP and IP protocols, AT commands, and it was selected because of its proliferation (network frequencies, and relatively small size). The power supply of 7.4v LiPo battery with a DC-DC step-down buck converter was used to regulate the voltage output.

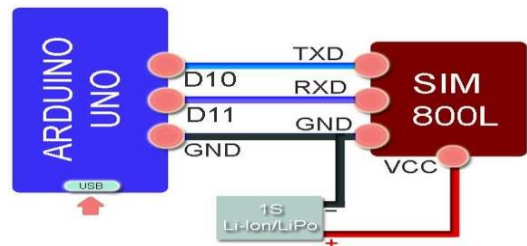


Fig.3. GSM module (Sim800L) logical connection

B. System Operation Principle and Design

The ultrasonic sensor (HC-SR04) is mounted on top of the automobile tank for liquid level monitoring which operates on the principle time of flight. This emitted waves from ultrasonic sensor used to determine the distance from a target (fluid surface) in the tank. The distance covered was used to determine the liquid level by setting trigger ultrasonic sensor to a logical high for 10 microseconds, then return to low, after the sensor emits waves and waits for reflected waves. Then, the echo pin of the sensor goes high for a duration time that is proportional to the distance of the target which allow the acquired data to be communicate to the microcontroller. The operation flowchart is illustrated in “Fig.4”.

The implementation of in-vehicle tracking system prototype (using telematics method) is integrated with automobile oil and gas tanker as shown in “Fig. 5” and “Fig. 6”. This prototype accomplished the objectives of geo-location tracking, volume monitoring in case of leakages or stealing and remote communication of geo-information to the server database.

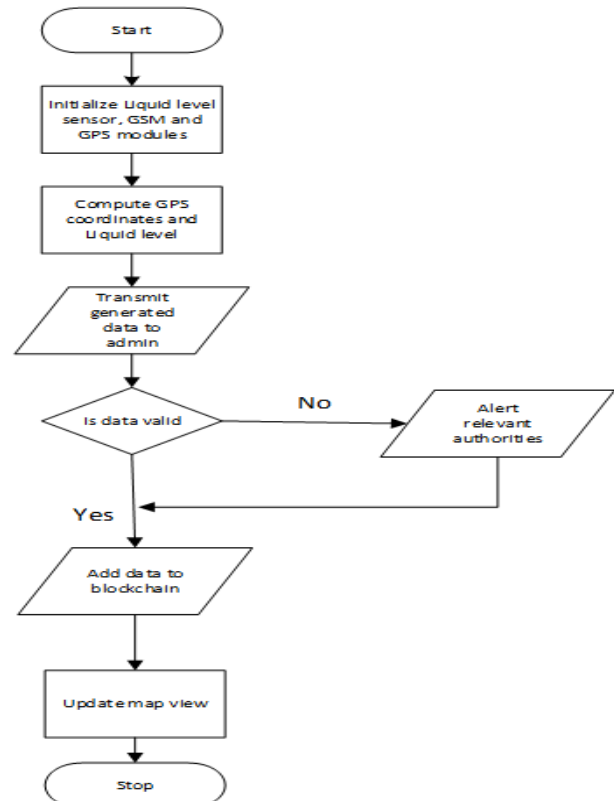


Fig.4. The hardware system operation flowchart

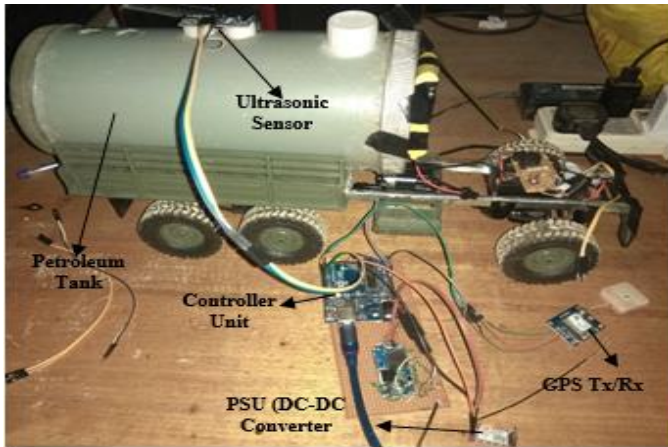


Fig. 5. A developed oil and gas automobile tanker tracking system prototype



Fig. 6. Packaging of oil and gas automobile tanker tracking system prototype

1) Time of flight (ToF) of emitted ultrasonic waves to determine distance

The Time of Flight (ToF) of sound wave produced by ultrasonic sensor can be described as a speedy dimension of distance for the various application of the in-vehicle based telematics system. These are motorized driver assistance system, drones, and some graphic user interfaces. This method require technicality in the design for the system performance benchmark which includes the system response time, accuracy, power consumption range and the available footprint. "Fig. 7" illustrate technical approach of measuring distance that correlate the transmitted and reflected signal to a target of the in-vehicle telematics system. In this scenario, a transmitter produces a square wave modulated signal while the target reflects sound back to the receiver which is correlated to the transmitted signal of an intelligent controller. The time of flight is measured by computing the range of distance to the target.

Therefore, amplitude of the reflected wave signal (A_r) emits can be express as in Eq. (1), refraction of emits wave signal transmitted from one medium to other experiences changes in its medium which can be calculated as expressed in Eq. (1).

$$A_r = \frac{R_1 - R_2}{R_1 + R_2} \tag{1}$$

Where,

$R_1 = \rho_1 c_1$
 $R_2 = \rho_2 c_2$
 $\rho =$ Density of each material
 $c =$ Speed of the signal wave source
 $A_r =$ Ratio between the reflected wave signal and incident amplitude.

$$\frac{\sin(\theta_1)}{\sin(\theta_2)} = \frac{c_1}{c_2} \tag{2}$$

The critical angle (θ_c), when there is total refraction ray can be calculated as express in Eq. (3).

$$\theta_c = \theta_1 = \sin^{-1} \frac{c_1}{c_2} \tag{3}$$

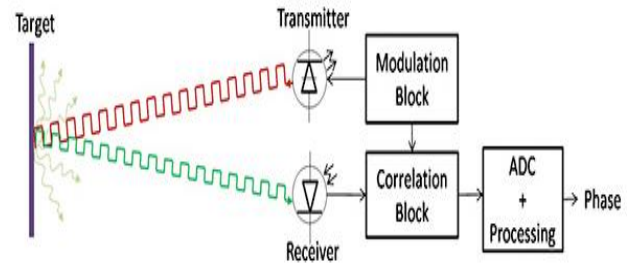


Fig.7. Time of flight computation to measure distance of signal transmitted to a target

2) Determining Vehicle Geo-location using the trilateration principle

The GPS receivers determine vehicle geo-location using the principle of trilateration. That is, principle of determining the absolute or relative geo-locations of a points in a geometry circle by measuring distances. This can be achieved when the distance of the receiver from the known locations is taken (four different satellites). Then, measurement of time taken for a signal to travel from a satellite to the receiver is used to determine the distance of the receiver from the satellite. The distance of the receiver (d), from a satellite illustrate that the receiver is located on a sphere (s) of radius (r) which found at centered on the location of the satellite [23].

The distance of the satellite from the location of the receiver can be shown by relating the coordinates of the receiver and GPS satellites in [19] from Eq. (4) to (7).

$$Pu_1 = \sqrt{(X - x_1)^2 + (Y - y_1)^2 + (Z - z_1)^2} - cd(T) \tag{4}$$

$$Pu_2 = \sqrt{(X - x_2)^2 + (Y - y_2)^2 + (Z - z_2)^2} - cd(T) \tag{5}$$

$$Pu_3 = \sqrt{(X - x_3)^2 + (Y - y_3)^2 + (Z - z_3)^2} - cd(T) \tag{6}$$

$$Pu_4 = \sqrt{(X - x_4)^2 + (Y - y_4)^2 + (Z - z_4)^2} - cd(T) \tag{7}$$

Where

P_{u_n} = distance from satellite n.

(X, Y, Z) = coordinates of the receiver's location.

(x_n, y_n, z_n) = coordinates of any of the satellites.

cd(T) = time correction from satellite clock.

3) Distance calculation the target and ultrasonic sensor

The ultrasonic sensor sound wave is used to determine the distance from itself to any target or obstacle in its front. The distance is calculated using the principle of time of flight of sound waves where the time taken for emitted sound waves to travel away from and back to the sensor is proportional to the distance. The relation is as follows:

$$\text{Distance (d)} = \frac{s * t}{2} \quad (8)$$

Where

s = speed of sound in air.

t = time taken for reflections to reach sensor.

Data charts which are typically black and white, but sometimes include color.

C. Secured Software System Design

The software system programming was used for hardware coding, building of web applications and secure database (blockchain) development. The database and web application were created using structured query language (SQL), PHP, JavaScript, HTML and CSS programming languages. Also, for the implementation of secure hash algorithm, permissioned blockchain type was used for securing the database which consist of four basic nodes. The administrator, oil and gas depot, distributed filling station and the in-vehicle transporter. The login page from the web application are shown in "Fig. 8" and "Fig. 9". The C-language program was used for coding microcontroller functions and telematics system in Arduino integrated development environment (AIDE) as a cross-platform application written in java programming language. A secure-tracking system and distributed database architecture is shown in "Fig. 10". The processes and implementation of the secure hash algorithm based on blockchain technology are highlighted here.

1: Takes input text and splits it into an array of the characters' ASCII codes.

2: Converts ASCII codes to binary.

3: Pad zeros to the front of each bit until they are 8 bits long.

4: Join them together and append them to one (1).

5: Pad the binary message with zeros until its length is 512 mod 448.

6: Take binary 8-bit ASCII code array from step 3, get its length in binary.

7: Pad with zeros until it is 64 characters.

8: Append to your previously created binary message from step 5.

9: Break the message into an array of chunks of 512 characters.

10: Break each chunk into subarray of sixteen 32-bit words.

11: Loop through each chunk array of sixteen 32-bit words and extend each array to 80 words using bitwise operations.

12: Initialize some variables.

13: Looping through each chunk: bitwise operations and variable reassignment.

14: Convert each of the five resulting variables to hexadecimal.

15: Append them together and the result is your hash value or message digest.

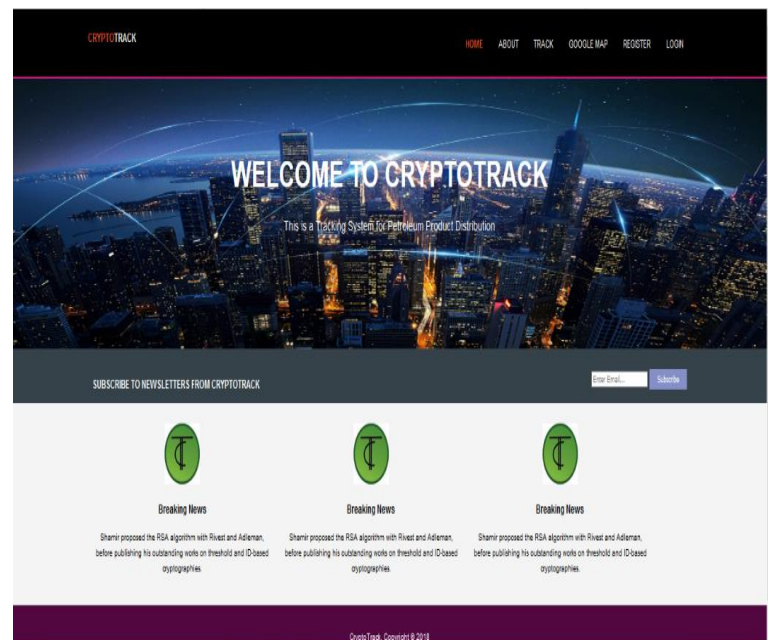


Fig.8. A secure-tracking database home page

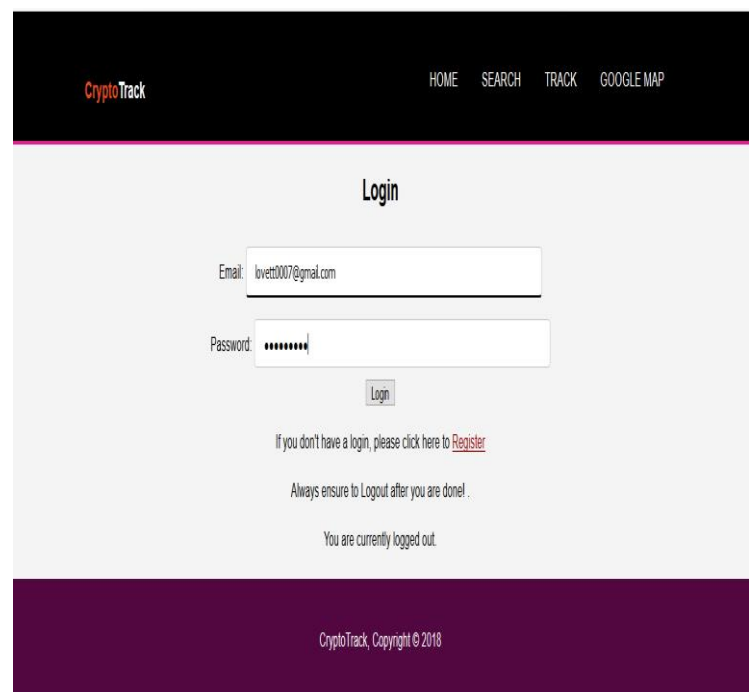


Fig. 9. Database login page

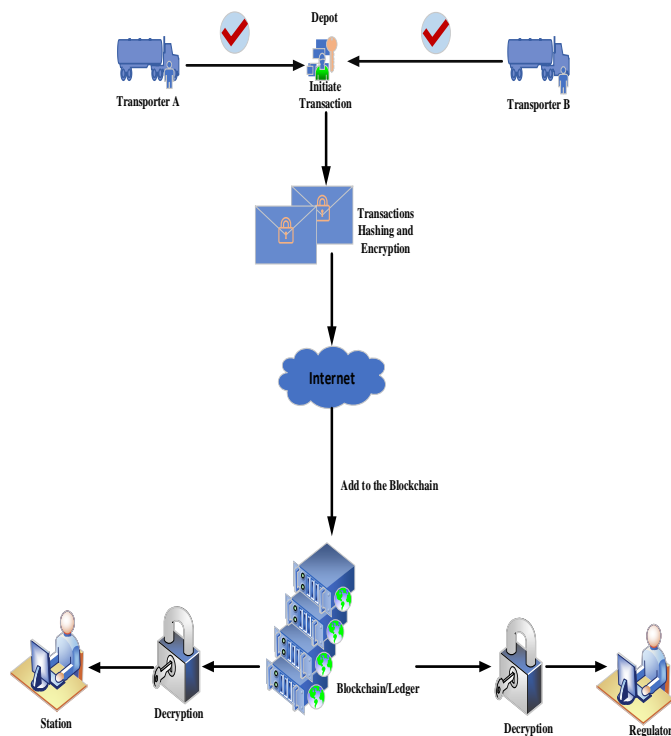


Fig.10. A secure-tracking system architecture

IV. RESULTS AND DISCUSSIONS

The result for telematics-based tracking system of the automobile geo-location during simulation in the Arduino IDE is illustrated in “Fig. 11”. This information includes longitude, latitude, distance, speed, date and time.

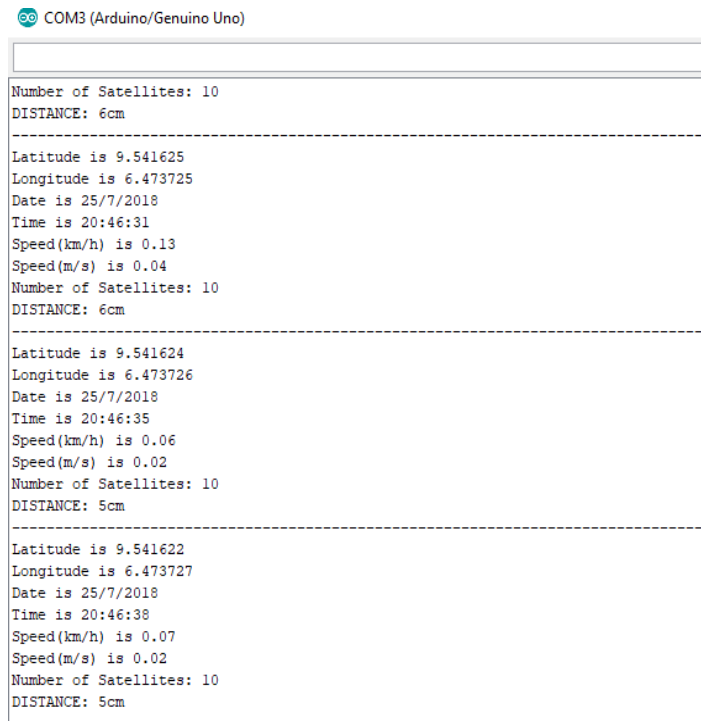


Fig. 11. Sensor readings displayed on serial monitor

Also, the data acquired from the GPS module are in NMEA format which was simulated and visualized in GPSview software as shown in “Fig. 12a” and “Fig. 12b”. This GPS visualizer contains the position of the GPS receiver, dilutions of precisions, relative positions and number of the satellites connected to as obtained from the GPS signals. The secure automobile tracking database is depicted in “Fig. 13”.

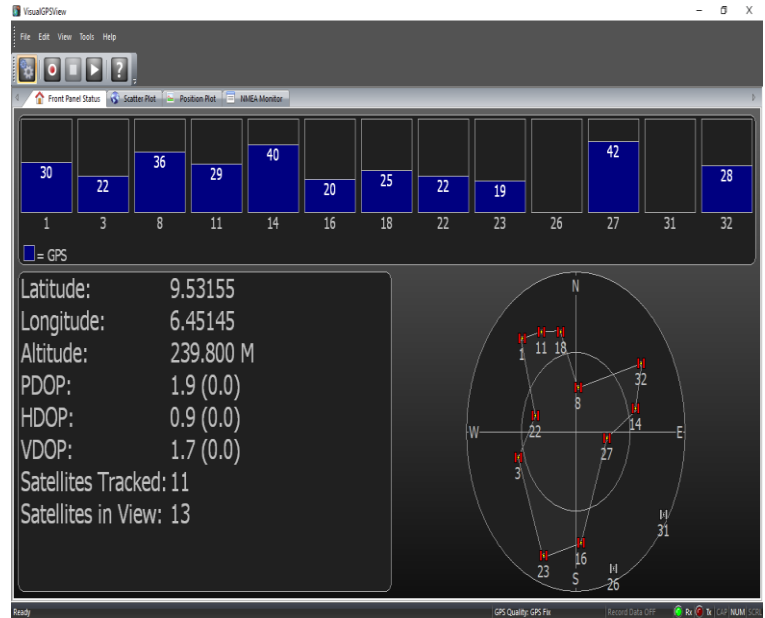


Fig. 12a. Visualization of GPS information

The remote data acquired based on geographic location, tracking, monitoring, automobile ID, Driver ID, filing station ID, time and date that are contained in the secure-database server using SHA-1 built-in blockchain technology for securing information. The result of geographic location tracking of automobile movement within the campus is displayed on a map interface as shown in “Fig. 14”.

The result gotten as shown in table 4.1 shows a disparity with the number of satellites captured. From the results It was observed that as the numerical strength of satellite captured intensifies, the longitude and latitude also vary correspondingly, and the larger the numbers of satellites captured the more accurate the GPS device as compared to the values of the coordinate obtained from google map. The system assessment was based on three elementary metrics which are; sensitivity, accuracy and success level. “Fig. 15” shows the tracking information stored in a secure database system. The “Table 1” contains detail analysis of tracking information send to secure database during testing of the prototype, and “Fig. 16” illustrate the graph of sensitivity, satellite level and the success level based on geo-location.

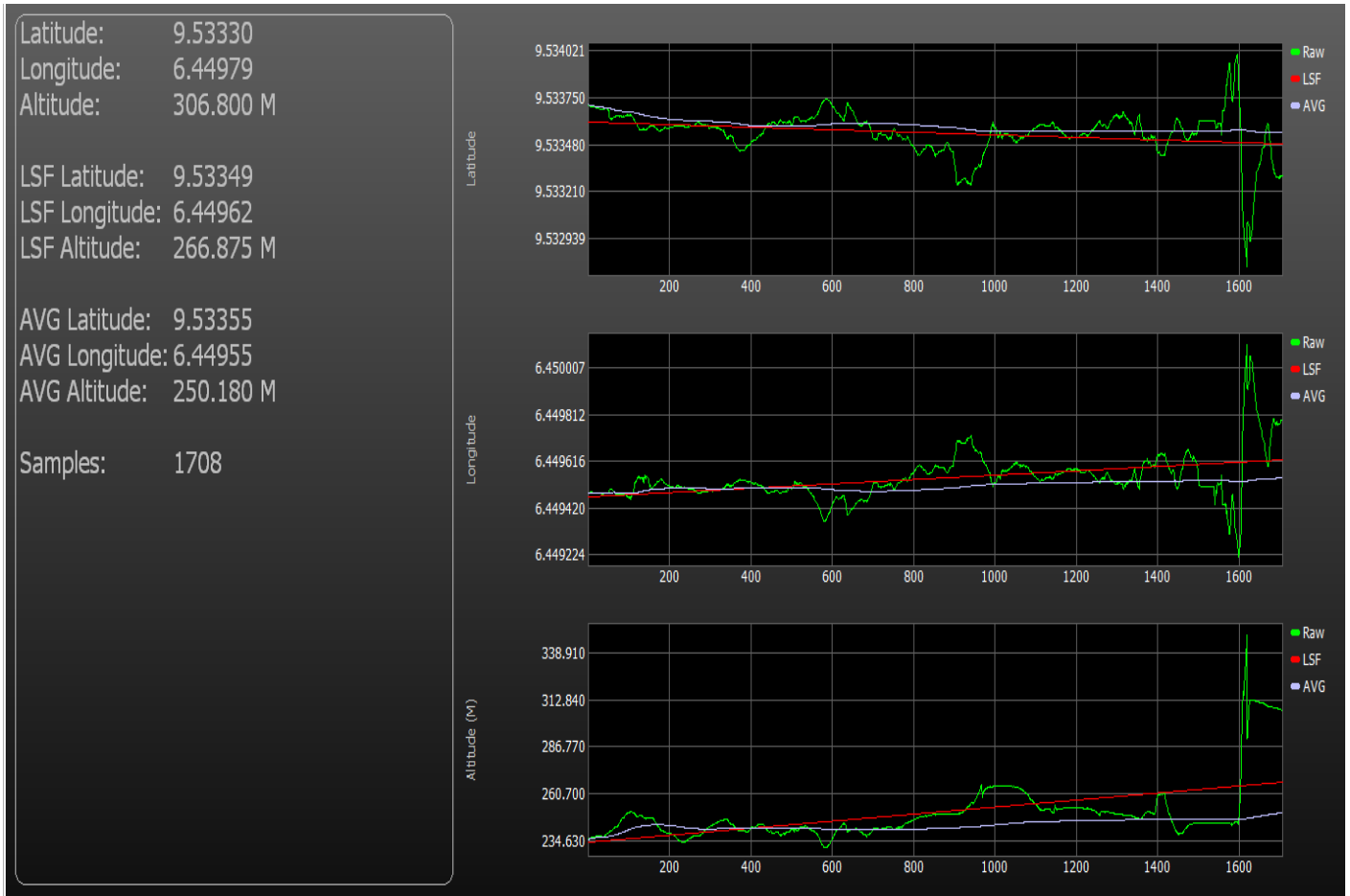


Figure 12b. Graphical analysis of vehicle geo-location tracking in GPS view

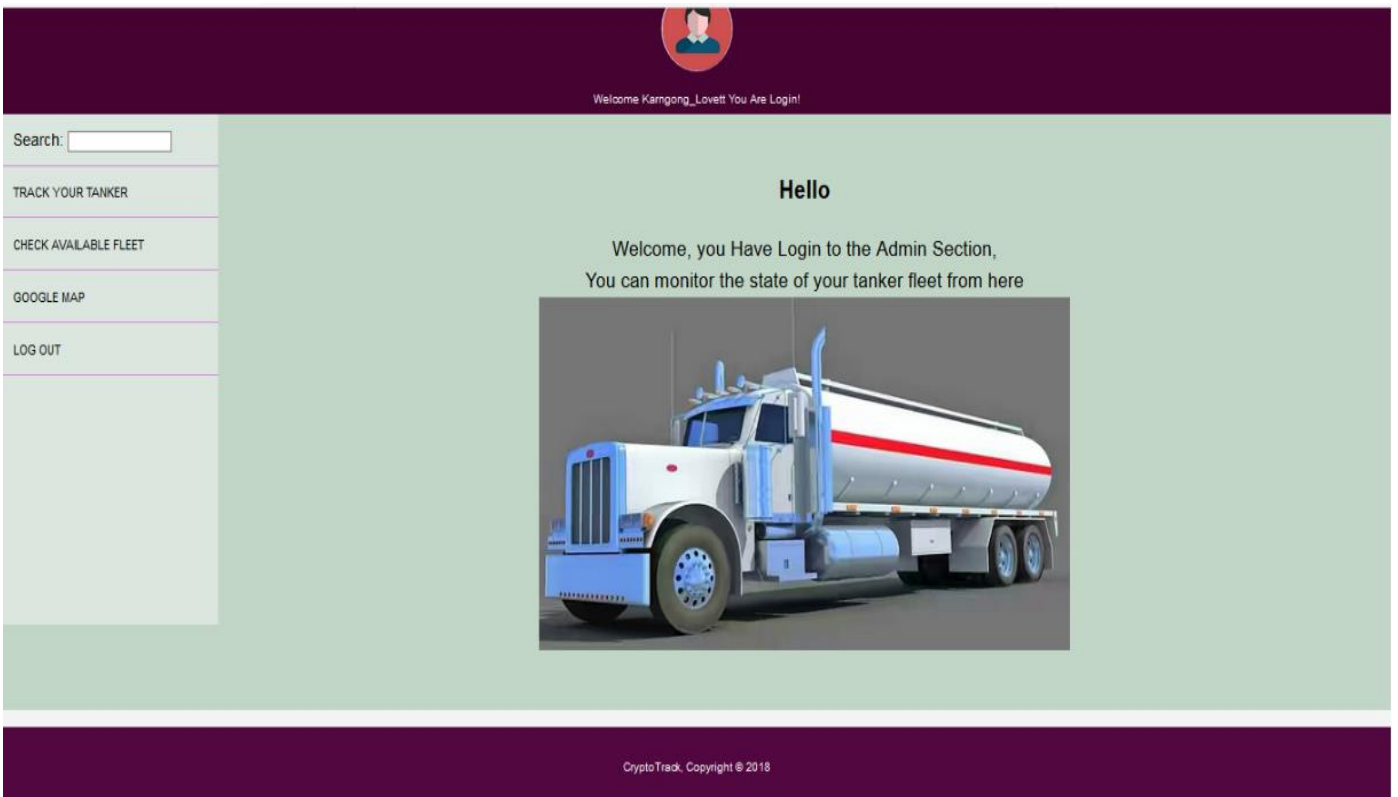


Fig. 13. A secure-tracking automobile database system

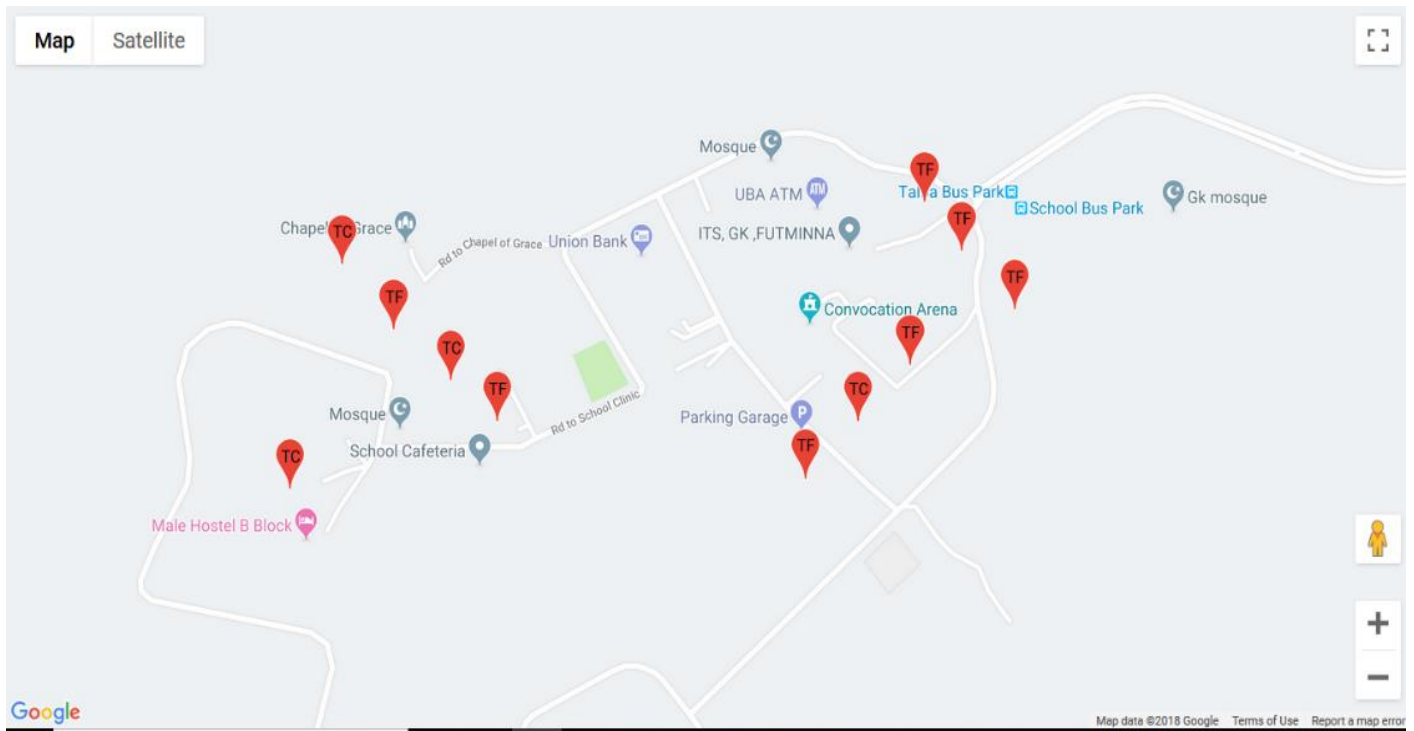


Fig. 14. FUTMinna metropolis geo-locations tracking displayed on a map interface

CRYPTOTRACK									
HOME SEARCH TRACK GOOGLE MAP LOGOUT									
LOCATION DATA									
S/N	TANKER ID	TIME	DATE	NO OF SATELITES	HDOP	LIQUID LEVEL (%)	SPEED(KMPH)	LATITUDE	LONGITUDE
149	865210031078669	6:15:44	8/10/2018	5	2.19	66	0.35	9.531407	6.451446
150	865210031078669	6:16:17	8/10/2018	6	1.92	89	0.37	9.531438	6.451479
151	865210031078669	6:16:50	8/10/2018	5	1.98	89	0.59	9.531368	6.451441
152	865210031078669	6:17:23	8/10/2018	6	2.03	89	0.44	9.531471	6.451372
153	865210031078669	6:17:56	8/10/2018	5	1.60	97	1.19	9.531489	6.451346
187	865210031078669	7:55:25	8/10/2018	5	2.56	100	1.20	9.530928	6.451571
188	865210031078669	7:55:58	8/10/2018	4	9.51	100	1.81	9.531051	6.451568
189	865210031078669	7:56:32	8/10/2018	5	2.50	100	1.04	9.530858	6.451453
190	865210031078669	7:57:5	8/10/2018	8	2.50	100	1.50	9.530884	6.451460
191	865210031078669	7:57:38	8/10/2018	6	4.99	100	1.98	9.531068	6.451518
192	865210031078669	7:58:11	8/10/2018	5	4.94	100	2.85	9.530917	6.451497
193	865210031078669	7:58:44	8/10/2018	6	2.48	100	1.87	9.530988	6.451460
284	865210031078669	18:20:29	8/10/2018	9	0.81	48	0.20	9.531387	6.451231

Fig.15. Tabular representation of a secure tracking information

TABLE I.
DETAIL ANALYSIS OF TRACKING INFORMATION SENDS TO SECURE DATABASE DURING TESTING

id	Tanker_ID	Time	Date	Satellite number	HDOP	Liquid level	Speed	Latitude	longitude
1.	865210031078669	06:15:44	08/10/2018	5	2.19	66	0.35	9.531407	6.451446
2.	865210031078669	06:16:17	08/10/2018	6	1.92	89	0.37	9.531438	6.451479
3.	865210031078669	06:16:50	08/10/2018	5	1.98	89	0.59	9.531368	6.451441
4.	865210031078669	06:17:23	08/10/2018	6	2.03	89	0.44	9.531471	6.451372
5.	865210031078669	06:17:56	08/10/2018	5	1.6	97	1.19	9.531489	6.451346
6.	865210031078669	07:55:25	08/10/2018	5	2.56	100	1.2	9.530928	6.451571
7.	865210031078669	07:55:58	08/10/2018	4	9.51	100	1.81	9.531051	6.451568
8.	865210031078669	07:56:32	08/10/2018	5	2.5	100	1.04	9.530858	6.451453
9.	865210031078669	07:57:05	08/10/2018	8	2.5	100	1.5	9.530884	6.45146
10.	865210031078669	07:57:38	08/10/2018	6	4.99	100	1.98	9.531068	6.451518
11.	865210031078669	07:58:11	08/10/2018	5	4.94	100	2.85	9.530917	6.451497
12.	865210031078669	07:58:44	08/10/2018	6	2.48	100	1.87	9.530988	6.45146
13.	865210031078669	18:20:29	08/10/2018	9	0.81	48	0.2	9.531387	6.451231
14.	865210031078669	18:21:02	08/10/2018	9	0.88	0	0.15	9.531398	6.451261
15.	865210031078669	18:21:35	08/10/2018	10	0.82	0	1.11	9.53142	6.451247
16.	865210031078669	18:22:08	08/10/2018	10	0.78	0	0.2	9.531483	6.451261
17.	865210031078669	18:22:41	08/10/2018	9	0.87	0	0.74	9.531522	6.451264
18.	865210031078669	18:23:14	08/10/2018	10	0.87	0	2.63	9.531484	6.451257
19.	865210031078669	18:23:47	08/10/2018	10	0.98	0	2.57	9.531505	6.451173
20.	865210031078669	18:24:20	08/10/2018	10	0.78	0	0.44	9.531486	6.451322
21.	865210031078669	18:24:53	08/10/2018	9	0.85	0	0.61	9.531514	6.451376
22.	865210031078669	18:25:26	08/10/2018	9	0.85	0	0.61	9.531542	6.451425
23.	865210031078669	18:25:59	08/10/2018	5	1.82	0	14.26	9.531661	6.451532
24.	865210031078669	18:26:32	08/10/2018	7	2.88	0	8.72	9.531518	6.451762
25.	865210031078669	18:27:06	08/10/2018	0	99.99	0	14.93	9.531453	6.452001
26.	865210031078669	18:27:40	08/10/2018	9	1.01	0	4.63	9.531857	6.451674
27.	865210031078669	18:28:13	08/10/2018	8	0.9	0	0.24	9.531544	6.451401
28.	865210031078669	00:37:47	09/12/2018	9	0.98	0	0.74	9.531361	6.451714
29.	865210031078669	00:38:34	09/12/2018	9	0.85	0	0.11	9.531422	6.451569
30.	865210031078669	00:39:21	09/12/2018	9	0.88	0	0.06	9.531407	6.451598
31.	865210031078669	00:40:08	09/12/2018	9	0.8	0	0.33	9.53139	6.451566
32.	865210031078669	00:40:55	09/12/2018	11	0.76	0	0.17	9.531413	6.451585
33.	865210031078669	00:41:42	09/12/2018	9	0.99	0	0.48	9.531431	6.45158
34.	865210031078669	00:42:29	09/12/2018	10	0.88	0	1	9.531427	6.4516
35.	865210031078669	00:43:16	09/12/2018	10	0.92	0	0.63	9.531411	6.45163
36.	865210031078669	00:44:03	09/12/2018	9	0.92	0	1.98	9.531393	6.451665

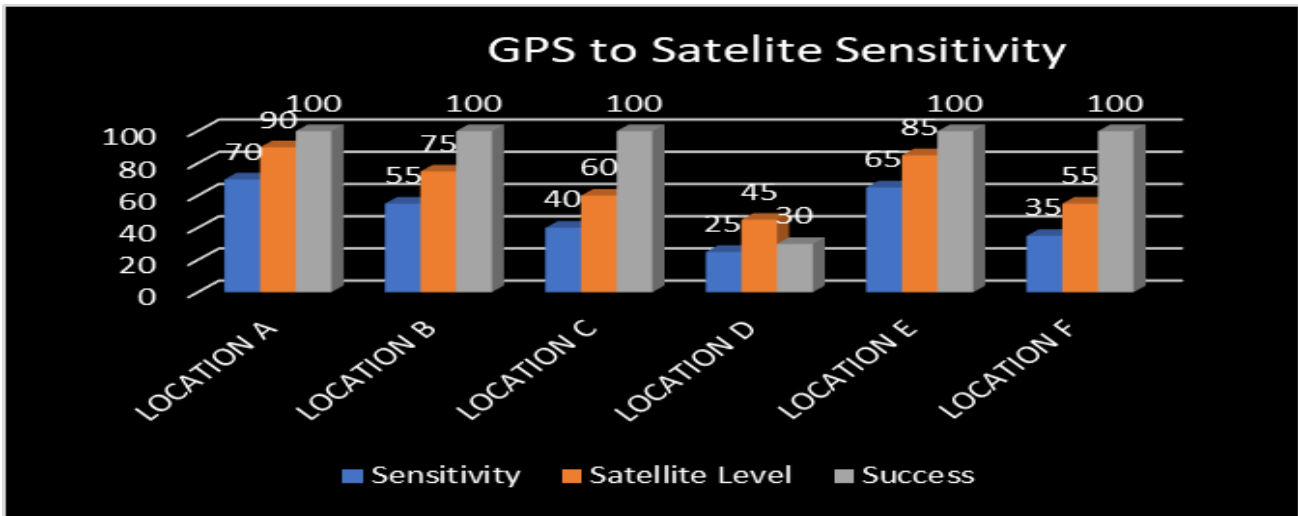


Fig. 16. GPS to satellite sensitivity of the tanker truck information

The graphs of change in speed against time and change in liquid level against time are depicted in “Fig. 17” and “Fig.18” respectively.

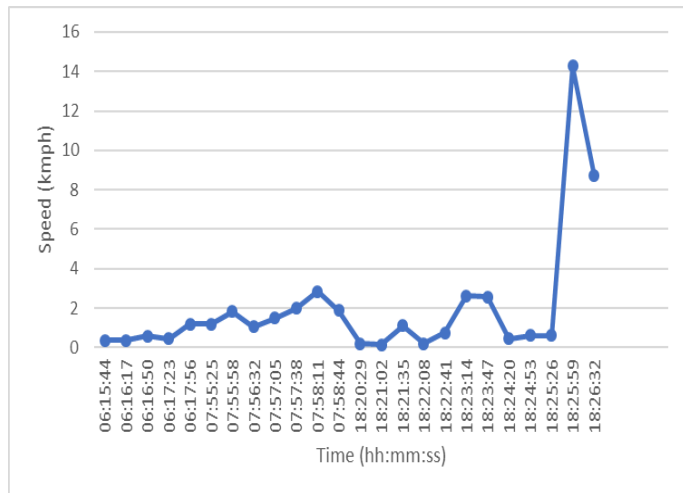


Fig. 17. Graph of speed against time

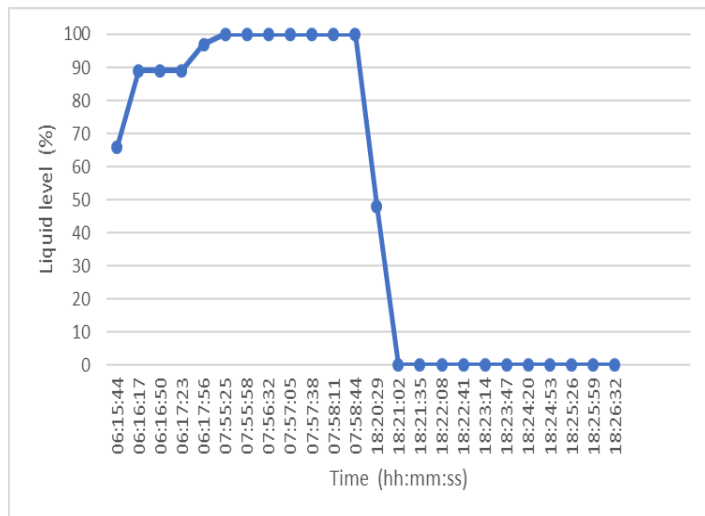


Fig. 18. Graph of liquid level against time

This system was evaluated in terms of accuracy and precision of the GPS receiver readings. The accuracy metric evaluated was the circular error probability of R95 GPS receiver. The circular error probability is the probability of the location information being within a given radius from the true location 95% of the time, the stated radius for the GPS receiver used is 15 meters. The claim was confirmed by testing within 22 location data points of the GPS receiver and determined within a 15meter radius of the true value as illustrated in “Fig. 19”.

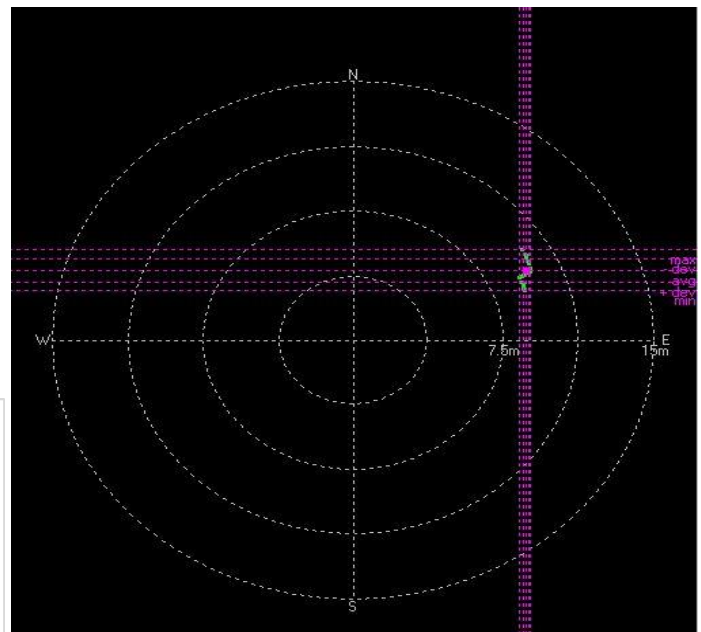


Fig. 19. GPS accuracy

The precision of the GPS readings, which is the measure of how close successive readings of the same location are to one another, was determined from the collected data to be 1.24 meters and this is shown in “Fig. 20”.

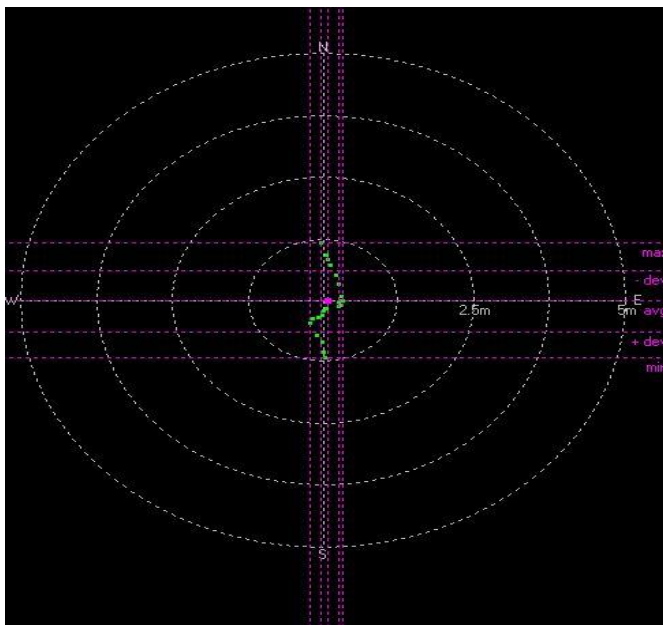


Fig. 20. GPS precision

V. CONCLUSION

The developed system allows effective monitoring of automobile distributed petroleum product. It also secured the remote information stored in the server database of a decentralized system and other related data. The successive truck information received are hashed and then linked to one another system in order to prevent unauthorized manipulation of the records by unscrupulous parties. The theft, diversification and leakages of oil and gas can be optimized by means of efficient tracking of vessel geo-location, monitoring of liquid levels and secured database records management. In this paper, the method proposed will enhanced the model or eliminates a traditional way of tracking systems with adoption of a decentralized server for processing information. This distributed server can be secure against online or offline attacker and hacker using secure hash algorithm (SHA) based blockchain technology. A blockchain based tracking system prevents unscrupulous alteration of information by requested for the approval and permission of majority parties concerned before data can be added to or altered in the database. This research can be further using machine learning approach for automobile geo-location tracking and oil theft or leakages prediction.

ACKNOWLEDGMENT

The authors are grateful to the management of Federal University of Technology Minna, Niger State, Nigeria for their support on this research project.

REFERENCES

[1] Onigbinde I. O., "Evaluation of petroleum products marketing in a globalizing economy: a conceptual evidence from Nigeria", *European Centre for Research Training and Development UK*, vol. 2, no. 2, 2014, pp. 71-81.

- [2] Adegboye M. A., Fung W-K., and Karnik A. "Recent advances in pipeline monitoring and oil leakages detection technologies: Principles and approaches", *MDPI Journal Sensors*, vol. 19, no. 2548, 1-36, 2019.
- [3] Adenigbo J. A. Balogun G. T. and Olisa T., "Transportation challenges of retailing petroleum products in akure, nigeria". *Journal of Research in National Development*, vol. 15, no. 1, pp. 238-243, 2017.
- [4] Baker B., "The Global Positioning System", Physics Capstone Project, vol. 44, 2017. Retrieved from https://digitalcommons.usu.edu/phys_capstoneproject/44
- [5] Dunbar B., "Global Positioning System History" 2012. Retrieved from NASA: https://www.nasa.gov/directorates/heo/scan/communications/policy/GPS_History.html.
- [6] Alexandar K., "U.S. Global Positioning System", Asian Pacific Economic Cooperation, 2018.
- [7] Eberspächer J., Vögel H.-J., Bettstetter C., and Hartmann C., "GSM-architecture, protocols and services". Munchen: Wiley, 2009.
- [8] Sauter M., "From GSM to LTE: An Introduction to Mobile Networks and Mobile Broadband", Germany, Wiley, 2011.
- [9] Ajao L. A., Agajo J., Kolo J. G., Maliki D., and Adegboye M. A., "Wireless sensor network based-internet of things for agro-climatic parameters monitoring and real-time data acquisition". *Journal of Asian Scientific Research (JASR)*, vol. 7, no. 6, 240-252, 2017.
- [10] Micheal, C. "What is Telematics", Geotab Inc, 2018. <https://www.geotab.com/blog/what-is-telematics/>
- [11] Handel P., Skog I., Wahlstrom J., Bonawiede F., Welch R., Ohlsson J., and Ohlsson M., "Insurance telematics: opportunities and challenges with the smartphone solution", *Intelligent Transportation Systems Magazine*, IEEE, vol.6, no.4, pp.57-70, 2014.
- [12] Barreto V., and Ciolek P., "What is OBD II? history of on-board diagnostics" Geotab Inc, 2017. <https://www.geotab.com/blog/obd-ii/>
- [13] Sundeep B. V., and Vardhan Ch. S., "Telematics and its applications in automobile industry", *International Journal of Engineering Trends and Technology (IJETT)*, Vol. 4, no. 4, pp. 554-557, 2013.
- [14] Dogo, E. M., Nwulu, N. I., Olaniyi, O. M., Aigbavboa, C. O., Nkonyana, T. "Blockchain 3.0: Towards A Secure Ballotcoin Democracy Through A Digitized Public Ledger in Developing Countries", *I-manager's Journal on Digital Signal Processing*, vol. 6, no. 2, 24-35, 2018.
- [15] Sikorski J. J., Haughton J., and Kraft M., "Blockchain technology in the chemical industry: Machine-to-machine electricity market", *Applied Energy*, vol. 195, pp. 234-246, 2017.
- [16] Lee S., Tewolde G., and Kwon J., "Design and implementation of vehicle tracking system using GPS/GSM/gprs technology and smartphone application". *IEEE World Forum on Internet of Things (WF-IoT)*, 353-358, 2014.
- [17] Dat P. H., Drieberg M., and Cuong N. C., "Development of vehicle tracking system using GPS and GSM modem", 2013 *IEEE Conference on Open Systems (ICOS)*, 89-94, 2013.
- [18] Brambilla G., Amoretti M., and Zanichelli F., "Using block chain for peer-to-peer proof-of-location", *Department of Engineering and Architecture, University of Parma, Italy*, 1-11, 2016.
- [19] Almomani I. M., Alkhalil N. Y., and Ahmad E. M., "Ubiquitous GPS vehicle tracking and management system", 2011 *IEEE Jordan Conference on Applied Electrical Engineering and Computing Technologies. Jordan*, 238-241, 2011.
- [20] Agajo J., Kolo J. G., Ajao L. A., Olusola K. Y., and Prince A., "Equipment and security personnel tracking and localization using gps/gsm geo-location technique incorporating ublox Neo 6 GPS module", *Journal of Engineering and Technology (JET)*, vol. 7, no. 2, pp. 87-102, 2016.
- [21] Hisham S., Tony N., and Peter P-H., "Utilizing telematics data to support effective equipment fleet-management decisions: utilization rate and hazard functions", *Journal of Computing in Civil Engineering*, pp. 1-11.
- [22] Christopher E., and Adepoju A., "An assessment of the distribution of Petroleum of Petroleum Product in Nigeria". *Journal of Business Management and Economics*, vol. 3, no. 6, 2012, pp. 232- 241.
- [23] Ajao L. A., Adedokun E. A., Nwishiyei C. P., Adegboye M. A., Agajo J., and kolo J. G., "An anti-theft oil pipeline vandalism detection: embedded system development". *International Journal of Engineering Science and Application (IJESA)*, vol. 2, no. 2, pp. 41-46, 2018.

BIOGRAPHIES



Lukman Adewale AJAO is a Senior Research Fellow from Department of Computer Engineering, Federal University of Technology, Minna, Nigeria. He received PGD and M.Eng in Computer Science and Engineering from Federal University of Technology, Minna, Nigeria. He is a Ph.D research associate in Computer Engineering at Ahamadu Bello University, Zaria, Nigeria. His memberships are NATE, IAENG, IACSIT, IRED, ISOC & COREN Reg. Research interests are Real-Time Embedded System, Internet of Things, Wireless Sensor Network, FPGA, Security Application and Machine Learning.



James AGAJO is Head of Computer Engineering Department, Federal University of Technology, Minna, Nigeria. He received B.Eng. in Electrical & Computer Engineering, Federal University of Technology, Minna, M.Eng. & Ph.D in Electronic and Computer Engineering, Nnamdi Azikiwe University, Awka, Nigeria. He is a member of IASCIT, IAENG MIRDA, MNSE, COREN Reg. His research interest includes Wireless Sensor Network, Computer network, Intelligent System, Digital Signal Processing (DSP), Artificial Intelligence, Internet of Things (IoT) and Embedded systems.



Olayemi Mikail OLANIYI (PhD) is a Associate Professor in the Department of Computer Engineering, Federal University of Technology, Minna, Nigeria. He received B.Tech. and M.Sc. in Computer and Electronics Engineering, Ph.D. in Computer Security from Ladoko Akintola University, Ogbomosho, Nigeria. He has published in a reputable Journals and learned Conferences. His research interest includes Computer Security, Intelligent/Embedded Systems design and Applied Informatics.



Jibril Zakariyah IBRAHIM he obtained B.Eng in Computer Engineering from Bayero University, Kano, Nigeria in 2012, M.Sc. in Information Technology from Heriot-Watt University, UK, in 2017, M.Eng in Computer Engineering, Federal University of Technology, Minna in 2019. His research interests are Embedded system, Computer Networks, Network Security, Internet of Things and Wireless Sensor Network.



Adedimeji Emmanuel SEBIOTIMO obtained his B.Eng in Computer Engineering from Federal University of Technology, Minna, Nigeria. He obtained Certifications in OCA Java SE 8 & HCNA

Routing & Switching. His research interests are Embedded Systems, Internet of Things, Wireless Sensor Networks and Application Programming.

Analyzes of Flyback DC-DC Converter for Submodule Level Maximum Power Point Tracking in Off-grid Photovoltaic Systems

M.E. BAŞOĞLU

Abstract—Submodule level maximum power point tracking (MPPT) systems have become popular due to its outstanding performance in partial shading conditions (PSCs) and basic algorithm requirement. MPPT is realized by DC-DC converters. They are power processing units between photovoltaic (PV) module and resistive load. Among DC-DC converter topologies, the flyback is a proper choice since it can either increase or decrease the voltage. Furthermore, power level is small in submodule level (SML) MPPT applications. In this study, analyzes and power circuit design of a flyback converter for continuous conduction mode (CCM) is carried out firstly. Then, the performance of the flyback converter on the SML MPPT system and its superiority over the module level MPPT is shown by using same converter topology and perturb and observe (P&O) algorithm. In order to validate the superior performance of SML MPPT, it is compared with module level MPPT in MATLAB/Simulink environment. Results show that SML MPPT guarantees global MPPT in any PSCs with any kind of basic MPPT algorithm. On the other hand, module level MPPT fails in many PSCs with the same algorithm. According to simulation results, SML MPPT generated more power by 61.2% in average than module level MPPT systems in simulation studies.

Index Terms— Distributed MPPT, flyback, maximum power point tracking, photovoltaic, submodule, MPPT.

I. INTRODUCTION


SOLAR energy is an important renewable energy sources used for generation of electrical energy in standalone and utility scale power systems. Photovoltaic (PV) modules are used in electrical energy generation. Due to the p-n junction in structure, PV modules are similar to a basic diode and their current-voltage (I-V) characteristic curve change logarithmic form. Therefore, obtaining maximum power from a PV module requires a special process [1]. Generally, a power converter is connected between the load and the PV source to extract the maximum power from a module and this converter is generally controlled by an MPPT algorithm [2]. While the

conventional system can perform MPPT if the solar irradiance received by a PV module surface is uniform; if the PV module panel is partially shaded, it is necessary to increase the number of power converter or to improve the algorithm, to perform MPPT efficiently. Because, a typical PV module has a few bypass diodes and the presence of these diodes cause multi-peak structure in power-voltage (P-V) curves. This makes the tracking of maximum power point (MPP) difficult or inefficient [3].

Distributed MPPT approach presents some advantage for the case that the PV system is not uniformly irradiated. In that approach, PV source is divided into some parts and MPPT is performed individually. For example, in a series connected PV string, each PV module performs its own MPPT which can be considered as a module level MPPT. On the other hand, if each submodule in a PV module performs its own MPPT, it is the SML MPPT. In these approaches, micro inverter and power optimizers are used as a power processing converter.

SML MPPT requires a few power converters with low power scale. Therefore, flyback converters are considerable good choices since they consist of a few components and have a big efficiency in small power level. Furthermore, it can be used in DC-AC and DC-DC converters for micro inverters and power optimizers, respectively. Current sensorless flyback inverter is proposed for small scale PV systems [4]. Although it seems as a cost effective solution, it cannot track MPP in PSCs. Smart PV module concepts are the other type of distributed MPPT (DMPPT) approach. In general, DC-AC converter is connected to the PV module in this approach. Feed forward control scheme is applied to flyback converter to obtain high quality output voltage from the inverter side [5]. For the SML MPPT applications, a novel flyback converter is presented to acquire maximum power from a PV module in PSCs [6]. This converter is used for the MPPT stage of microinverter. Since SML MPPT is realized, requirement of bypass diodes is eliminated and MPPT is performed by a basic algorithm. On the other hand, a current sensorless MPPT control scheme is proposed for interleaved flyback inverters [7]. This technique is complicated but offers a cost effective solution for microinverters. Voltage sensorless MPPT can be used in AC module applications [8], it is shown that voltage sensorless method has similar performance with P&O. But it needs less sensor and makes the MPPT cheaper than P&O. A bidirectional discontinuous mode flyback converter is used as

MUSTAFA ENGİN BAŞOĞLU, is with Department of Electrical and Electronics Engineering University of Gümüşhane, Gümüşhane, Turkey.(e-mail: menginbasoglu@gumushane.edu.tr).

 <https://orcid.org/0000-0002-6228-4112>

Manuscript received March 23, 2019; accepted June 8, 2019.
DOI: [10.17694/bajece.543668](https://doi.org/10.17694/bajece.543668)

a voltage equalizer used in global MPPT [9]. In this study, power processing is very small which increases the total efficiency. Results show that extracted power increases compared with the PV structure owning bypass diodes. A hybrid MPPT method containing conventional short circuit current pulse and P&O algorithm is used in a single stage flyback inverter [10]. However, this method is not capable of tracking of MPP in PSCs.

Submodule integrated DMPPT is proposed in [11]. Buck converter is connected to each cell group and output of the buck converters is connected in series. 20% of the total energy increase is obtained compared with the module level MPPT. Substring level MPPT is applied and it is resulted that remarkable power increase is obtained [12]. Differential power processing (DPP) is the latest approach aiming to decrease power processing to rise efficiency [13]. In that approach, power converters have small power levels compared with full power processing (FPP). Furthermore, rated value is low and cost of the converters is small [14]. A modified interleaved SEPIC converter is proposed aiming to equalize the voltage of the series connected PV module in the PV string [15]. It is presented that energy improvement ranges from 27% to 34%. A novel DPP approach is used as a module integrated converter in series connected PV systems [16]. Results show that it performs better than classical PV configurations.

It is surely clear that MPPT efficiency increases from string level to submodule level. In this study, advantages of the SML MPPT are presented by comparing module level MPPT concept. As a power processing unit, flyback converter is selected since flyback converters are the proper choice in small power scale. Comprehensive design of flyback converter operating CCM is presented. The remains of the study continue as follows. In Section II, theoretical analyzes and operation principle of a flyback converter is given. Design steps are also presented in this section. In Section III, SML MPPT structure has been compared with module level MPPT by simulations. These simulation studies are performed in MATLAB/Simulink. In Section IV, simulation results are evaluated briefly. Finally, the main outcomes of the study are summarized and some information about future studies is also mentioned.

II. PRINCIPLE OF FLYBACK CONVERTERS

Flyback converters are the most preferred switch mode power supply topologies below 100W since they have less components than the other topologies and they can have multiple outputs, if desired [17]. A typical flyback converter consists of transformer for energy storage and voltage conversion, a capacitor, a switching device and a diode as presented in Fig. 1. In flyback converters, transformer, which is also called as coupled inductor, provides galvanic isolation between the primary and secondary side of the transformer. However, its operation is quite different from normal transformer. While the primary winding of the transformer carries current, in the secondary side of the transformer,

current cannot flow since the polarity of the secondary winding is reversed.

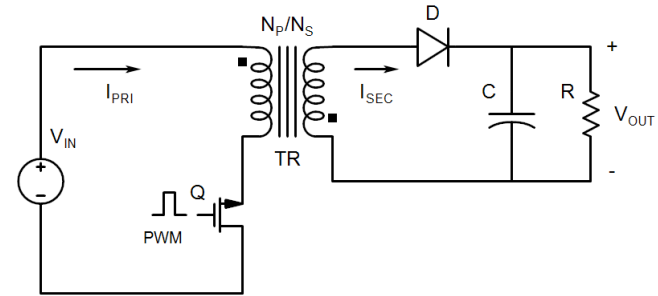


Fig.1. Electrical circuit of flyback converter

A. Operation Modes of Flyback Converters

There are three types of operation in DC-DC converters. They are CCM, discontinuous conduction mode (DCM) and boundary conduction mode (BCM). Normally, these operations are defined as the value of inductor current in a switching period. In a flyback converter, DC transformer is used as a magnetic energy storage component and there is no additional inductor. Therefore, the operation mode of a flyback is determined by the current continuity of the primary and secondary winding. Operation modes of a flyback converter are presented in Fig. 2.

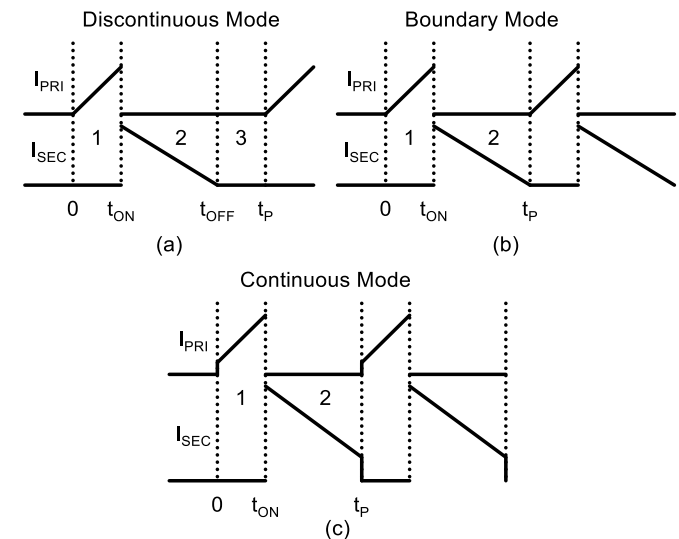


Fig.2. Operation modes of flyback converters a) Discontinuous b) Boundary c) Continuous

B. Design Steps of Flyback Converter in CCM

While analyzing the flyback converter, transformer can be modelled by an ideal transformer and magnetizing inductor [18]. This inductor is parallel to the primary winding of the transformer and it is modelled as the energy storage element in the circuit given in Fig. 2. In this circuit, when switch Q is turned on at $t=0$, magnetizing inductance is stored energy and its current of primary winding increases linearly up to $t=t_{ON}$. The diode is reverse biased due to the polarity of the secondary winding between $t=0$ and $t=t_{ON}$. So, current of the secondary winding is zero. Output load is supplied by the

capacitor in this period. The voltage across the magnetizing inductance is formulated as in (1). Primary current is calculated as in [18].

$$V_{Lm} = L_m \frac{di_{Lm}}{dt} \quad (1)$$

In (1), L_M is the magnetizing inductance. Switch current is equal to a current of magnetizing current when the switch is on. It can be calculated as in (2).

$$I_Q = I_{Lm} = I_{pri} = \frac{V_{IN} + V_{DS(ON)}}{L_M} t_{ON} + I_{ini} \quad (2)$$

In (2), I_Q is the switch current, I_{Lm} is the magnetizing current, I_{ini} is the initial current of the magnetizing inductor, V_{IN} is the input voltage, $V_{DS(ON)}$ is the voltage drop on the switch, t_{ON} is the conduction time of the switch. In order to calculate magnetizing inductance, (3) is rearranged as below.

$$I_{pri} - I_{ini} = \Delta I_{Lm} = \frac{V_{IN} + V_{DS(ON)}}{L_M} t_{ON} \quad (3)$$

By using (3), magnetizing inductance (inductance of the primary) can be calculated. The reverse voltage of the diode should not be bigger than the maximum reverse voltage between $t=0$ and $t=t_{ON}$. The maximum reverse voltage of diode is calculated as in (4).

$$V_{D(max)} = -\frac{V_{IN}}{n} + V_O \quad (4)$$

When the switch is turned off, the polarity of the secondary winding is reversed and diode turns on. Stored energy in the magnetizing inductor supplies to the resistive load and current of secondary winding increases linearly. The initial value of the secondary current is determined by the multiplication of peak current of primary winding and the turns ratio of the transformer (N_P/N_S). Current of the secondary winding is calculated as in (5).

$$I_{SEC} = \frac{I_{peak} N_P}{N_S} - \frac{(V_O + V_D) t_{OFF} N_P}{N_S L_M} \quad (5)$$

In (5), I_{peak} is the peak current of primary winding, N_P and N_S are the number of turns of primary and secondary windings, V_O is the output voltage of flyback converter, V_D is the voltage of drop of the diode, t_{OFF} is the conduction time of the diode. When the switch is turned off, voltage stress on the switch is the sum of the input voltage and reverse voltage due to the current of secondary side. Therefore, the switch has more voltage stress in the flyback compared with the non-

isolated buck-boost converter. The voltage across the switch is calculated as in (6).

$$V_{DS(max)} = V_{IN} + nV_O + V_{leak} \quad (6)$$

In (6), V_{leak} is the leakage voltage which is the result of parasitic inductance of primary and secondary windings. In order to select proper switch, leakage inductance, windings ratio are taken into account. The output of the flyback converter consists of a capacitor and load. This capacitor is generally is specified by the root mean square current and the permissible voltage ripple. The minimum value of this capacitor is calculated as in (7).

$$C_{min} = \frac{D_{max} V_O}{f_p R_{Lmin} \Delta V_O} \quad (7)$$

In (7), C_{min} is the minimum value of the output capacitor, D_{max} is the maximum value of duty ratio, R_{Lmin} is the minimum value of the load resistance, f_p is the switching frequency and ΔV_O is the voltage ripple of the capacitor. On the other hand, the relationship between input and output voltage, which is named as DC transfer function, is important for an MPPT application. So, the output voltage of flyback can be formulated by input voltage, duty ratio and windings ratio as in (8).

$$V_O = V_{IN} \frac{D}{1-D} \frac{N_S}{N_P} \quad (8)$$

It is clear in Fig. 2 that, the windings of the flyback transformer do not carry current between $t=off$ and $t=T_p$ in DCM operation. On the other hand, in BCM operation, primary and secondary windings carry current in different time period by triangular waveform. When the switch is turned on current of primary winding increases and energy is stored in the transformer. Between $t=0$ and $t=t_{ON}$, diode is reverse biased due to the polarity of secondary winding. When the switch is turned off, all energy stored in the transformer supplies the output capacitor and the load on the secondary side between $t=t_{ON}$ and $t=t_p$. In CCM operation, the windings of the transformers carry current in trapezoid form and there is no current shortage in a switching period as presented in Fig. 2. Some of the energy stored in the transformer is not transferred to the secondary side of the flyback.

C. Flyback MPPT Converter

Voltage of PV module changes in a big interval under PSCs. That is, input voltage of a converter changes in a large range. Therefore, buck-boost converters are the best choices for MPPT applications since they have the ability to increase and decrease the voltage. In addition, the flyback converter performs efficiently below one hundred watts and this power level is proper for SML MPPT. A typical block diagram of flyback MPPT is presented in Fig. 3.

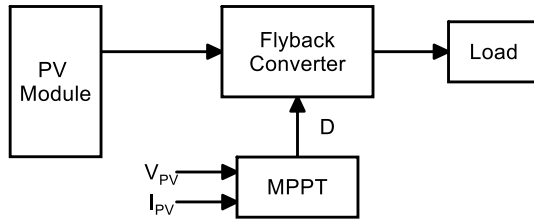


Fig. 3 Block diagram of flyback MPPT converter

In order to realize MPPT in flyback converter, transfer function between PV module and resistive load is obtained. First, power of PV module is given in (9).

$$P_{PV} = V_{PV} I_{PV} = I_{PV} R_{PV} \quad (9)$$

In (9), V_{PV} and I_{PV} are the voltage and current of PV module, respectively. The R_{PV} is the equivalent resistance of PV module. The voltage of a PV module is equal to;

$$V_{PV} = I_{PV} R_{PV} \quad (10)$$

For output of flyback converter, output power and output voltage are given by (11) and (12), respectively.

$$P_O = V_O I_O = I_O^2 R_L \quad (11)$$

$$V_O = I_O R_L \quad (12)$$

In (11) and (12), V_O and I_O are the output voltage and output current, respectively. Assuming the converter loss is zero, power, balance can be easily written as follows.

$$P_{IN} = P_O = V_{PV} I_{PV} = V_O I_O \quad (13)$$

By using (9) – (13), the equivalent resistance of PV module can be formulated as in (14), which is the core of the MPPT operation for flyback converters.

$$R_{PV} = R_L \frac{(1-D)^2}{D^2} \left(\frac{N_P}{N_S} \right)^2 \quad (14)$$

III. SIMULATION RESULTS

In order to validate the benefits of the SML MPPT with respect to the module level MPPT, some simulation studies have been performed in MATLAB Simulink software. SML MPPT owning three flyback converters has been modelled. A SML MPPT model is presented in Fig. 4. In this model, PV module has three bypass diodes. Each submodule is connected to its own flyback converter. MPPT is realized individually by P&O. On the other hand, module level MPPT model is presented in Fig. 5. The main parameters of the PV module

and flyback converter used in simulation studies are listed in Table I and Table II, respectively.

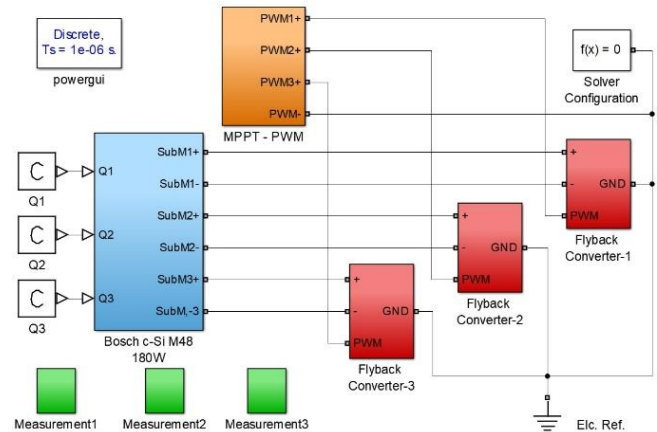


Fig. 4 Simulink model of the flyback converter based SML MPPT

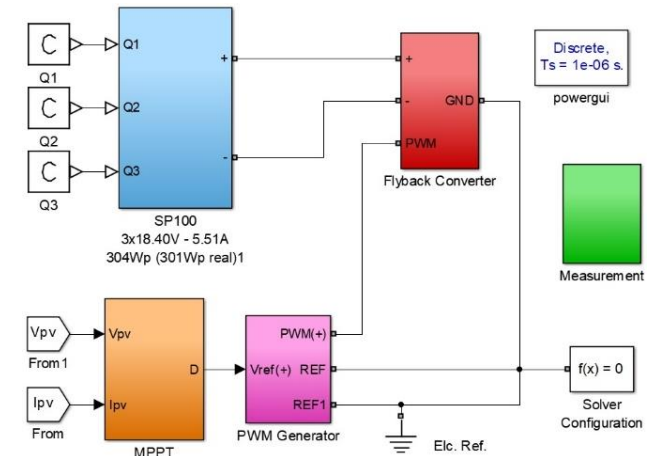


Fig. 5 Simulink model of the module level MPPT

 TABLE I
SPECIFICATIONS OF THE PV MODULE

Bosch PV Module c-Si M 48	Value
Short circuit current	8.5A
Open circuit voltage	28.9V
Maximum power voltage	23.4V
Maximum power current	7.9A
Maximum power	180W
Bypass diodes	3

 TABLE II
SPECIFICATIONS OF THE FLYBACK CONVERTERS IN SML MPPT

Features	Value
Input / output capacitor	1000μF / 100 μF
Magnetizing inductance	40mH
Windings turns ratio	0.5
Switching frequency	20kHz
Duty Step / Sample time	0.1% / 1ms

Two shading scenarios are created to verify the superior performance of the SML MPPT. First, submodules of the PV module receive 400W/m^2 , 700W/m^2 and 800W/m^2 , respectively. The initial value of duty ratio and the step size is set to 50% and 0.1%, respectively. In the first simulation

result, all submodules perform their own MPPT by P&O algorithm. A resistor valued by 10Ω is connected to the output of the each flyback converter. The P-V curve of the first P-V characteristic is presented in Fig. 6. The results of the first irradiance profile are presented in Fig. 7. It is clear in Fig. 7.a that all submodules generated different power and reaches their own MPPT with different tracking speed since they receive different irradiance. While the sub-module-1 receiving 400W/m² tracks the MPP in 18 milliseconds (ms), sub-module-2 receiving 500W/m² tracks its own MPP in 100ms. These times may change and/or can be optimized by the proper selection, initial value of duty ratio and using adaptive step size. In the first case, total tracking efficiency is calculated as 92.6% in 250ms.

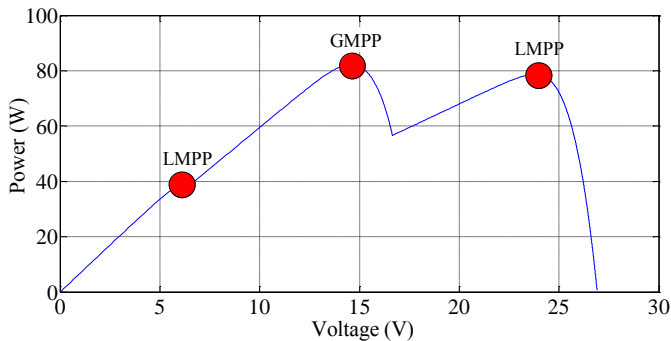


Fig. 6. P-V curve of 400W/m²-500W/m²-800W/m²

In the second irradiance profile, values of irradiances are 300W/m², 600W/m² and 1000W/m². Voltage, current, power variations of the submodules and duty ratio variations of each flyback converters are given in Fig. 8. a-d. Each submodule performs its own MPPT by P&O algorithm. Performing independent MPPT provides 100% tracking efficiency at

steady state condition. Tracking efficiencies in 250ms are 97.91%, 93.28% and 84.16% for submodule-1, submodule-2 and submodule-3, respectively. Total tracking efficiency is 91.81%. For SML MPPT, tracking efficiency is very big since global MPPT is realized regardless of the irradiance values.

In module level MPPT approach, multiple peak points occur on the P-V curve under PSCs due to the presence of bypass diodes included in a module. In addition, the available power of PV module decreases in a PSC. The P-V curve of the second irradiance profile is presented in Fig. 9. In the first case, three peak points occur on the P-V curve due to three different irradiance. It is clear in Fig. 8 that there are three peak points. Two of them are local MPP and another peak point is global MPP. Middle of the peak point corresponds to the global peak point. Power at global MPP is 82.22W. But, MPPT fails at the first local MPP and power at steady state is about 78W. In this case, tracking efficiency is calculated as 69.82%. However, for the same irradiance profile, SML MPPT extracts 110.92W from the PV module. That is, SML MPPT strategy generates more power by 34.9%. The results of the module level MPPT are presented in Fig. 10.

In the second shading scenario, GMPP is located in the middle MPP region as shown in Fig. 9. Power at global MPP is 73.51W. P&O algorithm fails at the first local MPP (LMPP) and PV module generated about 60W at this point. PV module generates less power by 18.37% compared with the global maximum power point (GMPP) seen in the Fig. 9. Tracking efficiency is calculated as 65.37% in 250ms. On the other hand, for the same shading scenario, SML MPPT approach obtains more power by 85.9% with respect to the module level MPPT.

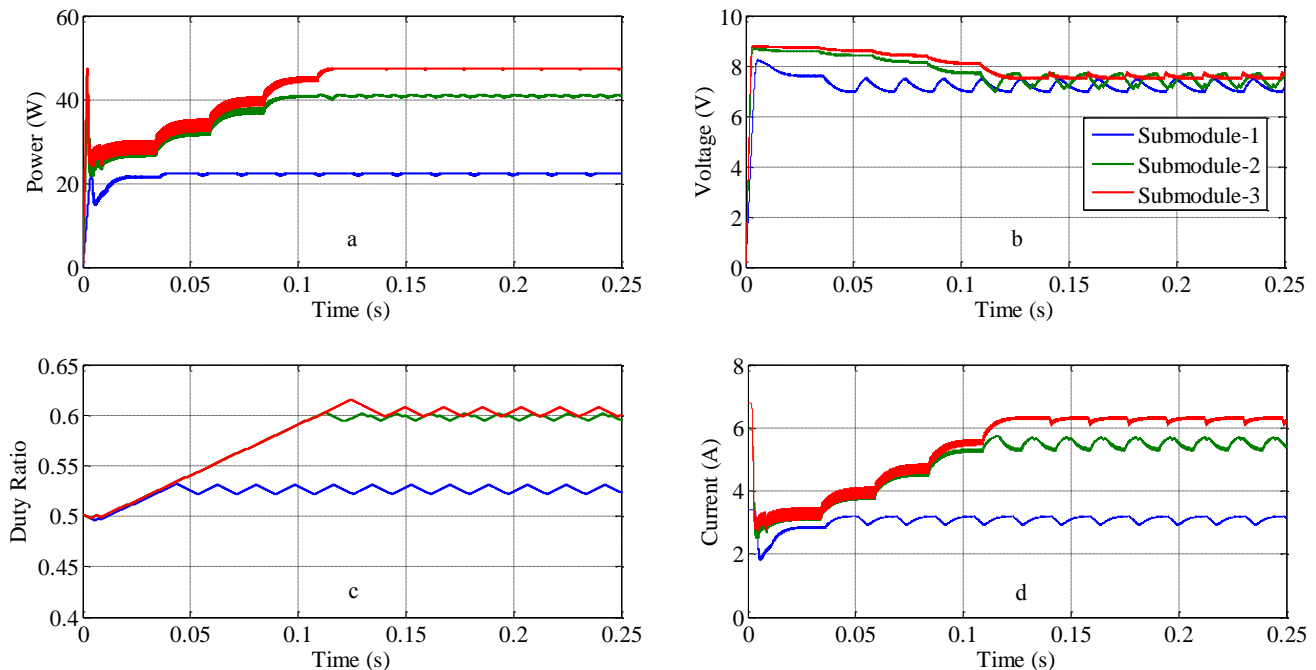


Fig. 7. Simulation results of irradiance profile-1 for SML MPPT a) Power b) Voltage c) Duty ratio d) Current

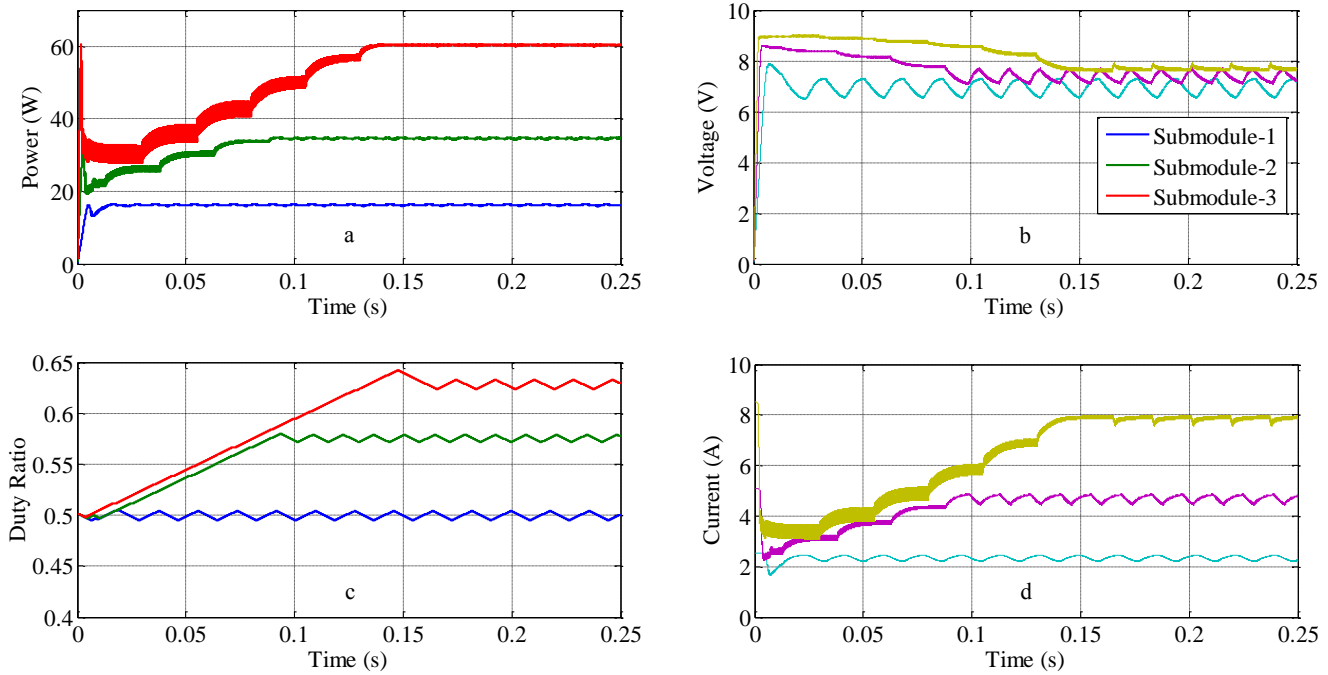


Fig. 8. Simulation results of irradiance profile-2 for SML MPPT a) Power b) Voltage c) Duty ratio d) Current

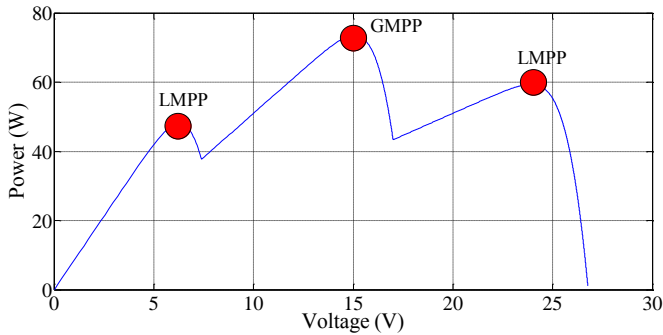


Fig. 9. P-V curve of 400W/m²-500W/m²-800W/m²

IV. DISCUSSION

Simulation results show that the module level MPPT strategy has superior performance than module level MPPT. The numerical results of the simulation studies performed are listed in Table III. It is clear that submodule level performs high quality MPPT with P&O algorithm. All submodules achieved satisfactory efficiencies in 250ms. It is obvious that tracking efficiencies increase if simulation time is selected bigger. The differences between the efficiency values depend on the irradiance value and the initial value of the duty ratio. On the other hand, module level MPPT fails at the first peak point since P&O is one of the hill climbing based technique. Tracking efficiency is very small in module level MPPT. Global MPP may not be tracked.

V. CONCLUSIONS AND FUTURE WORK

PV energy systems have small capacity factor since they have small power conversion efficiency and low full time operation capacity. Therefore, it is obliged that these systems should be operated with maximum available efficiency. Thus,

TABLE III
NUMERICAL RESULTS OF SIMULATION STUDIES

Irradiance Profile	Submodule Level MPPT		
	SM-1	SM-2	SM-3
400-700-800W/m ²	97.67%	91.35%	88.8%
Average: 92.6%			
300-600-1000W/m ²	97.91%	93.38%	84.16%
Average: 91.81%			
Irradiance Profile	Module Level MPPT		
400-700-800W/m ²	69.82%		
300-600-1000W/m ²	65.37%		

MPPT is an important process for these systems. In PSCs, the available power of the PV system decreases harshly and module level MPPT do not often provide available power. In this study, flyback converter based SML MPPT approach has been presented which is the improved strategy in MPPT applications. Design steps of CCM operated flyback converter are explained and theory of flyback MPPT is studied briefly. Advantages of the SML MPPT with respect to the module level MPPT are validated for two shading scenarios. As expected, module level MPPT fails at local MPP and provides low tracking efficiency with P&O algorithm. Simulation results show that SML MPPT performs superior than module level MPPT in PSCs. While total tracking efficiency is about 92.2% on average for SML MPPT, module level MPPT concept reaches to 67.59% efficiency. On the other hand, available power to be obtained is always bigger in SML MPPT than module level MPPT. In future studies, advantages of the SML MPPT approach will be validated by experimental studies.

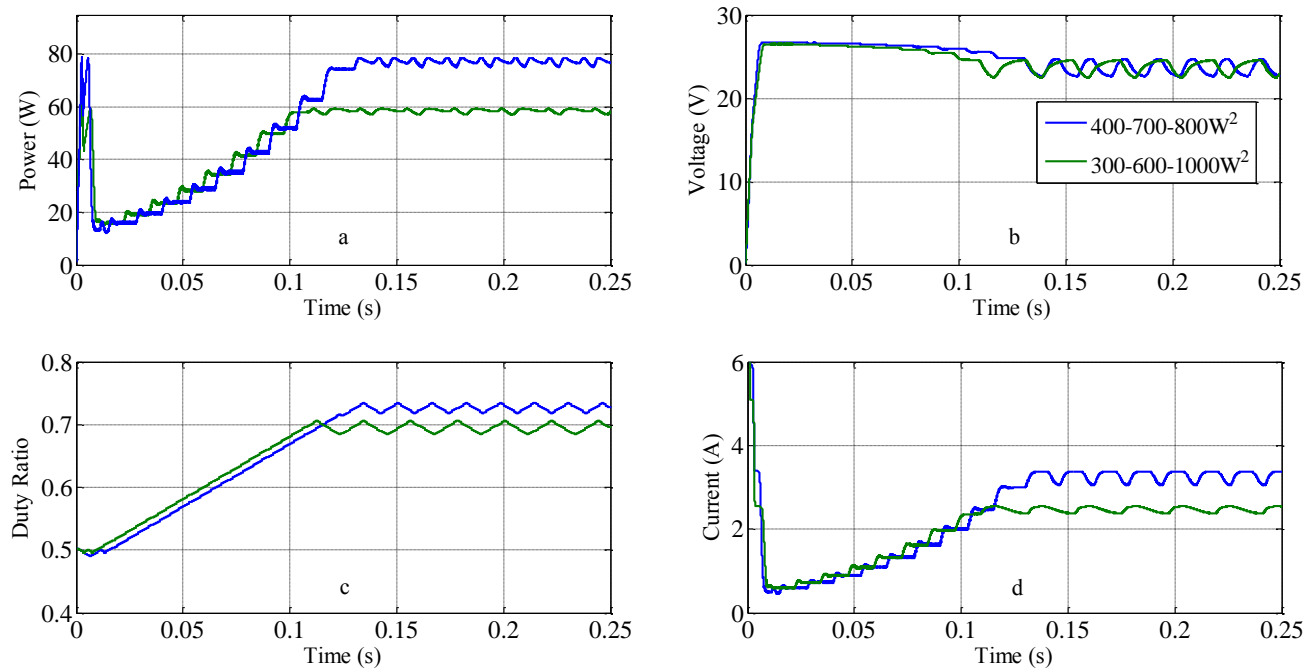


Fig. 10. Simulation results of module level MPPT a) Power b) Voltage c) Duty ratio d) Current

REFERENCES

- [1] Başoğlu M.E., Çakır B., An improved incremental conductance based MPPT approach for PV modules, *Turkish Journal of Electrical Engineering & Computer Sciences*, vol. 23, no. 6, pp. 1687-1697, 2015.
- [2] Başoğlu M.E., Çakır B., Comparisons of MPPT performances of isolated and non-isolated DC-DC converters by using a new approach, *Renewable & Sustainable Energy Reviews*, vol. 60, pp. 1100-1113, 2016.
- [3] Başoğlu M.E., Çakır B., A novel voltage-current characteristic based global maximum power point tracking algorithm in photovoltaic systems, *Energy*, vol. 112, pp. 153-163, 2016.
- [4] Kasa N., Iida T., Chen L., Flyback inverter controlled by sensorless current MPPT for photovoltaic power system, *IEEE Transactions on Industrial Electronics*, vol. 52, no. 4, pp. 1145-1152, 2005.
- [5] Mazumdar P., Enjeti P.N., Balog R.S., Analysis and design of smart PV modules, *IEEE Journal of Emerging and Selected Topics in Power Electronics*, vol. 2, no. 3, pp. 451-459, 2014.
- [6] Pragallapati N., Agarwal V., Flyback configuration based micro-inverter with distributed MPPT of partially shaded PV module and energy recovery scheme, *IEEE 39th Photovoltaic Specialists Conference*, Tampa, USA, pp. 2927-2931, 2013.
- [7] Lee J., Lee J. S., Lee K., Current sensorless MPPT method for a PV flyback microinverters using a dual-mode, *International Power Electronics Conference*, Hiroshima, pp. 532-537, 2014.
- [8] Kim Y., Kim J., Ji Y., Won C. Lee T., Flyback inverter using voltage sensorless MPPT for AC module systems, *International Power Electronics Conference*, Sapporo, pp. 948-953, 2010.
- [9] Zhang W.P., Li J., Mao P., A novel isolated-port voltage equalizer for photovoltaic systems under mismatch conditions, *43rd Annual Conference of the IEEE Industrial Electronics Society*, Beijing, pp. 639-644, 2017.
- [10] Sher H.A., Rizvi A.A., Addoweesh K.E., Al-Haddad K., A., Single-stage stand-alone photovoltaic energy system with high tracking efficiency, *IEEE Transactions on Sustainable Energy*, vol. 8, no. 2, pp. 755-782, 2017.
- [11] Pilawa-Podgurski R.C.N., Perreault D.J., Submodule integrated distributed maximum power point tracking for solar photovoltaic applications, *IEEE Transactions on Power Electronics*, vol. 28, no. 6, pp. 2957-2967, 2013.
- [12] Grasso A.D., Pennisi S., Ragusa M., Tina G.M., Ventura C., Performance evaluation of a multistring photovoltaic module with distributed DC-DC converters, *IET Renewable Power Generation*, vol. 9, no. 8, pp. 935-942, 2015.
- [13] Qin S., Barth C.B., Pilawa-Podgurski R.C.N., Enhancing microinverter energy capture with submodule differential power processing, *IEEE Transactions on Power Electronics*, vol. 31, no. 5, pp. 3575-3585, 2016.
- [14] Wang F., Zhu T., Zhuo F., Yang Y., Analysis and comparison of FPP and DPP structure based DMPPT PV system, *8th International Power Electronics and Motion Control Conference*, Hefei, pp. 1-5, 2016.
- [15] Pragallapati N., Agarwal V., Distributed PV power extraction based on a modified interleaved SEPIC for nonuniform irradiation conditions, *IEEE Journal of Photovoltaics*, vol. 5, no. 5, pp. 1442-1453, 2015.
- [16] Bose S.M., Badawy O., Sozer Y., A novel differential power processing architecture for a partially shaded PV string using distributed control, *IEEE Energy Conversion Congress and Exposition*, Portland, pp. 6220-6227, 2018.
- [17] TopSwitch Flyback Design Methodology, Application Note AN-16, https://ac-dc.power.com/system/files_force/product-docs/an16.pdf, (accessed: 20.01.2019).
- [18] Kazmierczuk, M.K., 2008, *Pulse-width modulated DC-DC power converters*, John Wiley & Sons, Ltd. United Kingdom, pp. 191-195.

BIOGRAPHY



MUSTAFA ENGİN BAŞOĞLU was born in 1988. He received the M.Sc. degree of Electrical Engineering at Kocaeli University, Turkey in 2013. He receives Ph.D. in 2017 with thesis "Development and implementation of a new maximum power point tracking method for photovoltaic systems". From 2012, he is research assistant in the department of Electrical Engineering in University Kocaeli. From 2018, he is assistant professor in Electrical and Electronics Department of Gümüşhane University. His research interests include: photovoltaic systems, renewable energy, maximum power point tracking algorithms, power electronics, switch mode power supplies and control of electrical machines.

Multi-loop Model Reference Adaptive PID Control for Fault-Tolerance

B. B. ALAGOZ, G. KAVURAN, A. ATES, C. YEROGLU and H. ALISOY


Abstract—This study demonstrates an application of multi-loop Model Reference Adaptive Control (MRAC) structure for enhancement of fault tolerance performance of closed-loop PID control systems. The presented multi-loop MRAC-PID control structure can be used to transform a conventional PID control system to an adaptive control system by combining an outer adaptation loop. This study shows that the proposed control structure can improve fault tolerance and fault detection performance of the existing closed-loop PID control systems without modifying any coefficients of PID controllers, and this asset is very useful for increasing robust control performance of the existing industrial control systems. This advantage originates from the reference input shaping technique that is implemented to combine adaptation and control loops. Numerical and experimental studies are presented to illustrate an application of the MRAC-PID control structure for rotor control applications.

Index Terms— Adaptive Control, Fault detection, Fault tolerant control, Fault diagnosis.


I. INTRODUCTION

Control systems are mainly designed according to mathematical models of controlled systems. The dependence on mathematical modeling is one of the factors, which leads to degradation of long-term control performance of static controller structures in real world control applications.


BARIS BAYKANT ALAGOZ, is with Department of Computer Engineering, Inonu University, Malatya, Turkey, (e-mail: baykant.alagoz@inonu.edu.tr).

 <https://orcid.org/0000-0001-5238-6433>


GURKAN KAVURAN, is with Department of Mechatronics Engineering, Firat University, Elazig, Turkey, (e-mail: gurkankavuran@gmail.com).

 <https://orcid.org/0000-0003-2651-5005>


ABDULLAH ATES, is with Department of Computer Engineering, Inonu University, Malatya, Turkey (e-mail: abdullah.ates@inonu.edu.tr).

 <https://orcid.org/0000-0002-4236-6794>

CELALEDDIN YEROGLU, is with Department of Computer Engineering, Inonu University, Malatya, Turkey (e-mail: c.yeroglu@inonu.edu.tr).

 <https://orcid.org/0000-0002-6106-2374>

HAFIZ ALISOY, is with Department of Electronics and Communication Engineering, Namik Kemal University, Tekirdag, Turkey, (e-mail: halisoy@nku.edu.tr).

 <https://orcid.org/0000-0002-9695-5594>

Manuscript received April 24, 2019; accepted July 6, 2019.

DOI: [10.17694/bajece.557674](https://doi.org/10.17694/bajece.557674)

Unpredictable temporal alterations can change in system behavior in real-world applications, and they generally cause change of system models. Model uncertainties and limitations of mathematical modeling methods decrease long-term validity of system models. In fact, component and material ageing or structural faults are inevitable and they leads to change of system models. Consequently, detection of performance deteriorations and corresponding retuning efforts of controller parameters are required to maintain long-term control performance under real world conditions. Instead of static controller structures, which cannot respond to those alterations, the flexible systems, which can adapt themselves for changing conditions and dynamics of controlled systems, can be more effective to achieve long-term real control performance. This type of flexible control systems are widely referred to as adaptive control systems so that they are capable of adapting themselves for changing operating conditions.

In addition to the external factors, namely environmental disturbances, there are also structural factors that can lead to fluctuation of model parameters depending on a number of temporal phenomenon, such as ageing of materials, failure of system components etc. Specifically, process engineers observed that automated systems can be vulnerable to component faults, defects in sensors or actuators in the process or even in the controllers. Some of these faults cannot be tolerated by closed-loop control systems and they can develop into the malfunction of the control loop [1]. This can be a serious problem, particularly for remote or mission-critical control applications, e.g. remote or interplanetary missions. In these control applications, spontaneous controller tuning efforts may risk the remote missions. The present study illustrates an application of the adaptive control scheme, which may reduce need for retuning efforts in feedback controllers.

Unmanned air vehicles (UAV) with electrical multi-rotor platforms can present several advantages for remote and planetary search missions inside gaseous or liquid environments. In these environments, unknown and complicated ground obstacles can be a problem for effective operation of unmanned ground vehicles. Multi-rotor UAVs can easily fly over blocking ground obstacles and trip over surface more energy-efficiently when compared to operation of unmanned ground vehicles. Performance of multi-rotor UAVs strongly depends on rotor control performance, and fault tolerance and adaptation skill are key assets for success of these type remote applications.

Due to their proven performance in real applications, PID controllers have become an industrial standard, and they are frequently used in UAV control applications [2-3]. PID controllers are simple in implementation and yet effective to respond control requirements of practical applications [4]. However, the constant coefficient PID controllers are quite vulnerable to system perturbations that may originate from external or structural factors. When a system perturbation occurs, they need retuning of controller coefficients to maintain control performance. Since increasing risks of instability and crash of UAVs while performing real-time retuning or online self-tuning actions, update of PID coefficients in operation may not be viable and secure for mission-critical applications. In this sense, motivation of the present study is to improve robust performance of PID control systems without need for retuning actions and this is performed by collaboration MIT rule of MRAC loop. Input shaping technique is used to combine existing PID control loop and MRAC loop because it does not need retuning of PID controller coefficients. The adaptation is performed by shaping the reference input by MRAC loop.

Researches on adaptive control system topic can be traced back to mid-sixties [5] and adaptive control structures have been studied for improvement of robust performance of flight control systems. Discussions on MRAC approaches initiated in late 70s [6]. Later, it has become a major topic of control literature [7-12]. MRAC approaches have been reported to improve robust performance of control systems [12] and therefore they have been widely utilized in the case that system models were inexact or prone to perturbations.

MRAC structures are essentially taken into account as an active control system, of which gain parameters are adjusted by update rules when system dynamics are altered [13-14]. A flight control system should deal with complicated aircraft dynamics, system nonlinearities and frequent variability of flight conditions depending on altitude, payload and weather conditions. One of the solutions is to use reference model based adaptive control strategies that aim to approximate response of reference model to maintain flight control performance under varying conditions of flights [15]. In this manner, we prefer MRAC-PID structures for adaptive rotor control application and investigate possible contributions of this structure to robust control performance. Recently, MRAC has been utilized in many complicated control problems such as for adaptive system control based on only input-output measurements [16], for uncertain switched systems with unmodeled input dynamics [17]. By comparing with performance of PID control, performance improvement of MRAC has been shown in extremum seeking control of photovoltaic systems [18].

A well-known and basic MRAC implementation uses gradient descent optimization for control law derivation, which was commonly referred to as MIT rule [9,11]. This control rule was developed at Massachusetts Institute of Technology (MIT) in 1960 [11]. Essentially, the solution of MIT rule continuously follows descending of gradient trends of model approximation errors while updating gain parameters of control systems. Although it cannot control stable plants, computational complexity of the method is not high and its

cooperation with other controller structure can improve adaptation skill of conventional control systems [19-22].

Fault-tolerant control is an important topic that has been widely discussed for industrial control applications [23] and flight control systems [24-25]. Blanke et al. have been defined the fault tolerance of control systems as "the ability of a controlled system to maintain its control objectives despite the occurrence of a fault" [1]. Particularly, main goal of fault-tolerant control is to prevent local faults to develop into system malfunctions that fail safety-critical or mission-critical control applications. For these applications, degradation in control performance cannot be tolerable, and a certain degree fault-tolerance is achievable by reconfiguring controller parameters for new conditions [1]. In literature, mainly, supervised automation schemes have been proposed to diagnose and recover fault status in control systems. These schemes may need additional blocks to manage detection and diagnosis process and these blocks take action for reconfiguring or retuning of the dynamic systems [26-27]. Retuning effort, while performing control actions, is not safe because it may cause short-time instability and control performance degradations.

In our previous work, multi-loop MRAC fractional-order PID control structure (MRAC-FOPID) has been theoretically investigated and improvement of fault tolerance skills of fractional-order PID control systems has been shown numerically [28]. Then, the multi-loop MRAC-FOPID control structure has been applied for control of experimental magnetic levitation system in order to demonstrate improvement in disturbance rejection performance of magnetic levitation control system [29]. Afterward, this method has been extended to additional loops and control performance improvements of this multi-loop approach has been shown for speed control of a servo plant [30]. The current study demonstrates performance of multi-loop MRAC-PID control structure to enhance fault tolerance and fault diagnosis capabilities of experimental electrical rotor PID control system. Since PID control is the most widely utilized industrial controller structure, demonstration of improvement in performance of PID control system can be very beneficial for industrial control applications.

II. METHODOLOGY

A. Preliminary Knowledge for Application of MRAC-PID Structure

Our control objective is to improve fault tolerance control performance of existing closed loop PID control systems by appending a MIT rule. For this purpose, the following two-step design methodology [28-29] was applied for MRAC-PID rotor control system:

Step 1: A transfer function model for an existing and operating closed loop control system is obtained by applying closed loop model identification, and then the transfer function of the closed loop control system is used as a reference model of MRAC loop.

Step 2: The closed loop PID control system is combined with the MRAC loop according to input shaping technique.

These tasks form a hierarchically connected two-feedback loops such that the one is inner loop, which is the existing closed loop PID control system and performs control actions and stability, and the other is outer loop, which only performs MIT rule to perform adaptation according to reference model. Accordingly, while the inner loop with PID control works for system stability, the outer loop with MIT rule works for approximation of response of the closed loop control system to the reference model, which is namely adaptation. Thus, a change in control performance of inner loop can be easily detected by observing model error signal and then this mismatch can be tolerated by contributions of the MIT rule.

Multi-loop control architectures have been addressed previously to improve certain weaknesses of conventional PID systems, and related works indicates potentials of multi-loop control structures to improve control performance [28-32]. Majority of these studies aim retuning of PID controller coefficients according to the model mismatch error. The proposed multi-loop MRAC-PID system does not tune any coefficients of the existing PID controller. Instead, an additional MIT rule as an outer loop is connected to reference input of the closed loop PID control systems. This additional loop only performs for shaping reference input of inner loop so that the response of the inner loop approximates to the response of the reference model. Thus, it can restore control performance of the closed loop PID control system (inner loop) according to response of the reference model.

In the current study, the reference model is taken as the transfer function model of well-tuned and operating closed loop PID rotor control system. This reference model represents a fault-free, normal state of the PID control system and it is used as a memory of normal system status. Thus it keeps the system input-output knowledge of the fault-free state (normal state) of the system and this knowledge is used for restoration of control performance in case of a fault state. This approach is very useful for maintaining initial and fault-free control performance of the existing PID control systems. It does not need any retuning efforts of PID controllers.

In the current study, it is assumed that fault events are not determined, however faults cause a change in the PID control system responses. Sometimes, a closed-loop control system can hide minor faults and these faults may not be detected until they develop a control-loop failure [1]. To deal with this problem, model mismatch error of the proposed MRAC-PID structure is useful for fault detection and monitoring: A change in closed loop control system (inner loop), which leads to a change in response of inner loop, is detectable by observing model error signal because the model error signal shows divergences of the closed loop control system response from its normal, fault-free responses that were retrieved by the reference model. Then, MIT rule takes action to decrease the magnitude of model error signal by applying reference input-shaping to closed loop control system. This enforces response of control system to approximate response of the reference model. Thus, it can recover control performance at certain degrees. This is the underlying mechanism of MRAC-PID structure that increases fault-tolerance and detection skills of conventional PID control system.

B. Theoretical Background and Fault Modeling

Figure 1 shows a block diagram of the proposed multi-loop MRAC-PID system. The inner loop performs closed loop PID control according to the control error $e_c = u_r - y$, and outer loop, which employs the MIT rule for adaptation of the system by using the model error $e_m = y - y_m$. Let us denote the transfer function of PID controller, $C(s) = k_p + \frac{k_i}{s} + k_d s$, and the controlled plant, $G(s)$. The transfer function of the inner loop can be expressed in the form of

$$T(s) = \frac{C(s)G(s)}{1 + C(s)G(s)} \tag{1}$$

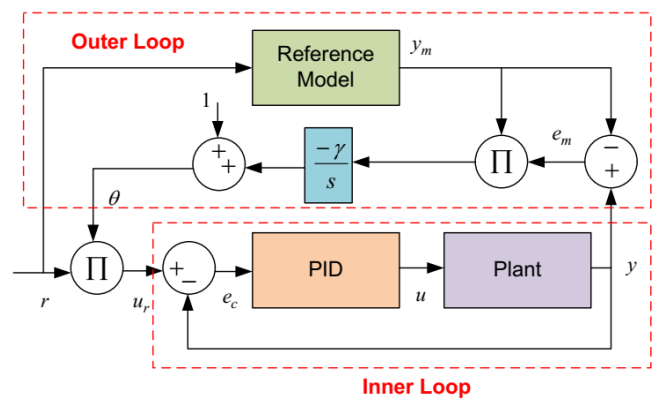


Fig. 1. Block diagram of multi-loop MRAC-PID control system

To maintain initial performance of the closed loop PID control system, the reference model is taken as the transfer function of inner loop when the PID control system is in normal, well tuned and fault-free state. Accordingly, transfer function of reference model can be expressed as,

$$T_m(s) = \frac{C_o(s)G_o(s)}{1 + C_o(s)G_o(s)} \tag{2}$$

where $C_o(s)$ and $G_o(s)$ are transfer functions of the controller and plant in normal operation state. Adaptation of system is carried out by shaping reference input of the inner loop according to $u_r = \theta r$. The adaptation gain θ is determined according to MIT rule, which is based on gradient descent optimization of the cost function J given by,

$$J = \frac{1}{2} e_m^2 \tag{3}$$

The MIT rule for MRAC [7-9] was commonly expressed in the form of

$$\frac{d\theta}{dt} = -\gamma \frac{dJ}{d\theta} \tag{4}$$

By taking Laplace transform of equation (4), it is written as follows,

$$\theta = -\gamma \frac{1}{s} \frac{dJ}{d\theta} = -\gamma \frac{1}{s} e_m \frac{de_m}{d\theta}. \quad (5)$$

One can consider the model error and reference input in the form

$e_m = y - y_m = T(s)u_r - T_m(s)r = T(s)\theta r - T_m(s)r$ and $r = y_m / T_m(s)$, respectively. Then, the sensitivity derivate of the system is written as,

$$\frac{de_m}{d\theta} = \frac{T(s)}{T_m(s)} y_m. \quad (6)$$

By using equation (6) in equation (5), MIT rule for the update of adaptation gain θ to minimize cost function J is obtained as,

$$\theta = -\gamma \frac{1}{s} \left(\frac{T(s)}{T_m(s)} y_m e_m \right). \quad (7)$$

A bias value of 1 is added to allow a faster build-up of the adaptation gain θ when the system is initiated. Otherwise, delay of reference model leads to a zero value of θ for while and it prolongs transient regime of the control system at the system start-up.

$$\theta = -\gamma \frac{1}{s} \left(\frac{T(s)}{T_m(s)} y_m e_m \right) + 1 \quad (8)$$

Let us investigate the normal and faulty cases for this system [28]:

* In case of normal operation, $T(s) = T_m(s)$, the adaptation gain θ becomes,

$$\theta = -\gamma \frac{1}{s} y_m e_m + 1 \quad (9)$$

* In case of fault or parametric perturbation, $T(s) \neq T_m(s)$, and one can consider two circumstances;

(i) The fault comes from plant function, in this case, one can consider the cases of $G(s) \neq G_o(s)$ and $C(s) = C_o(s)$, the adaptation gain θ goes to the value of,

$$\theta = -\gamma \frac{1}{s} \left(\frac{\Delta_o(s)G(s)}{\Delta(s)G_o(s)} \right) y_m e_m + 1 \quad (10)$$

(ii) The fault comes from PID controller, in this case $G(s) = G_o(s)$ and $C(s) \neq C_o(s)$, the adaptation gain θ goes to the value of,

$$\theta = -\gamma \frac{1}{s} \left(\frac{\Delta_o(s)C(s)}{\Delta(s)C_o(s)} \right) y_m e_m + 1 \quad (11)$$

where the $\Delta(s) = 1 + C(s)G(s)$ and $\Delta_o(s) = 1 + C_o(s)G_o(s)$ are characteristic polynomials of transfer functions of closed loop PID control system in faulty case and in normal case, respectively. The fault diagnosis can be carried out by observing value of θ signal. In case of normal operation ($T(s) = T_m(s)$), the condition $e_m = 0$ should be satisfied:

$$e_m = T(s)\theta r - T_m(s)r = T_m(s)(\theta - 1)r = 0 \quad (12)$$

This equation can be always valid in case of $\theta - 1 = 0$. Here, the reference signal r changes independent of the system. So, the normal operation of system (fault-free status) can be detected by the state of $\theta = 1$. Accordingly, the faulty case of system can be detected by the case of $\theta \neq 1$ because it yields a non-zero model error. Two types of fault models are investigated [28]:

i) Gain faults: The gain fault case can be modeled as $T(s) = kT_m(s)$, where the state of $k \neq 1$ is referred to as the gain fault of the system. The case of $k = 1$ infers normal state of system. By rearranging the equation (12) for this type of fault, one solves $T_m(s)(k\theta - 1)r = 0$ and obtains the $\theta = 1/k$ for recovery the system, which provides $e_m = 0$. Hence, any gain type fault case is detected by observing θ signal for a value of $k = 1/\theta$.

ii) Structural factorable faults: This case can be modeled as $T(s) = F(s)T_m(s)$, where the $F(s)$ is called transfer function of structural factored type fault. When equation (12) is rearranged for this fault case as $T_m(s)(F(s)\theta - 1)r = 0$, one observes evolution of the adaptation gain, which recovers fault case, as $\theta = F(s)^{-1}$. For instance, let's assume that a structural fault causes an additional system pole with a time constant τ_f , the fault model becomes $F(s) = 1/(\tau_f s + 1)$. In this circumstance, when this fault case is restored by MIT rule, structural faults can be detected by a θ response that is expressed by $\theta = F(s)^{-1} = (\tau_f s + 1)$.

III. SIMULATION STUDY

This section presents a numerical study to demonstrate application of multi-loop MRAC-PID control for rotor control. Simulation results were obtained by using numerical model of experimental rotor control test platform in

MATLAB/Simulink environment. The experimental system was tuned and controlled by a closed loop PID control system. In well-tuned and fault-free state, the closed loop model identification was carried out by means of model identification toolbox of MATLAB. The following transfer function of closed loop PID control system was identified,

$$T(s) = \frac{-59.91s^8 + 526.2s^7 + 1257s^6 + 9211s^5 + 6795s^4 + 2748s^3 + 569.8s^2 + 68.68s + 5.187}{s^{10} + 134.3s^9 + 934.7s^8 + 3890s^7 + 1.01 \cdot 10^4 s^6 + 1.395 \cdot 10^4 s^5 + 7846s^4 + 2732s^3 + 566s^2 + 66.44s + 5.195} \quad (13)$$

After modeling of tuned closed loop control system in fault-free state, the transfer function of the model, given by equation (13), was implemented as the reference model of the MRAC-PID control system. Then, the MRAC-PID system, which is depicted in Fig. 8, was implemented by appending outer loop (MRAC with MIT rule) to inner control loop (closed loop PID control system). The adaptation rate γ was set to 1 in simulation and experimental studies to provide enough fast system response in our tests. It should be noted that too large values of γ can lead to the instability of system. PID controller coefficients were not changed during simulation and experiments. Simulation study was performed for 10000 sec by applying square wave reference signal so that we can observe long-term system responses for low and high frequency components of square wave reference signal. Figures 2 compares simulation results, which are obtained for the proposed multi-loop MRAC-PID structure and the conventional PID control system in case of a gain fault of the closed loop PID control system, which is expressed as $T(s) = 0.7T_m(s)$. This synthetic fault state is initiated at 5000 sec by instantly switching DC gain of $T(s)$ function from 1 to 0.7. At the beginning of the fault, divergence of the multi-loop MRAC-PID system from reference model is shown in Fig. 3.

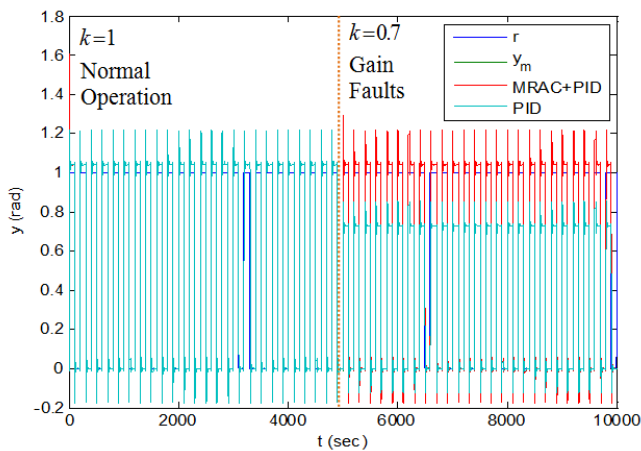


Fig. 2. Time responses of multi-loop MRAC-PID system and conventional PID control system for the case of gain fault of the closed loop PID control system at 5000 sec.

Fig 3 shows a close view of simulation results around 5000 sec in Fig 2. However, the response of multi-loop MRAC-PID system can be restored in 10 sec, and therefore the output of

multi-loop MRAC-PID system (y) is the same as the output of reference model (y_m) in Fig. 4. Whereas, the conventional PID control yields a steady state error. These results clearly show that the proposed system can deal with the gain fault of $k=0.7$.

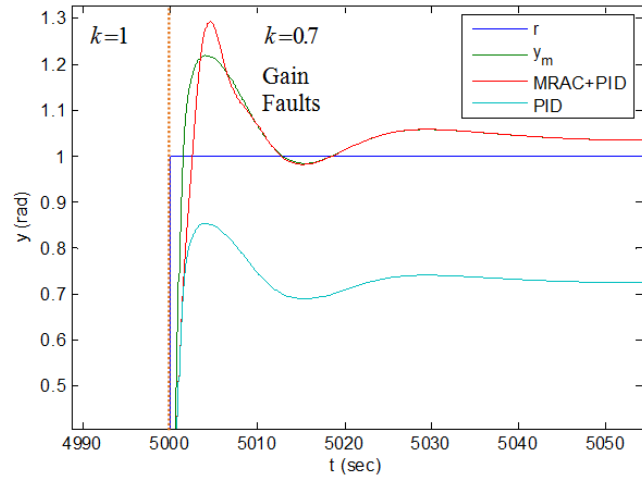


Fig. 3. A close view of Fig.2 to show responses of both control systems at the beginning of gain fault state at 5000 sec.

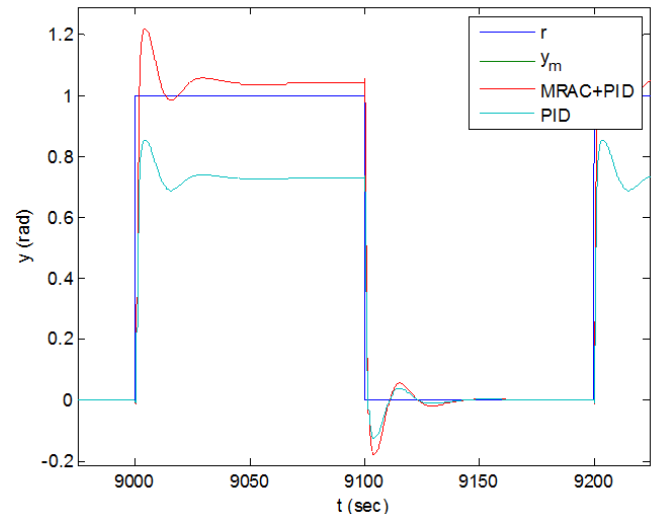


Fig. 4. A close view of Fig.2 to show responses of both control systems at 9000 sec.

In Fig. 5, it was observed that the adaptation parameter θ settles to the value of 1.4, which is very consistent with the result of theoretical formula, $\theta=1/k=1.4$, for gain type fault of closed loop transfer function. As expected, in normal (fault-free) case before the fault insertion at simulation time of 5000 sec, parameter θ settles to the value of 1 to indicate normal status of the system. Hence, the level of θ signal can be utilized to monitor gain type faults: One can define a gain fault index $k=1/\theta$ to detect gain type fault case. In this simulation, this index was accurately detected as $k=1/1.4=0.7$ and $T(s) = 0.7T_m(s)$ fault case was diagnosed by monitoring level of θ . Fig. 6 shows the evolution of model

error e_m during adaptation process. The figure clearly demonstrates the adaptation of the proposed system by settling of model error e_m to 0 again in 10 sec.

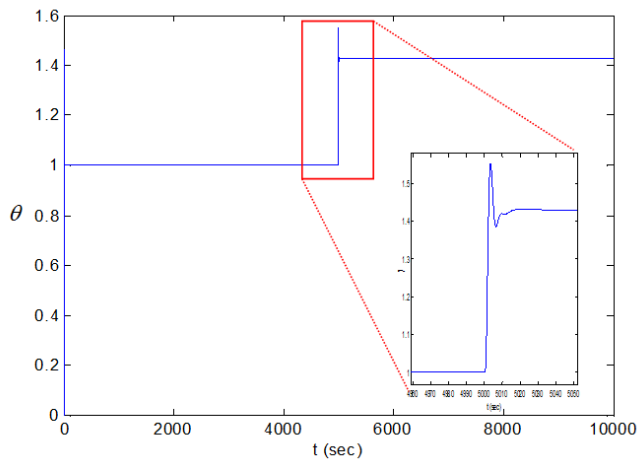


Fig.5. Change of θ at gain fault state.

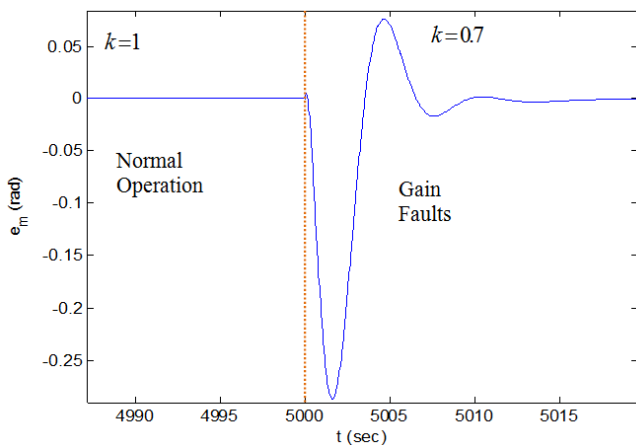


Fig.6. Change of e_m at the beginning of gain fault state.

IV. EXPERIMENTAL STUDY

Figure 7 shows a picture of rotor control test platform that was built for adaptive rotor control research studies. The system is composed of an electrical rotor, a rotary encoder, a shaft and a control card. The rotor hovers and the angle of shaft is controlled by the feedback of rotary encoder. Matlab/simulink environment was used to perform all tasks: control system simulation and design, digital implementation of the design on control card, monitoring of this experimental platform. Figure 8 shows an implementation of multi-loop MRAC-PID system and fault insertion model in experimental study. For normal (fault-free) state of the system, the fault model $F(s)$ was set to 1. Figures 9 and 10 demonstrate responses of the proposed multi-loop MRAC-PID system and the conventional PID control system for a type gain fault insertion, $T(s) = 0.7T_m(s)$, for experimental closed loop PID control system. This synthetic fault state was generated at 120 sec by switching

$F(s)=1$ to $F(s)=0.7$. The figures clearly show that the output of multi-loop MRAC-PID system can approximate to the output of reference model in about 30 sec period, and the system can deal with the DC gain fault $k=0.7$. But, conventional PID control system cannot deal with this fault type case of the PID control system. For the gain fault of $k=0.7$, theoretical formula suggests $\theta=1/k=1.4$ for adaptation action.

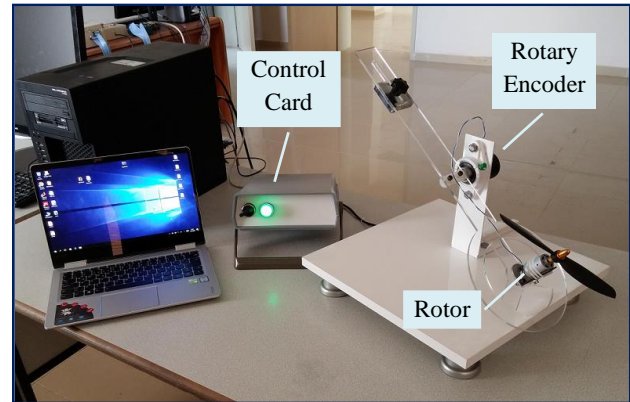


Fig. 7. A picture of experimental rotor control test platform

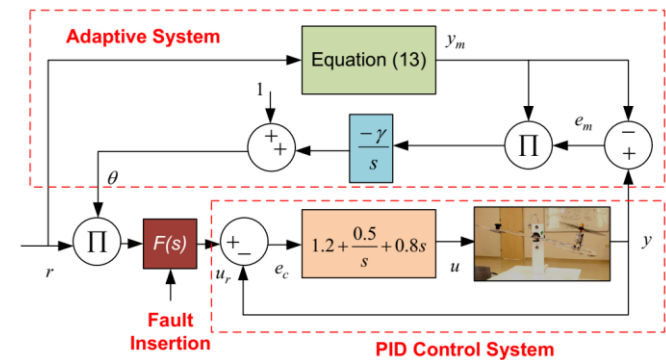


Fig. 8. Block diagram of multi-loop MRAC-PID system and fault insertion model for experimental study.

Figure 11 confirms this result by showing increase of θ up to the level of 1.4. In fault-free normal operation, the parameter θ stays at around the value of 1 in Fig. 11. These experimental results confirm that level of θ can be used to diagnose DC gain fault states of closed loop control systems. Fig. 12 shows the evolution of u_r during the adaptation process. The u_r signal was formed by shaping of the reference input r by MIT rule and it adjusts level to r to tolerate impacts of gain fault. Fig. 13 presents the evolution of model error that convergences again to zero after the recovery of the fault case. These results clearly show that gain type fault case can be easily diagnosed by monitoring θ signal and the proposed system can restore again the system response based on the response of the reference model. Experimental results are also in well-agreement with simulation results and theoretical analyses. Figures 14, 15 and 16 show test results of

the proposed multi-loop MRAC-PID system and conventional PID control system. We assumed that this structural fault results in an additional real system pole with a time constant $\tau_f = 3$ sec and it can be expressed as $F(s) = 1/(3s + 1)$. This synthetic fault case was initiated at 120 sec by connecting one pole $F(s)$ function to system. Figure 15 and 16 show that the multi-loop MRAC-PID system adapts itself for this fault case and approximates to the response of the reference model. Figure 16 shows the change of θ and Figure 17 shows the evolution of u_r during the adaptation process. Both experimental results show that multi-loop MRAC-PID system can approximate to response of the reference model in cases of these fault models and verify adaptation skill of the proposed MRAC-PID structure. Conventional PID control system more diverged from initial well-tuned system response (reference model response) in fault cases.

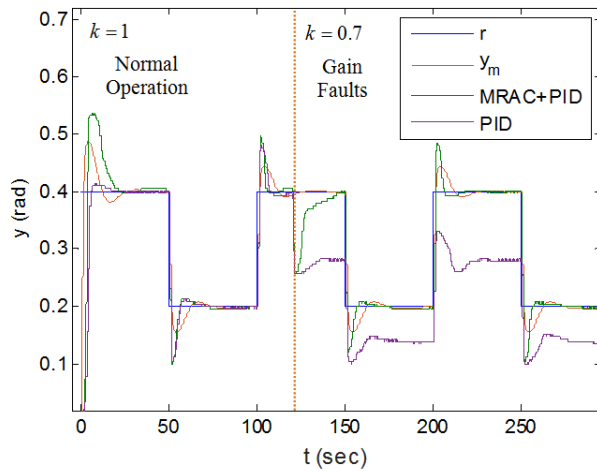


Fig. 9. Responses of multi-loop MRAC-PID system and conventional PID control system in the case of a gain fault of the closed loop PID control system at 120 sec.

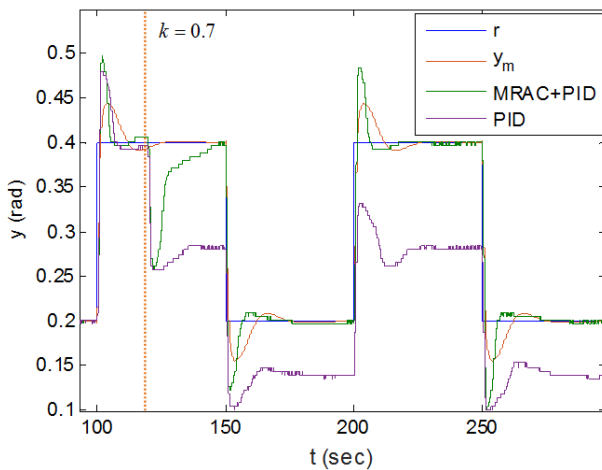


Fig. 10. A close view of Fig.9 to show responses of both control systems at the beginning of gain fault state at 120 sec.

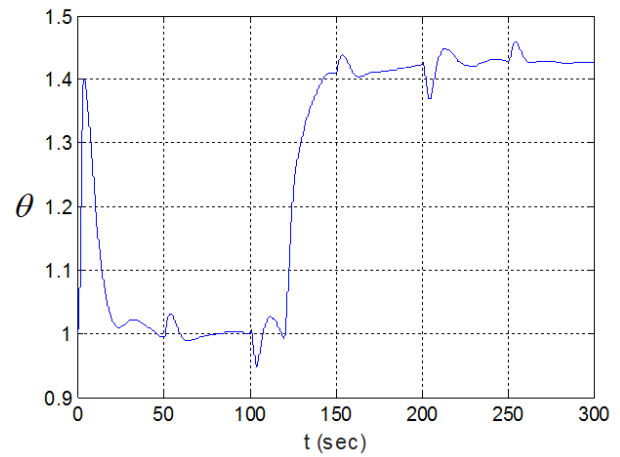


Fig. 11. Change of θ during experimental test of multi-loop MRAC-PID system

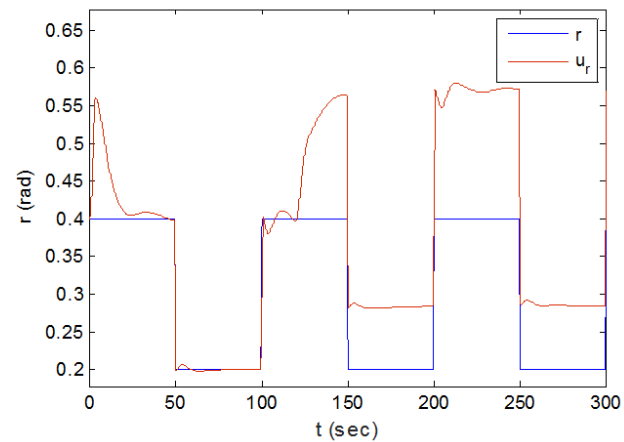


Fig. 12. u_r during experimental test of multi-loop MRAC-PID system

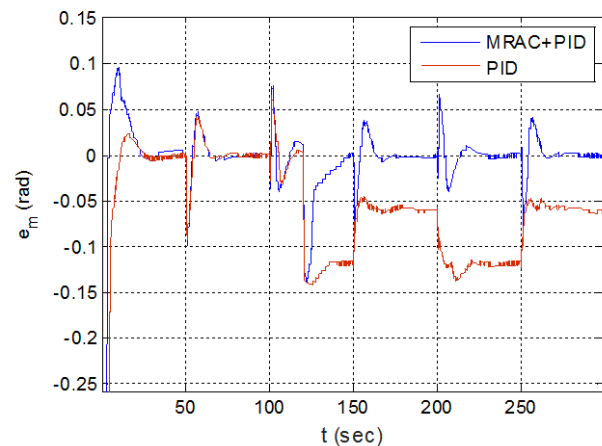


Fig. 13. Change of e_m during experimental test of multi-loop MRAC-PID system and conventional PID control system.

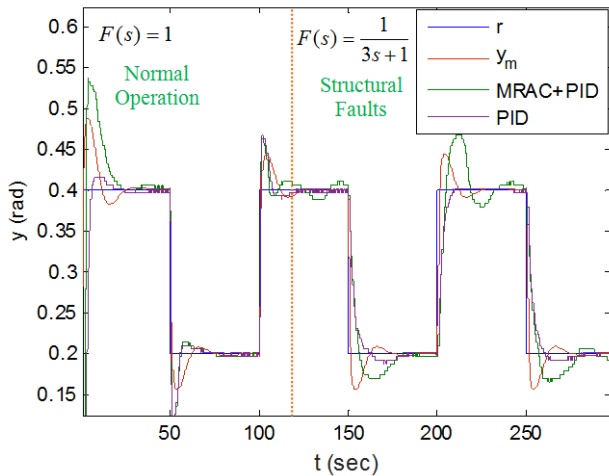


Fig. 14. Responses of multi-loop MRAC-PID system and conventional PID control system in the case of a structural fault of the closed loop PID control system at 120 sec

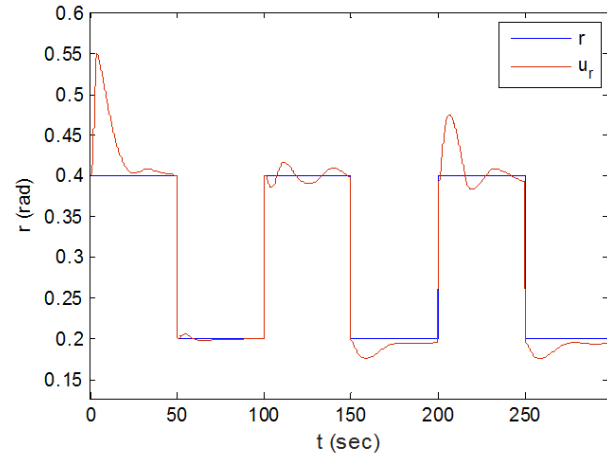


Fig. 17. Change of u_r during experimental test of multi-loop MRAC-PID system

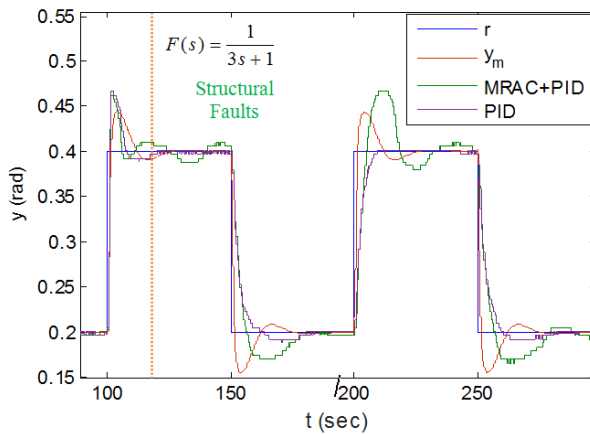


Fig. 15. A close view of Fig. 14 to show responses of both control systems at the beginning of gain fault state at 120 sec.

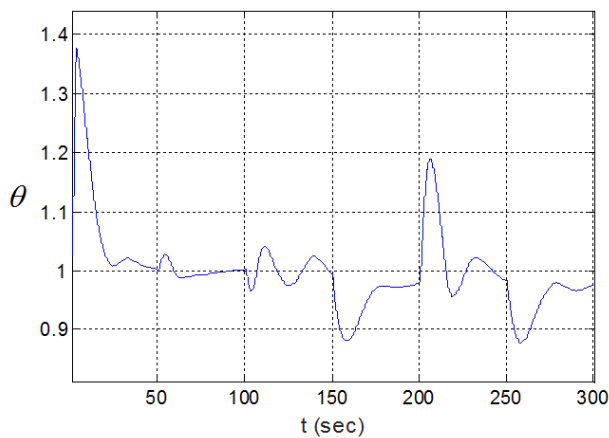


Fig. 16. Change of θ during experimental test of multi-loop MRAC-PID system

IV. CONCLUSIONS

This study demonstrated experimental study for application of MRAC-PID structure to implement adaptive PID control of electrical rotors. Transformation of the existing and operational PID control systems to multi-loop MRAC-PID structure is quite straightforward task, and this multi-loop structure has potential of enhancement of robust control performance of existing PID control systems. Numerical and experimental study results clearly show that the proposed approach can increase adaptation and fault tolerance capability of conventional PID control systems without need for any modification on parameters of PID control systems. In real applications, the closed-loop PID control can compensate the developing faults until they develop a serious failure of control system. The MRAC-PID structure allows detection and diagnosis of fault status of closed loop control systems by observing the state of θ signals. This property may have significance for mission-critical control. Some remarks can be summarized:

- * Simulation and experimental results show that the proposed multi-loop MRAC-PID system can be effective to compensate control performance deteriorations that are caused by gain type faults.
- * Implementation of the method is very straightforward; it can be applied to the existing PID control systems only by performing closed loop model identification. No need for modification of closed loop PID control loop. This is an important asset for improvement of exiting control systems.
- * Another practical advantage of this multi-loop MRAC-PID structure comes from performing reference input-shaping instead of dynamically updating PID controller coefficients for retuning the controller. This property is very desirable for mission-critical and remote control applications because online returning actions of controller coefficients can raise the risk of instantaneous instability or performance deteriorations.
- * Under harsh conditions, ageing or failing of system components can occur rather faster than normal conditions.

Fault tolerance capability of control systems can contribute to robust performance of control systems by dealing with such performance deteriorations that are caused from instantaneous or slowly developing faults or defects of system components. The multi-loop MRAC-PID control can contribute to maintain control performance in industrial application.

Acknowledgement

This research is supported by TUBITAK [grand number 215E261].

References

- [1] M. Blanke, M. Staroswiecki, N. E. Wu, "Concepts and methods in fault-tolerant control," Proc. ACC, vol.4, pp. 2606-2620, June, 2001.
- [2] A. L. Salih, M. Moghavvemi, H. A. Mohamed, K. S. Gaeid, "Flight PID controller design for a UAV quadrotor," *Scientific Research and Essays*, vol. no. 23, pp.3660-3667, 2010.
- [3] N. Hengameh, H. Kharrati, "PID controller design for unmanned aerial vehicle using genetic algorithm," 23rd International Symposium on Industrial Electronics, pp.213-217, June, 2014.
- [4] K. J. Astrom, T. Hagglund, "The future of PID control," *Control Engineering Practice*, vol.9, no. 11, pp. 1163-1175, 2001.
- [5] P. V. Osburn, H. P. Whitaker, A. Kezer, "Comparative studies of systems," *Institute of Aeronautical Science*, pp. 61-39, 1961.
- [6] I. D. Landau I.D., *Adaptive Control the Model Reference Approach*. New York: Marcel Dekker, 1979.
- [7] K. J. Astrom, B. Wittenmark, *Adaptive Control*. Massachusetts: Addison-Wesley, 1995.
- [8] H. Butler, *Model-Reference Adaptive Control-From Theory to Practice*. New Jersey: Prentice-Hall, 1992.
- [9] B. M. Vinagre, I. Petráš, I. Podlubny, Y. Q. Chen, "Using fractional order adjustment rules and fractional order reference models in model-reference adaptive control," *Nonlinear Dynamics*, vol. 29, no. 1-4, pp.269-279, 2001.
- [10] E. Lavretsky, *Adaptive control: Introduction, overview, and applications*. Adaptive Control Workshop, NASA Marshall Space Center, USA, 2009.
- [11] P. Jain, M.J. Nigam, "Design of a model reference adaptive controller using modified MIT rule for a second order system," *Advance in Electronic and Electric Engineering*, 3(4), 477-484, 2013.
- [12] M.D. Bernardo, U. Montanaro, J.M. Olm S. Santini, "Model reference adaptive control of discrete time piecewise linear systems," *International Journal of Robust and Nonlinear Control*, vol. 23i no. 7, pp. 709-730, 2013.
- [13] B. Jiang, Z. Gao, P. Shi, Y. Xu, "Adaptive fault-tolerant tracking control of near-space vehicle using Takagi-Sugeno fuzzy models," *IEEE Transactions on Fuzzy Systems*, vol. 18, no. 5, pp. 1000-1007, 2010.
- [14] I. Sadeghzadeh, A. Mehta, Y. Zhang, C. Rabbath, "Fault-tolerant trajectory tracking control of a quadrotor helicopter using gain-scheduled PID and model reference adaptive control," Annual Conference of the Prognostics and Health Management Society, Montreal, Canada, pp.1-10, 2011.
- [15] B.B. Alagoz, A. Ates, C. Yeroglu, "Auto-tuning of PID controller according to fractional-order reference model approximation for DC rotor control," *Mechatronics*, vol. 23, no. 7, pp. 789-797, 2013.
- [16] A. Znidi, K. Dehri, A. S. Nouri, "Discrete variable structure model reference adaptive control using only input-output measurements," *Transactions of the Institute of Measurement and Control*, vol.40, no. 3, pp. 861-872., 2018.
- [17] B. Sinafar, A. R. Ghiasi, A. K. Fazli, "A new model reference adaptive control structure for uncertain switched systems with unmodeled input dynamics," *Transactions of the Institute of Measurement and Control*, vol. 37, no. 10, pp. 1171-1180, 2015.
- [18] R. D. Tehrani, F. Shabaninia, "Two-level control of photovoltaic systems using global perturbation-based extremum seeking control and model reference adaptive control," *Transactions of the Institute of Measurement and Control*, vol. 40, no. 13, pp. 3709-3720.
- [19] P. Sarhadi, A. R. Noei, A. Khosravi, "Model reference adaptive PID control with anti-windup compensator for an autonomous underwater vehicle," *Robotics and Autonomous Systems*, vol.83, pp. 87-93, 2016.
- [20] W. Su, "A model reference-based adaptive PID controller for robot motion control of not explicitly known systems," *International Journal of Intelligent Control and Systems*, vol. 12, pp.237-244, 2007.
- [21] Xiao S., Li Y. and Liu J.: A model reference adaptive PID control for electromagnetic actuated micro-positioning stage. *8th IEEE International Conference on Automation Science and Engineering*, Seoul, Korea, pp. 97-102., 2012.
- [22] B. Singh, V. Kumar, "A real time application of model reference adaptive PID controller for magnetic levitation system," *Power, Communication and Information Technology Conference*, Bhubaneswar, India, pp.1-8., 2016.
- [23] H. Noura, D. Theilliol, J. C. Ponsart, A. Chamseddine, *Fault-tolerant Control Systems Design and Practical Applications*. London: Springer-Verlag, 2009.
- [24] G. J. J. Ducard, *Fault-tolerant flight control and guidance systems practical methods for small unmanned aerial vehicles*. London: Springer-Verlag, 2009.
- [25] S. Ding, Y. Yuan, N. Xue, X. Liu, "Online fault-tolerant onboard aeroengine model tuning structure," *International Journal of Aerospace Engineering*, pp.1-16, 2016.
- [26] W. M. Wonham, *A control theory for discrete event system, advanced computing concepts and techniques in control engineering*. Berlin: Springer-Verlag, pp.129-169., 1988.
- [27] K. Wang, J. Chen, Z. Song, "Data-driven sensor fault diagnosis systems for linear feedback control loops," *Journal of Process Control*, vol.54, pp. 152-171, 2017.
- [28] B. B. Alagoz, E. Petlenkov, C. Yeroglu, "Multi-loop model reference adaptive control of fractional-order PID control systems," 40th TSP, Barcelona, pp.702-705, July, 2017.
- [29] A. Tepljakov, B. B. Alagoz, E. Gonzalez, E. Petlenkov, C. Yeroglu, "Model reference adaptive control scheme for retuning method-based fractional-order PID control with disturbance rejection applied to closed-loop control of a magnetic levitation system," *Journal of Circuits Systems and Computers*, vol.27, no.11, 2018.
- [30] R. Rajesh, S. N. Deepa. "Design of Direct MRAC Augmented With 2 DoF PID Controller: An Application to Speed Control of a Servo Plant." *Journal of King Saud University-Engineering Sciences*, Available online 1 March 2019.
- [31] N. Penkov, "A new Approach for Adaptive Tuning of PI Controllers," *Application in Cascade Systems, Information Technologies and Control*, vol. 6, no.1 pp. 19-26, 2008.
- [32] A. S. Alekseev, S. V. Zamyatin, V. A. Rudnicki, "Multi-loop control system design," *Bulletin Of The Polish Academy Of Sciences, Technical Sciences*, vol. 60: 627-630, 2012.



B.B. Alagoz was graduated from Istanbul Technical University department of Electronics and Communication Engineering in 1998. He has PhD degree from Inonu University, department of Electrical-Electronics Engineering in 2015. His research interests are intelligent systems, control, simulation and modeling.



G. Kavuran received his B.Sc. degree in Electrical and Electronics Engineering from Firat University in 2008. He received PhD degree in Electrical and Electronics Engineering from Firat University in 2017. His research interests include robotics, fractional calculus, control theory and applications, modeling and simulation, signal processing.



A. Ates received his B. Sc. Degree in Electrical and Electronics Engineering from Erciyes University in 2011. He received PhD degree in Computer Engineering from Inonu University in 2018 respectively. His research interests

include optimization algorithm, analytical and numerical optimization method, fractional order control systems.



C. Yeroglu received his B.Sc. degree in Electrical and Electronics Engineering from Hacettepe University in 1990. He received his first Ph.D. degree in Computer Engineering from Trakya University in 2000 and his second Ph.D. degree in Electrical and Electronics Engineering from Inonu University in 2011. His research interests include

fractional order control systems, robust control, nonlinear control, modeling and simulation, optimization algorithm.



H. Alisoy was graduated from Moscow Technical University department of Electro-Physics Engineering 1982. He had his PhD degree from USSR Science Academy Physics Institute of P.N. Lebedyev and Doctor of Sciences degree (DSc) from International Ecology-Energy Academy. He works at Namik Kemal University, Department of

Electronics and Communication Engineering.

A Clustering Approach for Intrusion Detection with Big Data Processing on Parallel Computing Platform

B. REIS, S.B. KAYA, and O.K. SAHINGOZ*


Abstract— In recent years there is a growing number of attacks in the computer networks. Therefore, the use of a prevention mechanism is an inevitable need for security admins. Although firewalls are preferred as the first layer of protection, it is not sufficient for preventing lots of the attacks, especially from the insider attacks. Intrusion Detection Systems (IDSs) have emerged as an effective solution to these types of attacks. For increasing the efficiency of the IDS system, a dynamic solution, which can adapt itself and can detect new types of intrusions with a dynamic structure by the use of learning algorithms is mostly preferred. In previous years, some machine learning approaches are implemented in lots of IDSs. In the current position of artificial intelligence, most of the learning systems are transferred with the use of Deep Learning approaches due to its flexibility and the use of Big Data with high accuracy. In this paper, we propose a clustered approach to detect the intrusions in a network. Firstly, the system is trained with Deep Neural Network on a Big Data set by accelerating its performance with the use of CUDA architecture. Experimental results show that the proposed system has a very good accuracy rate and low runtime duration with the use of this parallel computation architecture. Additionally, the proposed system needs a relatively small duration for training the system

Index Terms— Deep Neural Network, Big Data, CUDA, GPU, Parallel Computation.


I. INTRODUCTION

DUE to the recent improvements in networking technologies, the global network, the Internet, increase its popularity and used in most of the real work activities. At the

SAMI BERK KAYA is with Istanbul Kultur University Computer Engineering Department, Istanbul, Turkey, (e-mail: saamiberk@gmail.com).

 <https://orcid.org/0000-0001-6887-9777>

BUMINHAN REIS, is with Istanbul Kultur University Computer Engineering Department, Istanbul, Turkey, (e-mail: buminhanreis@gmail.com).

 <https://orcid.org/0000-0002-7221-277X>

OZGUR KORAY SAHINGOZ, is with Istanbul Kultur University Computer Engineering Department, Istanbul, Turkey, (e-mail: o.sahingo@iku.edu.tr).

 <https://orcid.org/0000-0002-1588-8220>

* Corresponding Author

Manuscript received May 10, 2019; accepted June 17, 2019.
DOI: [10.17694/bajece.563167](https://doi.org/10.17694/bajece.563167)

same time, the number of hacking activities grows and directly affect the performance of the network [1]. The hackers/attackers aim to access the network in an unauthorized way and try to change some data in the network or sniff the communication between other networks, disable some network services during a specific time. Therefore, protecting networks against different types of attacks becomes an important research area not only for the network security managers but also for many scholars

Traditionally use of some antivirus programs, network authentication tools or firewalls are preferred for protecting the systems from these attacks [2]. Although they decrease the number of attacks, they are not enough for whole protection. In this point, intrusion detection and prevention systems emerged as an alternative solution for security threats. An intrusion detection mainly analyzes the whole networks activities, especially from the data communication view, and tries to catch the unauthorized and abnormal ones. In case of catching this type of intrusion, the intrusion detection system needs to create an alert message for the network security admins to get necessary precautions. However, the intrusion prevention system can automatically execute some services to prevent attacks such as blocking the IP addresses from which the intrusions occur.

This type of intrusion detection and prevention system firstly needs to identify intrusions, and this can be done with two different ways as signature-based detection and anomaly-based detections. In the former one system maintains and intrusion database which stores the patterns of the known attacks. If an incoming request/message match with the database, it is automatically labeled as an intrusion. Although this method is preferred in most of the commercial IDS systems, and it has very low false alarm rates. However, due to the static structure of the signature-based approach, systems can miss most of the unknown attacks, such as zero-day attacks. Additionally, intruders can evaluate their attack types according to created signatures. Therefore, signature-based systems are fragile in this manner.

On the other side, anomaly-based systems react to anomalous behaviors in the networks. According to the previous history of the monitored systems, if there are some anomalous messaging, they are labeled as intrusions. These systems can easily detect zero-day attacks due to its dynamic structure. However, for defining the normal behavior of the

system, huge training time is needed with a great data set which is not much suitable for traditional machine learning techniques [3].

In recent years, deep learning approaches are highly preferred in the processing of Big Data. These techniques result in better accuracy rates and low false positive rates. Therefore, in this paper, it is aimed to use a deep neural network approach for training the intrusion detection system. To increase the accuracy rate of the system a clustered approach is preferred and to decrease the training time, parallel execution is preferred. The details of the algorithmic design of the frameworks and obtained test results are presented in the ongoing sections.

The rest of the paper is organized as follows. In Section 2 the related works are surveyed. The proposed system's details with the clustering approach and the Experimental result of the system are presented in Section 3 and Section 4 respectively. Finally, conclusions and future works are drawn.

II. RELATED WORKS

In previous studies, different types of intrusion detection systems have been implemented. Each of them uses different approaches to increase the accuracy rate of the system. The trend of these works shows that's, current systems mainly focus on the use of machine learning approaches for setting up dynamic detection system. In some studies, Java based WEKA libraries, which are especially useful for different artificial intelligence problem solutions [4], are preferred, some works are focused on the use of Tensorflow libraries with Python programming language.

IDS can be applicable in many different application areas. In one of the current researches[5] authors focused on the security operations of smart grids. In this manner they mainly analyzed the 37 different cases in the intrusion detection and prevention systems concepts in smart grid environments

One of the recent works is presented by Farahnakian and Heikkonen in 2018, and they prefer the used of deep learning approach for IDSs with the use of Deep Auto-Encoder model. As a dataset, they use the KDDCUP'99 and use an unsupervised learning algorithm to avoid overfitting [6].

In [7], Spaffard et. Al. uses autonomous agents for intrusion detection and shortened the system as AAFID. AAFID has a distributed architecture; agents work as autonomous entities to monitor the message traffic in the host side. Due to its distributed structure, there is not a central authority to generate an alarm, and agents do not communicate with each other directly.

Sagha et al. proposed a real-time learning methodology for their IDS system with the use of reinforcement learning mechanism [8]. Their learning engine uses a fuzzy modeling technique and temporal difference learning which is a prediction method which estimates the status of the messages according to previous knowledge. They also used a Reward-Penalty Plane (RPP)structure to show the efficiency of the actions in a specific state.

An alternating decision tree approach is used in [9] for the

classification of intrusions. They used NSL-KDD dataset for testing their system and about 98 % accuracy rate is reached in the experiments. They planned to use some evolutionary algorithms to increase the efficiency of the system. The system also used a clustering approach. They clustered the dataset into four different clusters as DOS, Probe, R2L, and U2L. After that, they make a partition about each cluster into training and test sets.

At the same time, some hybrid detection mechanisms are also preferred in the literature. Desai mainly uses some signature-based matching algorithms, and for increasing efficiency, a fuzz genetic algorithm is adapted to the system [10]. The signature matching algorithm is used for identifying the inner attacks. However, the fuzzy genetic algorithm is preferred for detection of the external attacks. Due to the structure of the system, it can be executed either in offline or online environments.

A neural network-based approach was proposed in [11] with the use of single hidden layer with different number of neurons. In this paper, authors analyzed KDDCup99 Dataset and they claimed to reach acceptable accuracy rates in a shorter time depending on the attack types. In the same neural network-based approach, the effect of the training functions was examined in [12]. They showed that the training function can highly change the accuracy rate of the systems and "trainlm" function results the best between the compared functions.

III. PROPOSED SYSTEM

This section gives details about the proposed system. We initially discuss the NSL-KDD data set and the related stages of pre-processing and feature selection techniques. Later, we introduce the K-Means algorithm for partitioning the data set into clusters of train and test set pairs based on similarity. Finally, with the addition of the K-Means algorithm, we present a hybrid IDS with the ensemble of a GPU-accelerated Deep Neural Network (DNN) classifier. of the proposed system's framework is shown in Fig.1.

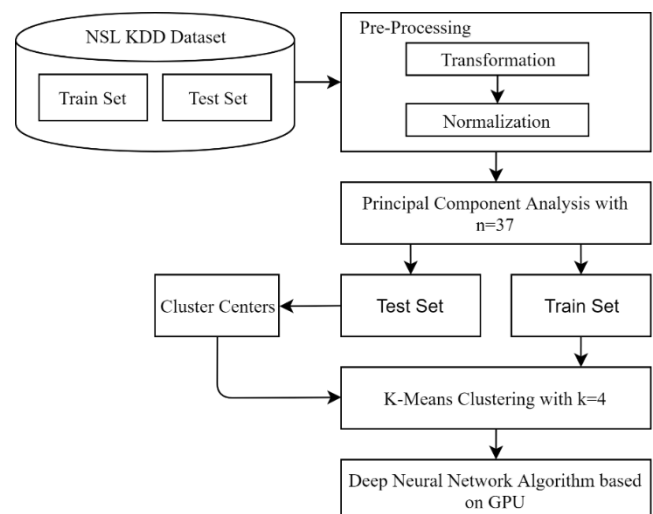


Fig.1. The Framework of the Proposed System

A. Dataset

The NSL-KDD dataset is a successor of DARPA’s KDD’99 dataset which was obtained from the previous 1998 DARPA intrusion detection evaluation program. The environment created in this program was aimed to acquire raw TCP/IP data for a Local Area Network (LAN). Every TCP/IP connection was represented with 41 various features [13]. Although it has been noted that this newer version of the KDD data set has some flaws as pointed out in [14], it is also a good candidate as a benchmark dataset in the Intrusion Detection field. The NSL-KDD data set has a total of 42 features, which 41 of them being the attributes that define the characteristics of the records.

In NSL-KDD data set, the total number of different attack types is 39. All the attacks can be grouped into four main categories as DoS, Probe, R2L, and U2R. While the NSL-KDD data set contains a total of 39 different attack types, the number of unique attack types contained in the train set and test set differentiate from each other. The attack types contained in the train set which are called as “known attacks” have a total number of twenty-two attack types. On the other hand, the test attacks have a total number of thirty-seven attacks. The additional attacks in the test set which are not present in the train set are called “novel attacks.” Having unknown attack types in the test set shows if the system can adapt to different scenarios when the testing is done. The attack types contained in the train and test sets are shown in Table 1 with the novel attacks being represented as bold.

TABLE I
ATTACK TYPES CONTAINED IN THE TRAIN AND TEST SETS OF NSL-KDD

Attack Groups	Attack Types
DOS	worm, processtable, mailbomb, pod, apache2, smurf, neptune, land, back, udpstorm, teardrop,
Probe	saint, mscan, portsweep, nmap, ipsweep, satan,
R2L	named, sendmail, httptunnel, snmpgue , ss, snmpgetattack, xsnoop, xlock, warezmaster, multi hop, guess_password, fip_write, phf, imap,
U2R	ps, xterm, sqlattack, perl, rootkit, buffer_overflow, loadmodule,

One of the advantages of the NSL-KDD over to its successor KDD’99 data set is that the amount of data contained in the train and test sets are reasonable so that every classifier can be evaluated on equal terms by using the same data sets. The number of data contained in the NSL-KDD train set is 125,973 and 22,544 for the test set. The Fig.2 shows the total number of data contained in NSL-KDD data set with the distribution to 5 classes. A sample record from the NSL-KDD data set is shown in Table 2.

B. Data Cleaning

After analyzing the training set, we encountered faulty data in the binary type attribute ‘su_attempted’ where 59 of the

samples are defined with the value of 2. We corrected the values of these samples as 0. Also, the attribute “num_outbound_cmds” has the same value across all the data set which is 0. Since the objective of the system is to find patterns in the data by examining the dissimilarities, we removed this feature from the data set. Thus, the total number of attributes present in the NSL-KDD data is reduced from 41 to 40.

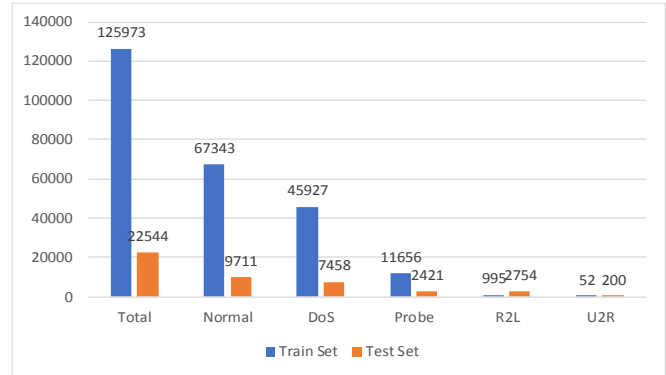


Fig.2. The number of data contained in the NSL-KDD data set

TABLE II
SAMPLE RECORD OF NSL-KDD DATA SET

```
0, udp, domain_u, SF, 79, 2766, 0, 0, 0, 3, 0, 1, 0, 0, 0, 4, 0, 0,
0, 0, 0, 0, 4, 4, 0.00, 0.00, 0.00, 0.00, 1.00, 0.00, 0.00, 255,
255, 0.89,0.11,0.06,0.03, 0.00, 0.00, 0.00, 0.00, normal, 21
```

C. Data Preprocessing

In this stage, we described the methods that we used for converting the categorical data into numerical representations so that the neural network could have a better understanding of these data, thereby it can have a wider perspective on detecting the attacks. In this stage, the categorical data present in the NSL-KDD data set, which are known to be the three features in the nominal category as “protocol_type”, “service” and “flag”, converted into numerical representations using One-Hot Encoding method.

After transforming the categorical features, the number of attributes is increased from 40 to 121. To get into account this increased in the dimensions of the data set, a feature selection algorithm needs to be considered. This feature selection algorithm is detailed in the ongoing subsection.

D. Feature Selection

Even though there are 121 features representing the data in the data set, not all of them might necessarily assure the best performance for the IDS. Using unnecessary features means increased computational costs and error rates for the system. For this reason, considering the feature correlations, a set of selected features can have the same or rather better results compared to using all of them. Therefore, we used a feature selection algorithm called as Principal Component Analysis (PCA) which is a technique that has the aim of transforming several variables that are correlated with each other to several

variables that are uncorrelated and called as Principal Components (PCs).

The aim of the PCA is to reduce the dimensions of the initial variables in the data set while keeping the variance as same as the initial state [15]. To find the best column vector sample to work with, we experimented every possible vector sample using the original NSL-KDD train set with the DNN classifier and found the column vector samples with the highest accuracy score to be 37. Fig.3 shows the error rate results obtained from an interval sample of the experiments.

E. Data Normalization

Scaling or normalization is a concept of transferring the data into forms and ranges so that the modeling can be done more appropriately. By this definition, we used a normalization technique called Min-Max Normalization.

In this technique, the original data is transformed linearly by finding the maximum and minimum values in every feature set. In [16], it is emphasized that when scaling is done for the training data set; the same process is also should be done on the test set using the numerical characteristics of the train data. Also, it is shown that the scaling method is improved the accuracy of the experimented classifiers.

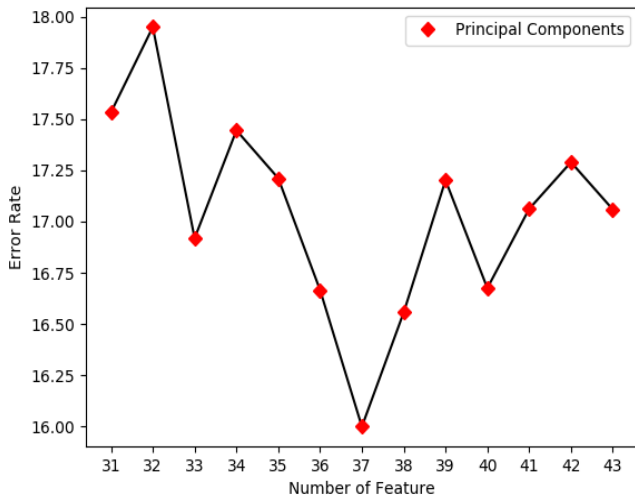


Fig.3. Best Correlated Features Chosen by the PCA

F. DNN Classifier

Using the TensorFlow framework, we built a GPU-accelerated DNN structure for classification of the data in NSL-KDD data set. The structure of the DNN classifier is composed of two hidden layers containing 64 neurons in the first layer and 32 neurons in the second layer. The parameters for the classifier’s initiation specified as 1,000 for the batch size and 500 for the number of epochs.

A pair of sigmoid functions are used as activation functions for both hidden layers. In Fig.4 [17], a general structure of the neural networks is shown.

G. K-Means Algorithm

The K-Means algorithm [18] which is one of the most commonly used clustering algorithms, finds the similarities

between the data points using a distance formula such as Euclidean, Manhattan or Minkowski distance [19].

In the proposed work, we used the Euclidean distance-based K-Means algorithm. The formula for the distance calculation is defined in the Equation (1) as:

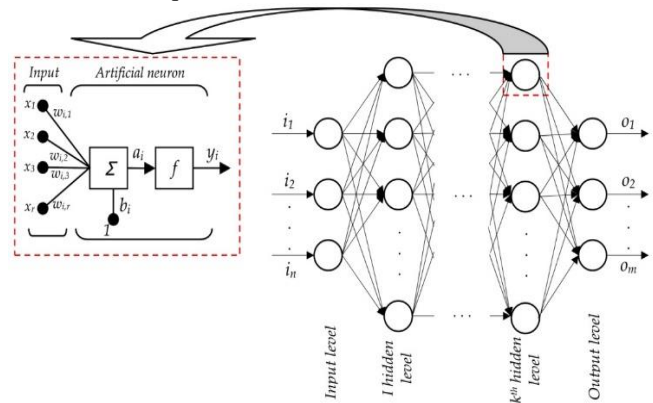


Fig.4. General Structure of Neural Networks

$$Dist_{xy} = \sqrt{\sum_{k=1}^m (X_{ik} - X_{jk})^2} \tag{1}$$

Using this formula, the steps for finding the clusters using the K-Means algorithm can be defined as:

- Let $X = \{x_1, x_2, x_3, \dots, x_n\}$ be the instances and $V = \{v_1, v_2, v_3, \dots, v_c\}$ be the set of centers.
- 1. Choose a cluster center ‘c’ randomly.
- 2. The distance between each instance is found, and the cluster center is recalculated.
- 3. Assign the data points to the cluster centers with minimum distances.
- 4. Cluster center is updated with using the Equation (2):

$$V_i = \left(\frac{1}{C_i}\right) \sum_1^{C_i} x_i \tag{2}$$

- where C_i represents the number of data in i^{th} the cluster.
- 5. Recalculate each instance distance to the center of the cluster.
- 6. Unless the state of the clusters does not change, repeat the steps 3-5.

H. Hybrid IDS Approach Using K-Means with DNN

Clustering is one of the well-known types of techniques for finding relations in the data and putting them into similar groups. The partitioning of the data into clusters happens such that the similarity of a cluster is greater than that among other clusters [20]. In this approach, a hybrid IDS structure has been built using the K-Means algorithm and a GPU-Accelerated DNN. The addition of the K-Means algorithm helps to cluster the NSL-KDD data set into groups of data based on similarity.

The implementation of the K-Means algorithm is based on the study made in [21]. In our approach, the training data set is partitioned into clusters using the K-Means algorithm. After the partitioning, the cluster centers of the training set are used for partitioning the test set into clusters. Using the cluster centers of the training set to partition the test set provides a good data distribution. This plays an important role in finding the best clusters containing pairs of the train and test sets with similar data. A visual representation of this process is shown in Fig.5.

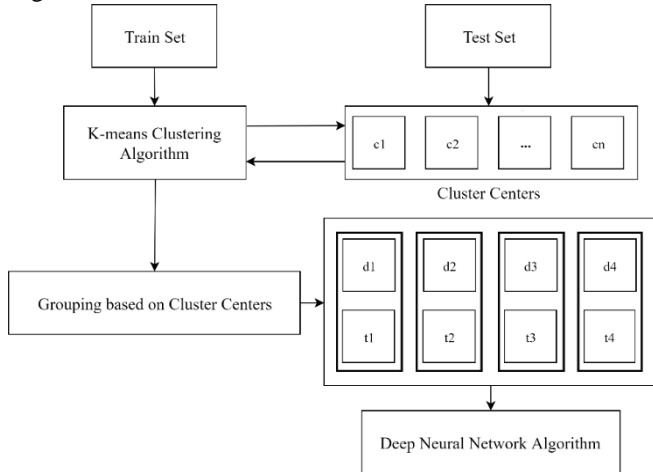


Fig.5. Visual Representation of the K-Means Algorithm Implementation

IV. EXPERIMENTAL RESULTS

The test environment contains a notebook with the features of Intel Core x64-based processor i5-4200H CPU @ 2.80 GHz, 12 GB Random Memory Access (RAM), 64-bit Windows 8.1 Pro Operating System. The NVIDIA GTX 1050Ti Graphics Processing Unit (GPU) is used for experimenting and building the GPU-Accelerated model. The specifications are shown in Table 3.

TABLE III
GPU SPECIFICATIONS

Property	Value
Processor	NVIDIA GeForce GTX 1050
NVIDIA Cuda Cores	768
Base Clock	1290 MHz
Boost Clock	1392MHz
Graphics Performance	high-6747
Memory Speed	7 Gbps
Memory Config	4GB GDDR5
Memory Interface	GDDR5
Memory Interface Width	128-bit
Memory Bandwidth	112(GB/sec)

The performance measures used for the evaluation of the neural network are the following:

- False positives (FP): defines the attacks that are detected incorrectly.
- False negatives (FN): instances of attacks detected as normal behavior.
- True positives (TP): correctly classified instances as normal behavior.
- True negatives (TN): correctly classified instances as attacks.
- The accuracy or True positive rate (TPR): the percentage of the ratio of correct predictions overall predictions:

$$\frac{TP + TN}{TP + TN + FP + FN} \times 100 \tag{3}$$

False alarm rate is defined as:

$$\frac{FP}{TN} \tag{4}$$

Detection rate is defined as:

$$\frac{TN - FN}{TN} \tag{5}$$

Precision (P) is defined as:

$$\frac{TP}{TP + FN} \tag{6}$$

Recall (R) is defined as the ratio of correctly predicted normal behaviors over all the correctly predicted instances:

$$\frac{TP}{TP + FP} \tag{7}$$

F-measure is defined as the consideration of both the precision and recall computing the score:

$$2 \times \frac{P \times R}{P + R} \tag{8}$$

According to these performance measures, Firstly, we tested our system without clustering approach. The prediction results obtained by the neural network trained on the original NSL-KDD data set is shown in Table 4. As can be seen form this table, system return acceptable results if there exist sufficient data as in Normal, DoS and Probe classification. However, in the other case the prediction rate is very small.

TABLE IV
PREDICTION RESULTS OF THE NEURAL NETWORK ON THE TEST DATA

Data Label	Test Data	Correct Predictions	Incorrect Predictions	Prediction Rate %
Normal	9711	9424	287	94.04
DoS	7458	7060	398	94.66
Probe	2421	2084	337	86.08
R2L	2754	815	1939	9.5
U2R	200	19	181	29.59

Addition to these prediction values, the confusion matrix values have great importance. Therefore, these values are listed in Table 5. Although, total accuracy rates are in acceptable level, in the R2L and U2R type packets, false values are too large.

TABLE V
NUMBER OF TP, TN, FP, AND FN FOR THE OPTIMAL NEURAL NETWORK RESULTS

True Positives	True Negatives	False Positives	False Negatives
9424	9978	287	285

If we get the sum of both these tables, the performance metrics can be summarized as in Table 6.

TABLE VI
PERFORMANCE MEASURES FOR THE OPTIMAL NEURAL NETWORK RESULTS

Accuracy	False Alarm	Detection Rate	Precision	Recall	F-measure
86.0628	0.02876	0.71387	0.76749	0.9705	0.85712

After analyzing the Table 4, the prediction rates of the attacks from the attack class of R2L and U2R took our attention as the neural network could not give good results predicting them. Finding the performance measure results showed that the performance of the neural network is indeed not as good as expected.

Therefore, a cluster-based solution is proposed in this paper as the flow is showed in Fig. 5 with data distribution of the 4 clusters. Additionally, the analysis of the NSL-KDD data set showed that the number of data contained in the train and test sets based on the attack classes R2L and U2R are not appropriate for the learning process. For this reason, we used a shuffled dataset in our proposed approach. According to the proposed system's approach, the results are shown in Table 7.

TABLE VII
PREDICTION RESULTS OF THE PROPOSED SYSTEM ON THE TEST DATA

Data Label	Test Data	Correct Predictions	Incorrect Predictions	Prediction Rate(%)
Normal	15,376	15,233	143	99.07
DoS	10,779	10,742	37	99.66
Probe	2,751	2,741	10	99.64
R2L	754	696	58	92.31
U2R	44	36	8	81.82

To understand the detailed performance of the proposed system, the confusion matrixes of clusters are listed in Table 8.

TABLE VIII
THE NUMBER OF TP, TN, FP, AND FN FOR CLUSTERS

Cluster #	True Positives	True Negatives	False Positives	False Negatives
1	29	7518	3	1
2	619	3395	8	5
3	10975	918	35	64
4	3610	2388	97	39

Table 7 shows the data distribution of the 4 clusters. Analyzing the clusters shows that the distributions are generally biased towards either more to the attack types or to the normal data. This proves that the K-Means algorithm does cluster the data that have similar identities. Another representation of the distributions of the clusters is shown in Fig.6.

As can be seen from this Figure, clustering based approach mainly collects the data group according to its similarities with the clusters and to make classifications. Each cluster does not correspond to a specific type of attack. Cluster1 and Cluster4 mainly stores lots of Normal type requests, other types distributed to the related clusters according to their similarities. According to these results, the performance measures are found as shown in Table 9.

After calculating the performance measures, an average of 99.15 % accuracy scores is found which is shown in Table 9. In the field of IDSs, the false alarm rate is an important factor to determine the effectiveness of the system. In our results, the average false alarm rate is found to be as 0.02. The average precision and recall rates obtained by our system are 0.97 and 0.99, respectively. From these results, the average F-measure is found as 0.98.

TABLE IX
PERFORMANCE MEASURES FOR THE PROPOSED SYSTEM'S RESULTS

Cluster #	Accuracy %	False Alarm	Precision	Recall	F-measure
1	99.947	0.0003	0.9063	0.967	0.9355
2	99.677	0.0023	0.9872	0.992	0.9896
3	99.175	0.0381	0.9968	0.994	0.9942
4	97.783	0.0406	0.9738	0.989	0.9815
Avg	99.145	0.0203	0.9660	0.986	0.9752

Finally, the performance of the proposed system is compared according to the CPU and GPU performances. The used IDE platform, Tensorflow, enables the use of GPU power. Therefore, the performance comparison of both CPU and GPU is depicted in the Table 10. The computing power and related parameters of the used GPU/CUDA platform is depicted in Table 3. Currently there are betted computing power GPUs, in the use of the it is expected to increase the efficiency of the system.

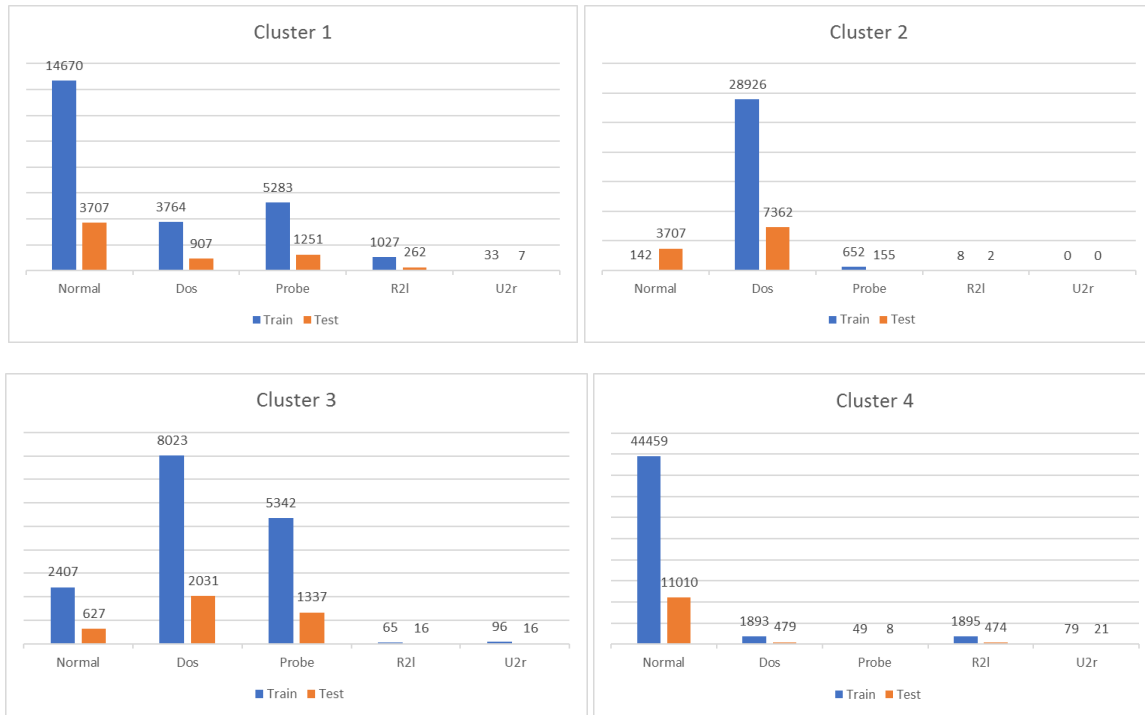


Fig.6. Data Distribution Across the 4 Clusters

TABLE X
TRAINING AND TESTING TIMES BASED ON CPU

Cluster #	GPU Time		CPU Time	
	Train	Test	Train	Test
1	31.659	0.0156	64.702	0.0158
2	21.016	0.0015	35.828	0.0015
3	59.438	0.0157	99.079	0.0159
4	37.879	0.0013	53.192	0.0014

According to these data, when comparing the GPU-Accelerated DNN times against CPU based DNN, an improvement can be seen. However, the performance improvement is also related with the design of the proposed Deep Learning approach. Therefore, if the level/complexity of the system increased, the performance improvement also enhanced.

V. CONCLUSION AND FUTURE WORK

In recent years, there is an increased number of computers and computing devices which are connected to the Internet and they are online with anytime and anywhere concept. As a result, there is a growing importance of the cybersecurity of not only single device but also networks. To prevent the anonymous attacks from both the outsiders and the insiders, firewalls and antiviruses cannot enable enough prevention. Therefore, some additional attack prevention and detection mechanisms are needed to be used.

In this paper, it is aimed to implement an Intrusion Detection System, which uses a deep neural network technology with Big Data for training the system. Although some previous works

prefer different static architecture such as rule based systems, a learning-based IDS system is aimed to develop. To diminish one of the important deficiencies of the use of the huge size of data, a parallel execution platform, as NVidia CUDA platform, is preferred. Additionally, to increase the accuracy rate of the system a clustered approach is preferred. The experimental results showed that the proposed system decreases the training time of the system with the use of CUDA platform and has a very good accuracy rate in the testing phase.

In the future work, it is aimed to use a modern updated dataset, with a bigger size of data. Additionally, there are new deep learning models that can be applied to Intrusion Detection Systems [22]. They can be also implemented for getting better accuracy rates.

REFERENCES

- [1] A. Borkar, A. Donode, and A. Kumari, "A survey on Intrusion Detection System (IDS) and Internal Intrusion Detection and protection system (IIDPS)," 2017 International Conference on Inventive Computing and Informatics (ICICI), Coimbatore, 2017, pp. 949-953.
- [2] S. Han, M. Xie, H. Chen and Y. Ling, "Intrusion Detection in Cyber-Physical Systems: Techniques and Challenges," in IEEE Systems Journal, vol. 8, no. 4, pp. 1052-1062, Dec. 2014. doi: 10.1109/JSYST.2013.2257594
- [3] L. Haripriya and M. A. Jabbar, "Role of Machine Learning in Intrusion Detection System: Review," 2018 Second International Conference on Electronics, Communication and Aerospace Technology (ICECA), Coimbatore, 2018, pp. 925-929.
- [4] E. Aydemir, "Weka ile Yapay Zekâ", Seekin, p:216, July 2018
- [5] P. I. Radoglou-Grammatikis and P. G. Sarigiannidis, "Securing the Smart Grid: A Comprehensive Compilation of Intrusion Detection and Prevention Systems," in IEEE Access, vol. 7, pp. 46595-46620, 2019. doi: 10.1109/ACCESS.2019.2909807
- [6] F. Farahnakian and J. Heikkonen, "A deep auto-encoder based approach for intrusion detection system," in Advanced Communication

- Technology (ICACT), 2018 20th International Conference on. IEEE, 2018, pp. 178–183.
- [7] E.H. Spafford, D. Zamboni, "Intrusion Detection Using Autonomous Agents. Computer Networks", The International Journal of Computer and Telecommunications Networking 34 (4), 547–570 (2000)
- [8] H. Sagha, S. B. Shouraki, H. Khasteh and M. Dehghani, "Real-Time IDS Using Reinforcement Learning," 2008 Second International Symposium on Intelligent Information Technology Application, Shanghai, 2008, pp. 593-597. doi: 10.1109/IITA.2008.512
- [9] M. A. Jabbar and S. Samreen, "Intelligent network intrusion detection using alternating decision trees," 2016 International Conference on Circuits, Controls, Communications and Computing (I4C), Bangalore, 2016, pp. 1-6. doi: 10.1109/CIMCA.2016.8053265
- [10] A. S. Desai and D. P. Gaikwad, "Real time hybrid intrusion detection system using signature matching algorithm and fuzzy-GA," 2016 IEEE International Conference on Advances in Electronics, Communication and Computer Technology (ICAECCT), Pune, 2016, pp. 291-294.
- [11] O. Can and O. K. Sahingoz, "An intrusion detection system based on neural network," 2015 23rd Signal Processing and Communications Applications Conference (SIU), Malatya, 2015, pp. 2302-2305. doi: 10.1109/SIU.2015.7130338
- [12] G. Karatas and O. K. Sahingoz, "Neural network based intrusion detection systems with different training functions," 2018 6th International Symposium on Digital Forensic and Security (ISDFS), Antalya, 2018, pp. 1-6. doi: 10.1109/ISDFS.2018.8355327
- [13] C.F. Tsai, Y.F. Hsu, C.-Y. Lin, W.-Y. Lin, "Intrusion detection by machine learning: A review", Expert Systems with Applications, 2009, vol. 36, no. 10, pp. 11994-120000.
- [14] W.C. Lin, S.W. Ke, C.F. Tsai, "CANN: An Intrusion Detection System Based on Combining Cluster Centers and Nearest Neighbors", Knowledge-Based Systems, 2015, vol. 78, pp. 13-21.
- [15] Z. Elkhadir, K. Chougali and M. Benattou, "Intrusion Detection System Using PCA and Kernel PCA Methods", In: El Oualkadi A., Choubani F., El Moussati A. (eds) Proceedings of the Mediterranean Conference on Information & Communication Technologies 2015. Lecture Notes in Electrical Engineering, vol. 381, Springer.
- [16] N. Paulauskas and J. Auskalis, "Analysis of Data Pre-Processing Influence on Intrusion Detection Using NSL-KDD Dataset", 2017 Open Conference of Electrical, Electronic and Information Sciences (eStream), 2017, Vilnius, pp. 1-5.
- [17] D. Tanikić and V. Despotovic, "Artificial Intelligence Techniques for Modelling of Temperature in the Metal Cutting Process", 2012, Metallurgy, Yogiraj Pardhi, IntechOpen, DOI 10.5772/47850
- [18] T. Velmurugan and T. Santhanam, "Performance Evaluation of K-Means and Fuzzy C-Means Clustering Algorithms for Statistical Distributions of Input Data Points" European Journal of Scientific Research, vol. 46, no. 3, pp. 320-330, 2010.
- [19] A. Singh, A. Yadav & A. Rana, "K-means with Three Different Distance Metrics", International Journal of Computer Applications, 2013, vol. 67, no. 10, pp. 13-17.
- [20] A.K. Jain, "Data clustering: 50 years beyond K-means", Pattern Recognition Letters, 2010, vol. 31, no. 8, pp. 651-666.
- [21] D. Y. Mahmood, M. A. Hussein, "Feature Based Unsupervised Intrusion Detection", International Journal of Computer and Information Engineering, 2014, vol. 8, no. 9, pp. 1665-1669.
- [22] G. Karatas, O. Demir and O. K. Sahingoz, "Deep Learning in Intrusion Detection Systems," 2018 International Congress on Big Data, Deep Learning and Fighting Cyber Terrorism (IBIGDELFT), Ankara, Turkey, 2018, pp. 113-116. doi: 10.1109/IBIGDELFT.2018.8625278

BIOGRAPHIES



BUMINHAN REIS received the B.S. degree in Computer Engineering from Istanbul Kultur University in 2018. He has been studying foreign languages (Chinese) from that time. His research interests are machine learning, computer security and software engineering.



SAMI BERK KAYA received the B.S. degree in Computer Engineering from Istanbul Kultur University. He worked as software developer and analyst and currently he has been working in BEEBOT software company since 2018. His research interests are big data processing, machine learning, computer security and software engineering.



OZGUR KORAY SAHINGOZ received the B.S. degree from the Computer Engineering Department of Bogaziçi University in 1993 and M.S. and PhD degrees in Computer Engineering Department of Istanbul Technical University in 1998 and 2006 respectively. He is currently working as an Associate Professor in the Computer Engineering Department of Istanbul Kultur University. He is the author of more than 95 papers and he is still working in two research projects. His research interests include artificial intelligence, machine/deep learning, data science, software engineering and UAV Networking.

Comparing of K-Means, K-Medodis and Fuzzy C-means Cluster Method for Analog Modulation Recognition

Y. KAYA, D. AVCI and M. GEDİKPINAR

Abstract—A modulation process is required to transmit analog signals with higher quality. Modulation is the process of transporting the signal by another carrier signal. This study aims to process analog signals. Using 200 samples of each of the six types of analog modulation modules. Nowadays these are Amplitude Modulation (AM), Double Side Band (DSB), Upper Side Band (USB), Lower Side Band (LSB), Frequency Modulation (FM) and Phase Modulation(PM) respectively. In the study an intelligent clustering method has been developed. The 5th level Discrete Wavelet Transform (DWT), Norm Entropy and Energy properties of AM, DSB, USB, LSB, FM and PM analog modulated signals have been removed during feature extraction phase. The results have been compared using K-Means, K-medoid and Fuzzy C-means (FCM) algorithms using a feature vector of 6x2x1200 obtained at the feature extraction stage and carrying out smart intelligent clustering for recognition. The most successful result has been obtained with FCM of 85.75%.


Index Terms —Analog modulation, wavelet transform, entropy, energy, K- Means, K-medoid, Fuzzy C-means

I. INTRODUCTION


THE INFORMATION to be used in communication is not used where it is produced. Information may need to be moved to different locations. This distance may also near or far distances. The information / signals produced are produced as low frequency. Low-frequency information is difficult to transport. Therefore, it uses high frequencies to carry this signal. The process of transmitting a low frequency.

Low-frequency information is difficult to transport. Therefore, it uses high frequencies to carry this signal. The process of transmitting a low frequency information from one place to another with a high frequency signal is called modulation. Information signal is moved by modulation of amplitude, phase and frequency of carrier signal by modulation [1]. The aim of this study is to select the appropriate method for the healthy transport and processing of analog signals. Also, using real human audio signals, a carrier-clustered intelligent clustering method has been developed for recognition using 200 samples from each of 6 kinds of analog modulation types. K-averages, K-medoid and Fuzzy C Averages (FCM) algorithms for the identification of the carrier with a clustered smart comparison was compared. Some of the previous modulation studies related to this field are given below. Erdem Yakut S. has formed an intelligent system for the purpose of analog modulation recognition. In the developed smart system, Wavelet Transform (WT), Artificial Neural Networks (ANN) have used Adaptive Network Based Fuzzy Inference System[2]. Guldemir, H. et al. have used 5 kinds of modulation (Amplitude Modulation, Double Side Band Modulation, Frequency Modulation, Upper Single Band Modulation, Lower Single Band Modulation) for clustering process. They compared performance using K-means, Fuzzy C-means, Mountain and Subtractive clustering methods [3]. Avci, E., made a strong feature in order to classify the targets created by the radar correctly. He used pattern recognition methods to accomplish this purpose. These analyzes were evaluated by integrated feature extraction methods [4]. Sengür, A. et al. have performed the modulation recognition process using Bayes decision rule method to classify analog modulated communication signals [5]. Fidan S. modeled electromagnetic waves emitted in a waveguide by wavelet transform. In study, he placed a wavelet transform filter and a reverse wavelet transform filter, respectively, at the beginning and the end of a waveguide. Thus, it has been shown that solutions can be produced with the desired accuracy by comparing the values obtained for the wavelet types [6]. Demren, E., aimed at the processing of signals with sudden changes in signals and static components. In order to achieve this, he examined a signal processing method to examine high frequency resolution and high time resolution together. In this study, “Wavelet Transformations”, another method of frequency-time analysis, has been investigated. In this study, the applicability of automotive, noise and vibration signals has been studied through examples [7]. Işık, M., has compared


YUSUF KAYA, is with Department of Institute of Science and Technology Firat University, Elazığ, Turkey, (e-mail: yucufkaya23@gmail.com).

 <https://orcid.org/0000-0003-2404-1678>

DERYA AVCI, is with Department of Computer Technology Firat University, Elazığ, Turkey, (e-mail: davci@firat.edu).

 <https://orcid.org/0000-0002-5204-0501>

MEHMET GEDİKPINAR, is with Department of Electrical and Electronics Engineering Firat University, Elazığ, Turkey, (e-mail: mgedikpinar@firat.edu).

 <https://orcid.org/0000-0002-1045-7384>

Manuscript received May 14, 2019; accepted June 6, 2019.

DOI: [10.17694/bajece.564960](https://doi.org/10.17694/bajece.564960)

the performance of algorithms by performing various tests on synthetic and real data sets by using partitioned clustering methods [8].

II. MATERIAL AND METHOD

In this study, using 200 samples from each of 6 types of analog modulation using human audio signals, a carrier-specific intelligent clustering method has been developed for recognition. The study consists of two stages as feature extraction and clustering. In the feature subtraction phase of the study, distinguishing features of the study by using Level 5 Discrete Wavelet Transform (DWT), energy and entropy methods have been determined. Using the feature vector obtained in the feature subtraction stage, K-averages, K-medoid and Fuzzy C Averages (FCM) algorithms have been used to perform intelligent clustering.

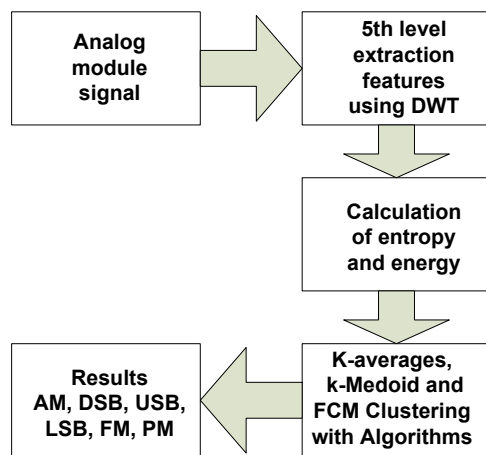


Fig. 1. Flow Diagram of the System Used

A. Discrete Wavelet Transform (DWT)

Discrete Wavelet Transform (DWT) is used to better analyze markers. DWT uses a narrower windowing dimension in the wider and low-frequency sections in high-frequency sections [6]. Distinguishes DWT from other conventional modulation recognition methods is the use of different windowing techniques [9]. Thus, the windows to be created for the transmission of the signal, where the frequency information, the window wide and also where the time zone is important window areas may be preferred. In this way, the time information of the transmitted signals is also visible. DWTs allow these non-stationary signals to be carried [10]. DWTs are used in applications such as astronomy, fingerprint verification, geophysics, internet traffic regulation, meteorology, computer graphics analysis, speech recognition [11]. With ADD, two signs called Approximate (A) and Details (D) are created. A sign is composed of wide time - low frequency and B is narrow time - high frequency. Figure 2 shows a simple block diagram of DWT.

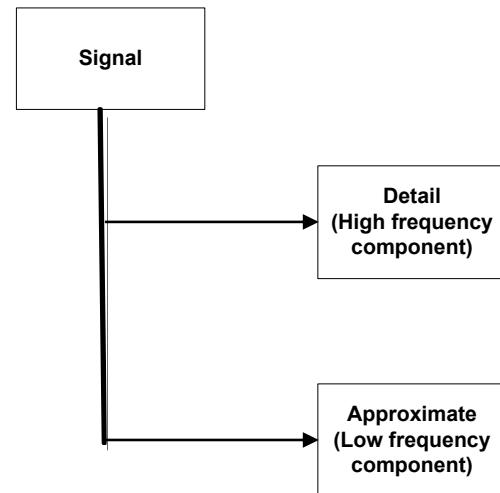


Fig. 2. DWT Simple Block Diagram

B. Entropy

The concept of entropy was first used by American scientist Claude Shannon in 1948 as part of the theory of probability and knowledge [12]. Entropy can be defined as randomness, irregularity or uncertainty in a system, if it is expressed in a comprehensive manner. Different entropy calculation techniques are used in signal processing field. Some of those; Shannon, Norm, Threshold and Logarithmic Energy methods. In the signal processing, if the sign is stationary, it has a low spectrum with a low spectrum in the frequency region. If the opposite sign is not stationary, the frequency spectrum is spread over a wide band and causes a large entropy value [13].

C. K-Means

K-means (KM), one of the first clustering methods, was proposed by Hugo Steinhaus in 1957. In 1967, this method was developed by J.B. by MacQueen [14].

It is defined as one of the learning methods without training. Once clustering with KM, objects most similar to each other are placed in the same set around a center. This placement is based on the distance of the objects to each other. Since each object will be in a group after KM, there is a noticeable difference between the groups. The determination of k points by a sample k-means clustering method and the clustering steps of the units are shown in Figure 3 [15],[16].

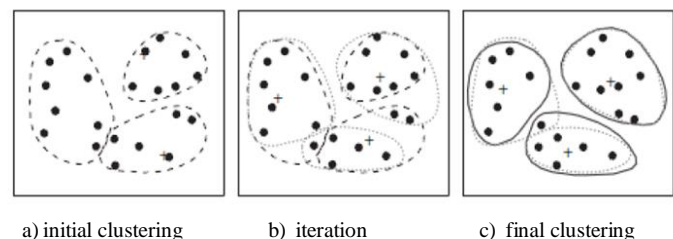


Fig. 3. Random Clustering of K

D. K-medoids

With the s , the medoid is taken instead of the midpoint of the cluster. Medoid refers to the data in the center of the cluster to be created. K-medoids consist of k -set and n -data. The number of k sets is determined by the user. According to the data at the specified k -points, the other n -data are assigned to clusters that are close to them [17]. The cluster center and the midpoint can vary considerably with new data to be included in the central point of clustering with KM. However, if large data is included in the system, the processes may be extended in this method. A clustering with K-medoids is as shown in Figure 4. The cluster is used as one of the central data [18].

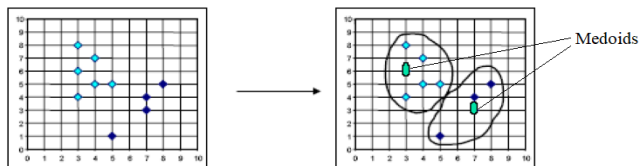


Fig. 4. Clustering with K-medoids

E. Fuzzy C-means

FCM was first proposed by Dunn in 1973. Performs clustering using fuzzy logic [19]. In classical clustering methods, each data must belong to a set and the data must be expressed as data "0" or "1". However, FCM transactions can also take any value that includes "0-1" range. When clustering with FCM, each data does not have to belong to a cluster. The sum of the value of each data belonging to all clusters should be "1" [20]. A clustering with classical clustering and comparison of the clustering with FCM is given in Figure 5. In Figure 5, H1 and H2 are classical clustering, F1 and F2 are clustering with FCM [21].

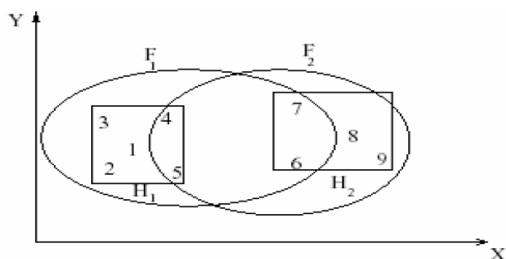


Fig. 5. Clustering with Classic Clustering and FCM

When the FCM is clustered with the FCM algorithm, the first data value is randomly assigned. Using these values, the location of the cluster center is determined with the help of iterative updates. FCM assigns the data to the group that is close to "1" according to the membership degree. FCM has advantages such as facilitates recognition of ambiguous situations, high ability to find overlapping clusters, a flexible structure, and little impact on noise [22].

III. APPLICATION

The actual audio signal is used as an information signal for use in the application. Generally, 6 types of analog modulation are used, including Amplitude Modulation (AM), Double Side Tape (DSB), Upper Side Band (USB), Lower Side Tape (LSB), Frequency Modulation (FM), Phase Modulation (PM). With the aim of recognizing by using 200 samples from each of the said modulation types, carrier-based intelligent clustering method has been developed. In order to obtain the signals with analog modulated, Gaussian white noise has been added to the signal between 0 - 70 dB S(Signal) / N (Noise) and 20 signals have been generated from each modulation type. The starting angle and modulation index (m) of the 20 signals created by adding the noise have been changed to 200 modal signs for each modulation type. DWT uses a narrower windowing dimension in the high-frequency sections and in the larger low-frequency sections to better analyze the signals. In the wavelet transform, there are two types of signs: Detail (D) and Approximate (A). In this study, the additive obtained from the 5th level decomposition of the wavelet transform is used. The 5-level decomposition of DWT has been used for feature extraction because the best value of the signal has been found to be Level 5 according to Entropy measurement. Since 5 level decomposition of DWT is taken, 6 signatures have been formed including 5 "D" and 1 "A" sign. Norm entropy and Energy values of each of these signals have been calculated and the feature has been removed for each signal. 6 (the number of DWT features of each modulated signal) X 2 (Norm entropy and number of energy properties of each modulated signal) X 6 (modulation type) x 200 (number of samples used for each modulation type) dimension vector has been obtained. By using the obtained feature vector, it has been carried out intelligent clustering with carrier to recognize by KM, K-medoid and FCM Algorithms. MATLAB 2018 software has been used in this study [23]. The pseudo-code representation of the processing steps used in the application is as follows:

Step 1: To make the Analog signals to be decomposed to create a more complex structure by adding noise in the range of 0-70 db to the signal to be separated,

Step 2: To increase the data set, replicate the signals by changing the initial angle and modulation index (m) of the signal,

Step 3: To feature extraction the 5-level decomposition of DWT and energy-entropy values to increase the number of attributes,

Step 4: Performing Clustering with the Removed feature vector.

A. Distinctive Features Extraction

In this study, in the 5th level division of the DWT, there are 5 Detail (D), 1 Approximate (A). 6 signals have been created. Norm entropy and Energy values of each of these signals have been calculated and the property has been omitted for each sign. 6 (the number of DWT features of each modulated signal) X 2 (Norm entropy and number of energy properties of each modulated signal) X 6 (modulation type) x 200 (number of

samples used for each modulation type) dimension vector has been obtained. 5 Detail (D) and 1 Approximate (A) signals have been obtained from each of the modulation signals used. Figure 6 shows the structure of the 5 level wavelet transform.

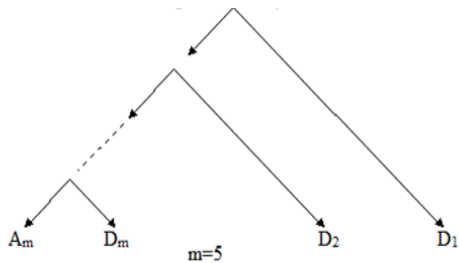


Fig. 6. Structure of 5th Level Wavelet Transform

B. Recognition of Modulation Type by Clustering Methods

Using the 6x2x1200 feature vector obtained in the feature subtraction phase, intelligent clustering with carrier has been performed for recognition by K-means, K-medoids and FCM

algorithms. For the K-means clustering method in Table 1, for the K-medoids clustering method in Table 2, for the FCM

clustering method in Table 3 show the confusion matrix The values in the row and column in the same row in the confusion matrix indicate that the clustering is done correctly, and that the different queues indicate clustering. For example, in Table 1, the intersection value of AM in the row with AM and 174 of the AM modulation were correct, AM was clustered as AM. AM states that 6, 6 AM at the intersection of the DSB are incorrectly clustered as the DSB. AM states that 5, AM at the intersection of the USB are incorrectly clustered as the USB. AM states that 7, 7 AM at the intersection of the LSB are incorrectly clustered as the LSB. AM states that 3, 3 AM at the intersection of the FM are incorrectly clustered as the FM. Since 5 PM states that are incorrectly clustered.

TABLE I
K-MEANS CONFUSION MATRIX FOR CLUSTERING METHOD

Modulation Type	AM	DSB	USB	LSB	FM	PM	Total Success
AM	174	6	5	7	3	5	%87
DSB	6	169	7	6	5	7	%84.5
USB	7	5	173	3	5	7	%86.5
LSB	8	5	7	165	7	8	%82.5
FM	2	6	4	3	170	5	%85
PM	3	5	6	4	4	168	%84
Average Performance							%84.916

TABLE II
K-MEDDOIDS CONFUSION MATRIX FOR CLUSTERING METHOD

Modulation Type	AM	DSB	USB	LSB	FM	PM	Total Success
AM	173	5	6	4	7	5	%86.5
DSB	4	176	3	6	5	6	%88
USB	6	7	166	7	6	8	%83
LSB	5	4	6	171	7	8	%85.5
FM	8	7	5	8	166	6	%83
PM	6	5	6	7	3	173	%86.5
Average Performance							%85.416

TABLE III
FCM CONFUSION MATRIX FOR CLUSTERING METHOD

Modulation Type	AM	DSB	USB	LSB	FM	PM	Total Success
AM	175	4	6	7	3	5	%87.5
DSB	8	167	7	6	7	5	%83.5
USB	5	7	169	6	7	6	%84.5
LSB	4	5	6	173	6	7	%86.5
FM	5	3	6	5	175	6	%87.5
PM	4	3	6	3	4	170	%85
Average Performance							%85.75

IV. RESULT CONCLUSION

Carrier intelligent clustering method is developed for recognition using 200 samples from each of 6 kinds of analog modulation types including AM, DSB, USB, LSB, FM, PM and 6x200 samples have been used in this method. The feature vector of 6x2x1200 has been used in the feature extraction stage. Table 1, Table 2 and Table 3 have been formed with the obtained data. The results obtained from the tables have been

analyzed and 84.916% for the K-means clustering method, 85.416% for the K-medoids clustering method and 85.75% for the FCM clustering method. As a result, 85.75% of the best performance has been found to belong to the FCM clustering method. Afterwards, different modulation types and different clustering algorithms can be used in the studies to be carried out.

REFERENCE

- [1] <https://slideplayer.biz.tr/slide/2683446> [Access: 23-Sep-2018]
- [2] S. Erdem Yakut. "An intelligent classification system based on wavelet transform in analog modulations." M.Sc. Thesis, F.Ü. Graduate School of Natural and Applied Sciences, Elazığ, 2007.
- [3] H. Guldemir, A. Sengur. "Comparison of clustering algorithms for analog modulation classification." Expert Systems with Applications, 30(4), 642-649K. Elissa, 2006.
- [4] E. Avcı. "Intelligent radar target recognition system." Ph.D. Thesis, F.Ü. Graduate School of Natural and Applied Sciences, Elazığ, 2005.
- [5] A.Şengür, İ.Türkoğlu. "Classifying Analogue Modulated Communication Signals Using Bayes Decision Criterion." Sakarya University Journal of Science, Vol.7, No.3, 2003, pp. 32-36.
- [6] S. Fidan. "Modeling of the electromagnetic wave emitted in the waveguide by wavelet transformation." M.Sc. Institute of Science and Technology, Ankara, 2006.
- [7] E. Demren. "Comparison of wavelet transform with fourier transform and its application." MS Thesis, İ.T.Ü. Institute of Science and Technology, İstanbul, 2015.
- [8] M. Işık. "Data mining applications with partitioned clustering methods." M.Sc. Institute of Science and Technology, İstanbul, 2016.
- [9] H. Polat, M. Akin, and M.S. Özerdem. "The comparison of wavelet and empirical mode decomposition method in prediction of sleep stages from EEG signals." In Artificial Intelligence and Data Processing Symposium (IDAP), 2017 International (pp. 1-5). IEEE.
- [10] E. Avcı, İ. Türkoğlu and M. Poyraz. "Intelligent Target Recognition Based on Wavelet Adaptive Network Based Fuzzy Inference System." Lecture Notes in Computer Science, Springer-Verlag, 3522, 594-601, 2005.
- [11] Ö. Arslan. "Investigating the most appropriate main wavelet function for Turkish phonemes." M.Sc. Institute of Science and Technology, İzmir. Gray, R. M., Entropy and information. In Entropy and Information Theory, Publisher: Springer, (pp. 21-55) New York, ISBN-13: 978-1441979698, 2014
- [12] R.R. Coifman, M.V. Wickerhauser. "Entropy based algorithms for best basis selection." IEEE Transaction on Information Theory, 38, 2, 713-718, 1992].
- [13] A. Çokgüngördü. "Base stations with the help of clustering method, using the assisted site." M.Sc. Institute of Science and Technology, İstanbul, 2017.
- [14] S. Atal. "Fuzzy clustering analysis and clustering of OECD countries in terms of development." Master Thesis, O.G.Ü. Graduate School of Natural and Applied Sciences, Eskişehir, 2015.
- [15] İ. Ş. İ. K. Meltem, A.Y. Çamurcu. "K-Means, K-Medoids Ve Bulanık C-Means Algoritmalarının Uygulamalı Olarak Performanslarının Tespiti." İstanbul Ticaret Üniversitesi Fen Bilimleri Dergisi, Vol.6, No11, 2007, pp.31-45.
- [16] B. Çağlar. "Evaluation of spatial data by clustering analysis." Master Thesis, N.E.Ü. Institute of Science and Technology, Konya, 2018.
- [17] S. Kırmızıgül Çalışkan. "K.KNN: detection of penetration in networks by clustering and closest neighboring method." Master Thesis, G.Y.T.E. Institute of Engineering and Science, Gebze, 2008.
- [18] O. Taşova. "Face recognition with artificial neural networks." MS Thesis, D.E.Ü. Institute of Science and Technology, İzmir, 2011.
- [19] K. Eset. "Investigation of segmentation methods in lung pet images" M.Sc. Institute of Science and Technology, Kayseri, 2016.
- [20] A.T. Alper. "Analog communication, Lecture Notes." M.Ü. Faculty of Engineering, Mersin, 2010.
- [21] A. Saygılı, "S. Albayrak. Meniscus segmentation and tear detection in the knee MR images by fuzzy c-means method." In 2017 IEEE International Conference on Signal Processing and Communications Applications Conference (SIU), IEEE, 2017. <https://doi.org/10.1109/SIU.2017.7960183>
- [22] Aydemir, E. "Weka ile Yapay Zeka", Secgin Yayınevi, 2018
- [23] MATLAB Company, 2018

BIOGRAPHIES



Yusuf KAYA – He was born in 1974 in Elazığ.

He completed his primary, secondary and high school education in Elazığ. In 1992, he graduated from Marmara University Faculty of Technical Education, Department of Electrical Education and graduated in 1996. He was appointed as a teacher of electricity to Afyonkarahisar by the Ministry of National Education. He is still performing this duty at Gazi Vocational and Technical Anatolian High School in Elazığ. He is master student in Firat University.



Derya AVCI– She was born in Malatya Turkey. She

received a master's degree from Firat University Electronic and Computer Education. She received Ph.D. degree from Firat University Electrical and Electronic Engineering. Her interesting areas are pattern recognition, image processing, intelligent systems, artificial intelligence systems.



Mehmet GEDIKPINAR- He received the BS degree from the Department of Electrical Education, Gazi University, the MSc degree from Institute of Science and Technology, Firat University, the PhD degree from Institute of Science and Technology,

Gazi University respectively. His research interests include intelligent control, electrical machines and designing, electronic instruments and measurements, analyzing of circuit.

Analysis and Suppressing Speed Fluctuations in Brushless DC Motors

M. Reşit ÇORAPSIZ, H. KAHVECİ and M. Fatih ÇORAPSIZ


Abstract—The fluctuations in both speed and torque magnitudes during operation are among the major disadvantages of brushless DC motors. These fluctuations occur due to both the commutation of the inverter switches and the phase winding inductances. This case can lead to major problems, especially in applications which are required constant speed and constant torque. In this work, it was aimed to reduce speed fluctuations that occur in brushless DC motors. Firstly, the simulation model was created by using the dynamic equations of the brushless DC motor. Secondly, a region selective circuit was designed for use in commutation regions. Finally, the commutation signals were generated from the magnitude of the torque produced by the motor. Consequently, the proposed technique was controlled under different speed conditions and was shown that the speed fluctuations can be reduced without the difficult calculations of the commutation time. According to the results obtained, it was observed that the speed fluctuations were significantly reduced.

Index Terms—BLDC Motor (BLDCM), Commutation, Reduction of Speed Fluctuation, DC Link Voltage Control, MATLAB/Simulink.


I. INTRODUCTION

IN RECENT YEARS, Brushless DC motor has started to be used frequently in many motion source applications. These motors are used to convert electrical energy into mechanical energy or to transfer energy as in other electric motors. These motors have a wide range of applications such as electric


MUHAMMED REŞİT ÇORAPSIZ, is with Department of Electric and Energy, Bayburt University, Bayburt, Turkey, (e-mail: rcorapsiz@bayburt.edu.tr).

 <https://orcid.org/0000-0001-5477-5299>

MUHAMMED FATİH ÇORAPSIZ, is with Department of Electrical-Electronics Engineering of Atatürk University, Erzurum, Turkey, (e-mail: corapsiz@atauni.edu.tr).

 <https://orcid.org/0000-0001-5692-8367>

HAKAN KAHVECİ, is with Department of Electrical-Electronics Engineering of Karadeniz Technical University, Trabzon, Turkey, (e-mail: hknhahveci@ktu.edu.tr).

 <https://orcid.org/0000-0001-9369-2330>

Manuscript received May 24, 2019; accepted July 9, 2019.

DOI: [10.17694/bajece.569774](https://doi.org/10.17694/bajece.569774)

vehicles, aerospace, space technologies and medical fields and have a number of advantages compared to DC and AC motors. The main advantages of using BLDC motors are high power efficiency, less noise, higher torque according to the weight/inertia ratio and higher speed. Besides these motors can be both manufactured in various sizes and easy controlled [1]. In addition, since BLDC motors do not have brushes and collectors that require extra equipment and increase friction factor, they need less maintenance, no arc is generated during operation, and have a longer life compared to DC motors. In spite of these advantages, the use of sensors in various structures to determine the rotor position in order for the BLDC motor to require an inverter and to control this inverter constitutes a disadvantage in terms of cost [2]. With the development of power electronic components, BLDCM has shown a very rapidly development. The major disadvantage of these motors is the fluctuations in torque, current and velocity in commutation intervals. The commutation operation on the BLDC motor is carried out electronically via an inverter. Since the currents of the phase windings change during the commutation process, the fluctuations in the phase currents are also seen in the torque and velocity magnitudes. These fluctuations are caused by the fact that the switches in the inverter are electrically change position in the direction of the information they receive from a hall effect sensor at every 60 degrees.

There are studies in the literature on the reduction of torque ripples rather than speed fluctuations. For example, a new DC link voltage control strategy was proposed with the SEPIC converter to equalize the slopes of the incoming and outgoing phase currents during the commutation and adjust the desired DC link voltage in order to reduce the torque fluctuations at both low and high speeds [3]. In [4], the modified SEPIC converter and diode clamped multilevel inverter (DCMLI) were used for the torque ripple reduction. With this study, both noise problems were reduced and higher yield was obtained from brushless DC motor. In [5], two different current control methods were used to reduce the torque ripples caused by the phase commutation. These methods; control of source current and control of the phase currents of the motor. These two control methods were compared and it was observed that the control of the phase currents is more effective. In order to keep constant of the non-conducting phase current, a region selective circuit was designed with a new switching technique and applied to the BLDCM at the commutation time, both the commutation times were analyzed and the CUK converter was used to obtain the desired voltage value at the time of commutation [6]. In [7], in order to reduce

the torque ripples in the commutation times, it was carried out by using a single current sensor, it was aimed to balance the current slopes of the incoming and outgoing phase currents with a suitable switching method. With this method, decreases and increases in the phase currents and output torque have been eliminated. In [8], a new PWM technique has been performed to keep both the non-commutation phase current constant and shorter the commutation time. This technique was applied to the non-commutation phase at commutation times and has been yielded very efficient results. In [9], a new current control method has been proposed in order to reduce the ripples in the conducting and commutation regions for Brushless DC motor with non-ideal back electromotive force (EMF). With this method, they were use both the calculation of the commutation times and the pulse width modulation (PWM) to disable the free-wheeling diode (FWD) in the inactive phase. In [10], has been designed a detailed current stabilization method and a commutation timer, both theoretical and experimental, which are highly effective in reducing both the commutation torque ripples and the determination of the commutation endpoint. In [11], has been proposed to reduce the torque ripples in brushless DC motor from the nominal speed to the moment of stopping and the effectiveness of the presented technique was analyzed in detail with theoretical and experimental results.

In this study, it was aimed to decrease the speed fluctuations occurring during the operation at the commutation intervals of the BLDC motor. Two different DC link voltages were used to perform this operation. The first one is for conduction regions and the second for commutation regions. In order to determine the commutation intervals, the relationship between the torque constant of the motor and the desired torque magnitude was calculated. When the results obtained were compared with the conventional BLDC speed control, it was observed that the fluctuations in the rotor speed were significantly suppressed.

II. ANALYSIS OF SPEED FLUCTUATION IN BRUSHLESS DC MOTOR

The equivalent circuit for the BLDCM drive system with three-phase symmetrical stator winding is shown in Fig.1.

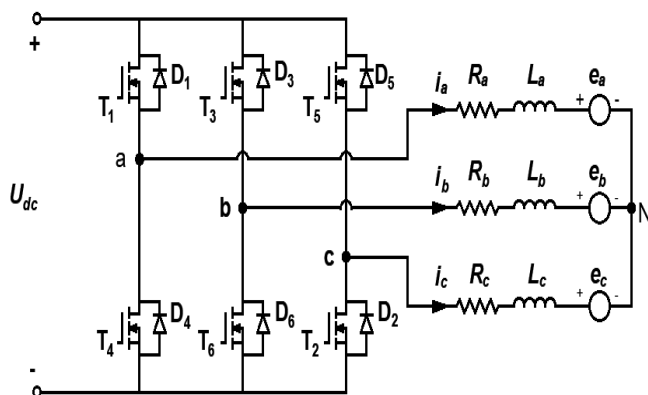


Fig. 1 Equivalent circuit for BLDC motor drive

As can be seen from Fig.1, a three-phase, two-level inverter was used for BLDCM in this study. All of the switches in the inverter was designed with power MOSFETs. Since

MOSFETs do not have the ability to block the voltage in the opposite direction, the anti-parallel free-wheeling diodes were connected to the switches. These diodes were used to reset the current which induced in the windings of the phase outgoing from the conduction. In this case, are occurs ripples on the speed, current and torque magnitude of the BLDC motor. In addition, in BLDC motors, the current of each phase is carried out in a finite current transfer process depending on the rotor speed. During this process, when the current ends in one phase and starts in the other phase, the ripples occurs due to the phase winding inductances. These ripples are mainly caused by the switching of the inverter, the non-ideal trapezoidal back EMFs and the commutations of the currents that are incoming and outgoing pahse. The ripples occuring due to the switching can be accomplished by adjusting the rotor inertia during the mechanical design of the brushless DC motor. But the commutation torque ripples, affects the motor performance at greater intensity and amplitude [12].

When the Kirchoff Voltage Law is applied to each phase separately in the BLDCM equivalent circuit in Fig.1, the three phase terminal voltages can be expressed as follows;

$$\begin{aligned} u_a &= R_a i_a + L_a \frac{di_a}{dt} + e_a + u_N \\ u_b &= R_b i_b + L_b \frac{di_b}{dt} + e_b + u_N \\ u_c &= R_c i_c + L_c \frac{di_c}{dt} + e_c + u_N \end{aligned} \quad (1)$$

The back EMFs waveforms, the phase winding currents waveforms and the produced torque waveforms of the BLDC motor were shown in Fig.2. The areas where the commutation process made are indicated by dashed lines. In Fig.2, although the currents of the phase windings and the produced torque are constant, these outputs are not exactly constant due to the inductance of the stator windings [13]. Usually three-phase BLDC motor has two operating regions. These regions are referred to as conduction region and commutation region. In the conduction region, the two phase determined by the rotor position is conducting and the other phase is in isolation. In the commutation region, the current of one phase remains constant and the current transfer was realized between other two phases. In addition, each of the three phases (incoming phase, outgoing phase and non-commutation phase) are conducting at the commutation region [14]. It can be assumed that BLDC motor works like a normal DC motor at the conduction region and as a three phase AC motor at the commutation region. In view of this situation, torque ripples can be eliminated in commutation regions by coordinate transformation theory used in AC motor control [15]. If these two regions are compared on time basis, the duration of the commutation region is considerably shorter than the duration of the conduction region. The above described studies can be performed for inverters with both 120 and 180-degree conduction mode. In this study, we have used a 120-degree conduction mode. In the 120-degree conduction mode, during one electrically period, the upper group and lower group switches of the inverter are conduction each 120-degree.

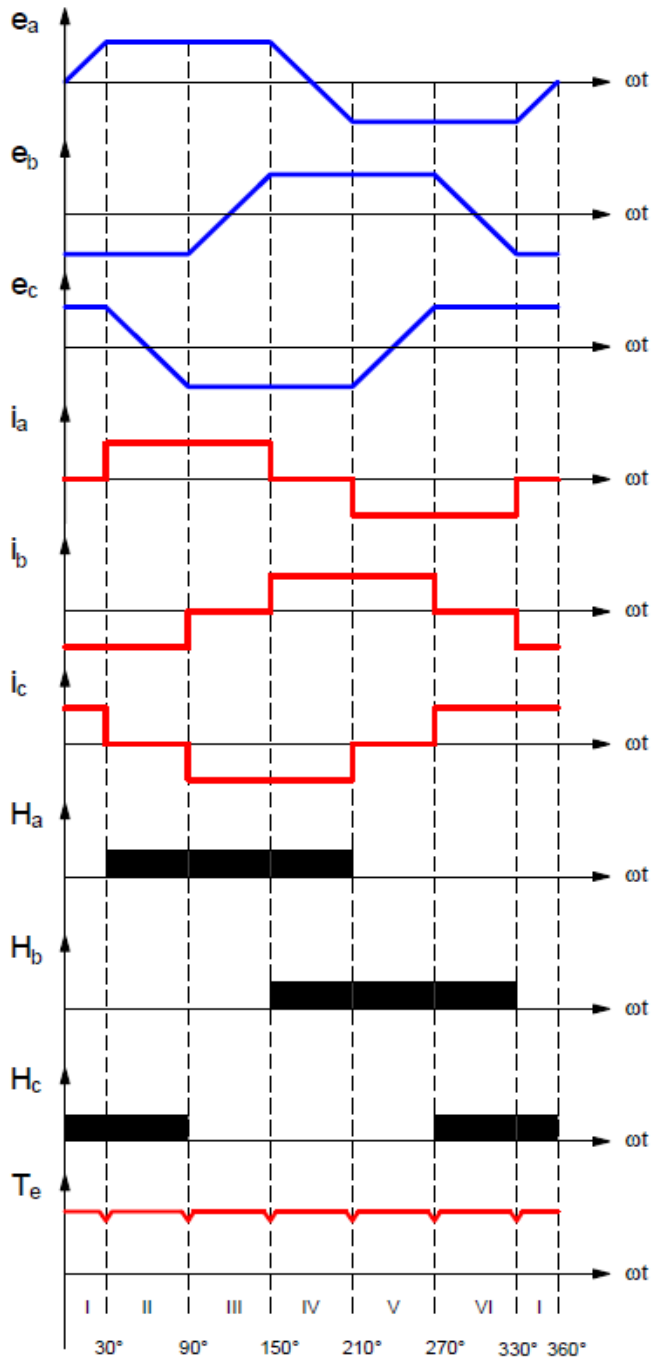


Fig. 2 The back EMFs, the phase winding currents, Hall sensor signal and the produced torque waveforms of the BLDCM

Assuming $R_a=R_b=R_c=R$ and $L_a=L_b=L_c=L$ then the mathematical model of BLDC motor from Eq. (1) can be obtained as follows;

$$\begin{bmatrix} u_a \\ u_b \\ u_c \end{bmatrix} = \begin{bmatrix} R & 0 & 0 \\ 0 & R & 0 \\ 0 & 0 & R \end{bmatrix} \begin{bmatrix} i_a \\ i_b \\ i_c \end{bmatrix} + \begin{bmatrix} L & 0 & 0 \\ 0 & L & 0 \\ 0 & 0 & L \end{bmatrix} \frac{d}{dt} \begin{bmatrix} i_a \\ i_b \\ i_c \end{bmatrix} + \begin{bmatrix} e_a \\ e_b \\ e_c \end{bmatrix} + \begin{bmatrix} u_N \\ u_N \\ u_N \end{bmatrix} \quad (2)$$

Where, u_a, u_b, u_c terminal phase voltages i_a, i_b, i_c phase currents, e_a, e_b, e_c phase back EMFs, R phase resistance, $L =$

$L_s - M$ phase inductance, L_s , phase self-inductance and M mutual inductance and u_N , the neutral point voltage of the star-connected motor, respectively.

The electrical power produced by each phase;

$$\begin{aligned} P_a &= e_a i_a \\ P_b &= e_b i_b \\ P_c &= e_c i_c \end{aligned} \quad (3)$$

Expression of total electromagnetic torque produced by BLDC motor is;

$$T_e = \frac{P_{sum}}{\omega_m} = \frac{P_a + P_b + P_c}{\omega_m} \quad (4)$$

$$T_e = \frac{e_a i_a + e_b i_b + e_c i_c}{\omega_m} \quad (5)$$

Where, represents, P_a, P_b, P_c the electrical powers produced by the phases, P_{sum} the sum of these powers, T_e , the electromagnetic torque and ω_m the mechanical speed of the rotor, respectively.

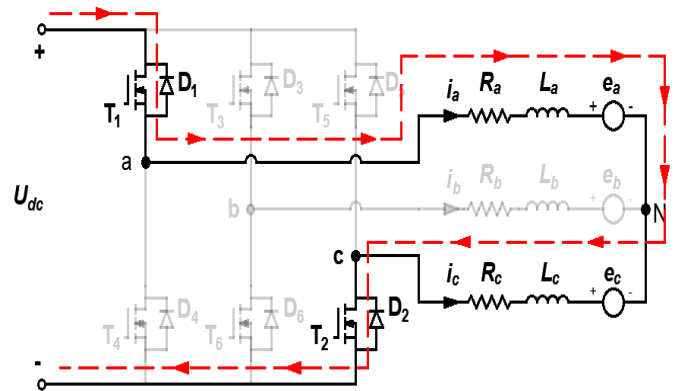


Fig. 3 The conduction region before commutation (a*c)

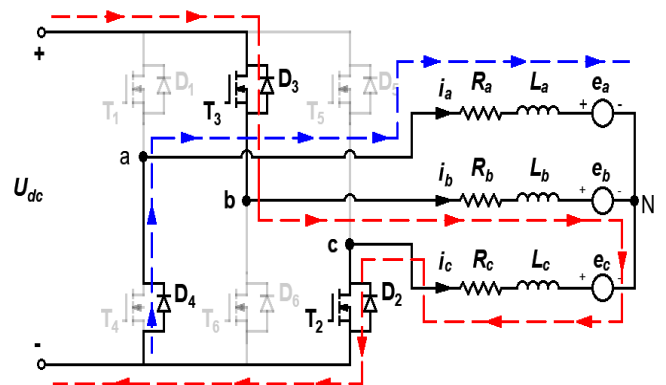


Fig. 4 The commutation region (Three phase are conducting)

All phase currents during the commutation will not be a square wave as shown in Fig.2 due to the inductance of the stator phase windings. In order to perform this analysis, it was assumed that the commutation process passes from phase a to

phase *b*, as seen from Figs.3, 4, 5. In this case, the phase *a* is named outgoing phase and phase *b* is named incoming phase.

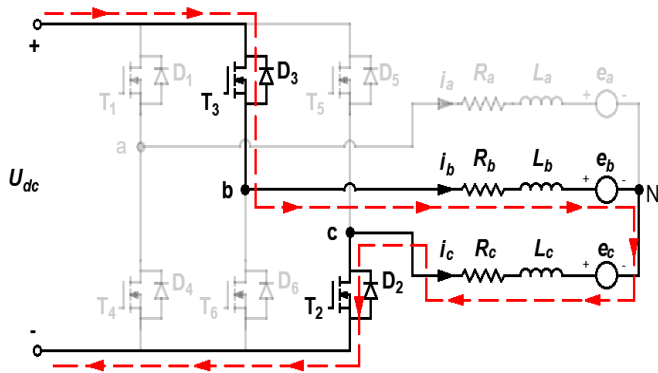


Fig. 5 The conduction region after commutation (b*c)

As seen from the Fig.3, the currents of the phase windings can be expressed as $i_a = -i_c = I_m$ and $i_b = 0$ in the conduction period and as seen from the Fig.4, $i_a = 0$ and $i_b = -i_c = I_m$ in the commutation period. I_m , is represent the maximum value of phase currents. The conduction region after commutation and the conduction region before commutation are same. There is only phase change (from *ac*, to *bc*) like Figs.3 and 5. The commutation phase sequence is *ab - ac - bc - ba - ca - cb*. This case is shown in Fig.6.

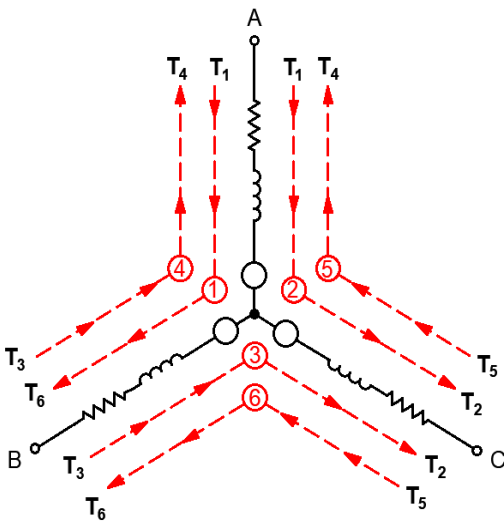


Fig. 6 The commutation phase sequence

Since the the commutation time is very short, within this period the back EMFs induced in the phases can be considered constant. $e_a = e_b = E_m$ and $e_c = -E_m$. If these magnitudes are substituted in Eq. (5);

$$T_e = \frac{e_a i_a + e_b i_b + e_c i_c}{\omega_m} = \frac{2E_m I_m}{\omega_m} = -\frac{2E_m i_c}{\omega_m} \tag{6}$$

$$\omega_m = -\frac{2E_m i_c}{T_e}$$

As seen from the second statement of Eq. (6), the fluctuations in the current of the non-commutation phase directly affect the rotor speed. By reducing the fluctuations in this current, the speed fluctuations can be eliminated. At the commutation time, the current of phase *a*, will flow through the free-wheeling diode D4, as similar Fig.4. In addition to this, the voltage on the free-wheeling diodes was neglected. If the expression of the three-phase terminal voltages substituted in Eq. (1) $u_a = u_c = 0$ and $u_b = U_{dc}$,

$$0 = Ri_a + L \frac{di_a}{dt} + e_a + u_N$$

$$U_{dc} = Ri_b + L \frac{di_b}{dt} + e_b + u_N \tag{7}$$

$$0 = Ri_c + L \frac{di_c}{dt} + e_c + u_N$$

The neutral point voltage of the star-connected phase windings of BLDC motor at the commutation times is different from zero [16]. If Eq. (7) is collected one under the other, the expression of neutral point voltage of BLDC motor is:

$$3u_N = U_{dc} - E_m$$

$$u_N = \frac{U_{dc} - E_m}{3} \tag{8}$$

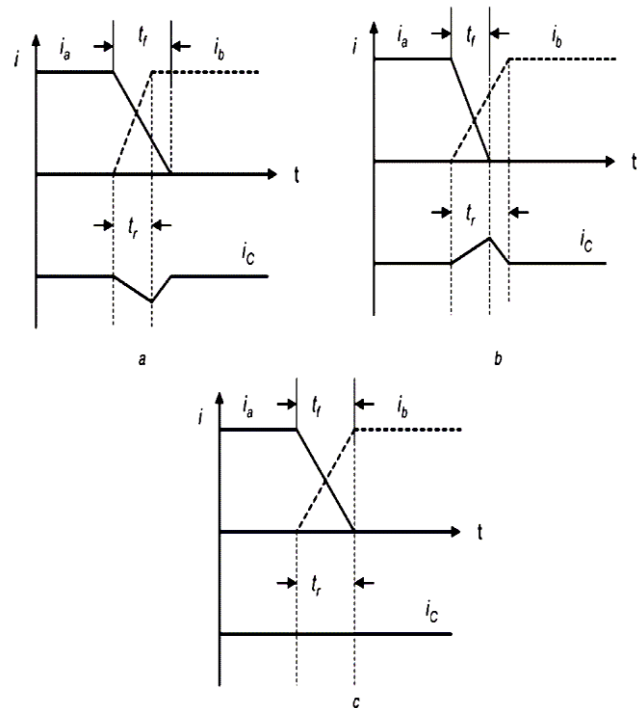


Fig. 7 The phase current behavior of commutation region, a.) $t_r > t_r'$, b.) $t_r < t_r'$, c.) $t_r = t_r'$, [4].

The slopes of the incoming and outgoing phase currents in the conventional BLDC motor speed control system are different each other at both high and low speeds. This difference is caused by the torque and speed fluctuations in commutation intervals. In order to eliminate the fluctuations in the rotor

speed, it is necessary to equalize the slopes of the incoming and outgoing phase currents at the commutation time or keep constant the current of the non-commutation phase. The current behavior of BLDC motor was shown in Fig.7. Where, t_f , represents the fall time of outgoing phase from the maximum to zero, t_r , represents the rise time of incoming phase from the zero to the maximum value. As seen in Fig.7a and 7b, the rise time is different from the fall time. In this case, are occurs fluctuations in the non-commutation phase. According to the Eq. (6), the amplitude of the non-commutation phase current is directly related to the generated torque. In this case, creates fluctuations in both the output torque and the output speed. However, in Fig.7c, it is seen that there is no fluctuation in the non-commutation phase when the slopes of the incoming and outgoing phase currents are equalized. When the Eqs. (7) and (8) are evaluated together, the slopes of the currents of incoming, outgoing and non-commutation phase at the commutation time can be expressed as follows;

$$\begin{aligned} \frac{di_a}{dt} &= -\frac{(U_{dc} + 2E_m)}{3L} \\ \frac{di_b}{dt} &= \frac{2(U_{dc} - E_m)}{3L} \\ \frac{di_a}{dt} + \frac{di_b}{dt} &= -\frac{di_c}{dt} \\ \frac{di_c}{dt} &= -\frac{(U_{dc} - 4E_m)}{3L} \end{aligned} \quad (9)$$

Where, U_{dc} represents DC link voltage and E_m , represents maximum value of the back EMF, respectively. In Eq. (10), the resistance of the phase windings R was neglected. This is because the commutation interval is much shorter than the electrical time constant L/R [3]. In this case, the fall time of phase a from the maximum value to zero and the rise time of phase b from the zero to maximum value, can be calculated as follows.

$$\begin{aligned} t_f &= \frac{3LI_m}{U_{dc} + 2E_m} \\ t_r &= \frac{3LI_m}{2(U_{dc} - E_m)} \end{aligned} \quad (10)$$

According to the Fig.7c, the fluctuations in produced torque, rotor speed and the non-commutation phase can be eliminated if the slopes of the incoming and outgoing phase currents are equal. If the fall and rise times in Eq. (10) are equalized;

$$\begin{aligned} t_f &= t_r \\ \frac{3LI_m}{U_{dc} + 2E_m} &= \frac{3LI_m}{2(U_{dc} - E_m)} \\ U_{dc} &= 4E_m \end{aligned} \quad (11)$$

As seen from Eq. (11), at the commutation intervals, the inverter input voltage U_{dc} must be equal to four times of the

back EMFs. So that the slopes of the incoming and outgoing phase currents are equal.

According to Eqs (6) and (9);

$$\begin{aligned} T_e &= -\frac{2E_m i_c}{\omega_m} \\ T_{com} &= \frac{2E_m}{\omega_m} \left(I_m + \frac{U_{dc} - 4E_m}{3L} t \right) \end{aligned} \quad (12)$$

When the two expressions written for the torque in Eq (12) are considered together, the magnitude of the relative fluctuation in the commutation intervals can be expressed as in Eq (13).

$$T_{rel} = T_{com} - T_e = \frac{U_{dc} - 4E_m}{3L} t \quad (13)$$

Where, T_{com} represents the value of the torque produced by BLDC motor, T_{rel} represents relative torque ripple in the commutation intervals. The following inferences can be made according to Eq. (13).

- a.) If $U_{dc} > 4E_m$, then $t_f > t_r$, and torque will continue to increase during commutation. The behavior of phase currents is similar to Fig.7a.
- b.) If $U_{dc} < 4E_m$, then $t_f < t_r$, and torque will continue to decrease during commutation. The behavior of phase currents is similar to Fig.7b.
- c.) If $U_{dc} = 4E_m$, then $t_f = t_r$, and torque remains constant during commutation. The behavior of phase currents is similar to Fig.7c.

According to the Eqs. (11) and (13), it is theoretically seen that if the input voltage of the inverter is equal to four times of the back EMF at the commutation intervals, torque ripples can be completely zero. This equalization was carried out using different DC-DC converters [6, 17-19]. In most of the studies, it was assumed that the rotor speed was constant in the commutation intervals. But in fact, the fluctuations occur at the rotor speed, as well as the produced torque. In this study, it was proposed to reduce the speed fluctuations by using DC link current. Commutation signals were produced for specific points of the current commutation and it was applied to designed voltage selective circuit. This study has been proposed for the suppression of speed fluctuations by synchronizing the inverter input voltage to four times of the produced back EMF, with a new switching technique at the commutation intervals.

III. PROPOSED CONTROL STRATEGY

The designed voltage selective circuit for the proposed method is shown in Fig.8. In this method, two different regulated voltage sources were used to reduce the speed fluctuations. These sources, generate voltage according to the signal from given their inputs. The source number I , will be conducting during commutation periods and will remain in isolation during non-commutation periods. A second feedback link was designed by taking four times the maximum value of the

produced back EMF by using a second adjustable voltage source. The source number 2, will only be conducting during non-commutation periods and will be kept in isolation during commutation periods.

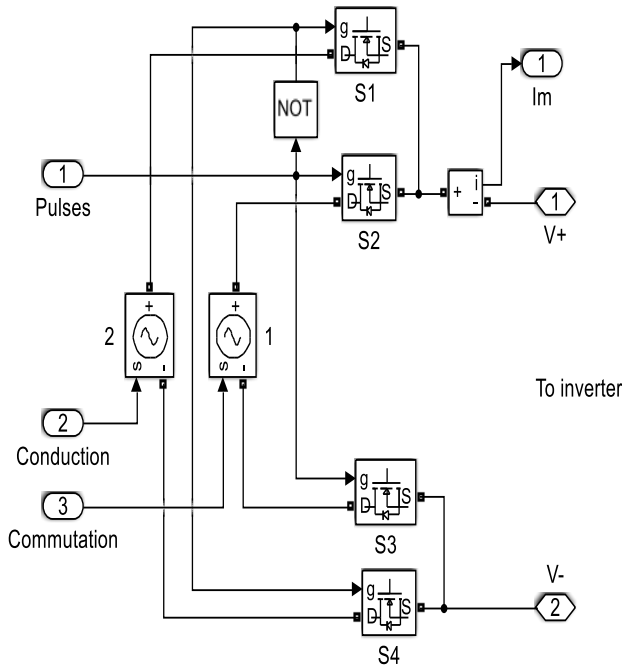


Fig. 8 Designed voltage selective circuit

In the proposed technique, there is no need to calculate the commutation time. A new switching technique has been proposed from the relation between the torque magnitude of the motor, the speed of the motor and the maximum value of the phase current. The expression of this relation;

$$T_e = k_t I$$

$$I = \frac{T_e}{k_t} \tag{14}$$

Where, k_t represents the motor torque constant, I the maximum value of the source current.

The following inferences can be made using the second expression of Eq. (14).

- a.) If $I < T_e / k_t$, then commutation process was started. In this case the inverter input voltage set to $U_{dc} = 4E_m$.
- b.) If $I \geq T_e / k_t$, then the commutation was finished. In this case the inverter input voltage set to U_{dc} .

According to these inferences, a commutation time switching signal was generated for the moments where the maximum source current falls below the T_e / k_t ratio and this signal was applied to the designed voltage selective circuit during the commutation period. The signal obtained by the proposed technique is shown in Fig.9. Inverter gate signals generated by hall effect sensors with respect to the rotor position is shown in Fig9a. These signals are applied to the power MOSTETs in the inverter. The inverter changes state according to these

signals. In Fig.9b, the sawtooth graph represents the maximum value of the source current (*magenta*), while the constant graph represents the T_e / k_t ratio (*dashed black*). Fig.9c shows the generated commutation signals when the source current falls below T_e / k_t ratio. These signals were applied to the voltage selective circuit at commutation time. In order to reduce the speed fluctuations occurring commutation intervals, it was tried to provided $U_{dc} = 4E_m$.

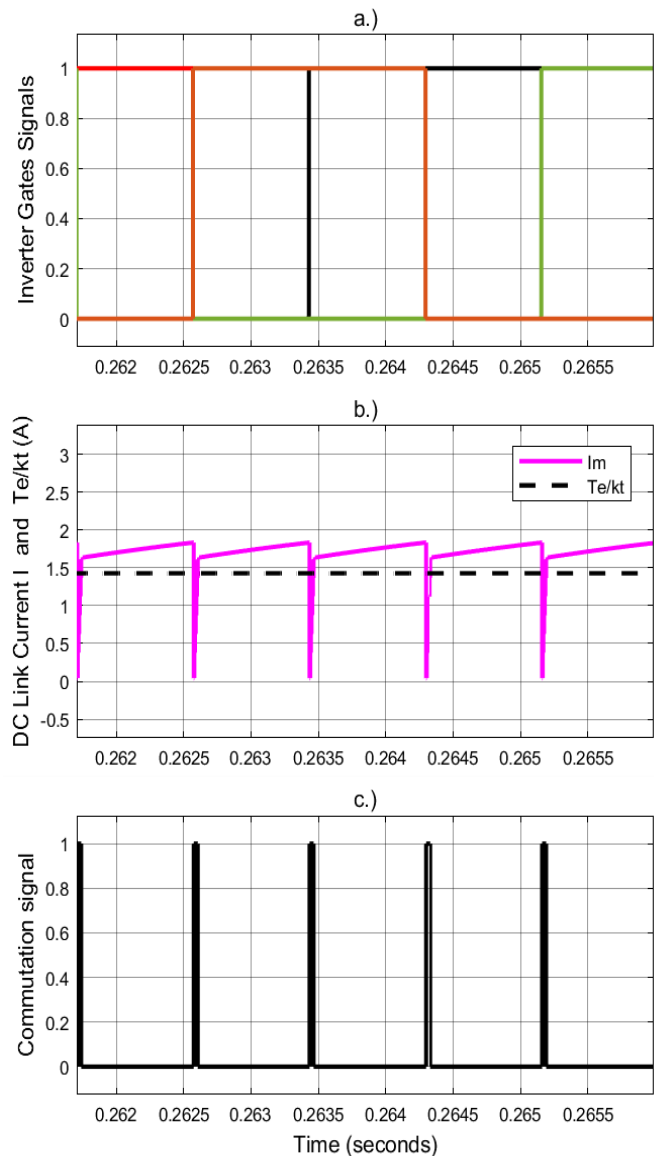


Fig. 9a.) Inverter gate signal, b.) Dc link current and T_e/k_t ratio c.) The produced commutation signal.

When the BLDC motor was started, the value of the maximum source current was measured and compared with the T_e / k_t ratio. If T_e / k_t ratio is smaller than the value of the source current, then the designed voltage selective circuit is providing $U_{dc} = 4E_m$ (S_1 and S_4 switch on). If the source current is greater than or equal to T_e / k_t , the inverter input voltage is not changed and remain U_{dc} (S_2 and S_3 switch on). The simulink models of the two control method for BLDC motor is shown in Fig.10.

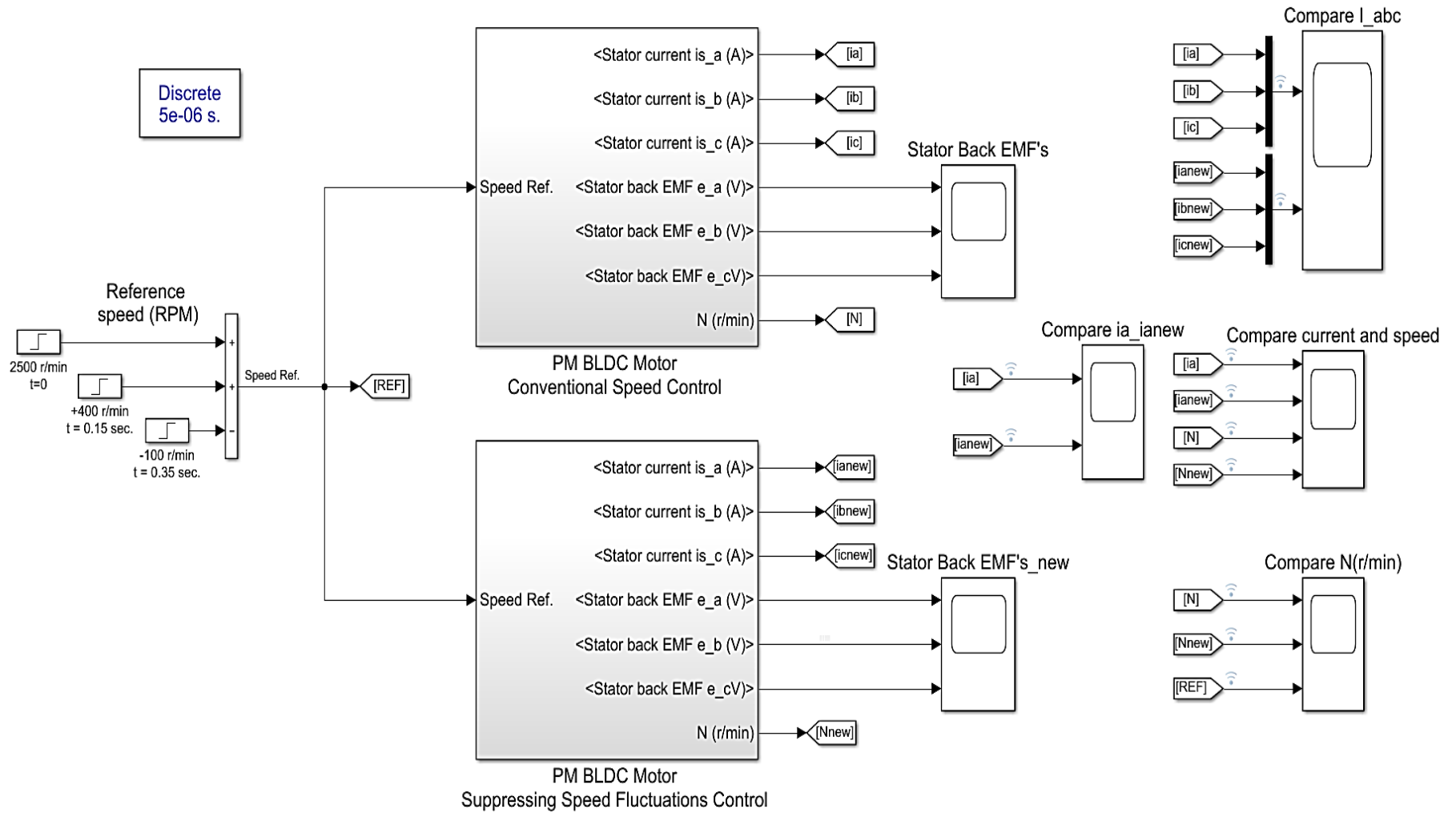


Fig. 10 Conventional and Proposed control method Simulink Models.

Parameters of the BLDC motor used in the simulation were given in Table I, and the flowchart of the proposed control method is shown in Fig.11.

TABLE I
BLDC MOTOR PARAMETERS USED IN SIMULATON.

Parameters	Unit	Value
Phase Resistance	Ω	2.875
Phase Inductance	mH	8.5
Back EMF Coefficient	V/(rad/s)	0.7
Pole Pairs		4
Rated Voltage	V	500
Rated Speed	r/min	3000
Rated Torque	N.m)	2
Rated Power	W	1000

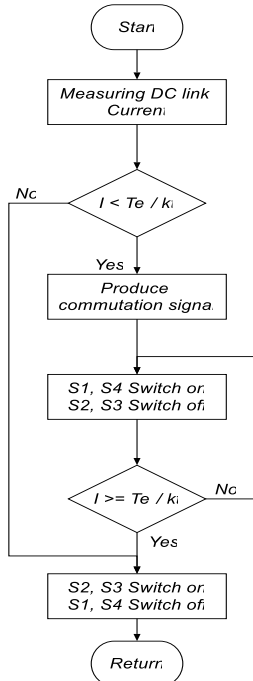


Fig. 11 The flowchart of the proposed control method

IV. SIMULATION RESULTS

As seen from the Fig.10, a reference speed of 2500 r/min was applied to BLDC motor at startup. Then, this speed was increased by 2900 r/min at $t = 0.15s$ and reduced by 2800 r/min at $t = 0.35s$. The currents of the phase windings for the two control methods, the current of the phase a, the rotor speeds are shown in Figs.12, 13, 14, respectively. Fig.12a shows the fluctuations of the phase currents in the conventional control method. These fluctuations negatively affect the output speed and cause power loss. In Fig. 12b, these fluctuations were tried to be suppressed by the proposed control method. Fig.13 shows the time-dependent current of phase a, both the conventional control method and the proposed control method. Fig.14 shows comparison of rotor speeds. In both control methods, rotor speeds followed the given reference speed in all speed ranges. But in conventional control method, the rotor speed fluctuation is considerably higher with respect to proposed control method. This case, is shown in Figs.15, 16, 17, respectively. According to the simulation results it was observed that the disturbances occurring in the phase currents affect the rotor speed directly. This effect is similar to the non-commutation phase current.

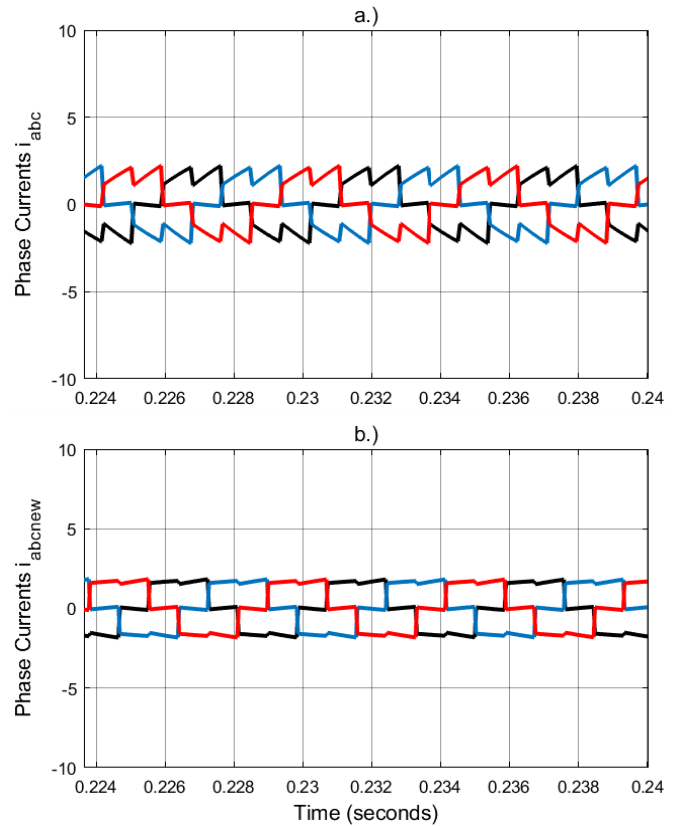


Fig. 12 The phase currents a.) Conventional control b.) Proposed Control

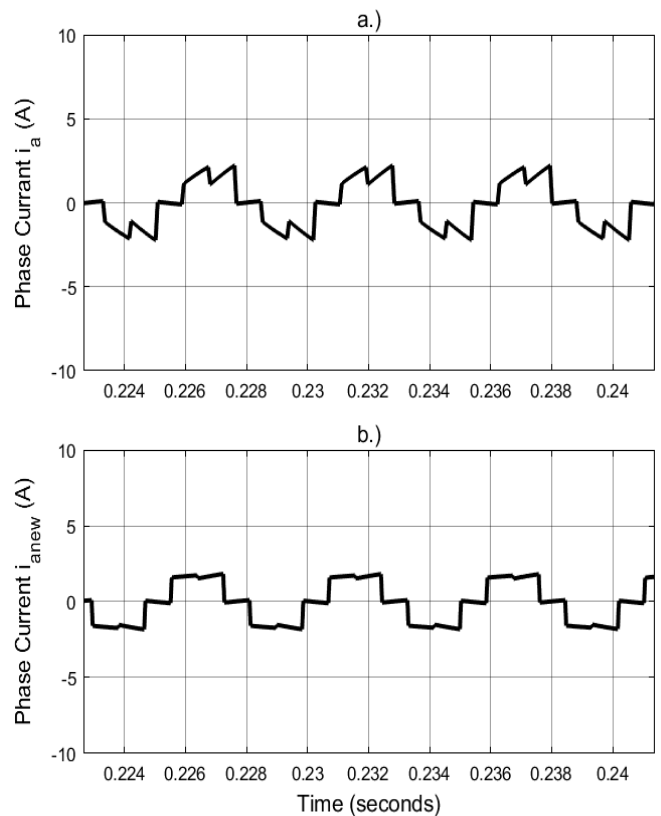


Fig. 13 The current of phase a, a.) Conventional control b.) Proposed Control

This effect can be calculated as a percentage in Eq. (15).

$$\omega_{fluct} = \frac{\omega_{max} - \omega_{min}}{\omega_{max} + \omega_{min}} * 100\% \quad (15)$$

The numerical results obtained from the simulation are given in Table II. As shown in Table II, the fluctuations in the rotor speed of the BLDC motor were greatly reduced with the proposed control method.

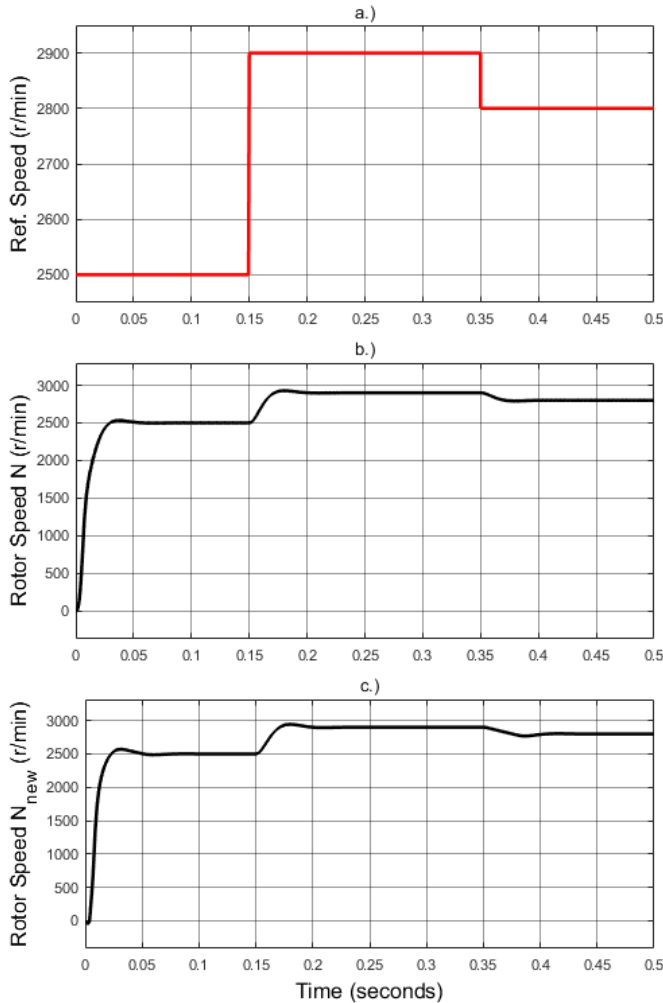


Fig. 14. The rotor speed a.) Reference b.) Conventional control c.) Proposed control

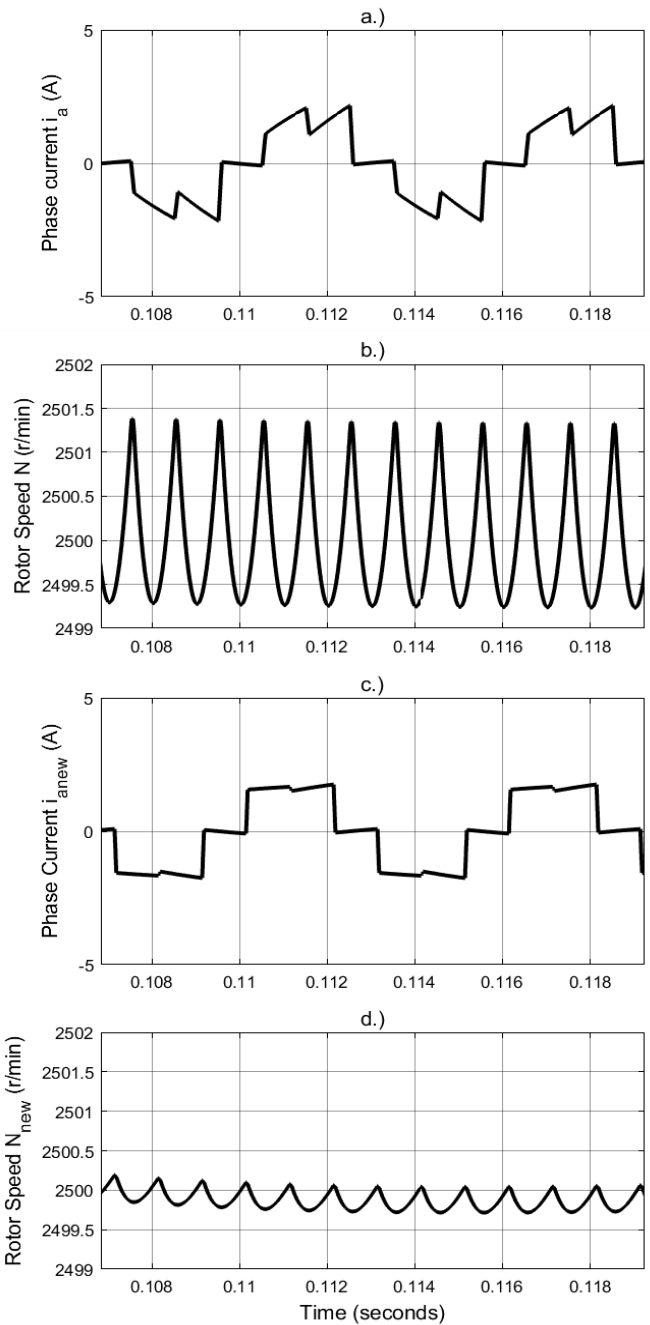


Fig. 15. Simulation results a.) Phase current and b.) Rotor speed, of conventional control, c.) Phase current and d.) Rotor speed, of proposed control, respectively. ($\omega_{ref}=2500r/min$, from $t=0$ to $t=0.15$ seconds)

TABLE II
SPEED FLUCTUATIONS FOR GIVEN REFERENCE

Ref. Speed (r/min)	2500 (from $t=0$ to $t=0.15$ seconds)		
Speed intervals and fluctuation	Max (r/min)	Min (r/min)	Fluctuation (r/ms)
Conventional control	2501.3	2499.3	2
Proposed control	2500.24	2499.9	0.34
Ref. Speed (r/min)	2900 (from $t=0.15$ to $t=0.35$ seconds)		
Speed intervals and fluctuation	Max (r/min)	Min (r/min)	Fluctuation (r/ms)
Conventional control	2901.3	2898.97	2.326
Proposed control	2900.12	2899.725	0.395
Ref. Speed (r/min)	2800 (from $t=0.35$ to $t=0.5$ seconds)		
Speed intervals and fluctuation	Max (r/min)	Min (r/min)	Fluctuation (r/ms)
Conventional control	2801.3	2799.066	2.234
Proposed control	2800.24	2799.9	0.379

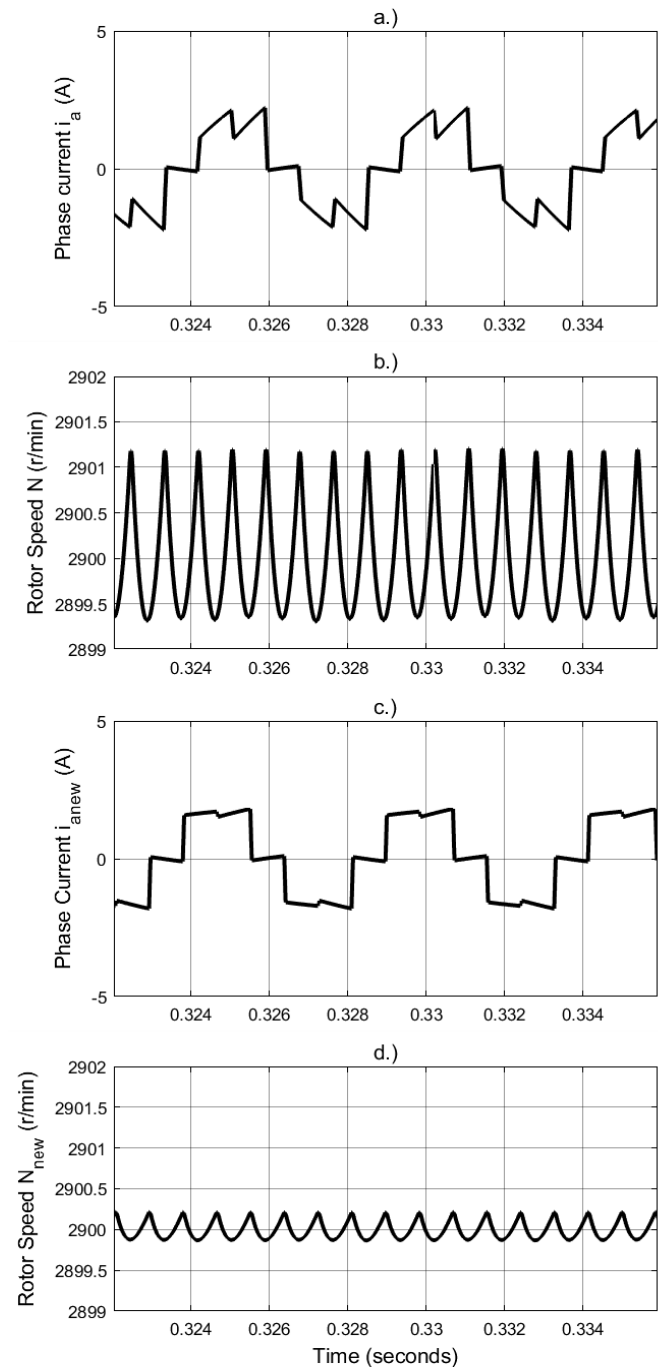


Fig. 16 Simulation results a.) Phase current and b.) Rotor speed, of conventional control, c.) Phase current and d.) Rotor speed, of proposed control, respectively, ($\omega_{ref}=2900r/min$, from $t=0.15$ to $t=0.35$ seconds).

V. CONCLUSIONS

In this study, a new control method has been proposed to reduce the speed fluctuations in the BLDC motors. In this method, it was aimed to equalize the slopes of the incoming and outgoing phase currents. Both theoretical calculations and simulation results, the fluctuation in the current, which is non-commutation phase, has been shown to directly affect the rotor speed. There is only a single voltage selective circuit was used to minimization these fluctuations. This circuit was only used in commutation regions. In non-commutation regions, the conventional BLDC motor control circuit was used. The

mainly advantage of the proposed method are that it does not require heavy theoretical calculations such as calculating commutation times.

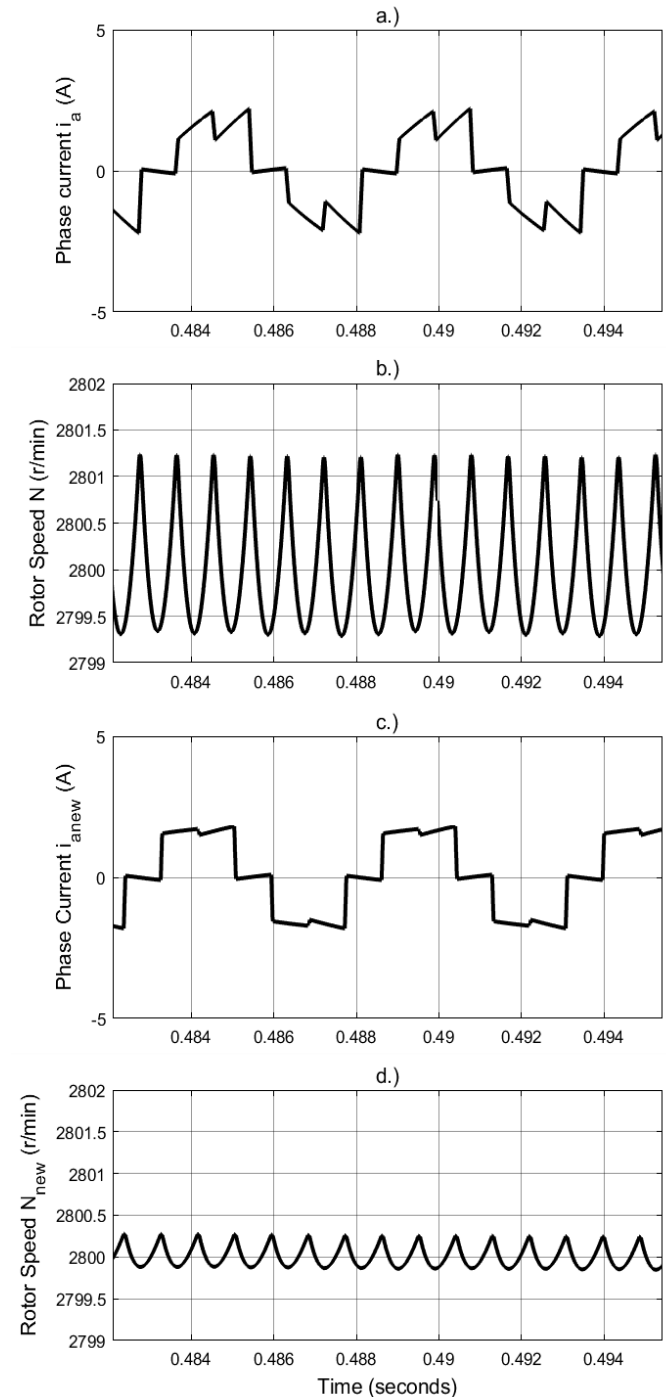


Fig. 17 Simulation results a.) Phase current and b.) Rotor speed, of conventional control, c.) Phase current and d.) Rotor speed, of proposed control, respectively, ($\omega_{ref}=2500r/min$, from $t=0.35$ to $t=0.5$ seconds).

According to the simulation results, it was observed that the speed fluctuations are greatly reduced for all speed ranges in steady state condition. Reducing these fluctuations is highly effective both the longer life and the more efficient operation of the BLDC motor.

REFERENCES

- [1] Shi, J. and Li, T. C., New Method to Eliminate Commutation Torque Ripple of Brushless DC Motor with Minimum Commutation Time, *IEEE Transactions on Industrial Electronics*, 60, 6 (2013) 2139-2146.
- [2] Xiaofeng, Z. and Zhengyu, L., A New BLDC Motor Drives Method Based on BUCK Converter for Torque Ripple Reduction, 5th International Power Electronics and Motion Control Conference (CES/IEEE), August 2006, Shanghai, China, 1-4.
- [3] Shi, T., Guo, Y., Song, P. and Xia, C., A New Approach of Minimizing Commutation Torque Ripple for Brushless DC Motor Based on DC-DC Converter, *IEEE Transactions on Industrial Electronics*, 57, 10 (2010) 3483-3490.
- [4] Viswanathan, V. and Seenithangom, J., Approach for Torque Ripple Reduction for Brushless DC Motor Based on Three-level Neutral-point-clamped Inverter with DC-DC Converter, *IET Power Electronics*, 8, 1 (2015) 47-55.
- [5] Carlson, R., Lajoie-Mazenc, M. and Fagundes, J. C. d. S., Analysis of Torque Ripple Due to Phase Commutation in Brushless DC Machines, *IEEE Transactions on Industry Applications*, 28, 3 (1992) 632-638.
- [6] Chen, W., Liu, Y., Li, X., Shi, T. and Xia, C., A Novel Method of Reduction Commutation Torque Ripple for Brushless DC Motor Based on Cuk Converter, *IEEE Transactions on Power Electronics*, 32, 7 (2017) 5497-5507.
- [7] Song, J. H. and Choy, I., Commutation Torque Ripple Reduction in Brushless DC Motor Drives using a Single DC Current Sensor, *IEEE Transactions on Power Electronics*, 19, 2 (2004) 312-319.
- [8] Cao, Y., Shi, T., Liu, Y. and Wang, Z. Commutation Torque Ripple Reduction for Brushless DC Motors with Commutation Time Shortened, *IEEE International Electric Machines and Drives Conference (IEMDC)*, May 2017, Miami, FL, USA, 1-7.
- [9] Fang, J., Li, H. and Han, B., Torque Ripple Reduction in BLDC Torque Motor with Nonideal Back EMF, *IEEE Transactions on Power Electronics*, 27, 11 (2012) 4630-4637.
- [10] Li, X., Xia, C., Cao, Y., Chen, W. and Shi, T., Commutation Torque Ripple Reduction Strategy of Z-Source Inverter Fed Brushless DC Motor, *IEEE Transactions on Power Electronics*, 31, 11 (2016) 7677-7690.
- [11] Shi, T., Niu, X., Chen, W. and Xia, C., Commutation Torque Ripple Reduction of Brushless DC Motor in Braking Operation, *IEEE Transactions on Power Electronics*, 33, 2 (2018) 1463-1475.
- [12] Lad, C. K. and Chudamani, R., A Simple Overlap Angle Control Strategy for Reducing Commutation Torque Ripple in a Brushless DC Motor Drive, *Engineering Science and Technology, an International Journal*, 20 (2017) 1406-1419.
- [13] Niasar, A. H., Vahedi, A. and Moghbelli, H., A Novel Method for Commutation Torque Ripple Reduction of Four-Switch, Three-Phase Brushless DC Motor Drive, *Iranian Journal of Electrical & Electronic Engineering*, 3, 3 (2007) 83-96.
- [14] Chuang, H. S., Ke, Y. L. and Chuang, Y. C., Analysis of Commutation Torque Ripple using Different PWM Modes in BLDC Motors, *IEEE Industrial & Commercial Power Systems Technical Conference*, May 2009, Calgary, Canada, 1-6.
- [15] Jiang, W., Huang, H., Wang, J., Gao, Y. and Wang, L., Commutation Analysis of Brushless DC Motor and Reducing Commutation Torque Ripple in the Two-Phase Stationary Frame, *IEEE Transactions on Power Electronics*, 32, 6 (2017) 4675-4682.
- [16] Brendsen, C. S., Champenois, G. and Bolopion, A., Commutation Strategies for Brushless DC Motors: Influence on Instant Torque, *IEEE Transactions on Power Electronics*, 8, 2 (1993) 231-236.
- [17] Amirthalingam, R. and Mahadevan, B., A New Approach for Minimizing Torque Ripple in a BLDC Motor Drive with a Front end IDO DC-DC Converter, *Turkish Journal of Electrical Engineering & Computer Science*, 25 (2017) 2910-2921.
- [18] Jogarao, R., Reddy, M. and Ashok, G., Analysis of Commutation Torque Ripple Minimization for Brushless DC Motor Based on SEPIC Converter, *International Journal of Engineering Research and Application*, 6, 11 (2016) 5-11.
- [19] Chen, Z., Zhang, H., Liu, X., Hu, H., Zhao, J. and Gao, C., A New Method to Suppress the Commutation Torque Ripple for BLDC Motor Based on ZETA Converter, 6th International Conference on Power Electronics Systems and Applications (PESA), December 2015, Hong Kong, China, 1-6.

BIOGRAPHIES



M. RESİT ÇORAPSIZ was born in Erzurum, Turkey, in 1984. He received the first B.S. degree from Firat University, Elazığ, Turkey, and the second B.S. degree from Ataturk University, Erzurum, Turkey, and the M.S. degree from Karadeniz Technical University, Trabzon, Turkey, in 2009, 2015, 2018, respectively, all in electrical engineering. Since 2018, he studies Ph.D. in electrical engineering at the Karadeniz Technical University. He has been a member of the Chamber of Electrical Engineers in Turkey.

Currently, he is an Instructor with the Department of Electrical and Energy, Vocational School of Technical Science, Bayburt University, Bayburt, Turkey. His research interests include power electronics and electric drive systems, control of electric machinery, electric vehicles, smart grid and power management in electric vehicles.



HAKAN KAHVECİ was born in Kırşehir, Turkey. He received his B.Sc degree in Electrical Engineering and Ph.D degree from Karadeniz Technical University (KTU), Turkey, in 2006 and 2013, respectively.

He is currently an assistant professor in Electrical and Electronics Engineering Department at KTU. He has been a member of the Chamber of Electrical Engineers in Turkey. He works on electrical machine control systems and power electronics.



M. FATİH ÇORAPSIZ was born in Erzurum, Turkey, in 1981. He received the first B.S. degree from Firat University, Elazığ, Turkey, in 2003, and the M.S. and Ph.D. degrees and the second B.S. degree from Ataturk University, Erzurum, Turkey, in 2009, 2014 and 2016, respectively, all in electrical engineering. He has been a member of the Chamber of Electrical Engineers in Turkey.

Currently, he is a Assistant Professor with the Department of Electrical and Electronics Engineering, College of Engineering, Ataturk University, Erzurum, Turkey. His research interests include theory of mechatronic and robotic systems, DC-DC converters, and motor drive circuits, with a focus on observation and estimation-based control.

A Novel Data Hiding Method based on Edge Detection and 2^k Correction with High Payload and High Visual Quality

T. TUNCER, Y.SÖNMEZ


Abstract— In this paper a novel edge adaptive data hiding method is proposed. The proposed edge adaptive steganography method is improved version of the Bai et al.'s [31] (A high payload steganographic algorithm based on edge detection) method. The main aim of the proposed method is to achieve high payload with high visual quality. This method consists of preprocessing, edge detection, classification of the secret data, data embedding and data extraction phases. In the preprocessing phase 6 and 7 least significant bits (LSB) elimination are applied on the cover image to get a better edge detection in the next phase. As edge detection methods Sobel, Canny, Laplacian Of Gaussian (LOG), block-based edge detection and hybrid edge detectors are used. After the edge detection, secret data is divided into 2 classes and then these are embedded into edge pixels and texture pixels of the image. In order to increase the visual quality 2^k correction is applied on the stego images. Modulus operator is utilized in the data extraction phase. In the experimental results, payload and visual quality measurements demonstrated the success of the proposed method.

Index Terms— Least Significant Bit (LSB) substitution; 2^k correction; Edge Detection; Data hiding


I. INTRODUCTION

THE ERA we live in is called information era. The vast majority of information is stored as digital media. As a result the information security has become a very important research topic in order to provide security of digital media, thus information security has become a hot-topic research area [1]. In the information security, cryptography and data hiding are widely used. While cryptography provides the confidentiality of digital data, aim of the data hiding is to provide security of the communication. Recently, data hiding has gained popularity over cryptography and started to appear more often in the literature [2-4]. Data hiding methods generally use spatial domain and frequency domain for data embedding.

TÜRKER TUNCER, is with Department of Digital Forensic Engineering of Firat University, Elazığ, Turkey, (e-mail: turkertuncer@firat.edu.tr).

 <https://orcid.org/0000-0002-1425-4664>

YASİN SÖNMEZ, is with technical sciences vocational high school of Dicle University, Diyarbakir, Turkey, (e-mail: yasin.sonmez@dicle.edu.tr).

 <https://orcid.org/0000-0001-9303-1735>

Manuscript received June 2, 2019; accepted July 11, 2019.

DOI: [10.17694/bajece.573514](https://doi.org/10.17694/bajece.573514)

Spatial domain based data hiding methods have shorter execution time, higher embedding Capacity and higher visual quality but these methods are not robust. In order to increase the robustness of the data hiding method, frequency domain is used [5-8]. In frequency domain, Discrete Wavelet Transform (DWT) [9], Integer Wavelet Transform (IWT) [10], Discrete Cosine Transform (DCT) [11,12], Discrete Fourier Transform (DFT) [13], etc. are used as transformation functions. Data hiding algorithms generally consist of host image, secret data, data hiding, stego image and data extraction. In addition to these basic components, cryptography, frequency transforms, heuristic optimization techniques, edge detectors, segmentation algorithms, secret sharing, visual cryptography, game rules, etc. are widely used in data hiding [14-20]. The most popular data hiding method is Least Significant Bit (LSB) substitution [21]. LSB is a practical method because LSB provides higher visual quality, higher payload Capacity and shorter execution times. Thus, LSB is the widely used method in the data hiding. Some of the previously presented data hiding methods are given as follows. Mahato et al. [22] presented a data hiding method based on the popular minesweeper game for secure communication. The authors generated a scenario for secure communication where the sender plays minesweeper game to embed the secret data and then he/she sends the game to the receiver. The secret message can be extracted from the received game-play. Liao et al. [23] suggested a data hiding method for medical images. To increase robustness against JPEG compression of this method DCT was used. Shiu et al. [24] proposed a reversible signal data hiding for physiological signals. They analyzed this method theoretically and they showed that this algorithms computational complexity is $O(n)$ and this method can be used for ECG and EMG signals. Yuan [25] suggested a secret sharing based image data hiding method with high visual quality. In this method, firstly secret sharing was used to generate minimal distorted secret shares and these secret shares were embedded into multi cover images by using LSB. Wu and Tsai [26] described a data hiding concept based on pixel value difference (PVD). In this method, cover image was divided into non-overlapping blocks and 2 connected pixels differences was modified for data hiding. Subhedar and Mankar [27] proposed a robust QR factorization based data hiding. To evaluate of this method, they used robustness and visual quality performance metrics. Maheswari and Hemanth [28] proposed a Fresnelet Trasform (FT) and QR code based

data hiding method. They utilized LSB as data hiding function. FT and QR coding provided robustness. Chen et al. [29] suggested a hybrid edge detector based data hiding method. Hybrid edge detector utilized Gaussian filter and sobel matrix. Capacity and visual quality was used to evaluate performance of this method. Tseng and Leng [30] proposed an extended edge based data hiding method to achieve minimal distortion. This method was a block based method and they calculate Mean Square Error (MSE) for each 4 x 4 blocks. Bai et al. [31] suggested an edge detection based image data hiding algorithm with high payload Capacity. This method consisted of 5LSBs elimination, edge detection by using Canny [32], Sobel [33] and Fuzzy Logic Edge Detector (FLED) [34], secret message classification in two sub-class, data hiding and data extraction phases. Capacity and visual quality were used to evaluate performance of this method. Sun [35] presented a edge based image data hiding method. In this method, Canny Edge Detector (CED) was used for edge detection, Huffman was used for secret data compression and 2k correction was used for data hiding and data extraction.

In this method, we proposed a novel edge adaptive data hiding method. This method consists of mLBSs elimination, edge detection, secret data classify, data hiding and data extraction phases. In this method, LSB is used for data hiding and data extraction. Briefly, the proposed method is an improved version of Bai et al.'s [31] method. The main aim of the proposed method is to provide higher payload with higher visual quality than Bai et al.'s [31] method. Technical contributions of the proposed method are given below.

mLSBs elimination is used for achieving high payload Capacity. Bai et al.'s [31] used 5LSBs elimination in order to increase Capacity. In this method, we used mLBSs elimination ($m \in \{6,7\}$) to find more edge pixel. A block based edge detector is presented in this paper. In this edge detector, OTSU [36] method and 2 x 2 non-overlapping blocks are used. This method detects edge pixel in the binary form.

A hybrid edge detector is proposed in this paper to achieve high payload Capacity. This detector uses Canny, Sobel, Laplacian of Gaussian and the proposed block based edge detectors. The main aim of the HED is to detect all of the edge pixels in an image. In this method, edge detectors are used for creating data hiding map. By using this map, secret data is divided into x and y classes. xLSBs and yLSBs data embedding method are used as data embedding function. To achieve high visual quality, 2^k correction is applied on the stego image. By using 2^k correction, higher visual quality is achieved than Bai et al.'s method.

II. PROPOSED EDGE DETECTOR

Canny, Sobel and LOG methods are used in this paper for known edge detection methods. In addition to these methods, a block based edge detection method which is a modified version of the FLED method and a hybrid edge detection method are used.

Block based Edge Detection (BED): This method is a modified version of the Fuzzy Logic Edge Detector (FLED) method. In this method, OTSU thresholding method, 2 x 2 size of non-overlapping blocks and a rule table are used. This

method detects edges of binary form of the images. The steps of the proposed edge extraction algorithm are as follows.

- **Step 1:** Convert binary image to original image by using OTSU threshold method.
- **Step 2:** Divide binary image into 2 x 2 size of non-overlapping blocks. A sample 2 x 2 size of block is shown in Fig. 1.

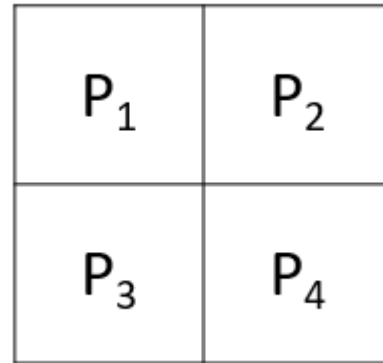


Fig. 1. 2 x 2 sized block.

- **Step 3:** Detect edges by using Eq. 1.

$$Edge = \begin{cases} 0, & \sum_{i=1}^4 p_i = 4 \text{ or } \sum_{i=1}^4 p_i = 0 \\ 1, & \text{Otherwise} \end{cases} \quad (1)$$

Hybrid Edge Detection (HED): Many edge detection methods are proposed in the literature. These methods yield different edge properties of images and edge detectors used in the literature have weak and superior features against each other. This has led to the development of an edge detection method that can obtain all edge data in the image. In this article, a hybrid edge detector which uses the widely used edge detection methods is proposed and this edge detector can obtain more edge information from the image. The main purpose of this method is to increase the Capacity of the edge based data hiding method by obtaining more edge information. BED, Canny, Sobel and LOG edge removal operators are used in this method. The steps of the HED is given in Eq. 2-6.

$$C = Edge(I, 'Canny') \quad (2)$$

$$S = Edge(I, 'Sobel') \quad (3)$$

$$L = Edge(I, 'LOG') \quad (4)$$

$$B = Edge(I, 'BED') \quad (5)$$

$$H = C \oplus S \oplus L \oplus B \quad (6)$$

Where C is edge image using canny edge detector, S is edge image using sobel edge detector, L is edge image using LoG edge detector, B is edge image using binary edge detector, \oplus is OR operator and H is edge image using hybrid edge detector.

III. THE PROPOSED EDGE ADAPTIVE DATA HIDING METHOD

Capacity and visual quality are the most important evaluation criteria in edge detection based data hiding methods [29-32]. In this study, a novel edge detection based data hiding method is proposed to improve Bai et al.'s [31] method. In this article, edge detection is used as data hiding map. To increase capacity, mLBSs elimination and a new hybrid edge detector

are used together and the proposed hybrid edge extractor uses Sobel, Canny, LOG and the block-based edge extraction algorithm. To provide high visual quality, 2^k correction [35] method is used. The proposed method generally consists of preprocessing, edge detection, secret data classification, data hiding and data extraction phases. Flowchart of the proposed method is shown in Fig. 2.

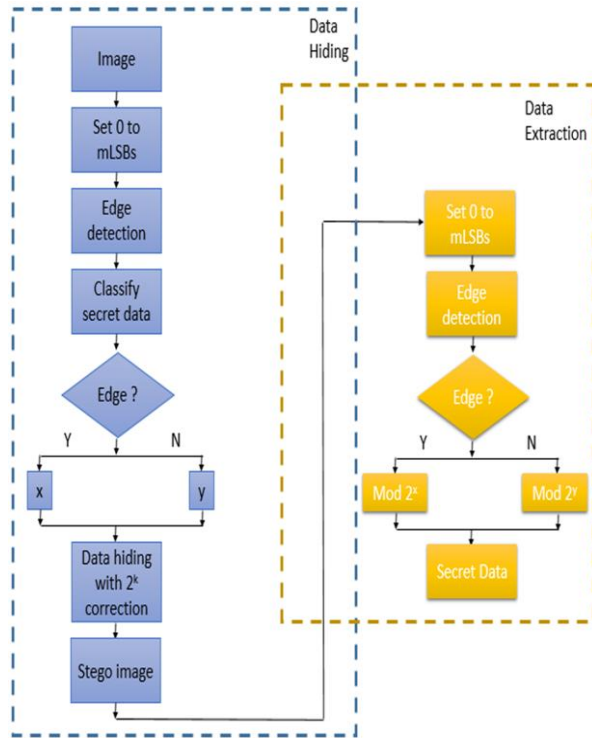


Fig. 2. Flow diagram of the proposed method.

Pre-processing, secret data classification and data embedding steps of the proposed edge based data hiding method are given below.

- **Step 1:** Load image
- **Step 2:** Set 0 to mLSBs by using Eq. 7. This step describes pre-processing phase of the proposed method
$$I = \left\lfloor \frac{I}{2^m} \right\rfloor \times 2^m, 5 < m < 8 \quad (7)$$
- **Step 3:** Apply edge detectors onto image. Edge image is used for secret data classification and data embedding.
- **Step 4:** Classify secret data using edge image. If pixel is edge, xLSBs secret data is embedded into the cover image. Otherwise, yLSBs secret data is embedded into the cover image. Eq. 8. mathematically describes the

presented data embedding function. Where OP is original pixel, SP is stego pixel and SD is secret data.

$$SP = \begin{cases} \left\lfloor \frac{OP}{2^x} \right\rfloor \times 2^x + SD, & \text{if } OP = \text{edge} \\ \left\lfloor \frac{OP}{2^y} \right\rfloor \times 2^y + SD, & \text{if } OP \neq \text{edge} \end{cases} \quad (8)$$

- **Step 5:** Apply 2^k correction to increase visual quality on the stego image. Mathematical description of the 2^k correction is shown in Eq. 9 [35].

$$NSP = \begin{cases} SP - 2^k, & \text{if } SP - OP > 2^{k-1} \text{ and } SP - 2^k \geq 0 \\ SP + 2^k, & \text{if } SP - OP < -2^{k-1} \text{ and } SP + 2^k \leq 255 \\ SP, & \text{Otherwise} \end{cases} \quad (9)$$

Where NSP is new stego pixel and data hiding function is kLSBs. If you use xLSBs data hiding function, k is x. If you use yLSBs data hiding function, k is y. The data extraction steps of the proposed edge adaptive data hiding methods are given below.

- **Step 1:** Load stego image.
- **Step 2:** Set 0 to mLSBs by using Eq. 7.
- **Step 3:** Apply edge detector to stego image. We use edge image as data extraction map.
- **Step 4:** If pixel value is edge, use Eq. 10. to data extraction. Where ED is extracted data.
$$ED = NSP \pmod{2^x} \quad (10)$$
- **Step 5:** If pixel value is not edge, use Eq. 11. to data extraction.
$$ED = NSP \pmod{2^y} \quad (11)$$

IV. EXPERIMENTAL RESULTS

In this section, payload (also called Capacity) and visual quality (also called imperceptibility) are utilized to evaluate performance of the recommended method. Tseng and Leng's [30], Chen et al.'s [29] and Bai et al.'s [31] methods are used to obtain comparisons.

Capacity: One of the commonly used measurement criteria of the steganography. To evaluate edge adaptive data hiding methods is Capacity. In this method, mLSBs elimination and a hybrid edge detector are used for increasing the payload. In addition to, Canny, Sobel, LOG and BED edge detectors are applied on the test images to obtain experiments. The mathematical description of the Capacity of the proposed method is given in Eq. 12.

$$PC = \frac{(NE \times x) + (W \times H - NE) \times y}{W \times H} \quad (12)$$

Where PC is payload and bit per-pixel (bpp) is used to expression it, NE is number of edge pixels, W is width of image and H is height of image. Fig. 3 shows number of edge pixels by Canny, Sobel, LOG, BED and HED edge detectors.




Edge Detector	mLSBs Elimination					
Canny	No	 1779	 1833	 2019	 1772	 2153
	Yes m=6	 2114	 2374	 2523	 2499	 2568
Sobel	No	 669	 827	 673	 927	 862
	Yes m=7	 1290	 1433	 1189	 1169	 1382
LOG	No	 1143	 1243	 1637	 1438	 1439
	Yes m=6	 1468	 1404	 2042	 1874	 1637
BED	No	 1061	 2147	 2133	 2583	 2636
	Yes m=6	 1561	 2415	 2809	 1799	 3001
HED	No	 3032	 3735	 4414	 4299	 4723
	Yes	 4349	 5305	 5897	 5161	 5782

Fig. 3. The number of edge pixels by used edge detectors with test images ‘Lena’, ‘Peppers’, ‘Goldhill’, ‘Boat’ and ‘Barbara’.

Fig. 3 shows that the mLSBs elimination method generally increases the Capacity. Additionally, Eq. 12 clearly showed that FLED Capacity of the Bai et al.'s [31]

method was incorrectly calculated and true payloads of the FLED and HED are shown in Table 1.

TABLE I
COMPARATIVELY RESULTS OF THE PROPOSED METHOD AND BAI ET AL.'S [31] METHOD FOR 128 X 128 SIZE OF IMAGES.





Image	FLED (Bai et al.'s [31] method)	HED (The proposed method)
 Lena	x=2, y=1 Payload=1.2072 bpp	x=2, y=1 Payload=1.2654 bpp
	x=3, y=2 Payload=2.2072 bpp	x=3, y=2 Payload=2.2654 bpp
	x=4, y=3 Payload=3.2072 bpp	x=4, y=3 Payload=3.2654 bpp
 Peppers	x=2, y=1 Payload=1.2089 bpp	x=2, y=1 Payload=1.3238 bpp
	x=3, y=2 Payload=2.2089 bpp	x=3, y=2 Payload=2.3238 bpp
	x=4, y=3 Payload=3.2089 bpp	x=4, y=3 Payload=3.3238 bpp
 Goldhill	x=2, y=1 Payload=1.2133 bpp	x=2, y=1 Payload=1.3599 bpp
	x=3, y=2 Payload=2.2133 bpp	x=3, y=2 Payload=2.3599 bpp
	x=4, y=3 Payload=3.2133 bpp	x=4, y=3 Payload=3.3599 bpp
 Boat	x=2, y=1 Payload=1.2197 bpp	x=2, y=1 Payload=1.3150 bpp
	x=3, y=2 Payload=2.2197 bpp	x=3, y=2 Payload=2.3150 bpp
	x=4, y=3 Payload=3.2197 bpp	x=4, y=3 Payload=3.3150 bpp

Table 1 clearly demonstrates that the proposed HED provides superior payload than FLED of Bai et al.'s [31] method. *Visual Quality*: Peak Signal Noise-to-Raito (PSNR) was used to measure visual quality in this model. The mathematical definition of PSNR is Eq. 13.

$$PSNR = 10 \times \log_{10} \left(\frac{255^2 \times W \times H}{\sum_{i=1}^W \sum_{j=1}^H (OI_{i,j} - SI_{i,j})^2} \right) \quad (13)$$

Where OI is original image, SI is stego image. In this work, 2^k correction is applied on the stego images to increase visual quality. Lena, Peppers, Goldhill, Sailboat, Barbara and Tiffany test images used to obtain the experimental results. These images are 128 x 128 sized and gray-level. The secret data is also randomly generated. The obtained results of the proposed method are shown in Table 2.

TABLE II
THE OBTAINED PSNR (DB) AND CAPACITY (BPP) RESULTS OF THE PROPOSED EDGE ADAPTIVE METHOD USING VARIABLE EDGE DETECTORS AND X AND Y VALUES

Image	x=2, y=1	x=3, y=2	x=4, y=3	x=5, y=4
Canny				
Lena	PSNR=50.12, C=1.12	PSNR=45.03, C=2.12	PSNR=39.28, C=3.12	PSNR=33.16, C=4.12
Peppers	PSNR=50.07, C=1.14	PSNR=44.96, C=2.14	PSNR=39.15, C=3.14	PSNR=33.16, C=4.14
Goldhill	PSNR=49.95, C=1.15	PSNR=44.86, C=2.15	PSNR=39.17, C=3.15	PSNR=33.18, C=4.15
Sailboat	PSNR=49.97, C=1.15	PSNR=44.88, C=2.15	PSNR=39.14, C=3.15	PSNR=33.19, C=4.15
Barbara	PSNR=49.93, C=1.15	PSNR=44.81, C=2.15	PSNR=39.13, C=3.15	PSNR=33.18, C=4.15
Tiffany	PSNR=50.02, C=1.14	PSNR=44.97, C=2.14	PSNR=39.17, C=3.14	PSNR=33.24, C=4.14
Sobel				
Lena	PSNR=50.45, C=1.07	PSNR=45.58, C=2.07	PSNR=39.84, C=3.07	PSNR=33.80, C=4.07
Peppers	PSNR=50.47, C=1.08	PSNR=45.46, C=2.08	PSNR=39.68, C=3.08	PSNR=33.75, C=4.08
Goldhill	PSNR=50.54, C=1.07	PSNR=45.50, C=2.07	PSNR=39.84, C=3.07	PSNR=33.95, C=4.07
Sailboat	PSNR=50.56, C=1.07	PSNR=45.60, C=2.07	PSNR=39.95, C=3.07	PSNR=33.99, C=4.07
Barbara	PSNR=50.42, C=1.08	PSNR=45.44, C=2.08	PSNR=39.79, C=3.08	PSNR=33.85, C=4.08
Tiffany	PSNR=50.57, C=1.07	PSNR=45.64, C=2.07	PSNR=39.92, C=3.07	PSNR=33.97, C=4.07
LOG				
Lena	PSNR=50.44, C=1.08	PSNR=45.46, C=2.08	PSNR=39.69, C=3.08	PSNR=33.73, C=4.08
Peppers	PSNR=50.43, C=1.09	PSNR=45.41, C=2.09	PSNR=39.68, C=3.09	PSNR=33.75, C=4.09
Goldhill	PSNR=50.16, C=1.12	PSNR=45.11, C=2.12	PSNR=39.41, C=3.12	PSNR=33.43, C=4.12
Sailboat	PSNR=50.24, C=1.11	PSNR=45.21, C=2.11	PSNR=39.49, C=3.11	PSNR=33.53, C=4.11
Barbara	PSNR=50.32, C=1.09	PSNR=45.36, C=2.09	PSNR=39.64, C=3.09	PSNR=33.68, C=4.09
Tiffany	PSNR=50.29, C=1.10	PSNR=45.25, C=2.10	PSNR=39.48, C=3.10	PSNR=33.57, C=4.10
BED				
Lena	PSNR=50.37, C=1.09	PSNR=45.45, C=2.09	PSNR=39.64, C=3.09	PSNR=33.69, C=4.09
Peppers	PSNR=49.90, C=1.14	PSNR=44.92, C=2.14	PSNR=39.18, C=3.14	PSNR=33.15, C=4.14
Goldhill	PSNR=49.83, C=1.17	PSNR=44.72, C=2.17	PSNR=38.95, C=3.17	PSNR=32.99, C=4.17
Sailboat	PSNR=50.30, C=1.10	PSNR=45.25, C=2.10	PSNR=39.51, C=3.10	PSNR=33.54, C=4.10
Barbara	PSNR=49.81, C=1.18	PSNR=44.60, C=2.18	PSNR=38.87, C=3.18	PSNR=32.90, C=4.18
Tiffany	PSNR=50.81, C=1.03	PSNR=45.97, C=2.03	PSNR=40.33, C=3.03	PSNR=34.33, C=4.03
HED				
Lena	PSNR=49.29, C=1.26	PSNR=43.97, C=2.26	PSNR=38.27, C=3.26	PSNR=32.17, C=4.26
Peppers	PSNR=48.92, C=1.32	PSNR=43.69, C=2.32	PSNR=37.85, C=3.32	PSNR=31.86, C=4.32
Goldhill	PSNR=48.79, C=1.35	PSNR=43.49, C=2.35	PSNR=37.60, C=3.35	PSNR=31.65, C=4.35
Sailboat	PSNR=49.03, C=1.31	PSNR=43.67, C=2.31	PSNR=37.97, C=3.31	PSNR=31.96, C=4.31
Barbara	PSNR=48.83, C=1.35	PSNR=43.51, C=2.35	PSNR=37.61, C=3.35	PSNR=31.69, C=4.35
Tiffany	PSNR=49.22, C=1.28	PSNR=43.90, C=2.28	PSNR=38.07, C=3.28	PSNR=32.10, C=4.28

The comparison results of the proposed method with existing state-of-art edge-based data hiding methods in the

literature are shown in Table 3. In this comparison, 128 x 128 size of gray level Lena image is used.

TABLE III
COMPARISON WITH THREE PREVIOUSLY PRESENTED EDGE BASED DATA HIDING METHOD.

	Tseng and Leng's [30] method	Chen et al.'s [29] method	Bai et al.'s [31] method		The proposed method	
			Canny	Sobel	Canny	Sobel
Parameters	y=3	x=4, y=3, n=4	x=4, y=3	x=4, y=3	x=4, y=3	x=4, y=3
PSNR (dB)	38.18	37.50	38.34	38.34	39.2866	39.8499
Capacity(bpp)	2.41	2.10	3.11	3.05	3.1290	3.0787
Parameters	y=4	x=5, y=4, n=3	x=5, y=4	x=5, y=4	x=5, y=4	x=5, y=4
PSNR (dB)	33.58	32	30.10	30.69	33.1663	33.8079
Capacity(bpp)	3.16	2.73	4.11	4.05	4.1290	4.0787

The merits of the proposed method are given as below. In this article two novel basic edge extractors are presented.

1- By using 2^k correction higher visual qualities are obtained than the other state of art methods.

- 2- HED based steganography method has very high payload.
- 3- In this article, flaw of the other steganography is presented. Mathematical notations of the edge adaptive steganography methods are defined.
- 4- The proposed methodology is very basic and effective.
- 5- Researchers and developers can simply apply the proposed method to their problem.
- 6- The proposed method is a cognitive method because there is not any meta-heuristic optimization method to increase either payload or visual quality.

The disadvantage of the proposed edge-based steganography method: It is not robust method because it uses pixel domain to embed hidden data.

V. CONCLUSIONS

In this article, a novel edge adaptive data hiding method is presented with high payload and high visual quality. The proposed method consists of preprocessing, secret data classification, data hiding and data extraction phases. In this method, edge detectors are used as data hiding map. 6LSBs and 7LSBs elimination methods are utilized to increase the capacity in the preprocessing phase. Canny, Sobel, Log, BED and HED are used as the edge detection method. Two edge detectors are proposed to increase the payload in this method. The BED method extracts binary edges using the OTSU thresholding method, 2×2 blocks and a rule table. Mathematical definition of this rule table is shown in Eq. 1. The HED method use Canny, Sobel, LoG and BED methods together. Briefly, HED is combination of Canny, Sobel, LoG and BED detectors. The main goal of the HED method is to obtain all edge data in an image. Two separate secret data classes named x and y are created using edge information. The x and y classes are embedded into edge and non-edge pixels using the x LSBs and y LSBs methods respectively. More secret data are embedded into edge pixels than texture pixels because Human Visual System (HVS) is more sensitive to changes in the texture pixels than edge pixels. To increase visual quality, 2^k correction is applied on the stego images. Modulus operator is utilized to data extraction. Briefly, HED and m LSBs elimination are used to increase the payload of the edge adaptive method, and 2^k correction is used for increasing the visual quality.

Experimental and comparative results have shown that the proposed method superior than other edge-based data hiding methods. In the future works, novel edge-based steganography methods can be proposed using this method. Also, the proposed method can be used an image transformation for instance tunable q wavelet transform, discrete wavelet transform, discrete cosine transforms together. The other edge extractor can be used in this method.

REFERENCES

- [1] S.A. Parah, J.A. Sheikh, A.M. Hafiz, G.M. Bhat, Data hiding in scrambled images: a new double layer security data hiding technique, *Comput. Electr. Eng.* (40) (2014) 70–82.
- [2] O. Cetin, A.T. Ozcerit, A new data hiding algorithm based on color histograms for data embedding into raw video streams, *Comput. Secur.* 28 (7) (2009) 670–682.
- [3] S.Y. Shen, L.-H. Huang, A data hiding scheme using pixel value differencing and improving exploiting modification directions, *Comput. Secur.* (48) (2015) 131–141.
- [4] G. Kipper, *Investigator's Guide to Data Hiding*, Auerbach Publications A CRC Press Company, Boca Raton, London, New York, Washington, DC, (2004) 20–26.
- [5] I.J. Cox, J. Killian, T. Leighton, T. Shamon, A secure robust watermark for multimedia, *IEEE Trans. Image Process.* (12) (1997) 1673–1687.
- [6] A. Phadikar, S.P. Maity, On protection of compressed image in fading channel using data hiding, *Comput. Electr. Eng.* 38 (5) (2012) 1278–1298.
- [7] N.F. Johnson, Z. Duric, S. Jajodia, *Information Hiding: Data Hiding and Watermarking-Attacks and Countermeasures*, Kluwer Academic Publishers, Boston, MA, 2001.
- [8] A. Miller, *Least Significant Bit Embeddings: Implementation and Detection*, May 2012.
- [9] S.H. Lee, DWT based coding DNA watermarking for DNA copyright protection, *Inform. Sci.* (273) (2014) 263–286.
- [10] E. Avci, T. Tuncer, D. Avci, A Novel Reversible Data Hiding Algorithm Based on Probabilistic XOR Secret Sharing in Wavelet Transform Domain, *Arabian Journal for Science and Engineering*, 41, (8), (2016) 3153-3161.
- [11] H. Noda, M. Niimi, E. Kawaguchi, High-performance JPEG data hiding using quantization index modulation in DCT domain, *Pattern Recogn. Lett.* 27 (5) (2006) 455–461.
- [12] P.C. Chang, K.L. Chung, J.J. Chen, C.H. Lin, T.J. Lin, A DCT/DST-based error propagation-free data hiding algorithm for HEVC intra-coded frames, *J. Vis. Commun. Image Represent.* (2) (2014) 239–253.
- [13] B. Chen, G. Coatrieux, G. Chen, X. Sun, J.L. Coatrieux, H. Shu, Full 4-D quaternion discrete Fourier transform based watermarking for color images, *Digit. Signal Process.* (28) (2014) 106–119.
- [14] P.-Y. Lin, C.-S. Chan, Invertible secret image sharing with data hiding, *Pattern Recognition Letters* (31) (2010) 1887–1893.
- [15] T. Tuncer, E. Avci, A reversible data hiding algorithm based on probabilistic DNA-XOR secret sharing scheme for color images, *Displays*, (41) (2016) 1-8.
- [16] M. I. S. Reddy, A. P. S. Kumar, Secured Data Transmission Using Wavelet Based Data Hiding and Cryptography by Using AES Algorithm, *International Conference on Computational Modeling and Security, Procedia Computer Science* (85) (2016) 62 – 69.
- [17] E. J. S, P. Ramu, R. Swaminathan, Imperceptibility—Robustness tradeoff studies for ECG data hiding using Continuous Ant Colony Optimization, *Expert Systems With Applications* (49) (2016) 123–135.
- [18] T.-S. Nguyen, C.-C. Chang, A reversible data hiding scheme based on the Sudoku technique, *Displays* (39) (2015) 109–116.
- [19] T. Tuncer, E. Avci, Data Hiding Application with Gokturk Alphabet Based Visual Cryptography Method, *Journal of the Faculty of Engineering and Architecture of Gazi University* (31:3) (2016) 781-789.
- [20] Z.-H. Ou, L.-H. Chen, A steganographic method based on tetris games, *Information Sciences* 276 (2014) 343–353.
- [21] C.K. Chan, L.M. Cheng, Hiding data in images by simple LSB substitution, *Pattern Recognit.* (27) (2004) 469–474.
- [22] S. Mahato, D. K. Yadav, D. A. Khan, A minesweeper game-based data hiding scheme, *Journal of Information Security and Applications* (32) (2017) 1–14.
- [23] X. Liao, J. Yin, S. Guo, X. Li, A. K. Sangaiah, Medical JPEG image data hiding based on preserving inter-block dependencies, *Computers and Electrical Engineering* (2017) 1–10.
- [24] H.-J. Shiu, B.-S. Lin, C.-H. Huang, P.-Y. Chiang, C.-L. Lei, Preserving privacy of online digital physiological signals using blind and reversible data hiding, *Computer Methods and Programs in Biomedicine* (151) (2017) 159–170.
- [25] H.D. Yuan, Secret sharing with multi-cover adaptive data hiding, *Inform. Sci.* (254) (2014) 197–212.
- [26] D. Wu, W.H. Tsai, A steganographic method for images by pixel value differencing, *Pattern Recognit. Lett.* (24) (2003) 1613–1626.

- [27] M. S. Subhedar, V. H. Mankar, Image data hiding using redundant discrete wavelet transform and QR factorization, *Computers and Electrical Engineering* (54) (2016) 406–422.
- [28] S. U. Maheswari, D. J. Hemanth, Frequency domain QR code based image data hiding using Fresnel transform, *Int. J. Electron. Commun.* (69) (2015) 539–544.
- [29] W.J. Chen, C.C. Chang, T.H.N. Le, High payload data hiding mechanism using hybrid edge detector, *Expert Syst. Appl.* (37) (2010) 3292–3301.
- [30] H.W. Tseng, H.S. Leng, High-payload block-based data hiding scheme using hybrid edge detector with minimal distortion, *IET Image Process.* (8) (2014) 647–654.
- [31] J. Bai, C.-C. Chang, T.-S. Nguyen, C. Zhu, Y. Liu, A high payload steganographic algorithm based on edge detection, *Displays* (46) (2017) 42–51.
- [32] J. Canny, A computational approach to edge detection, *IEEE Trans. Pattern Anal. Mach. Intell.* (6) (1986) 679–698.
- [33] R. Maini, H. Aggarwal, Study and comparison of various image edge detection techniques, *Int. J. Image Process.* (3) (2009) 1–11.
- [34] E.K. Kaur, E.V. Mutenja, E.I.S. Gill, Fuzzy logic based image edge detection algorithm in MATLAB, *Int. J. Comput. Appl.* (1) (2010) 55–58.
- [35] S. Sun, A novel edge based image steganography with 2^k correction and Huffman encoding, *Information Processing Letters* (116) (2016) 93–99.
- [36] T. Y. Goh, S. N. Basah, H. Yazid, M. J. A. Safar, F. S. A. Saad, Performance analysis of image thresholding: Otsu technique, *Measurement* (114) (2018) 298–307.

BIOGRAPHY



TÜRKER TUNCER, was born in Elazığ, Turkey in 1986. He received the B.S. degree from the Firat University, Technical Education Faculty, Department of Electronics and Computer Education in 2009, M.S. degree in telecommunication science from the Firat University in 2011 and Ph.D. degree department of software engineering at Firat University in 2016. He works as research assistant Digital Forensic Engineering, Firat University. His research interests include data hiding, image authentication, cryptanalysis, cryptography, feature extraction, machine learning and biomedical engineering.



YASİN SÖNMEZ, was born in Diyarbakır, Turkey in 1986. He received the B.S. degree from the Firat University, Technical Education Faculty, Department of Electronics and Computer Education in 2010, M.S. degree in computer science from the Firat University in 2012 and Ph.D. degree department of software engineering at Firat University in 2018. His research interests include, , artificial intelligence, , and information security.

The Impact of Emerging Renewable Energy on Capacity Mechanisms in Power Systems and Expert Opinion

M.R. TUR

Abstract—With the increasing energy demand, the growing capacity of renewable energy sources and the impact of developing competition, it is desirable to manage the market with appropriate investments along with the electricity market and optimum load distribution. In line with this demand, supply security and energy quality play an important role day by day. This includes the production capacity and the long-term security of the system, reflecting the system's ability to stand in unexpected events and sudden load changes. The demand side seems to have insufficient support to the market for new capacity planning to ensure this coverage. This problem can be solved by producing additional capacity. Basically, it is aimed to reduce investment risk for production companies and / or investors and to provide higher supply security and lower price fluctuations to consumers. The concern of not investing in electricity generation capacity to meet the maximum load level has led to investments in capacity utilization in the form of capacity mechanisms of developed and developing states. In this study, an academic analysis of the capacity mechanism of the renewable energy resources and the capacity analysis of the capacity mechanism were made and expert opinions were presented, the latest developments in the energy market were examined and the reliability solutions that could be appropriate to the national electricity market were proposed.

Index Terms— capacity mechanism, electricity market, operation reserves, power quality, supply security.


I. INTRODUCTION

POWER MARKETS are experiencing major changes in their investments in supply security and production capacity along with the search for improved technology and comfort. Together with these developments, there are increasing requirements for reserve production capacity. Production capacity varies depending on the increasing share of variable renewable energy sources (such as wind and solar energy) in line with the needs developed. In addition, these plants cause load factors due to shorter and more variable operating times. Thus, in some periods, the peak load on the

demand side cannot be met and in such cases the limits on how much electricity prices may increase may not be profitable. The increasing share of the electricity market reduces the wholesale electricity prices in a competitive market. This is mainly due to the fact that the marginal cost of variable renewable energies is low or close to zero. Therefore, the profitability of these power plants is decreasing due to the fact that both the working hours are variable and the wholesale prices are low. With the formation of trends, electricity services lack a comprehensive incentive to invest in new generation capacities. This situation is generally referred to as "the problem of lost money". Thus, only the best available power plants used during short periods of peak demand can be used. In the EU electricity sector, as in the electricity sectors of other countries, although generally characterized by excess capacity supply, capacity shortages may occur in case of high demand from low-capacity power plants (due to lack of wind or sun, for example). This leads to concerns that there will be insufficient production capacity in relation to the load distribution to ensure the safety of my electricity supply. The regulatory mechanism should review the main criteria to be considered in the design [1,2]. In addition to production resources, energy storage, demand side management, and flexible demand sources (demand side response) can also contribute to resource adequacy. All this determines the power system's ability to ensure the reliability of the electricity supply. Capacity mechanisms are generally argued to help reduce the cost of large-scale wind energy development to reduce the likelihood of loss of load. As a result of optimization, it is emphasized the importance of the capacity mechanism by identifying the most suitable type of heating system in terms of the heat load density in the unit area [3-5]. This mechanism is defined as the administrative measure to ensure the desired level of supply security by charging production plants for the availability of resources.

The Energy Market is considered to be an important part of the EU 2020 strategy, as it is recognized as an important means of providing economic, safe and sustainable electricity supply in the future [6]. Basically, it aims to increase competition by opening national markets to foreign participants, thereby increasing supply security and cost efficiency [7-10]. In addition, the European Commission has recently raised concern that these objectives could be harmed by weakly harmonized national market design changes across Europe [11]. In addition, non-coordinated capacities may disrupt cross-border trade and hinder the success of the Domestic Electricity Market in Europe [12,13].

MEHMET RIDA TUR, is with Department of Electrical and Energy University of Batman University, Batman, Turkey, (e-mail: mrida.tur@batman.edu.tr).

 <https://orcid.org/0000-0001-5688-4624>

Manuscript received June 11, 2019; accepted July 2, 2019.
DOI: [10.17694/bajece.575097](https://doi.org/10.17694/bajece.575097)

II. CAPACITY MECHANISM

Our national power system in January 2018, the rules regarding the capacity mechanism to be operated by Turkish Electricity Transmission Corporation (TEIAS) were determined in order to establish an adequate installed power capacity, including the reserve capacity required for supply security in the electricity market, and / or to maintain reliable installed power capacity for long-term system security. At the same time, in the light of concerns over energy resource adequacy, many countries, particularly EU Member States, have introduced capacity mechanisms. In the literature, alternate solutions are discussed consecutively in order to reach the capacity adequacy adopted in different markets. These solutions are the public offering of strategic capacity reserves, payments and capacity obligations for these capacities [14,15]. These mechanisms consist of measures to meet the electricity production capacity in order to meet the demand in the long term and medium term. Basically, two such capacity mechanisms are needed to ensure that the reserve production capacity is economically feasible, directly linked to the organization of the electricity market. The availability of battery energy storage systems to be used in the capacity mechanism in the network is taken into account and further analyzes have been carried out to take into account the overvoltage reduction by shaving the photovoltaic production at the highest level [16-18]. Basically, this capacity includes the capacity to take into account the capacity of the plants, the priorities to be allocated to the domestic resources, the annual budget based on the capacity payments, the budget to be used for the budget payments, the calculation of the cost components for the capacity payments, the capacity to be taken into the capacity It should be determined by including the procedures and principles regarding the calculation of the payments and the obstacles to payment. Whether capacity mechanisms are required or only in a time-based market, variant rare pricing can provide sufficient incentives to provide backup capacity. Taking into account the fact that the cooperation between countries can increase the cost efficiency by providing cooperation. Another important issue is the optimum geographical scope of capacity markets. However, as long as a limited amount of electricity can flow between the cross-border networks due to a limited interconnection capacity, a capacity mechanism between countries is not possible [19, 20].

III. TYPES OF CAPACITY MECHANISMS USED IN THE POWER MARKET

The Energy Regulators Cooperation Agency (ACER) states that there are six types of capacity mechanisms as shown in Figure 1 [21]. Decision-making unit policy makers in unit-centered mechanisms. They make decisions about the size of the capacity volume. In addition, policy-makers allow price setting based on marketing. In price-based mechanisms, policy makers also take an active role. Here, after determining the price, the management allows investors to decide that they are willing to invest in a certain price.

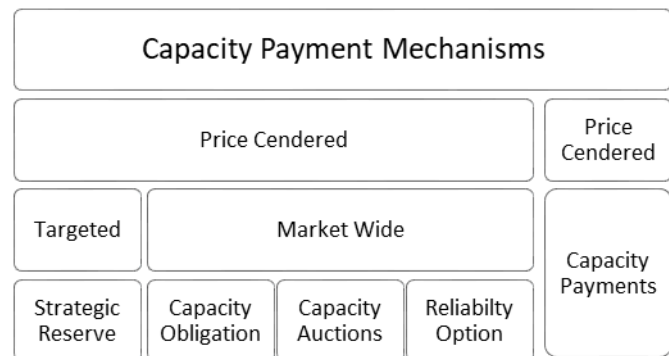


Fig. 1. Classification of capacity mechanism types

Although the targeted mechanisms cover only certain power plants or technologies, the mechanisms in the electricity market try to establish the system balance by meeting the needs of all capacity providers. An additional distinction is made between the decentralized management mechanisms in which contracts are regulated (eg capacity requirements) and the central mechanisms (eg through capacity tenders) where contracts are centrally provided. There are six major mechanism models under unit-centered and price-centered capacity mechanisms shown in Table I [22,23].

A. Strategic reserve

It is the type of reserve controlled by a central organization. These establishments determine the reserve capacity required for years. It then provides this capacity through a competitive tender (as a strategic alternative) to the contract. Power plants that have established bilateral agreements cannot participate in the electricity market, which only comes into play if there is a lack of capacity and a lack of capacity according to the predetermined criteria. Strategic reserves are mainly used by Belgium, Germany, Poland and Sweden.

B. Capacity obligation

The consumer or electricity suppliers involved in the power system have to reduce the amount of capacity or reserve capacity that they need to keep, along with their consumption or supplies in the planning. This is usually done by certificates and licenses issued by capacity providers. Energy providers or consumers face a financial penalty if they do not contract at the required quantity level. In general, these capacity mechanisms are used in France.

C. Capacity auctions

The total capacity required for the system is determined years in advance. This capacity is provided by the center of the auction. Energy providers in the system offer a capacity amount that reflects the cost of building new capacity for their payments. Thus, the new capacity created in line with the need is only achieved by joining the energy market. Tenders for the required capacities cover new capacity requirements to reduce existing capacity and not to make investment decisions based on market price signals. In general, this capacity is used by the UK to ensure security of supply.

D. Reliability options

The capacity provider involved in the power system arranges a mutual agreement to provide preference to the consumer or distribution company, which offers the other party the option of providing electricity from a predetermined transaction price. In the preferences offered to the consumer or distribution company, the spot market price uses the rare option when the option exceeds the trading price of the option. This option is generally used by Italy, where a capacity market is planned based on reliability options.

E. Capacity payments

Capacity fees and tariffs are determined by the market regulator, which is paid to capacity providers. In spite of the amount of capacity required, the receiving facilities only provide energy by continuing to participate in the energy market. The capacity payments for the production and consumption balance are currently used primarily in Italy, Poland, Portugal and Spain; Ireland is paying for a total capacity across the market.

F. Business Spares

The business reserve market does not completely eliminate the investment cycle, but it does not completely eliminate it. However, it may have an effect of increasing imports instead of investment in interconnected systems. Basically, the system operator is able to give the signals of the capacity demand early, just before the energy market, by providing high value.

TABLE I. CHARACTERISTICS OF APPLIED CAPACITY MECHANISMS

Title	A	B	C	D	E	F
Audit	Yes	Yes	No	No	Yes	Yes
Supply efficiency	--	+	++	+	-	±
Applicability	++	+	±	+	++	++
Market compatibility	+	±	+	-	+	+
Robustness against manipulation	+	±	+	±	±	+
Impact resistance	-	±	-	+	-	-
Demand for price elasticity of demand	±	+	++	+	±	±
Ensuring investment stability	±	++	+	++	-	±

All these capacity mechanisms vary depending on the structure of the electricity market. Since the factor that is the binding factor is the structure of the market, the reserves provided by the bilateral agreements are very important. In addition, the day ahead and day ahead market will have a more stable process with accurate prediction and load controls before real time. Thus, the correct planning of the mechanism is highly effective in energy quality. Voltage disturbances and

fluctuations that affect energy quality without impact are frequently encountered in poor network systems. The load currents in the system because non-sinusoidal voltage drops. With this effect, energy quality deteriorates [24]. On the basis of the voltage distortions, the supply demand imbalance is due to the production and consumption estimates, which are generally not done correctly. The most important factor affecting the unrealized estimates is the renewable production capacity.

IV. EXISTING EU CAPACITY MECHANISM PRACTICES

In the case of limited capacity in power systems, a system with no existing installed capacity (as MW) may be created to meet the service demand at a given time. In such a system, there are two important concerns regarding the participation of intermittent and variable renewable energy resources in capacity mechanisms. The first is the ability to be present when needed, and the second is the negative impact on the economic signals. A system with a capacity limitation attracts more attention in the world.

In a capacity-constrained system, time dependence of supply makes the cut-off an important factor. In such a system, there is a possibility that renewable resources may not be used during the famine. Therefore, the flexibility of such resources makes it harder to evaluate the actual contributions to improve supply security.

With all the developments, it is possible to reduce the capacity prices and create a negative impact on the economic signal by joining the renewable energy sources that have been supported under the current conditions in the capacity markets. As a result of this development, the capacity mechanism may offer an option to provide sufficient wages to overcome the missing money problem traditional and to provide an adequate incentive for the existing traditional capacity or new investment. Therefore, measures should be taken due to the risk that the capacity mechanism will be ineffective in achieving the final policy objectives. One way to address the concern about the artificial reduction of market price signals can be achieved by modifying renewable support programs to accept revenue streams derived from capacity mechanisms.

The capacity mechanisms used and / or deemed necessary in power systems directly affect competition between producers and consumers in the EU electricity market. This competition often requires state aid, which requires it to be subject to EU state aid rules. For the period of 2014-2020, the principles and principles of state aid for environmental protection and energy, which are organized within the framework of forward planning, explain the items of the programs and drafts for the evaluation of capacity mechanisms [25]. If the planned capacity mechanisms are over 15 million euros per project, they should notify the European Commission. The Commission considers the proposed capacity mechanisms based on six criteria. These criteria are listed below.

A. Criteria 1:

Measures should pursue the common goal, ie the problem of short or long-term production adequacy needs to be solved. Measures are mainly divided into two groups, of which short-term measures generally support the maintenance of existing backup capacities, while long-term measures encourage new investments and plans for the power system. The capacity mechanism should pay not only the electricity produced but the required capacity. The analysis of the unreachable energy against the production capability should be in accordance with the ENTSO-E estimations and the European production adequacy estimates.

B. Criteria 2:

The necessity of the capacity mechanism, the underlying causes of the existing problems, especially the identification of possible market failures and regulatory barriers, needs to be resolved. In addition, alternatives to the capacity mechanism will be examined.

C. Criteria 3:

Plans for capacity mechanism should not be independent of technology. Direct use of intelligent systems in decision-making systems. It should also be impartial between the participants involved in the system and the investors. It is also important to consider the development of connections.

D. Criteria 4:

The most fundamental mechanism should not have a negative impact on competition and trade movements. Thus, it should not interfere with the investment in the interconnections. In particular, it should not interfere with the functioning of the market match. The energy market should be open to all participants and the dominant situations should not be strengthened. It should also support low carbon technologies, which are generally considered in energy production planning, in the capacity mechanism.

More effective allocations should be made by working with Member States to ensure that the capacity-building commission complies with state aid rules for existing and planned capacity mechanisms.

E. Criteria 5:

It is important to make decisions based on cost-benefit analysis in planning as well as system reliability and sustainable energy. It should also encourage the costs to be paid or on measures that do not involve standard commercial risks.

F. Criteria 6:

Measures taken for system protection and energy sustainability should be proportionate. For this purpose, storage systems should be provided with the latest technologies and new applications such as pumping application should be preferred.

V. ACADEMIC ANALYSIS AND EXPERT OPINION

The development of renewable resources around the world can have a profound impact on revenues for traditional

producers and change the balance of energy and capacity market incomes, creating uncertainties in production forecasts. There are three main reasons for this effect on conventional plants. Firstly, intermittent and changed renewable resources reduce conventional generator revenue from the amount of electricity that is expected to be sold. Then, intermittent renewable sources reduce the cost of conventional generator revenue at low prices or plan energy directly to the markets, regardless of marginal cost. Finally, increased flexibility requirements increase costs resulting from more variable operations for traditional manufacturers. All of these effects drive traditional generators to reduce energy revenues. Consequently, restructured markets with a larger proportion of intermittent and variable renewable energy production should have higher capacity payments than those with non-intermittent renewable energy generation. This requires a mechanism for serious capacity planning.

In this study, a special effort has been made to evaluate the effects of capacity mechanisms on trade in the energy market. A large-scale sector survey was initiated on November 30, 2016 as a component and stage of clean energy planning, and a report was published as a result of the study, which is the first and only research focusing on the industry sector. It has been prepared based on an analysis of the existing or planned 35 capacity mechanisms of the EU member states, which report that member states often do not adequately assess the capacity mechanisms for their needs. The report also concluded that the assessment of cost-benefit assessments and capacity mechanisms is based on the rule. In many Member States, market and legal failures hamper the price signals needed to ensure appropriate levels of supply security. Therefore, he emphasized that the report should be accompanied by market reforms in accordance with the capacity mechanisms. The report identified that most of the capacity mechanisms offered by Member States were not designed to address a clearly defined problem with regard to security of supply. Thus, member states have not sufficiently assessed the situation on security of supply. They have also failed to provide capacity mechanisms for a security that is always justified for supply security.

This study summarizes the ways of improving the design of capacity mechanisms as outlined below:

- The capacity mechanism must match the requirements in the specified power system. While long-term competence is best handled by a market-wide mechanism, transient measures, such as strategic reserves, require transitional measures.
- For regionally limited production sufficiency issues, it is foreseen that improving network connections and adapting the geographic boundaries of the offer areas will probably provide an appropriate solution.
- In some rare cases, payments made to reduce electricity consumption may be appropriate to promote flexible demand. However, there is another point to note that this energy should not turn into subsidies for over-consumption.

- The cost paid for the capacity mechanism is determined by market conditions, which should be used in a competitive process to determine.

The capacity mechanisms obtained should be open to the participation of capacity producers in neighboring countries. Thus, domestic and foreign capacities and interconnections can be promoted, which also reduces system costs.

In the literature, market prices are currently faced by market and legal failures as the market prices do not meet the fixed cost of traditional production capacity, which affects the price and load factors of electricity demand, electrical ceiling prices and renewable electricity sources defined as variable. This situation leads to the failure to make new investments and to close the existing power plants. Within the scope of this study, the analysis of the situation analyzed, the examination of new capacity mechanisms, and the non-coordinated national capacity mechanisms, may disrupt the market and competition and hinder the completion of the internal energy market. National support given to non-economic power plants may affect price formation, but may hinder the transition to a low-carbon economy. In addition, there are non-market capacity mechanisms, which may lead to insufficient capacity investments. For this reason, non-market mechanisms may cause competition to deteriorate.

External capacity will be capacity without participation in the network, which will have minimal impacts on markets and investments, and capacity and capacity will change for the country. This study concludes that only the price signals from the energy market need to be taken into account if capacity investments are not made in time to the required production capacity. As there is currently no EU-wide capacity mechanism program, priority should be given to harmonized capacity mechanisms at the regional level. In 2016, the report was prepared by the International Energy Agency (IEA), which concluded that capacity mechanisms could play an important role in providing resource capacity in these liberalized markets. In addition, according to this report, an optimally designed capacity is based on three main components of the market:

- A predetermined demand level should be determined based on the assessment of resource qualification needs,
- Provide a working mechanism for price discovery,
- Create a well-defined capacity product that is technologically undefined and compatible with current innovations,

Well-designed capacity mechanisms should be provided in line with the targets set, which can help solve the problem of lost money without breaking the wholesale energy markets. IEA considers that properly designed wholesale electricity markets are a prerequisite for the functioning and process of capacity markets. It acknowledges that there are benefits in favor of the mechanism by ensuring that external cooperation is ensured by ensuring that regional cooperation moves beyond the boundaries of capacity, without the need to fully harmonize capacity mechanisms.

The report, prepared in 2016, focused on capacity mechanisms and carbon emissions, which were published by the Institute for Overseas Development. It is aimed to reduce the share of existing and planned capacity mechanisms, depending on fossil fuel power plants in the EU and the US, which will undermine carbohydrates. As a result, the implementation of the capacity mechanism is based on political motivations rather than strictly analyzing its needs. This study shows that governments should adopt a large-scale system to support decarbonization. This result uses market design to improve energy quality and improve system reliability. It also includes a detailed analysis of the role of demand-side management in the capacity mechanism, the state of the economically competitive market, optimum storage to ensure low carbon flexibility, and reliability issues that explain interconnection. New investment decisions simulation in electricity markets reveals that both capacity mechanisms and limited pricing are equally effective when investors are ready to take risks. It also determines that investors are more effective in risk avoidance than capacity mechanisms.

Together with the Ministry of Economic and Financial Affairs of the State, the Ministry of Energy conducts research, which is about competition policy and internal energy market. In preliminary studies, a non-discriminatory and competitive market design is proposed for capacity mechanisms. It is recommended to ensure that energy providers in all Member States are open to the market and that the price paid for capacity is determined by a competitive process. Clear rules have been advocated for the deployment of strategic reserves, which should not be used to keep energy prices in the market low or to strengthen their positions.

VI. RECOMMENDATIONS AND ROADMAP FOR CAPACITY MECHANISM

Energy capacity markets need to be examined in the context of increasing and / or changing renewable energy levels. There are significant differences between the incentives for operational performance provided by States, methods for calculating qualified capacity for variable renewable energy and energy storage, and demand curves for capacity. In addition, there are big differences in capacity market swap prices for production. In this study, it is argued that electricity market design should continue to develop in order to obtain cost-effective policies for resource adequacy.

New capacity investments can be realized by providing capacity signals when market-based supply security solutions are implemented. With these solutions, the capacity demand is expressed in a clear and explicit way, rather than implied by the signals of the price of electrical energy, reducing the investment risk of the manufacturing companies and providing higher supply security and lower price volatility benefits for the consumers. From the six different capacity mechanisms we have examined, it seems that the most effective solution is the capacity requirement mechanism. However, Turkey needs to be adapted to the market structure of the electricity market based on bilateral agreements. The central tenders and bilateral agreements of trust contracts seem to be more untested and innovative solutions. Emergency supply security

as a market-oriented solution with having to provide new capacity investment in the capacity of Turkey mechanism for electricity market practice fast, easy and inexpensive should be evaluated for applicability. From this perspective, the establishment of the Pennsylvania-New Jersey-Maryland type capacity market is costly and time consuming.

The ultimate solution for long-term security of supply in Turkey electricity market, while in that direction, the easiest and fastest solution to meet the immediate capacity needs in the short term, all retail companies to estimate fixed quantity made according to the load and spare capacity in addition to the optional transitional contracts, such as 15%, providing or to impose an option contract. In the future, it is useful to establish forward capacity market to complete the forward electricity market. More detailed examination of these issues and to produce the original market-oriented solutions to Turkey and supply security must be implemented.

The availability of the electricity market has been characterized by market interventions that have been freed from long-term equilibrium in the market. The most important issue among these interventions is the policy-driven expansion of renewable production capacity, especially based on solar and wind. Renewable capacity at the installed powers is characterized by operational and local characteristics, which are substantially different from the convective production capacity. At the same time, conventional plants need to be moved away due to the moratoriums on life, falling profitability, carbon emissions and nuclear energy. It is imperative to invest in the new capacity to meet the demands of a new electrical system, with the share of renewable and low carbon emission capacity for new technologies.

In addition to these developments, there are concerns about the ability of market models, such as the global target model, to provide adequate investment incentives. Therefore, the current electricity market model, which is the current investment climate, has many difficulties due to a number of policies and market uncertainties, which are summarized below.

- **Operation reserve Uncertainties:** In case of unforeseen events in power systems, these events can be both failure and supply-demand imbalance, energy sustainability in the system should be ensured. In interconnected systems, each generation plant involved in the grid shall maintain a portion of its capacity as a spinning reserve, defined as the operating reserve. Thus, if necessary, the required amount of energy should be provided with this reserve capacity.
- **Uncertainties in climate policy:** Climate policy negotiations and design processes for carbon emission are progressing very slowly. This leads to uncertainties in long-term outcomes, particularly in terms of the framework conditions for renewable production, including carbon pricing and targets and criteria, including regional and global policies.
- **Uncertainties in the Electricity Market:** With the renewable energy, the integration of the electricity

market is evolving day by day, but there are some uncertainties about market inferences in the long run, which is influenced by the impact of system challenges, the impact and implementation of flow-based market integration, and the degree of physical market integration. In addition, these uncertainties include the rapid developments in the gas markets in general and the implications for the implementation of gas prices.

- **System Uncertainty in regulatory parameters:** Some uncertainties in the Energy Market need to be solved, which are the market design situation as a result of changes in mechanisms such as flexibility payments, increased demand-side participation, and improved payment mechanisms for system services.
- **Uncertainties for technology and cost development:** Technologies need to be developed in line with the developing infrastructure and the needs of the society. At the same time, the modern model should be adopted by introducing these innovations and by changing the price structures and capacity needs and payments significantly. Energy investments and new production stations have infrastructure investment costs for design. The most obvious example is the rapid decline in solar energy in recent years and the large-scale reduction in installation costs. These and similar situations adversely affect investors' investment in new production capacities.
- **Economic Uncertainties:** There are general economic and financial conditions that affect investors' decisions negatively, which constitutes a major hitch in the energy sector. This situation shows that investors are directly dependent on state policies. Thus, governments need to present new projections for energy investments and planning.
- **Uncertainties in Renewable Energy:** Production systems such as wind and solar, which negatively affect the production balance in the energy market, directly affect production forecasts, which are a significant problem in the energy sector. This creates difficulties in maintaining the balance between production and consumption. Supply and demand imbalance bring about deterioration in energy quality. This situation, which is directly affected by the frequency, causes disruption to the network. In order to reduce the impact of these deteriorations, mechanisms are designed to meet the capacity requirements required to be carried out. For this reason, governments need to make adequate capacity and operational reserve planning for reserve and energy planning.

VII. CONCLUSION

As for the capacity mechanism, the long-term capacity of the energy markets remains uninterrupted and inadequate in academic studies. Considering the major changes in the electricity market, it is hard to conclude that the market target

model of the market target model on an empirical basis has the capacity to deliver capacity.

However, there is a clear consensus on the need to improve the efficiency of the domestic internal market: In the day ahead and day market, the implementation of the capacity mechanism should be increased in line with the target model and the cooperation between the parties in the balancing markets should be increased, which will provide better price signals and a better basis in the long term.

In line with government investments and newly developed regulations, it will provide liquidity along with strong investments and better competition in the markets. Market-based price signals need to be maintained for renewable energy generation (based on solar and wind power). In addition, new developments and investments in technologies need to be provided with sufficient support to encourage flexible solutions in production as well as in production.

As a result of all these developments and halves, sustainable energy can be provided to increase the energy quality in the power system, which will be achieved by the realization of the capacity mechanism. As system administrators expand the interconnected network in network models, as long as the required reserve requirement is determined correctly, as long as renewable energy production estimates based on wind and solar production are made more accurate and demand side management is well controlled, the capacity mechanism system will be more realistic.

REFERENCES

- [1] C. Battle, Ignacio J. Perez-Arriaga, "Design criteria for implementing a capacity mechanism in deregulated electricity markets" *Utilities Policy* Volume 16, Issue 3, September 2008, Pages 184-193
- [2] A. D. Baddeley, Denise Scott, Rosemary Drynan and Janet C. Smith, "Short- Term Memory and The Limited Capacity Hypothesis", *British Journal of Psychology*, Volume 60, Issue 1,
- [3] M. Cepeda, D. Finon, "How to correct for long-term externalities of large-scale wind power development by a capacity mechanism" *Energy Policy* Volume 61, October 2013, Pages 671-685,
- [4] Igor K. Shesho, Risto V. Filkoski and Done J. Tashevski, "Techno-Economic and Environmental Optimization of Heat Supply Systems in Urban Areas" *Thermal Science*: 2018, Vol. 22, Suppl. 5, pp. S1635-S1647
- [5] Bingtuan G., Xiaofeng L., Cheng W. and Yi T., "Game-theoretic energy management with storage capacity optimization in the smart grids" *J. Mod. Power Syst. Clean Energy* (2018) 6(4):656-667
- [6] European Commission, 2010. Communication from the Commission: *Energy 2020. A Strategy for Competitive, Sustainable and Secure Energy* (COM (2010) 639, November 10 m 2010).
- [7] Booz, Company, Newbery, D., Strbac, G., Pudjianto, D., Noël, P., LeighFisher, 2013. *Benefits of an integrated European Energy Market. Final Report Prepared for Directorate-General Energy European Commission* (July 20).
- [8] Creti, A., Fumagalli, E., Fumagalli, E., 2010. Integration of electricitymarkets in Europe: relevant issues for Italy. *Energy Policy* 38, 6966-6976
- [9] Jamasb, T., Pollitt, M., 2005. Electricity market reform in the European Union: review of progress toward liberalization & integration. *Energy J.* 26, 11-41.
- [10] Pellini, E., 2012. Measuring the impact of market coupling on the Italian electricity market. *Energy Policy* 48, 322-333
- [11] European Commission, 2013. Communication from the commission: delivering the internal electricity market and making the most of public intervention. C (2013), 7243 (November 5).
- [12] ACER, 2013. Capacity remuneration mechanisms and the internal market for electricity. The Agency for the Cooperation of Energy Regulators Report (July 30).
- [13] RAP, 2013. Capacity markets and European market coupling — can they co-exist? The Regulatory Assistance Project Discussion Draft (March 13, 2013)
- [14] D. Finona, V. Pignob, "Electricity and long-term capacity adequacy: The quest for regulatory mechanism compatible with electricity market", *Utilities Policy*, Volume 16, Issue 3, September 2008, Pages 143-158, doi.org/10.1016/j.jup.2008.01.002
- [15] H. Chao, "Demand Response in Wholesale Electricity Markets: The Choice of the Consumer Baseline," *Journal of Regulatory Economics*, (2011).
- [16] W. Hogan William "Electricity Market Design Energy and Capacity Markets and Resource Adequacy", Mossavar-Rahmani Center for Business and Government John F. Kennedy School of Government Harvard University, 2015
- [17] Dario Garozzo, Giuseppe Marco Tina and Dezso Sera, "Comparison of The Reactive Control Strategies in Low Voltage Network with Photovoltaic Generation and Storage" *Thermal Science*: 2018, Vol. 22, Suppl. 3, pp. S887-S896
- [18] Bin L., Xingchen L., Xiaoqing B. and Zhineng L., "Storage capacity allocation strategy for distribution network with distributed photovoltaic generators", *J. Mod. Power Syst. Clean Energy* (2018) 6(6):1234-1243
- [19] J. Grigorjeva, "Capacity Mechanisms In the Eu: Nationalizing Energy Security", Jacques Delors Institut – Policy Paper, 134, Berlin, 21 MAY 2015
- [20] S. Andoura, J.A. Vinois, "From the European Energy Community to the Energy Union, A Policy Proposal for the short and long-term", Policy Paper No. 107, Jacques Delors Institute, January 2015.
- [21] ACER (2013), The Agency for The Cooperation of Energy Regulators, Capacity Remuneration Mechanisms and The Internal Market for Electricity Of 30 July 2013 Pursuant to Article 11 Of Regulation (Ec) No 713/2009
- [22] European Commission, DG Energy, Energy Union Package. A Framework Strategy for a Resilient Energy Union with a Forward-Looking Climate Change Policy, February 2015.
- [23] European Commission, DG Energy, Energy Union Package. Achieving 10% electricity interconnection target, February 2015.
- [24] S. Biricik, "Design of Unified Power Quality Conditioner for Power Quality Improvement in Distribution Network", *Balkan Journal Of Electrical & Computer Engineering*, Vol. 6, No. 1, February 2018
- [25] G. Erbach, Briefing, "Capacity mechanisms for electricity", European parliament, May 2017.

BIOGRAPHIES



MEHMET RIDA TUR Batman, Turkey, in 1983. He received the B.S. and M.S. degrees in electrical electronics engineering from the University of Marmara, Istanbul, in 2005 and the Ph.D. degree in electrical engineering from Yildiz Technical University, Istanbul, Turkey, in 2018. Now he is work in Batman University as an

Assistant Professor. He provides training in power systems and network applications and production systems and network connections. He is working on reliability, conservation, energy economy and energy quality in power systems. Capacity Mechanism, National grid system, smart network requirements for network infrastructure, network integration problem and cyber security studies are continuing.

LabVIEW Based Software System: Quantitative Determination of Main Electronic Parameters for Schottky Junction Structures

O. ÇIÇEK and S. KURNAZ

Abstract— LabVIEW is a software development platform that can be programmed with a graphical interface and so, measurement and instrumentation problems are used to deliver a solution. In the sensor applications, it is very important to calculate the main electronic parameters of the produced samples and it takes a lot of time to calculate these parameters and evaluate results. Therefore, LabVIEW based software system was developed to minimize the time spent. In this way, it was used to make the analysis as fast as possible. This study aimed to calculate quickly the obtained results from the measurement system. For this purpose, AuPd/n-GaAs Schottky Junction Structure (SJS) was produced by using RF and DC sputtering techniques to investigate on electronic parameters of SJS. The forward and reverse current-voltage (I-V) of SJS at $\pm 3V$ were measured at room temperature (295 K). By using thermionic emission (TE) theory, Ohm's law, Cheung and Cheung's function and modified Norde's function, the electronics parameters such as the series resistance (R_s), the shunt resistance (R_{sh}), the barrier height (Φ_{B0}) and the ideality factor (n) were calculated and graphics, which were drawn according to these models, via the developed software platform.


Index Terms—LabVIEW, Current-Voltage, Electronic Parameters, Schottky Junction Structures.

I. INTRODUCTION


RECENTLY, it has been focused seriously on semiconductor-based electronic circuit devices such as solar cells [1,2], light-emitting diodes [3], laser diodes [4], photodiodes [5], field-effect transistors [6], Schottky Junction Structures (SJSs) [7,8], etc.

Schottky junction structures (SJSs), which work at low

OSMAN ÇIÇEK, is with Department of Electrical and Electronics Engineering, Faculty of Engineering and Architecture, Kastamonu University, Kastamonu, Turkey, (e-mail: ocicek@kastamonu.edu.tr).

 0000-0002-2765-4165

SEDAT KURNAZ, is with Central Research Laboratory, Kastamonu University, Kastamonu, Turkey, (e-mail: sedatkurnaz@kastamonu.edu.tr).

 0000-0003-3657-2628

Manuscript received June 12, 2019; accepted July 2, 2019.

DOI: [10.17694/bajece.576303](https://doi.org/10.17694/bajece.576303)

forward voltages and have extremely fast switching capability, have attracted intense attention in the past few years owing to their potential application in electronics such as sensors, memory elements and rectifying devices [7,8]. In consequence of the potential barrier of SJSs, which is formed by tight contact with metal (M) and semiconductor (S), the rectifying devices are formed. Many researchers are interested in improving an electronic and optoelectronic performance of SJSs as inserting interfacial layer. Many parameters such as surface preparation process, barrier height, interfacial homogeneity, density of interfacial and dislocations, impurities, applied voltage and series resistance (R_s) are important in rectifying devices [9,10]. For calculating the main electronic properties from I-V measurement there are many techniques such as the thermionic emission (TE) theory, the Ohm's law, the Cheung and Cheung's function and the modified Norde's functions [11-14].

Virtual Instruments (VIs) in LabVIEW is used to build a Graphical User Interface (GUI) as the time-saving [15,16]. At the same time, it is very useful in terms of accuracy and reliability of the results. It has replaced the conventional programming languages, and also it comes with an effective user interface. In this way, LabVIEW is used many industries such as automotive, semiconductor, energy, aerospace, etc. [17]. Several researchers have used different ways to analyze the output characteristics of SJSs, using the MATLAB [18,19].

In light of these information, Au-Pd/n-GaAs SJS was produced by using DC and RF sputter. LabVIEW based program was developed to calculate these parameters and evaluate the results from I-V measurement. Then, the main electronic parameters of SJS were calculated and the obtained results were evaluated. Finally, it was found that the main electronic parameters of SJS were compatible with literature and the program was seen to work properly and reliably.

II. EXPERIMENTAL PROCEDURE

A. Measurement System

Au-Pd/n-GaAs SJS produced using RF and DC sputtering techniques, current-voltage (I-V) were measured in the measurement system for the characterized sensor applications under various conditions (Fig. 1). This system is also used for gas sensing measurements. It consists of Wayne Kerr 6500B,

Keithley 2400, LakeShore 325, Alicat MFC, Scientech SF300A and vacuum chamber. Current-voltage (I-V), capacitance-time (C-t), capacitance-voltage (C-V), current-time (I-t), etc. are measured depending on time, temperature, light and gas concentration.

B. LabVIEW based software system

LabVIEW is system engineering software that is used in applications that require testing, measurement and control. In spite of text-based programming, LabVIEW uses dataflow programming. Additionally, instead of writing line-by-line code in conventional programming such as C, C++, python,

etc., it uses graphical icons. In this way, a user interface is created with tools and objects. The user interface is known as the front panel. To control front panel objects, you add code using the graphical objects of the functions. The block diagram contains this code. There is a dataflow of the application, here. LabVIEW programs are also called VIs, because it simulates physical instruments such as oscilloscope and multimeter using the graphical objects in the front panel interface. Each VI uses functions that process the input from the user interface or other sources, and display it, or move it to other files or other computers [20].

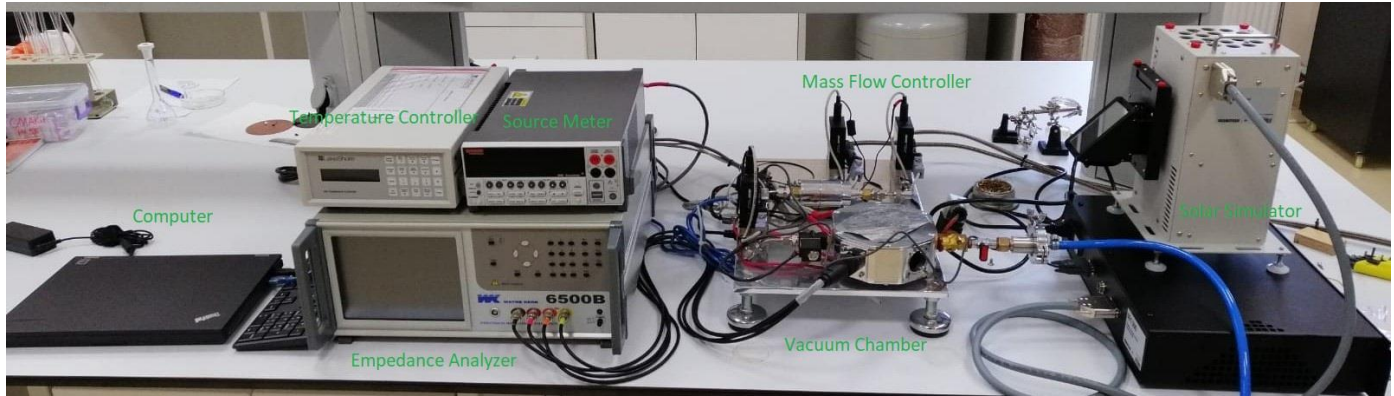


Fig.1. Measurement system for the characterized sensor applications under various conditions.

C. Mathematical Background

The TE theory, the Ohm's law, the Cheung and Cheung's function and the modified Norde's function are used in literature for calculating the main electronics parameters such as the shunt resistance (R_{sh}), the series resistance (R_s), the barrier height (Φ_{B0}) and the ideality factor (n). The purpose of these models is to obtain valid and reliable results and also to compare the results with each other. According to the TE model, its parametric equations (1-4) are used.

$$I = I_o \left[\exp\left(\frac{q(V - IR_s)}{nkT}\right) - 1 \right] \quad (1)$$

$$I_o = AA^* T^2 \exp\left(-\frac{q\Phi_{B0}}{kT}\right) \quad (2)$$

$$n = \frac{q}{kT} \left(\frac{dV}{d(\ln I)} \right) \quad (3)$$

$$\Phi_{B0} = \frac{kT}{q} \ln\left(\frac{AA^* T^2}{I_o}\right) \quad (4)$$

Here, the parameters denoted by I_o , n , q , V , IR_s , k , T , Φ_{B0} , A and A^* can be expressed as the saturation current, the ideality factor, the charge of electron, the applied bias voltage on the structure, the voltage drop on the series resistance (R_s), the Boltzmann's constant, the temperature, the zero-bias barrier

height, the rectifier contact area and the effective Richardson constant, respectively.

For Ohm's law, Eq. 5 is used to calculate R_s (at maximum V) and R_{sh} (at minimum V) from the I-V measurement, respectively.

$$R_i = \frac{dV_i}{dI_i} \quad (5)$$

The other method to calculate the R_s values of SJS is the Cheung and Cheung's function which has been acquired from the forward-bias of I-V measurement. The following equations are referred to as the Cheng and Cheng's functions in the literature.

$$\frac{dV}{d(\ln I)} = IR_s + \left(\frac{nkT}{q}\right) \quad (6)$$

$$H(I) = V - \frac{nkT}{q} \ln\left(\frac{I}{AA^* T^2}\right) = IR_s + n\Phi_{B0} \quad (7)$$

The modified Norde's function is another method to determine Φ_{B0} and R_s values of the SJS.

$$F(V) = \frac{V}{\gamma} - \frac{kT}{q} \ln\left(\frac{I(V)}{AA^* T^2}\right) \quad (8)$$

where γ is greater than n values. $F(V)$ - V graphs have minimum points of V_{min} and I_{min} values which use calculating Φ_{B0} and R_s values from Eq. (8a) and (8b).

$$\Phi_{B0} = F(V_{min}) + \frac{V_{min}}{\gamma} - \frac{kT}{q} \tag{9a}$$

$$R_s = \frac{(\gamma - n)kT}{qI_{min}} \tag{9b}$$

III. RESULTS AND DISCUSSION

The electrical characteristics of the prepared AuPd / n-GaAs MS type SJS under dark conditions were measured by the use of a Keithley 2400 Sourcemeter at $\pm 3V$ by 20mV steps at in room temperature (295 K). The basic electrical parameters of SJSs (Φ_{B0} , n , I_0 , R_s , R_{sh} , etc.) were calculated from the I-V data via a developed Labview software program, which was formed from mathematical expressions of TE, Ohm's law, Cheung method and modified Norde method.

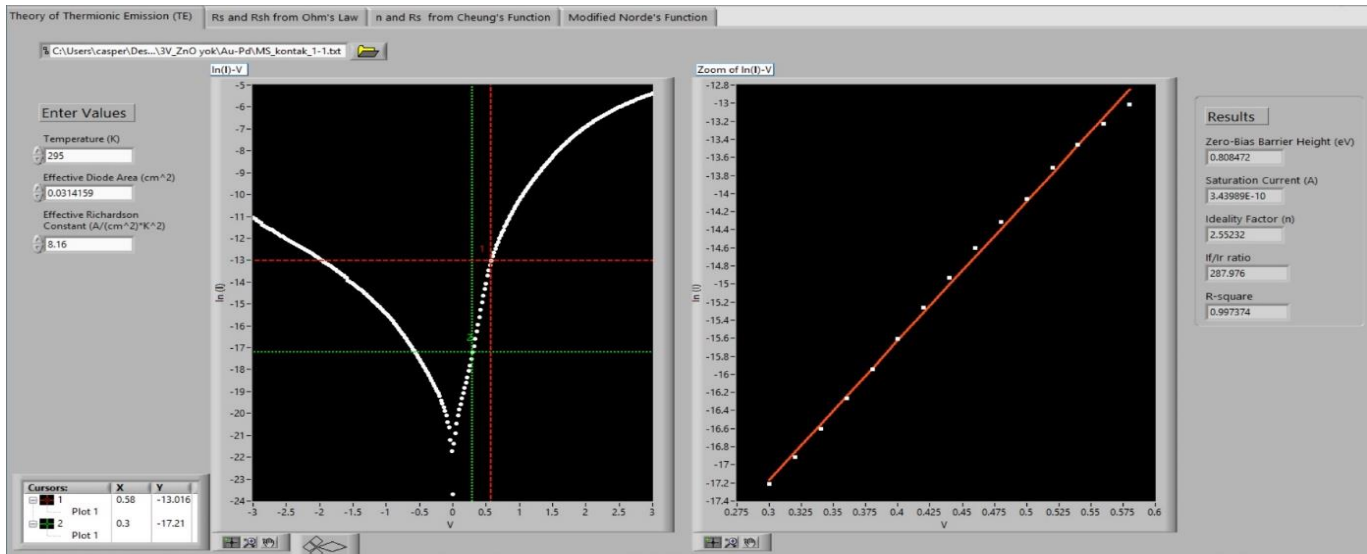


Fig. 2. Front panel of the thermionic emission (TE) theory

Utilizing the developed LabVIEW based program, the output of TE program was obtained from the using the source I-V data and the input parameters such as temperature (K), effective contact area (cm^2), the effective Richardson constant (A/cm^2-K^2) (Fig.2).

The data obtained from the measurement system is defined in the first section. Because the current values under forward

or reverse bias voltage are important for modeling. In the second section, by using the separated data, the parameters are determined according to the formulas mentioned above.

In Fig. 3, for Ohm's law, another algorithm can be seen to obtain the R_s and R_{sh} values obtained from the forward and reverse biases regions of the I-V characteristics of SJS.

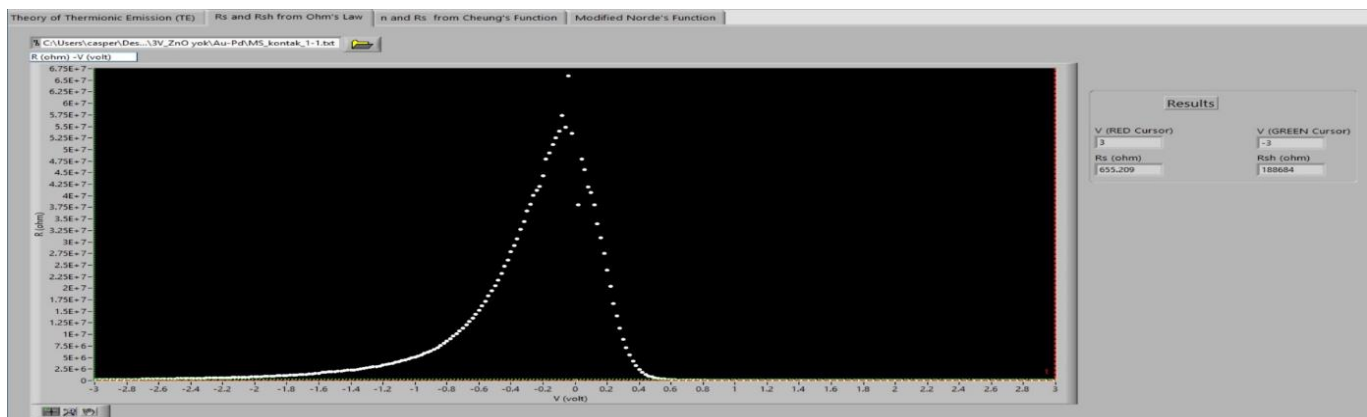


Fig. 3. Front panel of the Ohm's law

The other calculation methods for main electronic parameters are the Cheung and Cheung's function and the modified Norde's function are shown and drawn in Fig. 4 and 5, respectively. To explain how the program works, first select the file with I-V data. Secondly, input values such as

temperature, contact area and Richardson constant are entered. By specifying the desired regions with 2 cursors, the program is executed. So, graphics are drawn according to these models and the main electronic parameters are calculated

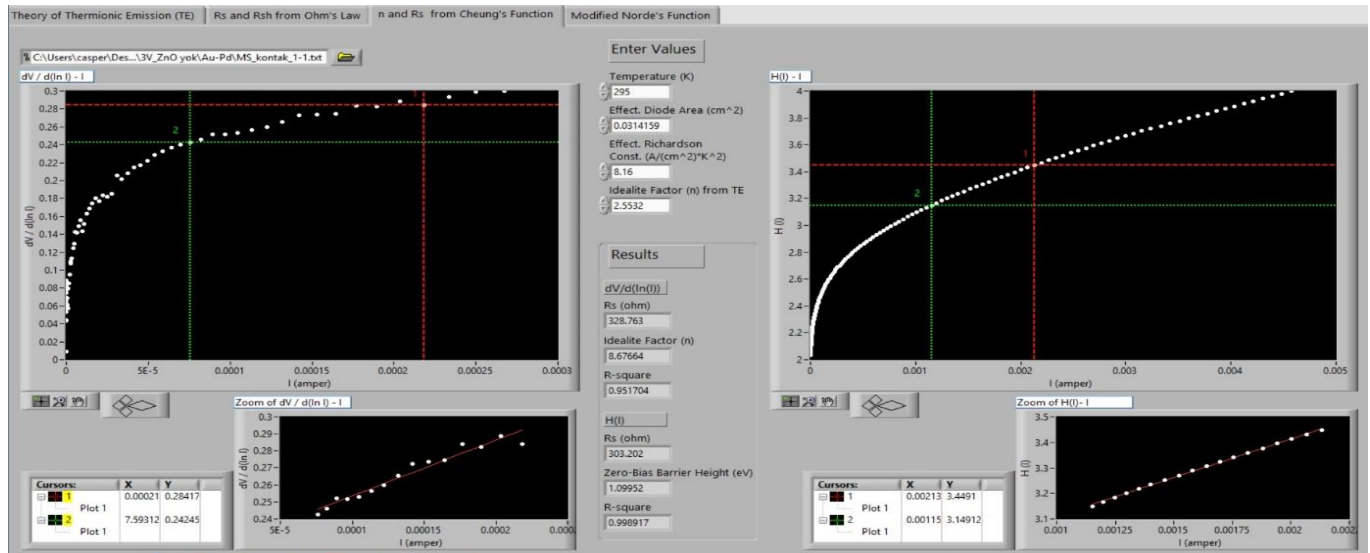
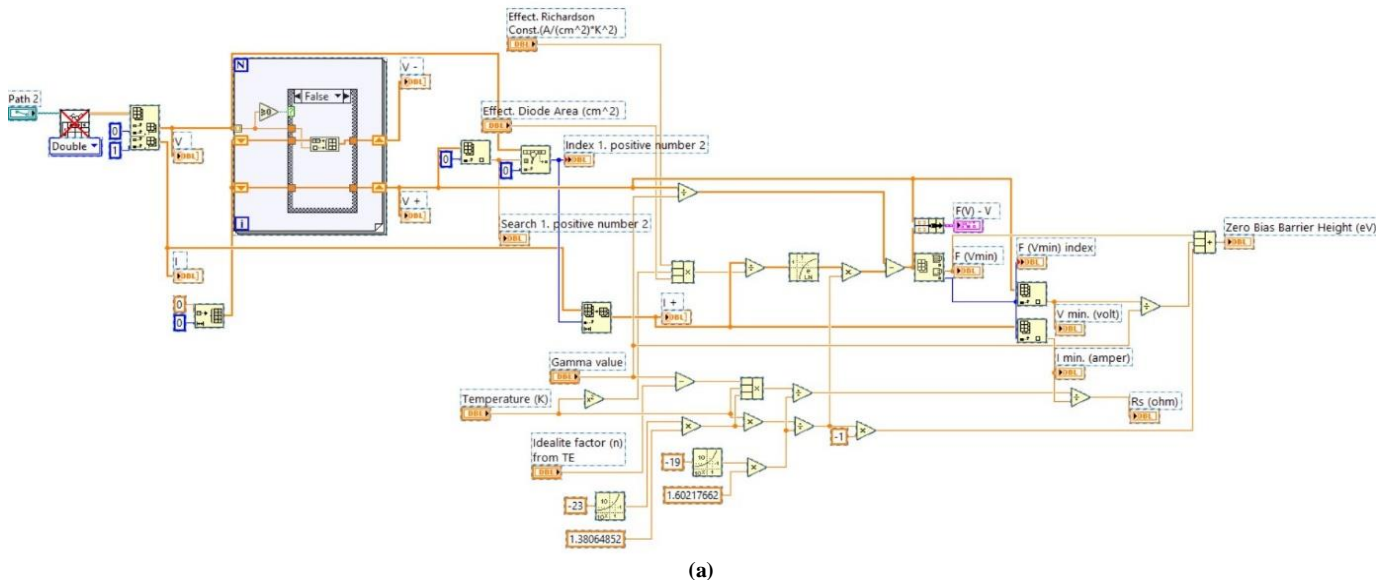
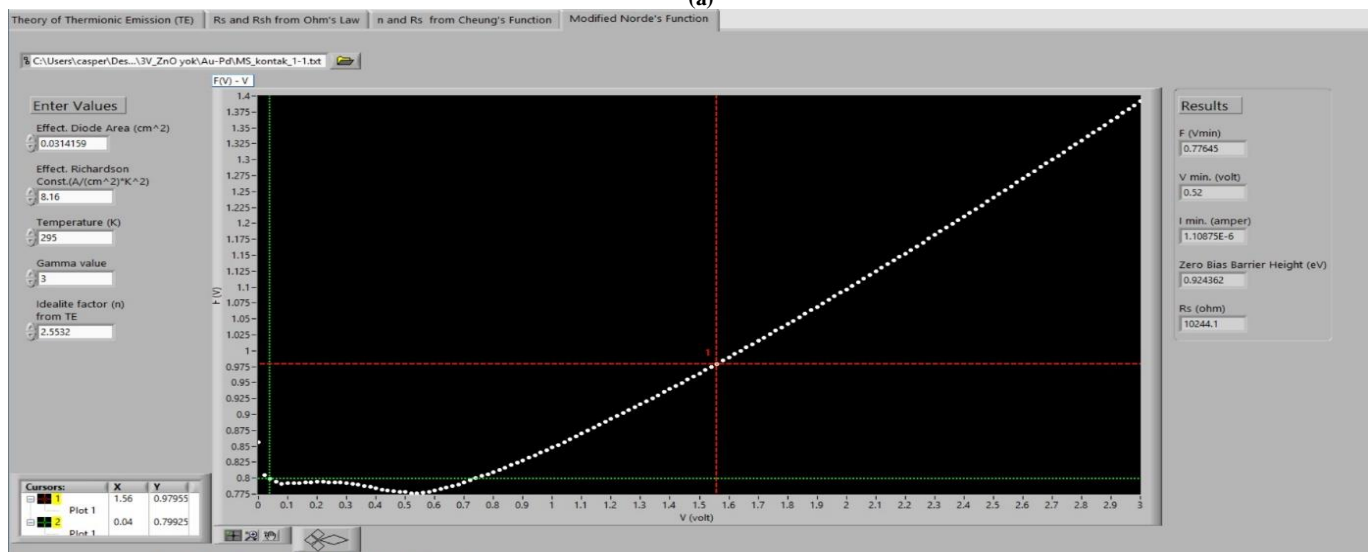


Fig. 4. Front panel of the Cheung and Cheung's function.



(a)



(b)

Fig. 5. Block diagram (a) and front panel (b) of the modified Norde's function in LabVIEW.

The main electronic parameters of SJS, which are calculated different methods via the developed software program, are given in Table I. The results obtained from the program are almost consistent with the papers [8,21,22,23]. Minor differences in results could be referred to as many situations

such as using GaAs crystals, impurity, barrier inhomogeneity, image-force effect, series resistance, tunneling process and non-uniformity distribution of rectifier contact metal.

TABLE I
RESULTS OF SJS BY USING THE TE THEORY, THE OHM'S LAW, THE CHEUNG AND CHEUNG'S FUNCTION AND THE MODIFIED NORDE'S FUNCTION.

from Theory of Thermionic Emission (TE)					from Ohm's Law			
I_o , [A]	n	Φ_{Bo} , [eV]	RR, [I_F/I_R]	R^2	R_s , [K Ω]	R_{sh} , [K Ω]		
3.44×10^{-10}	2.55	0.808	287.9	0.997	0.655	188.684		
from the Cheung and Cheung's function					from modified Norde's function			
$dV/dlnI$ (Ω)			$H(I)-I$ (Ω)					
R_s , [Ω]	R^2	R_s , [Ω]	Φ_{Bo} , [eV]	R^2	$F(V_{min})$, [V]	V_{min} , [V]	Φ_{Bo} , [eV]	R_s , [K Ω]
328.76	0.952	303.202	1.099	0.999	0.776	0.52	0.924	10.244

IV. CONCLUSION

Our main goal is to prevent time loss by developing a Labview based software system and shortening the analysis time. For this purpose, a program was developed to analyze Schottky junction structures (SJSs) according to many different models. The block diagram is shown in detail in this paper. Graphical user interfaces (front panels) are designed in LabVIEW. In this context, AuPd/n-GaAs MS type SJS was produced by using RF and DC sputtering techniques. I-V measurement was done. Then, according to the TE theory, the Ohm's law, the Cheung and Cheung's function and the modified Norde's function, this program is executed in this work to draw the collected data (I-V) of SJS from the photovoltaic measurement system. The main electronic parameters are obtained in a short time. The results are consistent with the literature. This indicates that the program works correctly and reliably.

ACKNOWLEDGMENT

The authors would like to thank Kastamonu University, Central Research Laboratory and its research team for its supports and contributions during this study. At the same time, a little part of this study was presented at the International Congress on Engineering and Life Science (ICELIS) 2019 symposium in Kastamonu/TURKEY.

REFERENCES

- [1] H. Šamić, S. Makham, "The Influence of Radiation on the Solar Cell Efficiency.pdf (2)," Balkan Journal of Electrical and Computer Engineering, vol. 2, no. 1, 2014, pp. 2-5.
- [2] N. Ekren, "Researches on Anti-Reflection Coating (ARC) Methods Used in PV Systems," Balkan Journal of Electrical & Computer Engineering, vol. 6, no. 1, 2018, pp.42-46.
- [3] S. Shin, J. Kim, Y.-H. Kim, S.-I. Kim. "Enhanced performance of organic light-emitting diodes by using hybrid anodes composed of graphene and conducting polymer," Current Applied Physics, vol. 13, no. 2, 2013, pp. 144-147.
- [4] A. Uğur and M. Yilmaz, "A GaN-Based Synchronous Buck Converter for High Power Laser Diode Drive Applications," Balkan Journal of Electrical & Computer Engineering, vol. 6, no. 1, 2018, pp. 62-68.
- [5] T. Knežević, X. Liu, E. Hardeveld, T. Suligoj and L. K. Nanver, "Limits on Thinning of Boron Layers With/Without Metal Contacting in PureB Si (Photo)Diodes," IEEE Electron Device Letters, vol. 40, no. 6, June 2019, pp. 858-861.
- [6] Y. Lan et al., "Flexible Graphene Field-Effect Transistors with Extrinsic f_{max} of 28 GHz," IEEE Electron Device Letters, vol. 39, no. 12, Dec. 2018, pp. 1944-1947.
- [7] S. O. Tan, H. Uslu Tecimer, O. Çiçek, H. Tecimer, İ. Orak and Ş. Altındal, "Electrical characterizations of Au/ZnO/n-GaAs Schottky diodes under distinct illumination intensities," Journal of Material Science: Material Electron, vol. 27, no. 8, 2016, pp. 8340-8347.
- [8] O. Çiçek, H. Uslu Tecimer, S. Tan, H. Tecimer, Ş. Altındal and I. Uslu, "Evaluation of electrical and photovoltaic behaviors as comparative of Au/n-GaAs (MS) diodes with and without pure and graphene (Gr)-doped polyvinyl alcohol (PVA) interfacial layer under dark and illuminated conditions," Composites Part B, vol. 98, 2016, pp. 260-268.
- [9] Ü. Özgür, Y. I. Alivov, A. Teke, M. A. Reshchikov, S. Doğan, V. Avrutı, S. J. Cho and H. Morkoç, "A comprehensive review of ZnO materials and devices," Journal of Applied Physics, vol. 98, no. 4, 2005, 041301.
- [10] F. Z. Pür ve A. Tataroğlu, "Analysis of the series resistance and interface states of Au/Si₃N₄/n-Si (metal-insulator-semiconductor) Schottky diodes using IV characteristics in a wide temperature range," Physica Scripta, vol. 86, no. 3, 2012.
- [11] S.K. Cheung and N.W. Cheung, "Extraction of Schottky diode parameters from forward current-voltage characteristics," Applied Physics Letters, vol. 49, no. 2, 1986, pp. 85-87.
- [12] H. Norde, "A modified forward I-V plot for Schottky diodes with high series resistance," Journal of Applied Physics, vol. 50, no. 7, 1979, pp.5052-5053.
- [13] K. E. Böhlin, "Generalized Norde plot including determination of the ideality factor," Journal of Applied Physics, vol. 60, 1986.
- [14] S. M. Sze, "Semiconductor Devices: Physics and Technology," New York: Wiley, 1985.
- [15] J. Travis and J. King, "LabVIEW for Everyone: Graphical Programming Made Easy and Fun", 2006.
- [16] R. Bitter, T. Mohiuddin, and M. Nawrocki, "LabVIEW: Advanced programming techniques". Crc Press, 2006.
- [17] LabVIEW applications by 2019 Viewpoint Systems, Inc., Available: <https://www.viewpointusa.com/labview/where-is-labview-used-who-uses-it-companies-that-use-it/>, [Jun 5, 2019].
- [18] T. Salmi, M. Bouzguenda, A. Gastli and A. Masmoudi, "MATLAB/Simulink Based Modelling of Solar Photovoltaic Cell," International Journal of Renewable Energy Research, vol. 2, no. 2, 2012.
- [19] S. Nema, R.K. Nema and G. Agnihotri, "MATLAB/Simulink based study of photovoltaic cells/modules /array and their experimental verification", International Journal of Energy and Environment, vol. 1, no. 3, 2010.
- [20] LabVIEW User Manuel, National Instruments, 2003.
- [21] Ş. Karataş and A. Turut, "The determination of electronic and interface state density distributions of Au/n-type GaAs Schottky barrier diodes," Physica B, vol. 381, 2006, pp. 199-203.
- [22] M. Soyulu and F. Yakuphanoglu, "Photovoltaic and interface state density properties of the Au/n-GaAs Schottky barrier solar cell," Thin Solid Films, vol. 519, 2011, pp. 1950-1954.
- [23] A. Bobby, N. Shiwakoti, P. S. Gupta and B. K. Antony, "Barrier modification of Au/n-GaAs Schottky structure by organic interlayer," Indian Journal of Physics, vol. 90, no. 3, 2006, pp.307-312.

BIOGRAPHIES



OSMAN ÇİÇEK Bozkır, Konya, in 1986. He received the bachelor's degrees in the Electrical Teaching Department from Gazi University, and the M.S. and Ph.D. degrees in Electrical and Electronics Engineering Department from Karabük University, Karabük, Turkey, in 2013 and 2016, respectively.

From 2011 to 2016, he was a lecturer with the Department of Electrical and Energy, Kastamonu University. Since 2017, he has been an Assistant Professor with the Electrical and Electronics Engineering Department, Kastamonu University. He is the author of more than 15 articles, and more than 10 projects. His research interests include solar cells and applications, enhancing the performance of solar cells, Schottky junction structures, and innovation sensor applications.



SEDAT KURNAZ Alaçam, Samsun, in 1989. He received the B.S. degrees in the Physics Engineering Department from Hacettepe University in 2013 and the M.S. degrees in Physics Department from Karadeniz Technical University in 2016. He has been a lecturer at Central Research Laboratory, Kastamonu University since

2017. He continues his Ph.D. at Kastamonu University. His main research interests are superconductor and semiconductor materials, thin film deposition, Schottky junction structures, solar cells.

Power Control of Single Phase Active Rectifier

A. KARAFIL and H. OZBAY

Abstract—The most important feature of active rectifier circuits is the ability to adjust the power factor and DC bus voltage, when compared to diode rectifiers. However, odd current harmonics occur in the grid since hard switching state occurs in the active rectifier circuit. A filter should be used on the grid side to reduce the current harmonics. Although there are many types of filters, one of the most suitable filter types is LCL filter when considering the factors such as cost and size. In this study, LCL filter design calculation is performed and PSIM simulation results of active-reactive power controlled LCL filter proportional resonant (PR) current controlled single phase active rectifier circuit is given. The system is designed according to the active power of 600 W. Then, by adding reactive power to the system, it is proved that the power control is carried out successfully.

Index Terms— LCL filter, Power control, PR current controller, Single phase active rectifier.

I. INTRODUCTION

THE SINGLE phase rectifier circuits are used in many industrial applications requiring DC bus voltage such as electrical railway transportation [1], [2], uninterruptible power supply [3], electrical vehicle charger [4], micro turbine generator units [5] and renewable energy applications as wind energy [6]. While the control of power factor and dc bus voltage is an important advantage in active rectifiers, the increase of switching losses and current harmonics occurring due to hard switching are the disadvantages of this system. A filter should be used on grid side in order to decrease the high order current harmonics. In the advance power electronics technology it is desirable to have small and light circuit sizes. One of the circuit elements that increases the size of the circuit is the filter. For this purpose, the filter used in the system should be effective, light and with small size. The LCL filter is one of the most suitable filter types considering the reduction of harmonics, cost and size [7-10].

In the case of single phase active rectifier circuits, it is necessary to perform current and power control so that the DC voltage can be adjusted and the power factor can be

AKİF KARAFİL, is with Department of Electric and Energy Bilecik Seyh Edebali University, Bilecik, Turkey, (e-mail: akif.karafil@bilecik.edu.tr).
<https://orcid.org/0000-0002-7844-9014>

HARUN OZBAY, is with Department of Electrical Engineering Bandirma Onyedi Eylül University, Balıkesir, Turkey, (e-mail: hobay@bandirma.edu.tr).
<https://orcid.org/0000-0003-1068-244X>

Manuscript received December 26, 2018; accepted July 6, 2019.
DOI: [10.17694/bajece.503207](https://doi.org/10.17694/bajece.503207)

controlled. Many control methods are used in current and power control [11], [12] such as model predictive [12], hysteresis [13], proportional integral (PI) [14], proportional resonant (PR) [15], repetitive [16], sliding mode [17], fuzzy neural [18]. PI and PR, which are among the linear control techniques, are the most widely used controllers. Although other control techniques show a good dynamic response, they create a time delay in the system [19].

In order to ensure synchronization with the grid in active rectifier circuits, phase locked loop (PLL) is required. The PLL algorithm provides control of the grid frequency. Many PLL algorithms are used in active rectifier circuits. T/4 delay PLL is one of the easy algorithms for obtaining the phase angle in single phase applications [20].

In this study, an analysis of the active-reactive power controlled LCL filter PR current controlled single phase active rectifier circuit was conducted and the simulation results were given. T/4 delay PLL was used as PLL algorithm. System was firstly tested without reactive power control and then reactive power was added and active and reactive power controlled simulation results were obtained.

This paper is organized as follows: Section II presents the PLL structured used by calculating the LCL filter parameters. In section III, power control and PR current control technique used in the system are introduced. Section IV gives the simulation results. In the conclusion part, the simulation results are interpreted.

II. DESIGN OF SINGLE PHASE ACTIVE RECTIFIER BASED LCL FILTER

A. Determination of the LCL Filter Values

The connection diagram of the designed LCL filter single phase active rectifier circuit is shown in Fig.1.

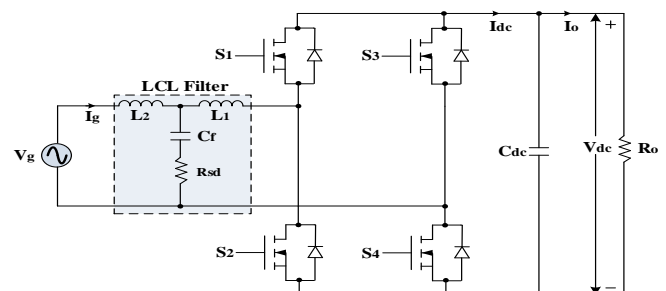


Fig.1. Single phase active rectifier based LCL filter

Before determining LCL filter parameters, it is necessary to determine the parameters of the single phase active rectifier circuit. Table 1 presents the parameter values to be used in the system.

TABLE I
PARAMETER VALUES REQUIRED FOR RECTIFIER CIRCUIT

Parameters of Rectifier	
Parameter	Value
Grid Voltage (V_g)	220 V
Output Power of Rectifier (P_n)	600 W
DC Bus Voltage (V_{DC})	400 V
Grid Frequency (f)	50 Hz
Switching Frequency (f_{sw})	10 kHz

The inductor (L_1) value on the converter side is calculated by the following equations.

$$\Delta I_{L-\max} = a \cdot \frac{P_n \sqrt{2}}{V_g} \quad (1)$$

$$L_1 = \frac{V_{DC}}{16 \cdot f_{sw} \cdot \Delta I_{L-\max}} \quad (2)$$

Where “ a ” is the current ripple ratio. Impedance and capacitor values of the circuit are calculated as follows:

$$Z_b = \frac{V_g^2}{P_n} \quad (3)$$

$$C_b = \frac{1}{2\pi f \cdot Z_b} \quad (4)$$

When determining the value of the filter capacitor, 5 % of the ideal C_b value is taken. However, a factor (k) greater than 5 % can be preferred.

$$C_f = k \cdot C_b \quad (5)$$

There is a relationship between the grid and the inductors on the converter side when determining the inductor value (L_2) on the grid side. This relationship is indicated by “ r ” coefficient and in the range of $0 < r \leq 1$. Therefore, the L_2 value is calculated by the following equation [21], [22].

$$L_2 = r \cdot L_1 \quad (6)$$

By the equations, it was calculated that $L_1=3.24$ mH, $C_f=7.892$ μ F and $L_2=0.972$ mH. Once the LCL filter parameters are determined, the resonance frequency can be calculated as follows:

$$f_{res} = \frac{1}{2\pi} \sqrt{\frac{L_1 + L_2}{L_1 \cdot L_2 \cdot C_f}} \quad (7)$$

Moreover, the resonance frequency (f_{res}) should be within the ranges shown in Equation (8) [22].

$$10f < f_{res} < 0.5f_{sw} \quad (8)$$

A series resistor is connected to the capacitor in order to reduce the oscillations and prevent the filter from unstable state. This resistor is called as “damping resistor” and is calculated by the following equation.

$$R_{sd} \geq \frac{1}{3 \cdot \omega_{res} \cdot C_f} \quad (9)$$

B. PLL Structure

The control of the grid frequency is performed by the PLL algorithm. In this study, T/4 delay PLL algorithm is used. T/4 delay PLL algorithm needs α - β and d-q reference frames. In order to obtain the orthogonal imaginary signal (β component), α component must be shifted as $\pi/2$. Between them α component is in the real and the β component is in the imaginary axis. Equation (10) was used to transform the α - β into d-q axis frame with Park Transform in the T/4 delay PLL circuit [20]. Fig.2 shows the α - β transform and T/4 delay PLL structure.

$$\begin{bmatrix} V_d \\ V_q \end{bmatrix} = \begin{bmatrix} \cos \omega t & \sin \omega t \\ -\sin \omega t & \cos \omega t \end{bmatrix} \begin{bmatrix} V_\alpha \\ V_\beta \end{bmatrix} \quad (10)$$

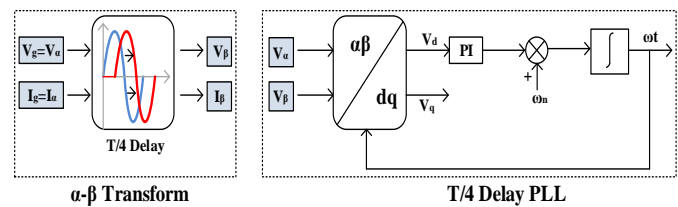


Fig.2. The block diagram of α - β Transform and T/4 delay PLL structure

III. POWER CONTROL AND PR CURRENT CONTROL TECHNIQUE

The control block diagram of the system is shown in Fig.3.

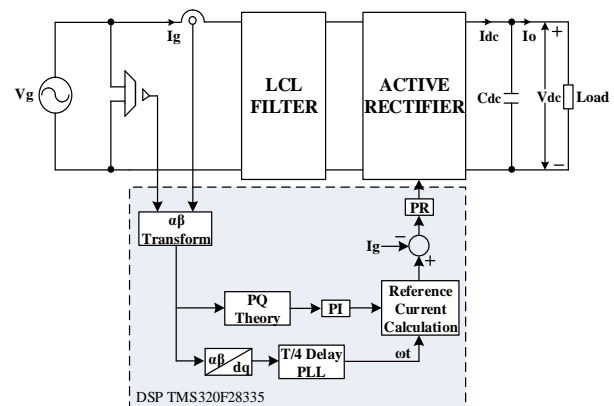


Fig.3. The control block diagram of the single phase active rectifier

Active-reactive power (PQ theory) calculation was conducted by the following equations.

$$P = \frac{1}{2} (V_\alpha \cdot I_\alpha + V_\beta \cdot I_\beta) \quad (11)$$

$$Q = -\frac{1}{2} (V_\alpha \cdot I_\beta + V_\beta \cdot I_\alpha) \quad (12)$$

The obtained power error values are passed through the PI controller and added to the ωt formula obtained by PLL algorithm and therefore the reference current is calculated. The reference current formula is found using the following equations: [12], [23].

$$\theta = \tan^{-1} \left(\frac{Q_{ref}}{P_{ref}} \right) \tag{13}$$

$$I_g = \frac{P_{ref}}{V_q \cdot \cos \theta} \tag{14}$$

$$i_{ref} = \sqrt{2} \cdot I_g \cdot \sin(\omega t - \theta) \tag{15}$$

The obtained reference current is subtracted from the I_g (I_a) current value to obtain the error current. The error current is passed through the PR current controller to generate the switching signals.

PR controller is one of the control methods used in single or three phase systems connected to the grid. PI and PR are controllers that are similar to each other and have many common points. The PR controller is generally preferred to obtain a zero steady-state error in the control of grid-connected systems. There are some problems in the implementation of the PR controller. In ideal PR controller, unlimited gain harmonics components increase. The formula for the non-ideal PR controller used to reduce the harmonic components is given in Equation (16).

$$G_{nipr}(s) = K_p + \frac{2K_i \omega_c s}{s^2 + 2\omega_c s + \omega_n^2} \tag{16}$$

Where, ω_n is the angular frequency of the grid and the K_p and K_i values are proportional and integral gain values, respectively. ω_c is the cut-off frequency. Non-ideal PR controller has lower gain and band range [24-26].

IV. SIMULATION RESULTS

The simulation screen image of a single phase active rectifier circuit was given in Fig.4. In the circuit the parameters were determined as follows: $R_o=266 \Omega$, damping resistor $R_{sd}=5 \Omega$ and DC capacitor value $C_{dc}=470 \mu F$.

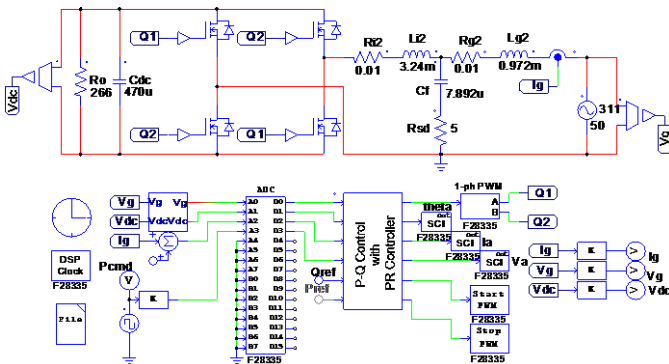


Fig.4. The simulation of the single phase active rectifier circuit

Grid voltage is detected by PLL algorithm and zero transition points are caught and the angular velocity values synchronized with the grid for each period are produced. The grid voltage and the angular velocity values produced as synchronized are shown in Fig.5.

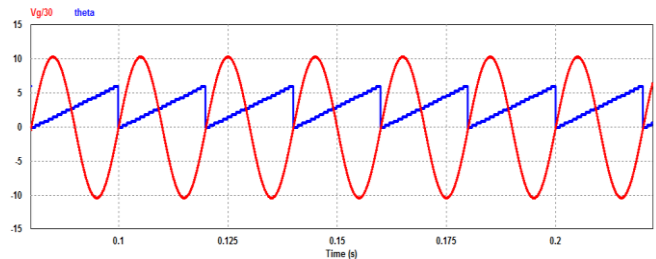


Fig.5. The production of angular speed values by PLL

When the active power of the system is $P=400 \text{ W}$ and the reactive power is $Q=0 \text{ VAR}$, the current and the voltage wave forms of the circuit was shown in Fig.6.

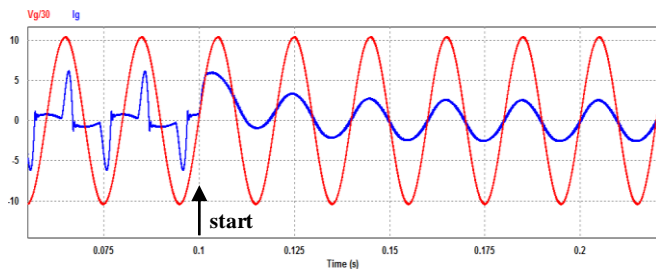


Fig.6. The initial current and voltage of the grid at 400 W active power

The current and voltage waveforms of the grid when the active power was increased from 400 W to 600 were given in Fig.7.

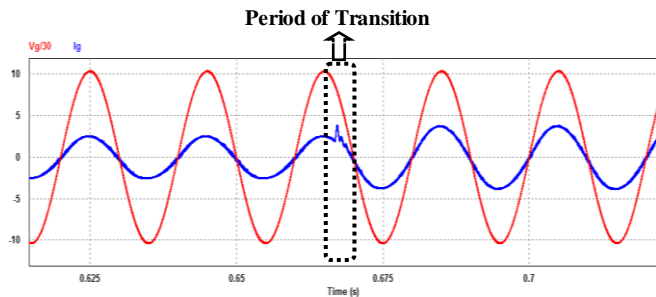


Fig.7. The period of transition from 400 W to 600 W

When $P=400-600 \text{ W}$ and $Q=0 \text{ VAR}$, DC voltage change on the load was shown in Fig.8.

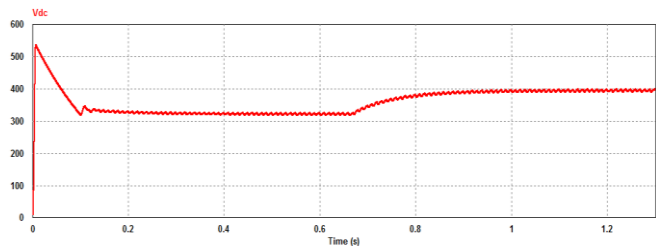


Fig.8. DC bus voltage changing

When $P=600$ W and $Q=0$ VAR, the power factor value was found as 0.99 and shown in Fig.9.

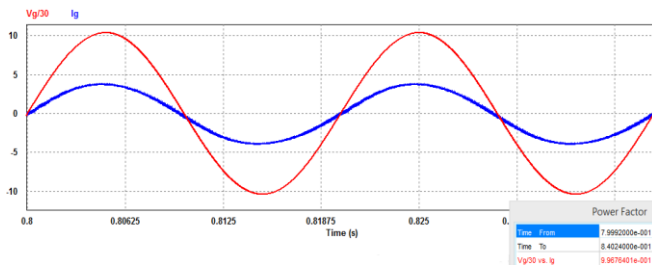


Fig.9. Power factor value at $P=600$ W and $Q=0$ VAR power values

The power control of the system was tested by adding reactive power to the system. Current and the voltage wave forms at $P=600$ W and $Q=400$ VAR power values were given in Fig.10.

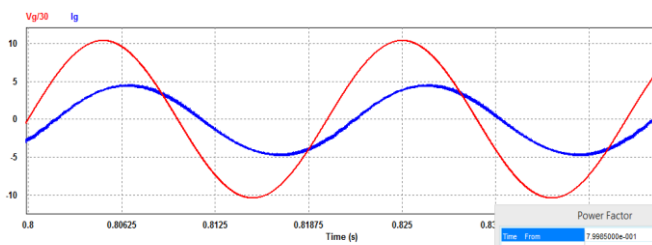


Fig.10. Power factor value at $P=600$ W, $Q=400$ VAR power values

At $P=600$ W and $Q=400$ VAR power values, power factor was found as 0.83.

Current and the voltage wave forms of the grid at $P=600$ W and $Q=-400$ VAR power values were given in Fig.11.

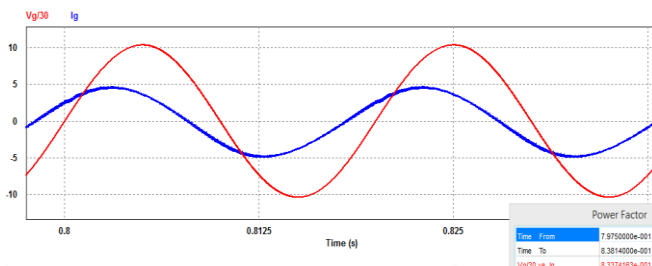


Fig.11. Power factor value at $P=600$ W, $Q=-400$ VAR power values

At $P=600$ W and $Q=-400$ VAR power values, power factor was found as 0.83.

V. CONCLUSION

In this study, the active-reactive power control of a LCL filter single phase active rectifier circuit was obtained by the simulation study. PI for power control, PR controller for current control and T/4 delay PLL algorithm for grid frequency control were used. Active power control was performed for $P=600$ W, $Q = 0$ VAR system power values and power factor value was found as 0.99. Then, reactive power was added to the system and $P=600$ W, $Q=400$ VAR and $P=600$ W, $Q=-400$ VAR power values were tested respectively and the power factor was found as 0.83. In this study, active-

reactive power control of a single phase active rectifier circuit with LCL filter was performed.

REFERENCES

- [1] W. Song, S. Wang, C. Xiong, X. Ge, X. Feng, "Single-phase three-level space vector pulse width modulation algorithm for grid-side railway traction converter and its relationship of carrier-based pulse width modulation", *IET Electrical Systems in Transportation*, Vol.4, No.3, 2014, pp.78-87.
- [2] V. Blahnik, J. Talla, "Single-phase synchronization for traction active rectifier", *IEEE Conference on Applied Electronics*, 2016, pp.23-26.
- [3] H. Komurcigil, N. Altin, S. Ozdemir, I. Sefa, "An extended Lyapunov-Function-Based control strategy for single-phase UPS inverters", *IEEE Transactions on Power Electronics*, Vol.30, No.7, 2015, pp.3976-3983.
- [4] L. Pan, C. Zhang, "Model predictive control of a single-phase PWM rectifier for electric vehicle charger", *Energy Procedia*, Vol.105, 2017, pp.4027-4033.
- [5] D. A. Khaburi, A. Nazempour, "Design and simulation of a PWM rectifier connected to a PM generator of micro turbine unit", *Scientia Iranica*, Vol.19, No.3, 2012, pp.820-828.
- [6] A. Mirecki, X. Roboam, F. Richardeau, "Architecture complexity and energy efficiency of a small wind turbines", *IEEE Transactions on Industrial Electronics*, Vol.54, No.1, 2007, pp.660-670.
- [7] W. Jiang, Y. Wang, J. Wang, L. Wang, H. Huang, "Maximizing instantaneous active power capability for PWM rectifier under unbalanced grid voltage dips considering the limitation of phase current", *IEEE Transactions on Industrial Electronics*, Vol.63, No.10, 2016, pp.5998-6009.
- [8] M. Liserre, F. Blaabjerg, S. Hansen, "Design and control of an LCL-filter-based three-phase active rectifier", *IEEE Transactions on Industry Applications*, Vol.41, No.5, 2005, pp.1281-1291.
- [9] M. Orellana, R. Grino, "Power flow limitations for LCL grid-connected power converters", *IEEE 11th International Multi-Conference on Systems, Signals & Devices (SSD)*, 2014, pp.1-5.
- [10] L. Wei, R. A. Lukaszewski, "Optimization of the main inductor in a LCL filter for three phase active rectifier", in *Proc. Conf. Rec. IEEE Ind. Appl. Conf.*, 42nd IAS Annu. Meeting, 2007, pp.1816-1822.
- [11] S. Kwak, J. C. Park, "Model-predictive direct power control with vector preselection technique for highly efficient active rectifiers", *IEEE Transactions on Industrial Informatics*, Vol.11, No.1, 2015, pp.44-52.
- [12] W. Song, Z. Deng, S. Wang, X. Feng, "A simple model predictive power control strategy for single-phase PWM converters with modulation function optimization", *IEEE Transactions on Power Electronics*, Vol.31, No.7, 2016, pp.5279-5289.
- [13] L. Dalessandro, U. Drofenik, S. D. Round, J. W. Kolar, "A novel hysteresis current control for three-phase three-level PWM rectifiers", *IEEE Twentieth Annual Applied Power Electronics Conference and Exposition (APEC)*, Vol.1, 2005, pp.501-507.
- [14] M. Malinowski, M. Jasinski, M. P. Kazmierkowski, "Simple direct power control of three-phase PWM rectifier using space-vector modulation (DPC-SVM)", *IEEE Transactions on Industrial Electronics*, Vol.51, No.2, 2004, pp.447-454.
- [15] D. N. Zmood, D. G. Holmes, "Stationary frame current regulation of PWM inverters with zero steady-state error", *IEEE Transactions on Power Electronics*, Vol.18, No.3, 2003, pp.814-822.
- [16] X. Wang, Z. Pan, T. T. G. Hoang, L. Tian, Y. Chen, "New repetitive current controller for PWM rectifier", *IFAC-PapersOnLine*, Vol.51, No.4, 2018, pp.154-159.
- [17] H. Özbay, S. Öncü, M. Kesler "SMC-DPC based active and reactive power control of grid-tied three phase inverter for PV systems", *International Journal of Hydrogen Energy*, Vol.42, No.28, 2017, pp.17713-17722.
- [18] R. Coteli, H. Acikgoz, F. Ucar, B. Dandil, "Design and implementation of type-2 fuzzy neural system controller for PWM rectifiers", *International Journal of Hydrogen Energy*, Vol.42, No.32, 2017, pp.20759-20771.
- [19] M. L. Sowjanya, "Improved control strategy of grid interactive inverter system with LCL filter using active and passive damping methods", M. Sc. Thesis, Department of Electrical Engineering National Institute of Technology, Rourkela, India, 2014.
- [20] Y. Yang, F. Blaabjerg, "Synchronization in single-phase grid-connected photovoltaic systems under grid faults", *IEEE 3rd*

- International Symposium on Power Electronics for Distributed Generation Systems (PEDG), 2012, pp.476-482.
- [21] J. F. Ardashir, M. Sabahi, S. H. Hosseini, F. Blaabjerg, E. Babaei, G. B. Gharehpetian, "A single-phase transformerless inverter with charge pump circuit concept for grid-tied PV applications", *IEEE Transactions on Industrial Electronics*, Vol.64, No.7, 2017, pp.5403-5415.
- [22] A. Reznik, M. G. Simoes, A. Al-Durra, S. M. Mueeen, "LCL filter design and performance analysis for grid-interconnected systems", *IEEE Transactions on Industry Applications*, Vol.50, No.2, 2014, pp.1225-1232.
- [23] M. C. Kisacikoglu, M. Kesler, L. M. Tolbert, "Single-phase on-board bidirectional PEV charger for V2G reactive power operation", *IEEE Transactions on Smart Grid*, Vol.6, No.2, 2015, pp.767-775.
- [24] H. Athari, M. Niroomand, M. Ataei, "Review and classification of control systems in grid-tied inverters", *Renewable and Sustainable Energy Reviews*, Vol.72, 2017, pp.1167-1176.
- [25] D. Zammit, C. S. Staines, M. Apap, J. Licari, "Design of PR current control with selective harmonic compensators using Matlab", *Journal of Electrical Systems and Information Technology*, Vol.4, No.3, 2017, pp.347-358.
- [26] H. Komurcigil, N. Altin, S. Ozdemir, I. Sefa, "Lyapunov-function and proportional-resonant-based control strategy for single-phase grid-connected VSI with LCL filter", *IEEE Transactions on Industrial Electronics*, Vol.63, No.5, pp.2838-2849.

BIOGRAPHIES



AKİF KARAFİL was born in Bursa, Turkey, in 1983. He received the B.S. degree in Electrical Education from Marmara University, İstanbul, Turkey, in 2007, the M.S. degree in Electrical and Electronics Engineering from Karadeniz Technical University, Trabzon, Turkey, in 2011 and the Ph.D. degree in Electrical

and Electronics Engineering from Karabük University, Karabük, Turkey, in 2018.

He is currently working at Bilecik Seyh Edebali University Vocational High School. His research interests include pulse density modulation control, resonant converter, soft switching, MPPT, single phase grid connected inverter and PV system applications.



HARUN ÖZBAY was born in Bursa, Turkey, in 1984. He received the B.S. degree in Electrical Education from Gazi University, Ankara, Turkey, in 2008, the M.S. degree in Electrical Education from Gazi University, Ankara, Turkey, in 2011 and the Ph.D. degree in Electrical and Electronics Engineering from Karabük University, Karabük, Turkey, in 2017.

He is currently working at Bandırma Onyedi Eylül University Engineering Faculty. His research interests include power electronics, electric machines, MPPT, grid connected inverter and PV system applications, electric vehicle and battery charger.

Forming and Co-simulation of Square and Triangular Waveforms by Using System Generator

M.A. ARSERİM, C. HAYDAROĞLU, H. ACAR and A. UÇAR

Abstract—Nowadays Field Programmable Gate Arrays (FPGAs) are used to implement several processes in different areas such as military defense, medical devices, automation, telecommunication, and image processing etc. Some of the advantages of FPGA are parallel and hardware processing. On the other hand programming FPGAs by classic design methodologies requires much effort. Therefore, design tools like System Generator can provide facilities about programming FPGAs. System Generator is a design tool from Xilinx to program the Xilinx FPGAs in MATLAB/Simulink graphic based editor. Also its block set is limited with respect to Simulink, has.

In this study square, and triangular waveforms are built with the basic blocks of System Generator tool. These waveforms belong to basic sources for signal processing. Generally, they are used in power electronics especially for producing PWM, or sinus PWM. Also co-simulation can be done by using System Generator. Square waveform block, which is implemented, has variable amplitude, frequency, duty cycle, and offset values whereas triangular waveform has variable amplitude, frequency, and offset values. Triangular waveform has an error as 2 % due to data bus width.

Index Terms—FPGA, waveforms, co-simulation, BASYS3 FPGA Board.

I. INTRODUCTION

FPGA belongs to Programmable Logic Devices (PLDs) and is a very large scaled integrated circuit (VLSI) [1]. Also FPGA is formed as a matrix of configurable logic block which can be connected to each other via fully programmable

MEHMET ALİ ARSERİM, is with Department of Electrical Engineering, University of Dicle, Diyarbakır, Turkey, (e-mail: marsirim@dicle.edu.tr). <https://orcid.org/0000-0002-9913-5946>

CEM HAYDAROĞLU, is with Department of Electrical Engineering, University of Dicle, Diyarbakır, Turkey, (e-mail: c.haydaroglu@dicle.edu.tr). <https://orcid.org/0000-0003-0830-5530>

HÜSEYİN ACAR, is with Department of Electrical Engineering, University of Dicle, Diyarbakır, Turkey, (e-mail: hacar@dicle.edu.tr). <https://orcid.org/0000-0001-5127-4632>

AYŞEGÜL UÇAR, is with Department of Mechatronics Engineering, University of Firat, Elazığ, Turkey, (e-mail: agulucar@firat.edu.tr). <https://orcid.org/0000-0002-5253-3779>

Manuscript received December 31, 2018; accepted June 27, 2019.
DOI: [10.17694/bajece.505842](https://doi.org/10.17694/bajece.505842)

interconnections [2]. Its clocking rate can be multiples of 100 Mega Hertz, which can be seen low with respect to computer has. Since it makes parallel processing, has capability of making operations as hardware, and consumes low power, it is preferred in today's electronic devices such as led tv, mobile phones, modems, imaging devices etc. So processing rate of FPGA increase enormously.

System generator is a tool for MATLAB/Simulink graphic-based editor, which is provided by XILINX firm in order to program its FPGAs [4]. Therefore, previous knowledge about design methodologies, or hardware descriptive language shouldn't be necessary by using System Generator. Also System Generator tool has co-simulation choice. Co-simulation provides both processing validation of the algorithm in a hardware, and increase in simulation speed. However, the number of Xilinx blocks are limited with regarding to Simulink blocks. In co-simulation process all of the Xilinx specific blocks are implemented and run in the target FPGA.

A periodic waveform is a waveform which repeats itself in time. Periodic waveforms are important in electronic circuits, and can be used for different purposes such as clocking, switching, triggering, producing different wave shapes as PWM signal vice versa [5]. Besides basic periodic waveforms are sine, square, rectangular, triangular, saw tooth, and pulse waveforms.

In this study it is aimed to implement two new blocks as square and triangular waveform for System Generator by using existed Xilinx specific blocks in Simulink. Several parameters as amplitude, frequency, and offset of these blocks can be tuned. After all, co-simulation is done for validation.

II. MATERIALS AND METHODS

Square and triangular periodic waveforms are two of the basic waveforms used in electronic circuits. They can also be used in power electronics for different purposes.

A. Square waveform

Square wave is a type of periodic waveform which alternates between two levels [6]. Its shape is given in Fig 1

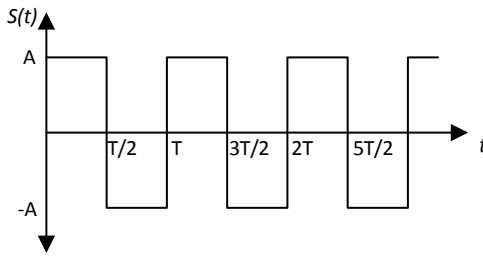


Fig. 1. Square waveform

and described as

$$S(t) = A(-1)^{\text{floor}(2(t-t_0)/T)} + d \quad (1)$$

Where: A – is amplitude;
 f floor – is floor function;
 t – is time, [s];
 t_0 – is offset, [s];
 T – is period, [s];
 d – is offset in amplitude;

Also square waveform can be used as a pulse train if its amplitude changes between A and 0 . Besides duty cycle can be changed and PWM signal is obtained.

B. Triangular waveform

Triangular wave is a non-sinusoidal two directional waveform [5]. It is linearly increases, and decreases between these two points. and it is alternated between two points by a ramp shape. Triangular waveform is shown in Fig.2

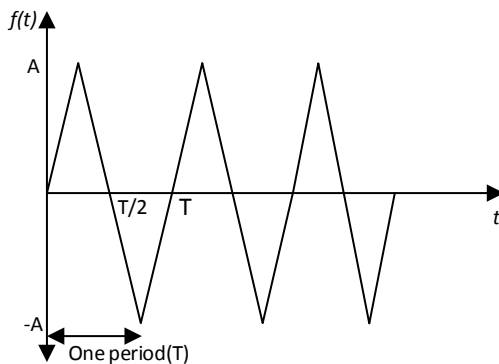


Fig. 2. Triangular waveform

It is defined as

$$f(t) = \begin{cases} \frac{2A}{T}(t-nT) & 0+nT < t < T/2+nt & n=0,\pm 1,\pm 2,\dots \\ \frac{-2A}{T}(t-T/2-nT)+A & t+T/2+nT \leq t < t+3T/2+nT & n=0,\pm 1,\pm 2,\dots \\ \frac{2A}{T}(t-T/2-nT)-A & t+3T/2+nT \leq t < t+2T+nT & n=0,\pm 1,\pm 2,\dots \end{cases}$$

Where: A – is amplitude;
 n – period number
 t – is time, [s];
 T – is period, [s];

Also an offset value, or time delay can be added to the signal. In practise triangular waveform can be obtained by electronic circuits. Examples of such circuits are operational

transresistance amplifier (OTRA) and current feedback operational amplifier [7,8]. Besides triangular waveform can be implemented by using up-down counter in software tools. Also look up tables can be used for any desired signal shape [9].

C. System Generator

System Generator is tool provided by Xilinx firm for MATLAB/Simulink, for programming its FPGAs visually. Xilinx blockset is added to Simulink by System Generator, and a Simulink model can be implemented with consisting of Xilinx specific blocks, and then FPGA program is built automatically. Therefore, there is no need to know programming language, and design methodologies [4].

If it is desired to make simulation with Xilinx blocks, initially System Generator icon should be added to the model. A window, which is shown in Figure 3, to make the various settings is open after double clicking this icon. In this window FPGA type, clock rate, operation type is chosen.



Fig. 3 System Generator window

Co-simulation option can be chosen, in order to make co-simulation with the specific FPGA. Vivado software runs in background to produce the bitstream file after pressing the Generate button. After all co-simulation can be done by loading bitstream file to FPGA.

D. BASYS3 FPGA training card

BASYS3 has Xilinx Artix-7 architecture and is a cheap and entry-level FPGA development card for Vivado. It has 33280 logic cell and its clocking rate is 150 MHz. BASYS3 FPGA training card is shown in Figure 4[10].



Fig. 4 BASYS3 FPGA training card

III. FINDINGS

In this study, periodic square and triangular waveform blocks are implemented by using Xilinx specific blocks in MATLAB/Simulink. Therefore, these blocks simulated and co-simulated.

Periodic square waveform, implemented with Xilinx blocks are shown in Figure 5

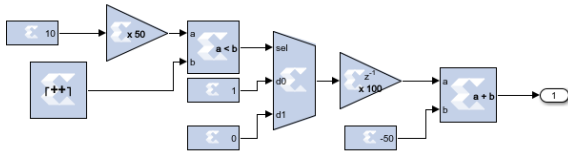


Fig. 5. Square waveform model with Xilinx specific blocks

Besides this model is masked and a block is created. The block parameters window is shown in Figure 5;

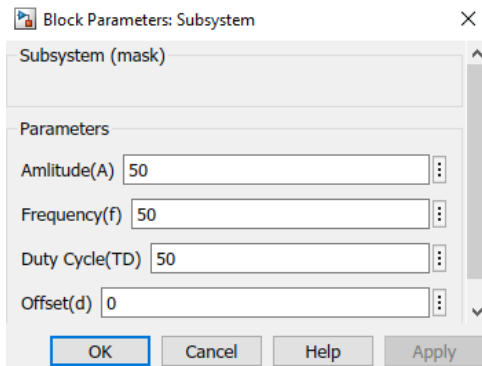


Fig. 6. square waveform block parameters window

Here amplitude, frequency, offset of the square waveform can be adapted. Also, if it is desired to use this block as a PWM signal generator there is an option for duty cycle.

In the application firstly, this block is simulated with the parameters for peak amplitude, frequency, and offset as 50, 50, and 0 respectively. Then co-simulation block of square waveform is generated by System Generator and added to the model as shown in Figure 7;

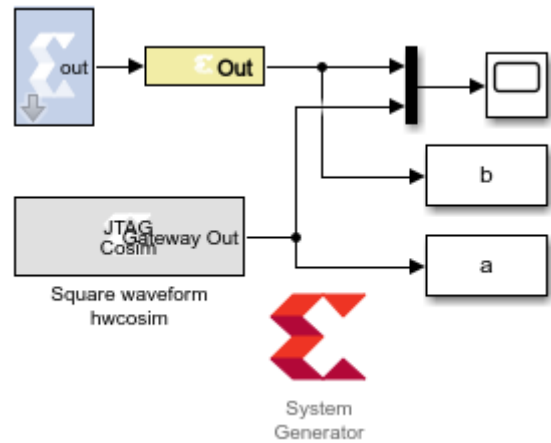


Fig. 7 The square waveform model with co-simulation block

As mentioned above, triangular waveform is built with the Xilinx specific blocks as shown in Figure 8;

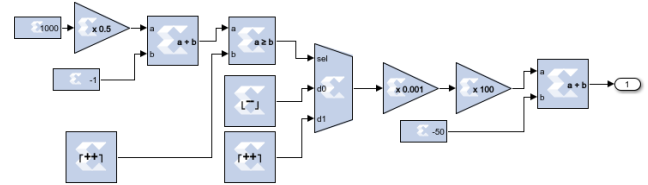


Fig. 8. Triangular waveform model with Xilinx specific blocks

In this model an up-counter is used for control logic, and one up-counter and one down-counter is used for forming triangular wave. Later amplitude, and offset of this wave is adapted. Thus, this model is masked, and then triangular waveform block is built. Block parameter window of this block is shown in Figure 9;

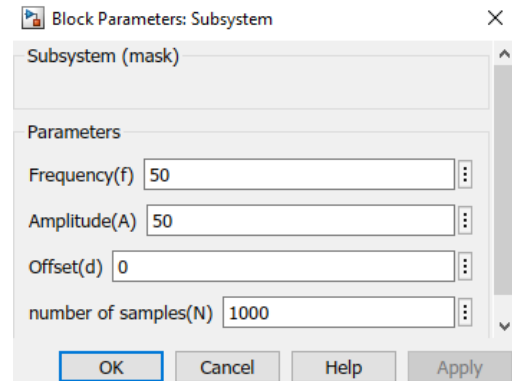


Fig. 9. Triangular waveform block parameter window

In this window frequency, amplitude, offset, and step size of the counters can be adapted.

Therefore, frequency, amplitude, offset, frequency, and step size of the counters are selected as 50, 50, 0, and 1000 respectively. The model with co-simulation block, generated is shown in Figure 10;

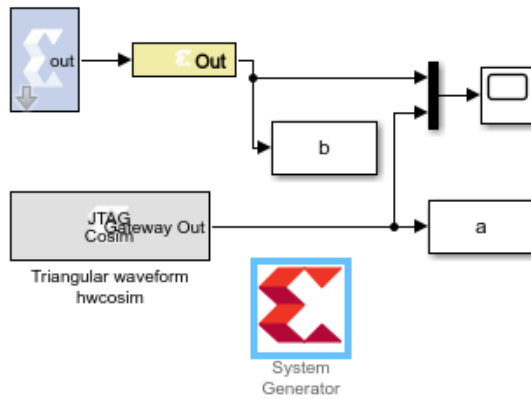


Fig. 10. The triangular waveform model with co-simulation block

Two models are run and simulation, and co-simulation results for square, and triangular waves are obtained as in Figure 11, and 12 respectively.

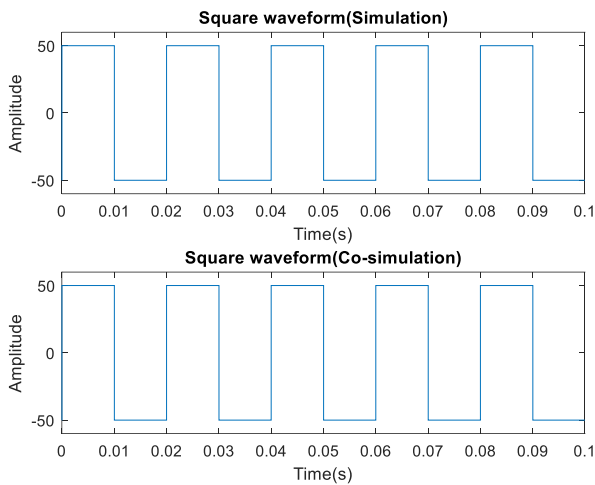


Fig. 11. Simulation, and co-simulation outputs of square waveform block

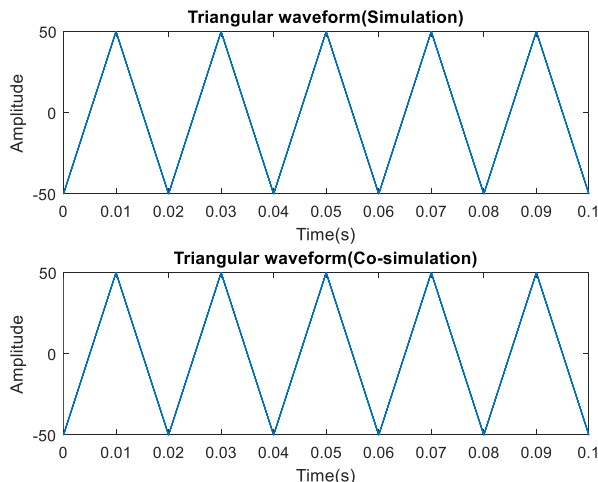


Fig. 12. Simulation, and co-simulation outputs of triangular waveform block

It can be seen from the figures 11, and 12 that simulation, and co-simulation results are same for both square, and triangular waveforms. This means that validation for the associated hardware is performed. Also in detailed analysis of the waveforms, there is an error as % 1.2 in the amplitude of triangular waveform. This error is occurred to the signed

number bit bus width of block. Also, the error can be decrease by increasing the bit bus width, or using floating point math.

IV. CONCLUSION

In this study it is aimed to add two new blocks as square and triangular waveforms to Xilinx blockset, provided by System Generator, in MATLAB/Simulink graph-based editor.

Also, these waveforms are among fundamental signals in electronics. Square waveform has harmonics of basic frequency, so it can be uses in harmonic analysis. In addition, this block has an extra choice as duty cycle. So this wave can be used as square wave PWM.

Triangular wave can be used in sinus PWM. Resulted signal of the block is satisfactorily from the viewpoint of sampling number, and the shape of the signal. Besides, BASYS3 FPGA card has a 100 MHz clock rate. So it can support PWM signals with high speed, and resolution.

Co-simulation results shown that the card can be used as a signal generator in practical circuits. This card can be used with Pmode (Peripheral mode) accessories for real time applications. Since FPGA can make parallel operations, this card can be used as multiple signal generator due to the range of Pmode accessory outputs.

Finally, this two block is sent to Xilinx Firm with the hope of contribution to Xilinx blockset provided by System Generator to MATLAB/Simulink.

Acknowledgment

The authors thank to Xilinx firm for Vivado design suite program licenses, and BASYS3 FPGA training cards.

References

- [1] C. Maxfield, "The design warrior's guide To FPGAs: Devices, Tools And Flows." Elsevier, 2004.
- [2] E. Monmasson, M.N Cirstea, "FPGA design methodology for industrial control systems-a review", IEEE Transactions On Industrial Electronics, Vol. 54, No. 4, 2007, pp.1824-1842.
- [3] E. Saritaş, S. Karataş. "Her yönüyle FPGA ve VHDL" Palme, 2013.
- [4] https://www.xilinx.com/support/documentation/sw_manuals/xilinx2017_2/ug897-vivado-sysgen-user.pdf
- [5] <https://www.electronics-tutorials.ws/waveforms/waveforms.html>.
- [6] <http://mathworld.wolfram.com/SquareWave.html>
- [7] Y. Lo, H. Chien., "Switch-controllable OTRA-based square/triangular waveform generator.", IEEE Transactions On Circuits And Systems II: Express Briefs, Vol.54, No. 12, 2007, pp. 1110-1114.
- [8] A. S., Haque, M. M. Hossain, , W. A. Davis, , H. T. Russell, & R. L. Carter, "Design of sinusoidal, triangular, and square wave generator using current feedback operational amplifier (CFOA)", In Region 5 Conference, 2008 IEEE, pp. 1-5.
- [9] M. Lakka, E. Koutroulis, A. Dollas, "Development of an FPGA-based SPWM Generator for high switching frequency DC/AC inverters" IEEE Transactions on power electronics, Vol.29, No.1, 2014, pp. 356-365.
- [10] <https://store.digilentinc.com/basys-3-artix-7-fpga-trainer-board-recommended-for-introductory-users/>.

BIOGRAPHIES



Muhammet Ali ARSERİM Şanlıurfa City, Turkey, in 1975. He received the B.S. degree in Electrical & Electronics Engineering from the University of Çukurova, Adana, Turkey, in 1999, M.S. degree in Electrical & Electronics Engineering from the University of Dicle, Diyarbakır, Turkey, in 2001 and the Ph.D.

degree in Electrical & Electronics Engineering from the University of Firat, Elazığ, Turkey, in 2009.

From 1998 to 2011, he was a Research Assistant with the Electrical & Electronics Engineering Department from the University of Dicle. Since 2011, he has been an Assistant Professor with the Electrical & Electronics Engineering Department from the University of Dicle. He is the author of several articles. His research interests include image processing, embedded systems and applications, FPGA, and system design.



Cem HAYDAROĞLU, Elazığ City, Turkey, in 1989. He received the B.S. degree in Electrical & Electronics Engineering from the University of Firat, Elazığ, Turkey, in 2011, M.S. degrees in Electrical & Electronics Engineering from the University of Dicle, Diyarbakır, Turkey, in 2017. He is currently PhD

student in Dicle University, Electrical & Electronics Engineering.

From 2014 to present, he is a Research Assistant with the Electrical & Electronics Engineering Department in Dicle University. His research interests are smart grids, power system analysis.



Hüseyin ACAR, Midyat, Mardin City, in 1983. He received the B.S. degree in Electronics Engineering from Uludağ University, Bursa, Turkey, in 2006, M.S. degree in Electrical & Electronics Engineering from Dicle University, Diyarbakır, Turkey, in 2010. He is currently PhD student in Dicle University

Electrical & Electronics Engineering.

From 2007 to present, he is a Research Assistant with the Electrical & Electronics Engineering Department at Dicle University. His research interests remote sensing, image processing and embedded systems.



Ayşegül UÇAR received a BS degree, MS degree, and PhD degree from the Electrical and Electronics Engineering Department at the University of Firat of Turkey in 1998, 2000, and 2006, respectively. In 2013, she was a visiting professor at Louisiana State University in the USA. She has been an associate

professor in the Department of Mechatronics Engineering since 2014. Her research interests include modeling and control, artificial intelligence systems, robotics vision, pattern recognition, and signal processing.

Secrecy Analysis of Multi-user Half/Full-Duplex Wireless Bi-directional Relaying Network

Volkan Ozduran, *Member, IEEE*

Abstract—This study investigates the secrecy performance of the relay-assisted orthogonal frequency division multiplexing technique. The investigation utilizes a multi-user illegitimate half/full-duplex based bi-directional relaying, which is under the effect of a finite number of friendly jammers, system model. In reference to Monte-Carlo computer simulation results, the system model that operates in half-duplex mode achieves slightly better secrecy outage performance than the system model that operates in full-duplex mode. The results also show that the information leakage can be minimized by using friendly jammers, yet the friendly jammers degrade the system secrecy performance and result in system coding gain losses in high signal-to-noise ratios.

Index Terms—Physical Layer Security, OFDM, Bi-directional Relay, Half/Full-Duplex Relay

I. INTRODUCTION

IN RECENT years, the number of mobile users/applications have increased dramatically. This results severe mobile data traffic in the cellular coverage areas. A combined orthogonal frequency division multiplexing (OFDM) technique and relay-assisted networks have made a great contribution to cover these capacity and throughput demands. However, information security demands are still an open challenge, which needs to be enhanced with cutting edge techniques. Until quite recently, the higher level encryption techniques, Rivest Shamir Adleman (RSA) [1] and advanced encryption standard (AES) [2], have been considered. However, these techniques do not provide a broad solution for the secure communication demands. In this regard, Wyner's [3] wiretap channels brought a new perspective and turn out to be a pioneering technique for the physical layer (PHY) security of wireless communications.

Recently, non-orthogonal multiple access (NOMA) strategy [4] has got much attention in the eyes of the researcher for the multi-user information exchange process. This is because, the NOMA strategy allows each user to access all sub-carrier channels, which directly affects the spectral efficiency [4]. It is also reported in [4] that the NOMA strategy achieves better performance than orthogonal multiple access strategies. However, since the NOMA technique employs the successive interference cancellation technique for the signal decoding, the last user should wait the other users' decoding process. This challenge is named as user-delay decoding process in the literature. This is indeed a big challenge especially in

dense wireless/internet-of-things networks. To overcome this challenge, the OFDM technique is considered in this study.

In this regard, some of the studies in the literature that consider the OFDM/orthogonal frequency division multiple access (OFDMA) techniques to conduct information are summarized as: Reference [5] assumes that source terminal communicates with L destinations by means of a single amplify-and-forward (AF) one-way relay (OWR). [5] also assumes that each mobile station utilizes the OFDM transceiver with N subcarriers. Reference [5] considers a joint optimization of power allocation, subcarrier allocation, and subcarrier pairing to maximize the secrecy rate. Reference [6] utilizes a system that source terminal communicates with the destination by means of a single decode-and-forward (DF) relay. [6] also considers that the communication overhears by an illegitimate terminal. [6] also considers the OFDM technique for the information exchange and also assumes three possible transmission scenarios: no communication, direct communication, and relay communication. In addition, [6] utilizes the power allocation strategy for maximizing the system sum-secrecy rate.

Reference [7] considers that M pre-assigned partner users communicate via two-way relay (TWR) terminal, which has an OFDMA technique, in the presence of an eavesdropper with/without cooperative jamming. [7] also considers that relay terminal operates in the half-duplex (HD) mode with an AF strategy. [7] also utilizes power allocation strategies for maximizing the system secrecy sum-rate. [8] considers an OFDMA downlink network, which contains a single antenna K mobile users and multiple antennas equipped M HD based DF relays and also a multiple antenna base station. [8] also assumes that system structure contains an eavesdropper with multiple antenna. [8] also considers optimization for the secure resource allocations and scheduling. [9] considers the single antenna OFDMA based multi-user and multi AF based OWR network with an eavesdropper. [9] also considers resource optimization PHY security of such a system model. Reference [10] assumes that the source terminal conducts information with the destination terminal via L available DF based OWR terminals in the presence of a single illegitimate terminal. [10] also assumes that each terminal in the system model poses an OFDM transceiver that has N sub-carriers. [10] investigates the system secrecy rates and outage performance.

The aforementioned studies consider various types of system structures and also considers that the trustworthy/untrustworthy relay terminal run in HD mode. Alternatively, [11] considers multi-user one-way information exchange traffic with an untrustworthy full-duplex (FD) relay terminal by using OFDM strategy. In addition, to mitigate the information leakage, [11] also considers that the illegitimate terminal is under the effect

VOLKAN OZDURAN is with Department of Electrical and Electronics Engineering, Istanbul University-Cerrahpasa, Istanbul, Turkey, (email: volkan@istanbul.edu.tr).

<https://orcid.org/0000-0002-9442-9099>

Manuscript received January 28, 2019; accepted July 2, 2019.

DOI:10.17694/bajece.518904

of a finite number of friendly jammers and also investigates secrecy outage probability (SOP) performance. This paper distinguishes itself from aforementioned studies in a several ways. The differences can be summarized as: First, this paper utilizes a multi-user untrustworthy AF HD/FD based TWR system structure that considers OFDM strategy. Second, this paper utilizes the SOP performance metric and investigates the secrecy performance of given system structure, which is presented in figure 1.

The rest of the paper is organized as follows: Section II provides the channel statistics and system structure details. Section III presents the analytical derivations. Section IV provides the numerical results and the paper is finalized in section V.

Notations: The $F_h(\cdot)$ and $f_h(\cdot)$ represent the cumulative distribution function (CDF) and the probability density function (PDF) of a random variables (RVs) h , respectively. The $\mathbb{E}[\cdot]$ term represents the expectation, while the $\Pr(\cdot)$ represents the probability. All log are considered base 2. The term $G_{p,q}^{m,n}$ represents the Meijer-G function [12] and the term $G_{q,p;p_1,q_1;p_2,q_2}^{m,0;m_1,n_1;m_2,n_2}$ is the extended generalized bivariate Meijer-G function (EGBMGF) [13, Eq. (13)].

II. SYSTEM MODEL AND CHANNEL STATISTICS

Figure 1 plots a multi-user AF based untrustworthy two-way HD/FD based relaying network. Figure 1 also plots that to mitigate the information leakage, the illegitimate terminal is under the effect of a finite number of friendly jammers. Here, x_k and y_k , $\forall k = 1, \dots, N$, conduct information exchange, by means of k^{th} sub-carrier among N , via a single HD/FD based untrustworthy TWR terminal. In the case that the untrustworthy relay terminal in HD mode, the user terminals conduct information exchange in two phases, which are multiple access (MAC) and broadcast (BC), while it requires a single phase, which is MAC, for the FD mode. Please note that MAC and BC channels are considered as reciprocal in such a system model. x_k and y_k terminals do not have a direct-link because of the possible obstacles. It is also assumed that legitimate/illegitimate terminals possess a single omnidirectional antenna in the system model.

In figure 1, h_k and g_k , $\forall k = 1, \dots, N$ represent the channel impulse responses between $x_k \rightarrow$ untrustworthy relay and $y_k \rightarrow$ untrustworthy relay, respectively. h_k are independent and identically distributed (i.i.d.) complex Gaussian RVs with zero mean and variances $\sigma_{h_k}^2$. (i.e. $h_k \sim \mathcal{CN}(0, \sigma_{h_k}^2)$). Likewise, g_k are also i.i.d. and $g_k \sim \mathcal{CN}(0, \sigma_{g_k}^2)$. $a_k \sim \mathcal{CN}(0, \sigma_{a_k}^2)$, $b_k \sim \mathcal{CN}(0, \sigma_{b_k}^2)$, and $c_k \sim \mathcal{CN}(0, \sigma_{c_k}^2)$ represent the loop-interference (LI), which is caused by transmitting and receiving the signal at the same time period, at x_k , y_k , and untrustworthy relay, respectively. f_j are also i.i.d. and $f_j \sim \mathcal{CN}(0, \sigma_{f_j}^2)$, $\forall j = 1, \dots, M$ is the channel impulse response, j^{th} friendly jammer \rightarrow relay. Amplitudes of all channels are distributed according to the Rayleigh distributions.

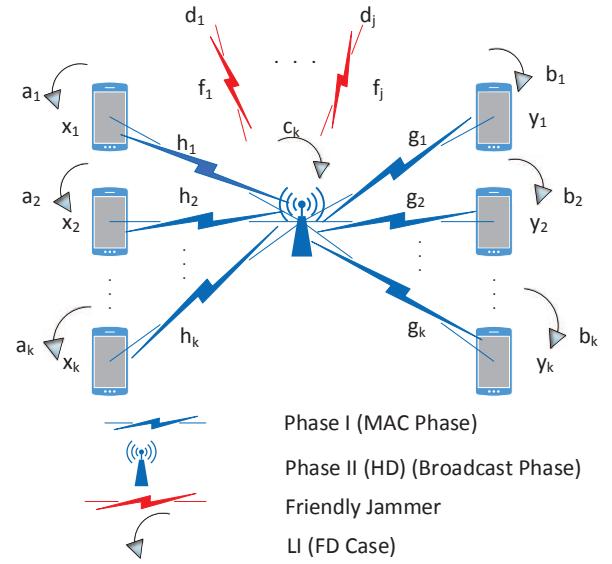


Fig. 1: The OFDM based multi-user AF HD/FD TWR.

A. The Half-Duplex Case

This subsection now turns its attention to the illegitimate terminal operates in the HD mode. The received signals at the HD based illegitimate relay terminal on k^{th} sub-carrier can be written as

$$Z_{r_k}^{HD} = \sqrt{P_s} m_{x_k} h_k + \sqrt{P_s} m_{y_k} g_k + \sum_{j=1}^M \sqrt{P_J} f_j d_j + n_{r_k} \quad (1)$$

Here, m_{x_k} and m_{y_k} represent the corresponding transmit information of x_k and y_k on k^{th} sub-carrier, respectively. Here, $\mathbb{E}[|m_{x_k}|^2] = 1$, $\mathbb{E}[|m_{y_k}|^2] = 1$, and $\mathbb{E}[|d_j|^2] = 1$. P_s represents the corresponding transmit power of x_k and y_k terminals. P_J represents the j^{th} friendly jammer's transmit power. n_{r_k} is the additive white Gaussian noise (AWGN) at the untrustworthy relay terminal on k^{th} sub-carrier. The leakage rate (LR) expressions with regard to x_k and y_k on k^{th} sub-carrier can be written as

$$LR_{x_k}^{HD} = \frac{1}{2} \log \left(1 + \frac{\gamma_x}{\gamma_y + \gamma_J + \sigma^2} \right) \quad (2)$$

$$LR_{y_k}^{HD} = \frac{1}{2} \log \left(1 + \frac{\gamma_y}{\gamma_x + \gamma_J + \sigma^2} \right) \quad (3)$$

where σ^2 is the noise variance, $\gamma_{x_k} = \frac{P_s |h_k|^2}{\sigma^2}$, $\gamma_{y_k} = \frac{P_s |g_k|^2}{\sigma^2}$, and $\gamma_J = \sum_{j=1}^M \frac{P_J |f_j|^2}{\sigma^2}$. Since the untrustworthy relay terminal in AF mode, the amplification factor, which is G , on k^{th} sub-carrier can be calculated as

$$G_k^{HD} = \sqrt{\frac{P_r}{P_s |h_k|^2 + P_s |g_k|^2 + \sum_{j=1}^M P_J |f_j|^2 + \sigma^2}} \quad (4)$$

where P_r represents the untrustworthy relay terminal's transmit power. In the second phase, the untrustworthy relay terminal broadcasts the amplified version of the received signals to the user-pairs. The received signal at x_k on k^{th} sub-carrier can be calculated as

$$Z_{x_k}^{HD} = G^{HD} \sqrt{P_s} m_{x_k} h_k^2 + G^{HD} \sqrt{P_s} m_{y_k} g_k h_k + G^{HD} \sum_{j=1}^M \sqrt{P_J} f_j d_j h_k + G^{HD} n_r h_k + n_{x_k} \quad (5)$$

Substituting (4) into (5), the signal-to-interference noise ratio (SINR) at x_k on k^{th} sub-carrier can be calculated as

$$\gamma_{x_k}^{HD} = \frac{\frac{\varphi \gamma_x \gamma_y}{[\gamma_J + \sigma^2]}}{\varphi \gamma_x + \frac{\varphi \gamma_x + \gamma_x + \gamma_y}{[\gamma_J + \sigma^2]} + 1} \quad (6)$$

where $\varphi = \frac{P_r}{P_s}$ [14]. Likewise, γ_{y_k} on k^{th} sub-carrier can be calculated as

$$\gamma_{y_k}^{HD} = \frac{\frac{\varphi \gamma_x \gamma_y}{[\gamma_J + \sigma^2]}}{\varphi \gamma_y + \frac{\varphi \gamma_x + \gamma_x + \gamma_y}{[\gamma_J + \sigma^2]} + 1} \quad (7)$$

B. Full-Duplex Case

The subsection assumes that the illegitimate terminal runs in the FD mode. In this regard, the received signal at the illegitimate terminal on k^{th} sub-carrier can be written as

$$Z_{r_k}^{FD} = \sqrt{P_s} m_{x_k} h_k + \sqrt{P_s} m_{y_k} g_k + \sum_{j=1}^M \sqrt{P_J} f_j d_j + \sqrt{P_r} c_k + n_r \quad (8)$$

By using (8), the LR expressions with respect to x_k and y_k on k^{th} sub-carrier can be calculated as

$$LR_{x_k}^{FD} = \log \left(1 + \frac{\gamma_x}{\gamma_y + \gamma_J + \gamma_{c_k} + \sigma^2} \right) \quad (9)$$

$$LR_{y_k}^{FD} = \log \left(1 + \frac{\gamma_y}{\gamma_x + \gamma_J + \gamma_{c_k} + \sigma^2} \right) \quad (10)$$

Here, $\gamma_{c_k} = \frac{P_r |c_k|^2}{\sigma^2}$. The G amplification factor on k^{th} sub-carrier for the FD case can be re-calculated as

$$G_k^{FD} = \sqrt{\frac{P_r}{P_s |h_k|^2 + P_s |g_k|^2 + \sum_{j=1}^M P_J |f_j|^2 + P_r |c_k|^2 + \sigma^2}} \quad (11)$$

The received signal at x_k on k^{th} sub-carrier can be calculated as

$$Z_{x_k}^{FD} = G^{FD} \sqrt{P_s} m_{x_k} h_k^2 + G^{FD} \sqrt{P_s} m_{y_k} g_k h_k + G^{FD} \sum_{j=1}^M \sqrt{P_J} f_j d_j h_k + G^{FD} \sqrt{P_r} c_k h_k + G^{FD} n_r h_k + \sqrt{P_s} a_k + n_{x_k} \quad (12)$$

Substituting (11) into (12) and doing some mathematical manipulations, the received SINR at x_k on k^{th} sub-carrier can be calculated as in (13). Likewise, the received SINR at y_k on k^{th} sub-carrier can be calculated as in (14).

III. PERFORMANCE ANALYSIS

This section gives analytical derivations related to the secrecy of the multi-user HD/FD based relay-assisted TWR with OFDM strategy. In this regard, the SOP is considered as a performance metric and the details are presented in following subsection.

A. The Secrecy Outage Probability

The SOP is defined as the secrecy achievable rate, which is based on subtracting the LR expression from the system total achievable rate, cannot support R in bps/Hz, which is a pre-defined target rate. From the analytical perspective, by using the logarithm properties, the SOP can also be defined as the CDF of the secrecy achievable rate's received SINR evaluated at target threshold rate, γ_{th} . The total secrecy rate expression at X line users with respect to HD and FD strategies are given as follows:

$$R_X^{HD} = \frac{1}{2} \left[\sum_{k=1}^N \log(1 + \gamma_{x_k}^{HD}) - \log(1 + \gamma_{x_k,R}^{HD}) \right]^+ \quad (15)$$

$$R_X^{FD} = \left[\sum_{k=1}^N \log(1 + \gamma_{x_k}^{FD}) - \log(1 + \gamma_{x_k,R}^{FD}) \right]^+ \quad (16)$$

where $[x]^+ = \max(0, x)$. The end-to-end (e2e) SOP for HD and FD cases can be written as

$$R_{e2e}^{HD} = \Pr(\min(R_X^{HD}, R_Y^{HD}) \leq R) \quad (17)$$

$$R_{e2e}^{FD} = \Pr(\min(R_X^{FD}, R_Y^{FD}) \leq R) \quad (18)$$

Here, R_Y^{HD} and R_Y^{FD} are the symmetry of R_X^{HD} and R_X^{FD} , respectively. The CDF expressions of (17) and (18) can be calculated as in the proposition 1 and proposition 2, respectively.

IV. NUMERICAL RESULTS

This section provides numerical results, which is based on monte-carlo simulations, regarding the system e2e secrecy outage performance. The friendly jammers are located by using the Euclidean distance formulation, which is d^{-v} [15], in the system model. The d term represents the distance and v term represents the path-loss exponent, which takes values between 2-6 [15]. In simulation setup, the d and v terms are set to 10 and 2, respectively. In this regard, the friendly jammers' transmit power, P_J , is chosen relatively low, which is $P_J \ll P_T$, $P_J = P_T/100$, in comparison to user-pairs' total transmit powers, which is $P_T = 2NP_s + P_r$. In an equal interference and user-pairs' transmit power case, the external interference severely degrades the system performance [16]. The number of the friendly jammer, which is M , is set to 1 and the friendly jammers' channel variances, which is $\sigma_{f_j}^2$ are set to 10^{-2} .

$$\gamma_{x_k}^{FD} = \frac{\frac{\varphi\gamma_x\gamma_y}{[\gamma_J+\sigma^2][\gamma_c+\sigma^2][\gamma_{a_k}+\sigma^2]}}{\left[\frac{\varphi\gamma_x}{[\gamma_c+\sigma^2][\gamma_{a_k}+\sigma^2]} + \frac{\gamma_x(\varphi+1)+\gamma_y}{[\gamma_J+\sigma^2][\gamma_{a_k}+\sigma^2][\gamma_c+\sigma^2]} + \frac{\varphi\gamma_x}{[\gamma_J+\sigma^2][\gamma_{a_k}+\sigma^2]} + \frac{\gamma_x+\gamma_y}{[\gamma_J+\sigma^2][\gamma_c+\sigma^2]} + 1 \right]} \quad (13)$$

$$\gamma_{y_k}^{FD} = \frac{\frac{\varphi\gamma_x\gamma_y}{[\gamma_J+\sigma^2][\gamma_c+\sigma^2][\gamma_{b_k}+\sigma^2]}}{\left[\frac{\varphi\gamma_y}{[\gamma_c+\sigma^2][\gamma_{b_k}+\sigma^2]} + \frac{\gamma_y(\varphi+1)+\gamma_x}{[\gamma_J+\sigma^2][\gamma_{b_k}+\sigma^2][\gamma_c+\sigma^2]} + \frac{\varphi\gamma_y}{[\gamma_J+\sigma^2][\gamma_{b_k}+\sigma^2]} + \frac{\gamma_x+\gamma_y}{[\gamma_J+\sigma^2][\gamma_c+\sigma^2]} + 1 \right]} \quad (14)$$

By using the signal processing strategies and special antenna design, the LI effects can be minimized. In this regard, the LI variances at x_k and y_k , which are $\sigma_{a_k}^2$ and $\sigma_{c_k}^2$, and at untrustworthy relay terminal, which is $\sigma_{b_k}^2$, are modeled as: $P_s^{\lambda-1}$ and $P_r^{\lambda-1}$, respectively. The λ term takes values between $0 \leq \lambda \leq 1$ [17]. The λ term is set to 0.1 in the simulation setup. The number of the mobile terminal, which is N , is set to 2, 4, 6, 8, and 10 in the system model setup. The x_k and y_k have P_s transmit power and the untrustworthy relay terminal has P_r transmit power. In this regard, as earlier mentioned the system total transmit power is equal to $P_T = 2NP_s + P_r$. Two different target rates, which are $R = 1$ bps/Hz and $R = 3$ bps/Hz, are considered in the performance analysis. Figure 2 and figure 3 utilize $R = 1$ bps/Hz and $R = 3$ bps/Hz target rates, respectively. Commenting the figure 2 and 3 based on the aforementioned system model configurations, following results can be obtained.

Figure 2 presents the e2e secrecy outage performance comparison of the HD and FD based system model configurations. According to figure 2, a large number of user achieve better e2e secrecy outage performance than a small number of user in low and high SNR regimes. This is because a large number of sub-carrier allow more users to conduct information exchange compared to a small number of users. This also means that a large number of users posses more total transmit powers, which is directly related to $P_T = 2NP_s + P_r$. Results also show that the secrecy outage performance curves tend to saturate in high SNR regimes. This is because the friendly jammers' negative effects on the system secrecy performance. In addition, the system model that operates in HD mode achieves slightly better outage performance than FD mode. This is because the LI effect on the FD mode. A large number of user reach the 10^{-5} outage levels while a small number of users saturate in high outage regimes, which is around 10^{-2} and 10^{-4} .

Figure 3 also plots the e2e secrecy outage performance comparison of the HD and FD based system model. Differently from figure 2, the figure 3 utilizes the $R = 3$ bps/Hz. As in figure 2, a large number of users achieve better secrecy outage performance than a small number of users. In addition, the HD based system model achieves slightly better performance than FD mode. However, the outage performance gap between two modes become less then $R = 1$ bps/Hz. This is because the pre-log factor differences as described in (15) and (16). In addition, by definition of the secrecy outage probability, which is described in section III A, the outage performance curves

slightly move to the high SNR regimes.

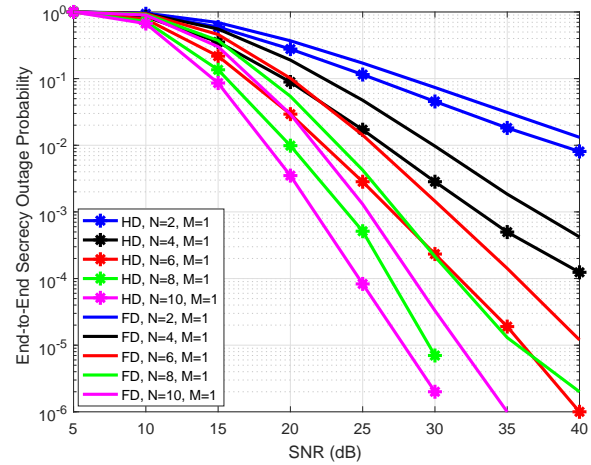


Fig. 2: The e2e secrecy outage performance comparison of the OFDM based multi-user HD/FD based TWR network with $N = 2, 4, 6, 8, 10, M = 1$, and $R = 1$ bps/Hz.

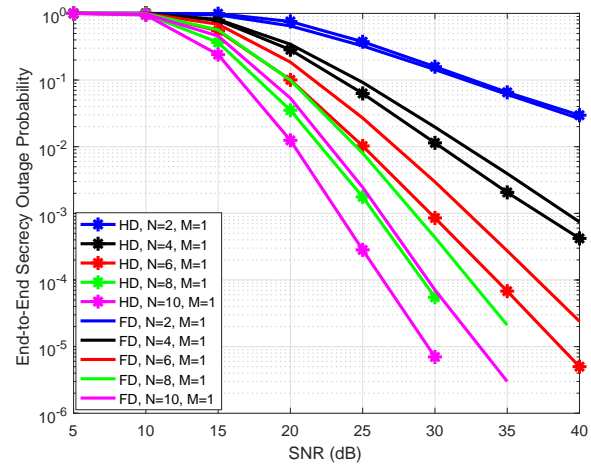


Fig. 3: The e2e secrecy outage performance comparison of the OFDM based multi-user HD/FD based TWR network with $N = 2, 4, 6, 8, 10, M = 1$, and $R = 3$ bps/Hz.

Proposition 1: The CDF expression of the R_{e2e}^{HD} can be re-written as

$$\begin{aligned}
F_{R_{e2e}^{HD}}^{\text{up}}(\gamma_{th}^{HD}) &= 1 - \left[\frac{P_s \Omega_{gk}}{\Gamma(2)\Gamma(M)} G_{1,0:1,1:1,1}^{1,0:1,1:1,1} \left(\begin{matrix} 1 & -1 & 1-M \\ - & 0 & 0 \end{matrix} \middle| P_s \Omega_{gk}, P_J \Omega_{fj} \right) \right. \\
&+ M \frac{P_J \Omega_{fj}}{\Gamma(M+1)} G_{1,0:1,1:1,1}^{1,0:1,1:1,1} \left(\begin{matrix} 1 & 0 & -M \\ - & 0 & 0 \end{matrix} \middle| P_s \Omega_{gk}, P_J \Omega_{fj} \right) + \frac{1}{\Gamma(M)} G_{1,0:1,1:1,1}^{1,0:1,1:1,1} \left(\begin{matrix} 1 & 0 & 1-M \\ - & 0 & 0 \end{matrix} \middle| P_s \Omega_{gk}, P_J \Omega_{fj} \right) \\
&- \left(\frac{P_s \Omega_{gk}}{P_s \Omega_{h_k}} \right) \Theta^{-1} \sum_{i=1}^M \frac{A_i}{\Gamma(i)} G_{2,1}^{1,2} \left(\frac{\left(\frac{P_J \Omega_{fj} \gamma_{th}^{HD}}{P_s \Omega_{gk}} \right)}{\Theta} \middle| 1-i, 0 \right) - \left(\frac{P_s \Omega_{gk}}{P_s \Omega_{h_k}} \right) \Theta^{-1} \frac{V}{\Gamma(2)} G_{2,1}^{1,2} \left(\frac{\left(\frac{P_s \Omega_{gk}}{P_s \Omega_{h_k}} \right)}{\Theta} \middle| -1, 0 \right) \\
&- \left(\frac{P_s \Omega_{gk}}{P_s \Omega_{h_k}} \right) \Theta^{-1} \sum_{l=1}^M \frac{C_l}{\Gamma(l)} G_{2,1}^{1,2} \left(\frac{\left(\frac{P_J \Omega_{fj}}{P_s \Omega_{h_k}} \right)}{\Theta} \middle| 1-l, 0 \right) - M \left(\frac{P_J \Omega_{fj}}{P_s \Omega_{h_k}} \right) \Theta^{-1} \sum_{aa=1}^M \frac{D_{aa}}{\Gamma(aa)} G_{2,1}^{1,2} \left(\frac{\left(\frac{P_J \Omega_{fj} \gamma_{th}^{HD}}{P_s \Omega_{gk}} \right)}{\Theta} \middle| 1-aa, 0 \right) \\
&- M \left(\frac{P_J \Omega_{fj}}{P_s \Omega_{h_k}} \right) E \Theta^{-1} G_{2,1}^{1,2} \left(\frac{\left(\frac{P_s \Omega_{gk}}{P_s \Omega_{h_k}} \right)}{\Theta} \middle| 0, 0 \right) - M \left(\frac{P_J \Omega_{fj}}{P_s \Omega_{h_k}} \right) \Theta^{-1} \sum_{bb=1}^{M+1} \frac{F_{bb}}{\Gamma(bb)} G_{2,1}^{1,2} \left(\frac{\left(\frac{P_J \Omega_{fj}}{P_s \Omega_{h_k}} \right)}{\Theta} \middle| 1-bb, 0 \right) \\
&- \left(\frac{1}{P_s \Omega_{h_k}} \right) \Theta^{-1} \sum_{cc=1}^M \frac{G_{cc}}{\Gamma(cc)} G_{2,1}^{1,2} \left(\frac{\left(\frac{P_J \Omega_{fj} \gamma_{th}^{HD}}{P_s \Omega_{gk}} \right)}{\Theta} \middle| 1-cc, 0 \right) - \left(\frac{1}{P_s \Omega_{h_k}} \right) \Theta^{-1} \frac{H}{\Gamma(1)} G_{2,1}^{1,2} \left(\frac{\left(\frac{P_s \Omega_{gk}}{P_s \Omega_{h_k}} \right)}{\Theta} \middle| 0, 0 \right) \\
&- \left. \left(\frac{1}{P_s \Omega_{h_k}} \right) \Theta^{-1} \sum_{bb=1}^M \frac{I_{dd}}{\Gamma(dd)} G_{2,1}^{1,2} \left(\frac{\left(\frac{P_J \Omega_{fj}}{P_s \Omega_{h_k}} \right)}{\Theta} \middle| 1-dd, 0 \right) \right] \times \left[\frac{P_s \Omega_{h_k}}{\Gamma(2)\Gamma(M)} G_{1,0:1,1:1,1}^{1,0:1,1:1,1} \left(\begin{matrix} 1 & -1 & 1-M \\ - & 0 & 0 \end{matrix} \middle| P_s \Omega_{h_k}, P_J \Omega_{fj} \right) \right. \\
&+ M \frac{P_J \Omega_{fj}}{\Gamma(M+1)} G_{1,0:1,1:1,1}^{1,0:1,1:1,1} \left(\begin{matrix} 1 & 0 & -M \\ - & 0 & 0 \end{matrix} \middle| P_s \Omega_{h_k}, P_J \Omega_{fj} \right) + \frac{1}{\Gamma(M)} G_{1,0:1,1:1,1}^{1,0:1,1:1,1} \left(\begin{matrix} 1 & 0 & 1-M \\ - & 0 & 0 \end{matrix} \middle| P_s \Omega_{h_k}, P_J \Omega_{fj} \right) \\
&- \left(\frac{P_s \Omega_{h_k}}{P_s \Omega_{gk}} \right) \Lambda^{-1} \sum_{ee=1}^M \frac{J_{ee}}{\Gamma(ee)} G_{2,1}^{1,2} \left(\frac{\left(\frac{P_J \Omega_{fj} \gamma_{th}^{HD}}{P_s \Omega_{h_k}} \right)}{\Lambda} \middle| 1-ee, 0 \right) - \left(\frac{P_s \Omega_{h_k}}{P_s \Omega_{gk}} \right) \Lambda^{-1} \frac{K}{\Gamma(2)} G_{2,1}^{1,2} \left(\frac{\left(\frac{P_s \Omega_{h_k}}{P_s \Omega_{gk}} \right)}{\Theta} \middle| -1, 0 \right) \\
&- \left(\frac{P_s \Omega_{h_k}}{P_s \Omega_{gk}} \right) \Lambda^{-1} \sum_{l=1}^M \frac{L_{ff}}{\Gamma(ff)} G_{2,1}^{1,2} \left(\frac{\left(\frac{P_J \Omega_{fj}}{P_s \Omega_{gk}} \right)}{\Theta} \middle| 1-ff, 0 \right) - M \left(\frac{P_J \Omega_{fj}}{P_s \Omega_{gk}} \right) \Lambda^{-1} \sum_{gg=1}^M \frac{M_{gg}}{\Gamma(gg)} G_{2,1}^{1,2} \left(\frac{\left(\frac{P_J \Omega_{fj} \gamma_{th}^{HD}}{P_s \Omega_{h_k}} \right)}{\Lambda} \middle| 1-gg, 0 \right) \\
&- M \left(\frac{P_J \Omega_{fj}}{P_s \Omega_{gk}} \right) N^{***} \Lambda^{-1} G_{2,1}^{1,2} \left(\frac{\left(\frac{P_s \Omega_{h_k}}{P_s \Omega_{gk}} \right)}{\Lambda} \middle| 0, 0 \right) - M \left(\frac{P_J \Omega_{fj}}{P_s \Omega_{gk}} \right) \Lambda^{-1} \sum_{hh=1}^{M+1} \frac{O_{hh}}{\Gamma(hh)} G_{2,1}^{1,2} \left(\frac{\left(\frac{P_J \Omega_{fj}}{P_s \Omega_{gk}} \right)}{\Lambda} \middle| 1-hh, 0 \right) \\
&- \left(\frac{1}{P_s \Omega_{gk}} \right) \Lambda^{-1} \sum_{ii=1}^M \frac{P_{ii}}{\Gamma(ii)} G_{2,1}^{1,2} \left(\frac{\left(\frac{P_J \Omega_{fj} \gamma_{th}^{HD}}{P_s \Omega_{h_k}} \right)}{\Lambda} \middle| 1-ii, 0 \right) - R \left(\frac{1}{P_s \Omega_{gk}} \right) \Lambda^{-1} G_{2,1}^{1,2} \left(\frac{\left(\frac{P_s \Omega_{h_k}}{P_s \Omega_{gk}} \right)}{\Lambda} \middle| 0, 0 \right) \\
&- \left. \left(\frac{1}{P_s \Omega_{gk}} \right) \Lambda^{-1} \sum_{jj=1}^M \frac{S_{jj}}{\Gamma(jj)} G_{2,1}^{1,2} \left(\frac{\left(\frac{P_J \Omega_{fj}}{P_s \Omega_{gk}} \right)}{\Lambda} \middle| 1-jj, 0 \right) \right] \quad (19)
\end{aligned}$$

where $\Theta = \left(\frac{\gamma_{th}^{HD} \varphi^{-1}}{P_s \Omega_{h_k}} + \frac{\gamma_{th}^{HD} \varphi^{-1} (2\varphi+1)}{P_s \Omega_{gk}} + \frac{1}{P_s \Omega_{h_k}} \right)$ and $\Lambda = \left(\frac{\gamma_{th}^{HD} \varphi^{-1}}{P_s \Omega_{gk}} + \frac{\gamma_{th}^{HD} \varphi^{-1} (2\varphi+1)}{P_s \Omega_{h_k}} + \frac{1}{P_s \Omega_{gk}} \right)$.

Proof: See Appendix A. ■

V. CONCLUSION

This study has investigated the secrecy performance of the multi-user HD/FD based relay-assisted TWR with OFDM strategy. In reference to Monte-Carlo computer simulations, the HD based untrustworthy relaying system achieves better

secrecy outage performance in comparison to FD case. Results have also showed that the friendly jammers beside minimizing the information leakage also result in system coding gain losses in high SNR regimes. In addition, in the case that the target rate increases the system secrecy performance gets worse.

Proposition 2: The CDF expression of R_{e2e}^{FD} can be calculated as

$$\begin{aligned}
 F_{R_{e2e}^{FD}}^{\text{up}}(\gamma_{th}^{FD}) &= 1 - \left[\left(\frac{P_s \Omega_{gk}}{P_s \Omega_{hk}} \right) A^* \frac{P_s \Omega_{hk}}{\Gamma(2)} G_{2,1}^{1,2} \left(P_s \Omega_{gk} \mid \begin{matrix} -1, 0 \\ 0, - \end{matrix} \right) + \left(\frac{P_s \Omega_{gk}}{P_s \Omega_{hk}} \right) \sum_{a^3=1}^M B_{a^3}^* \frac{P_s \Omega_{hk}}{\Gamma(a^3)} G_{2,1}^{1,2} \left(P_j \Omega_{fj} \mid \begin{matrix} 1 - a^3, 0 \\ 0, - \end{matrix} \right) \right. \\
 &+ \left(\frac{P_s \Omega_{gk}}{P_s \Omega_{hk}} \right) C^* P_s \Omega_{hk} G_{2,1}^{1,2} \left(P_r \Omega_{ck} \mid \begin{matrix} 0, 0 \\ 0, - \end{matrix} \right) + D^* P_s \Omega_{hk} G_{2,1}^{1,2} \left(P_s \Omega_{gk} \mid \begin{matrix} 0, 0 \\ 0, - \end{matrix} \right) \\
 &+ \sum_{b^3=1}^{M+1} E_{b^3}^* \frac{P_s \Omega_{hk}}{\Gamma(b^3)} G_{2,1}^{1,2} \left(P_j \Omega_{fj} \mid \begin{matrix} 1 - b^3, 0 \\ 0, - \end{matrix} \right) + F^* P_s \Omega_{hk} G_{2,1}^{1,2} \left(P_r \Omega_{ck} \mid \begin{matrix} 0, 0 \\ 0, - \end{matrix} \right) \\
 &+ G^* P_s \Omega_{hk} G_{2,1}^{1,2} \left(P_s \Omega_{gk} \mid \begin{matrix} 0, 0 \\ 0, - \end{matrix} \right) + \sum_{c^3=1}^M H_{c^3}^* \frac{P_s \Omega_{hk}}{\Gamma(c^3)} G_{2,1}^{1,2} \left(P_j \Omega_{fj} \mid \begin{matrix} 1 - c^3, 0 \\ 0, - \end{matrix} \right) \\
 &+ I^* \frac{P_s \Omega_{hk}}{\Gamma(2)} G_{2,1}^{1,2} \left(P_r \Omega_{ck} \mid \begin{matrix} -1, 0 \\ 0, - \end{matrix} \right) + J^* P_s \Omega_{hk} G_{2,1}^{1,2} \left(P_s \Omega_{gk} \mid \begin{matrix} 0, 0 \\ 0, - \end{matrix} \right) \\
 &+ \sum_{d^3=1}^M K_{d^3}^* \frac{P_s \Omega_{hk}}{\Gamma(d^3)} G_{2,1}^{1,2} \left(P_j \Omega_{fj} \mid \begin{matrix} 1 - d^3, 0 \\ 0, - \end{matrix} \right) + L^* \frac{P_s \Omega_{hk}}{\Gamma(2)} G_{2,1}^{1,2} \left(P_r \Omega_{ck} \mid \begin{matrix} 0, 0 \\ 0, - \end{matrix} \right) \\
 &- \left(\frac{P_s \Omega_{gk}}{P_s \Omega_{hk}} \right) \delta^{-1} \sum_{e^3=1}^M \frac{M_{e^3}^*}{\Gamma(e^3)} G_{2,1}^{1,2} \left(\frac{P_j \Omega_{fj} \gamma_{th}^{FD}}{P_s \Omega_{gk}} \mid \begin{matrix} 1 - e^3, 0 \\ 0, - \end{matrix} \right) - \left(\frac{P_s \Omega_{gk}}{P_s \Omega_{hk}} \right) \delta^{-1} N^* G_{2,1}^{1,2} \left(\frac{P_r \Omega_{ck} \gamma_{th}^{FD}}{P_s \Omega_{gk}} \mid \begin{matrix} 0, 0 \\ 0, - \end{matrix} \right) \\
 &- \left(\frac{P_s \Omega_{gk}}{P_s \Omega_{hk}} \right) \delta^{-1} O^* G_{2,1}^{1,2} \left(\frac{\left(\varphi^{-1} P_s \Omega_{ak} P_s \Omega_{gk} \gamma_{th}^{FD} + \varphi^{-1} P_s \Omega_{ak} P_s \Omega_{hk} \gamma_{th}^{FD} \right)}{P_s \Omega_{hk} P_s \Omega_{gk}} \mid \begin{matrix} 0, 0 \\ 0, - \end{matrix} \right) - \left(\frac{P_s \Omega_{gk}}{P_s \Omega_{hk}} \right) \delta^{-1} \frac{P^*}{\Gamma(2)} G_{2,1}^{1,2} \left(\frac{P_s \Omega_{gk}}{\delta} \mid \begin{matrix} -1, 0 \\ 0, - \end{matrix} \right) \\
 &\left. - \left(\frac{P_s \Omega_{gk}}{P_s \Omega_{hk}} \right) \delta^{-1} \sum_{f^3=1}^M \frac{R_{f^3}^*}{\Gamma(f^3)} G_{2,1}^{1,2} \left(\frac{P_j \Omega_{fj}}{\delta} \mid \begin{matrix} 1 - f^3, 0 \\ 0, - \end{matrix} \right) - \left(\frac{P_s \Omega_{gk}}{P_s \Omega_{hk}} \right) \delta^{-1} S^* G_{2,1}^{1,2} \left(\frac{P_r \Omega_{ck}}{\delta} \mid \begin{matrix} 0, 0 \\ 0, - \end{matrix} \right) \right] \quad (20)
 \end{aligned}$$

where $\delta = \left(\frac{2\varphi^{-1} \gamma_{th}^{FD}}{P_s \Omega_{hk}} + \frac{2\varphi^{-1} + 3}{P_s \Omega_{gk}} + \frac{\gamma_{th}^{FD}}{P_s \Omega_{hk}} \right)$

Proof: See Appendix B. ■

PROOF OF PROPOSITION 1

Considering (15) and utilizing the definition of the logarithm properties and Appendix II of [16] and also Appendix A of [11], R_X^{HD} can be re-written as

$$\begin{aligned}
 R_X^{HD} &= \frac{1}{2} \left[\sum_{k=1}^N (\log_2(1 + \gamma_{x_k}^{HD}) - \log_2(1 + \gamma_{x_k, R}^{HD})) \right]^+ \leq R \\
 &\approx \frac{\gamma_{x_k}^{HD}}{\gamma_{x_k, R}^{HD}} \leq \frac{2R}{\gamma_{th}^{HD}} \quad (21)
 \end{aligned}$$

Following the same procedures as in (21), R_Y^{HD} can be written as $\frac{\gamma_{y_k}^{HD}}{\gamma_{y_k, R}^{HD}} \leq \frac{2R}{\gamma_{th}^{HD}}$. With the help of these expressions, (17) can be written as

$$\begin{aligned}
 F_{R_{e2e}^{HD}}(\gamma_{th}^{HD}) &= P_r(\min(R_X^{HD}, R_Y^{HD}) \leq R) \\
 &= P_r \left(\min \left(\frac{\gamma_{x_k}^{HD}}{\gamma_{x_k, R}^{HD}}, \frac{\gamma_{y_k}^{HD}}{\gamma_{y_k, R}^{HD}} \right) \leq \gamma_{th}^{HD} \right)
 \end{aligned}$$

$$\begin{aligned}
 &= 1 - \Pr \left(\frac{\gamma_{x_k}^{HD}}{\gamma_{x_k, R}^{HD}} \geq \gamma_{th}^{HD}, \frac{\gamma_{y_k}^{HD}}{\gamma_{y_k, R}^{HD}} \geq \gamma_{th}^{HD} \right) \\
 &= 1 - \Pr \left(\gamma_{x_k}^{HD} \geq \gamma_{th}^{HD} \gamma_{x_k, R}^{HD}, \gamma_{y_k}^{HD} \geq \gamma_{th}^{HD} \gamma_{y_k, R}^{HD} \right) \\
 &= 1 - \left(\underbrace{\int_0^\infty F_{\gamma_{x_k}^{HD}}(\gamma_{th}^{HD} \gamma_{x_k, R}^{HD}) f_{\gamma_{x_k, R}^{HD}}(\gamma_{x_k, R}^{HD}) d\gamma_{x_k, R}^{HD}}_{\Delta} \right) \\
 &\quad \times \left(\underbrace{\int_0^\infty F_{\gamma_{y_k}^{HD}}(\gamma_{th}^{HD} \gamma_{y_k, R}^{HD}) f_{\gamma_{y_k, R}^{HD}}(\gamma_{y_k, R}^{HD}) d\gamma_{y_k, R}^{HD}}_{\Upsilon} \right) \quad (22)
 \end{aligned}$$

In order to continue the analysis, (22) requires $F_{\gamma_{x_k}^{HD}}$ and $F_{\gamma_{y_k}^{HD}}$ expressions. Before starting these derivations, because of the intractable form of (6) and (7), this paper upper-bound these expressions by using the $\frac{XY}{X+Y} \leq \min(X, Y)$ as in (23) and

(24), respectively.

$$\begin{aligned} \gamma_{x_k}^{HD} &= \frac{\frac{\varphi\gamma_{s1}\gamma_{s2}}{(\varphi\gamma_A+\varphi+1)}}{\gamma_{s1} + \frac{\gamma_{s2}}{(\varphi\gamma_A+\varphi+1)}} = \varphi \frac{AB}{A+B} \\ &\leq \gamma_{x_k}^{HD(\text{up})} = \varphi \min(A, B) \end{aligned} \quad (23)$$

$$\begin{aligned} \gamma_{y_k}^{HD} &= \frac{\frac{\varphi\gamma_{s1}\gamma_{s2}}{(\varphi\gamma_A+\varphi+1)}}{\frac{\gamma_{s1}}{(\varphi\gamma_A+\varphi+1)} + \gamma_{s2}} = \varphi \frac{CD}{C+D} \\ &\leq \gamma_{y_k}^{HD(\text{up})} = \varphi \min(C, D) \end{aligned} \quad (24)$$

where $A = \gamma_{s1}$, $B = \frac{\gamma_{s2}}{(\varphi\gamma_A+\varphi+1)}$, $C = \frac{\gamma_{s1}}{(\varphi\gamma_A+\varphi+1)}$, $D = \gamma_{s2}$, and $\gamma_A = \gamma_J + 1$. The CDF expression of (23) can be calculated as in (25).

$$\begin{aligned} F_{\gamma_{x_k}^{HD}} &= Pr(\varphi \min(A, B) \leq \gamma_{th}^{HD}) \\ &= Pr\left(\varphi \min\left(\gamma_{s1}, \frac{\gamma_{s2}}{(\varphi\gamma_A + \varphi + 1)}\right) \leq \gamma_{th}^{HD}\right) \\ &= 1 - Pr\left(\gamma_{s1} \geq \gamma_{th}^{HD} \varphi^{-1}, \right. \\ &\quad \left. \times \gamma_{s2} \geq \gamma_{th}^{HD} \varphi^{-1} (\varphi\gamma_A + \varphi + 1)\right) \\ &= 1 - (1 - F_{\gamma_{s1}}(\gamma_{th}^{HD} \varphi^{-1})) \\ &\quad \times (1 - F_{\gamma_{s2}}(\gamma_{th}^{HD} \varphi^{-1} (\varphi\gamma_A + \varphi + 1))) \end{aligned} \quad (25)$$

Since the amplitude of all channels are distributed according to the Rayleigh distribution, the PDF expressions of γ_{s1} and γ_{s2} can be written as: $f_{\gamma_{s1}}(\gamma_{th}) = \frac{1}{P_s \Omega_h} e^{-\frac{\gamma_{th}}{P_s \Omega_h}}$ and $f_{\gamma_{s2}}(\gamma_{th}) = \frac{1}{P_s \Omega_g} e^{-\frac{\gamma_{th}}{P_s \Omega_g}}$, respectively [18]. where $\Omega_h = \mathbb{E}[|h|^2]$ and $\Omega_g = \mathbb{E}[|g|^2]$. In light of all these information, $F_{\gamma_{s1}}(\gamma_{th} \varphi^{-1})$ and $F_{\gamma_{s2}}(\gamma_{th} \varphi^{-1} (\varphi\gamma_A + \varphi + 1))$ can be computed as:

$$\begin{aligned} F_{\gamma_{x_k}^{HD}} &= 1 - \mathbb{E}_{\gamma_J} \left[e^{-\gamma_{th}^{HD} \left(\frac{\varphi^{-1}}{P_s \Omega_{h_k}} + \frac{\varphi^{-1}(\varphi\gamma_J + 2\varphi + 1)}{P_s \Omega_{g_k}} \right)} \right] \Big| \gamma_J \\ &= 1 - \left[e^{-\gamma_{th}^{HD} \left(\frac{\varphi^{-1}}{P_s \Omega_{h_k}} + \frac{\varphi^{-1}(2\varphi + 1)}{P_s \Omega_{g_k}} \right)} \right. \\ &\quad \left. \times \int_0^\infty e^{-\gamma_J \left(\frac{\gamma_{th}^{HD}}{P_s \Omega_{g_k}} \right)} f_{\gamma_J}(\gamma_J) d\gamma_J \right] \end{aligned} \quad (26)$$

Sum of M i.i.d. Rayleigh distribution become a Gamma distribution [18]. Within this scope, the PDF expression of γ_J can be expressed as: $f_{\gamma_J}(\gamma) = \frac{\gamma^{M-1}}{(P_J \Omega_f)^M (M-1)!} e^{-\frac{\gamma}{P_J \Omega_f}}$ [18], where $\Omega_f = \mathbb{E}[|f|^2]$. Substituting $f_{\gamma_J}(\gamma)$ into (26) and utilizing [19, Eq. (3.351³)] for the integral expression, the final expression can be computed as

$$\begin{aligned} F_{\gamma_{x_k}^{HD}}(\gamma_{th}^{HD}) &= 1 - \left(\frac{P_j \Omega_{f_j} \gamma_{th}^{HD}}{P_s \Omega_{g_k}} + 1 \right)^{-M} \\ &\quad \times e^{-\gamma_{th}^{HD} \left(\frac{\varphi^{-1}}{P_s \Omega_{h_k}} + \frac{\varphi^{-1}(2\varphi + 1)}{P_s \Omega_{g_k}} \right)} \end{aligned} \quad (27)$$

Following the same procedures, $F_{\gamma_{y_k}^{HD}}(\gamma_{th}^{HD})$ can be computed as

$$\begin{aligned} F_{\gamma_{y_k}^{HD}}(\gamma_{th}^{HD}) &= 1 - \left(\frac{P_j \Omega_{f_j} \gamma_{th}^{HD}}{P_s \Omega_{h_k}} + 1 \right)^{-M} \\ &\quad \times e^{-\gamma_{th}^{HD} \left(\frac{\varphi^{-1}(2\varphi + 1)}{P_s \Omega_{h_k}} + \frac{\varphi^{-1}}{P_s \Omega_{g_k}} \right)} \end{aligned} \quad (28)$$

To continue the analysis, (22) also requires the $f_{\gamma_{x_k,R}}(\gamma)$ and $f_{\gamma_{y_k,R}}(\gamma)$ derivations. Starting with (2), following expressions can be obtained.

$$\begin{aligned} F_{\gamma_{x_k,R}}(\gamma_{th}^{HD}) &= Pr\left(\frac{\gamma_x}{\gamma_y + \gamma_J + 1} \leq \gamma_{th}^{HD}\right) \\ &= \int_0^\infty \int_0^\infty \int_0^{(\gamma_y + \gamma_J + 1)} f_{\gamma_x}(\gamma_x) f_{\gamma_y}(\gamma_y) f_{\gamma_J}(\gamma_J) d\gamma_x d\gamma_y d\gamma_J \\ &= 1 - \int_0^\infty \int_0^\infty e^{-\gamma_{th}^{HD} \left(\frac{\gamma_y + \gamma_J + 1}{P_s \Omega_{h_k}} \right)} f_{\gamma_y}(\gamma_y) f_{\gamma_J}(\gamma_J) d\gamma_y d\gamma_J \\ &= 1 - e^{-\left(\frac{\gamma_{th}^{HD}}{P_s \Omega_{h_k}} \right)} \int_0^\infty e^{-\gamma_y \left(\frac{\gamma_{th}^{HD}}{P_s \Omega_{h_k}} \right)} f_{\gamma_y}(\gamma_y) d\gamma_y \\ &\quad \times \int_0^\infty e^{-\gamma_J \left(\frac{\gamma_{th}^{HD}}{P_s \Omega_{h_k}} \right)} f_{\gamma_J}(\gamma_J) d\gamma_J \end{aligned} \quad (29)$$

Substituting $f_{\gamma_y}(\gamma)$ and $f_{\gamma_J}(\gamma)$ into (29) and also solving the integral expressions by using [19, Eq. (3.310¹¹, 3.351³)], the final CDF expression can be achieved as in (30)

$$\begin{aligned} F_{\gamma_{x_k,R}}(\gamma_{th}^{HD}) &= 1 - \left(\frac{P_s \Omega_{g_k} \gamma_{th}^{HD}}{P_s \Omega_{h_k}} + 1 \right)^{-1} \\ &\quad \times \left(\frac{P_j \Omega_{f_j} \gamma_{th}^{HD}}{P_s \Omega_{h_k}} + 1 \right)^{-M} e^{-\left(\frac{\gamma_{th}^{HD}}{P_s \Omega_{h_k}} \right)} \end{aligned} \quad (30)$$

The derivative of (30) yields the $f_{\gamma_{x_k,R}}(\gamma)$ as

$$\begin{aligned} f_{\gamma_{x_k,R}}(\gamma_{th}^{HD}) &= e^{-\left(\frac{\gamma_{th}^{HD}}{P_s \Omega_{h_k}} \right)} \left[\left(\frac{P_s \Omega_{g_k} \gamma_{th}^{HD}}{P_s \Omega_{h_k}} + 1 \right)^{-2} \left(\frac{P_s \Omega_{g_k}}{P_s \Omega_{h_k}} \right) \left(\frac{P_j \Omega_{f_j} \gamma_{th}^{HD}}{P_s \Omega_{h_k}} + 1 \right)^{-M} \right. \\ &\quad \left. + \left(\frac{P_s \Omega_{g_k} \gamma_{th}^{HD}}{P_s \Omega_{h_k}} + 1 \right)^{-1} M \left(\frac{P_j \Omega_{f_j} \gamma_{th}^{HD}}{P_s \Omega_{h_k}} + 1 \right)^{-M-1} \left(\frac{P_j \Omega_{f_j}}{P_s \Omega_{h_k}} \right) \right. \\ &\quad \left. + \left(\frac{1}{P_s \Omega_{h_k}} \right) \left(\frac{P_s \Omega_{g_k} \gamma_{th}^{HD}}{P_s \Omega_{h_k}} + 1 \right)^{-1} \left(\frac{P_j \Omega_{f_j} \gamma_{th}^{HD}}{P_s \Omega_{h_k}} + 1 \right)^{-M} \right] \end{aligned} \quad (31)$$

Likewise, $f_{\gamma_{y_k,R}}(\gamma)$ computed as

$$\begin{aligned} f_{\gamma_{y_k,R}}(\gamma_{th}^{HD}) &= e^{-\left(\frac{\gamma_{th}^{HD}}{P_s \Omega_{g_k}} \right)} \left[\left(\frac{P_s \Omega_{h_k} \gamma_{th}^{HD}}{P_s \Omega_{g_k}} + 1 \right)^{-2} \left(\frac{P_s \Omega_{h_k}}{P_s \Omega_{g_k}} \right) \left(\frac{P_j \Omega_{f_j} \gamma_{th}^{HD}}{P_s \Omega_{g_k}} + 1 \right)^{-M} \right. \\ &\quad \left. + \left(\frac{P_s \Omega_{h_k} \gamma_{th}^{HD}}{P_s \Omega_{g_k}} + 1 \right)^{-1} M \left(\frac{P_j \Omega_{f_j} \gamma_{th}^{HD}}{P_s \Omega_{g_k}} + 1 \right)^{-M-1} \left(\frac{P_j \Omega_{f_j}}{P_s \Omega_{g_k}} \right) \right. \\ &\quad \left. + \left(\frac{1}{P_s \Omega_{g_k}} \right) \left(\frac{P_s \Omega_{h_k} \gamma_{th}^{HD}}{P_s \Omega_{g_k}} + 1 \right)^{-1} \left(\frac{P_j \Omega_{f_j} \gamma_{th}^{HD}}{P_s \Omega_{g_k}} + 1 \right)^{-M} \right] \end{aligned} \quad (32)$$

Substituting (27) and (31) into (22), the Δ term in (22) can be re-written as in (33).

$$\Delta = \int_0^\infty \left(1 - \left(\frac{P_j \Omega_{f_j} \gamma_{th}^{HD}}{P_s \Omega_{g_k}} y + 1 \right)^{-M} e^{-y \left(\frac{\gamma_{th}^{HD} \varphi^{-1}}{P_s \Omega_{h_k}} + \frac{\gamma_{th}^{HD} \varphi^{-1}(2\varphi + 1)}{P_s \Omega_{g_k}} \right)} \right)$$

$$\begin{aligned} \Delta = & \left(\frac{P_s \Omega_{gk}}{P_s \Omega_{hk}}\right) \int_0^\infty e^{-\left(\frac{y}{P_s \Omega_{hk}}\right)} \left(\frac{P_s \Omega_{gk}}{P_s \Omega_{hk}} y + 1\right)^{-2} \left(\frac{P_j \Omega_{fj}}{P_s \Omega_{hk}} y + 1\right)^{-M} dy \\ & + M \left(\frac{P_j \Omega_{fj}}{P_s \Omega_{hk}}\right) \int_0^\infty e^{-\left(\frac{y}{P_s \Omega_{hk}}\right)} \left(\frac{P_s \Omega_{gk}}{P_s \Omega_{hk}} y + 1\right)^{-1} \left(\frac{P_j \Omega_{fj}}{P_s \Omega_{hk}} y + 1\right)^{-M-1} dy \\ & + \left(\frac{1}{P_s \Omega_{hk}}\right) \int_0^\infty e^{-\left(\frac{y}{P_s \Omega_{hk}}\right)} \left(\frac{P_s \Omega_{gk}}{P_s \Omega_{hk}} y + 1\right)^{-1} \left(\frac{P_j \Omega_{fj}}{P_s \Omega_{hk}} y + 1\right)^{-M} dy \\ & - \left(\frac{P_s \Omega_{gk}}{P_s \Omega_{hk}}\right) \int_0^\infty e^{-y\left(\frac{\gamma_{th}^{HD} \varphi^{-1}}{P_s \Omega_{hk}} + \frac{\gamma_{th}^{HD} \varphi^{-1}(2\varphi+1)}{P_s \Omega_{gk}} + \frac{1}{P_s \Omega_{hk}}\right)} \left(\frac{P_j \Omega_{fj} \gamma_{th}^{HD}}{P_s \Omega_{gk}} y + 1\right)^{-M} \left(\frac{P_s \Omega_{gk}}{P_s \Omega_{hk}} y + 1\right)^{-2} \left(\frac{P_j \Omega_{fj}}{P_s \Omega_{hk}} y + 1\right)^{-M} dy \\ & - M \left(\frac{P_j \Omega_{fj}}{P_s \Omega_{hk}}\right) \int_0^\infty e^{-y\left(\frac{\gamma_{th}^{HD} \varphi^{-1}}{P_s \Omega_{hk}} + \frac{\gamma_{th}^{HD} \varphi^{-1}(2\varphi+1)}{P_s \Omega_{gk}} + \frac{1}{P_s \Omega_{hk}}\right)} \left(\frac{P_j \Omega_{fj} \gamma_{th}^{HD}}{P_s \Omega_{gk}} y + 1\right)^{-M} \left(\frac{P_s \Omega_{gk}}{P_s \Omega_{hk}} y + 1\right)^{-1} \left(\frac{P_j \Omega_{fj}}{P_s \Omega_{hk}} y + 1\right)^{-M-1} dy \\ & - \left(\frac{1}{P_s \Omega_{hk}}\right) \int_0^\infty e^{-y\left(\frac{\gamma_{th}^{HD} \varphi^{-1}}{P_s \Omega_{hk}} + \frac{\gamma_{th}^{HD} \varphi^{-1}(2\varphi+1)}{P_s \Omega_{gk}} + \frac{1}{P_s \Omega_{hk}}\right)} \left(\frac{P_j \Omega_{fj} \gamma_{th}^{HD}}{P_s \Omega_{gk}} y + 1\right)^{-M} \left(\frac{P_s \Omega_{gk}}{P_s \Omega_{hk}} y + 1\right)^{-1} \left(\frac{P_j \Omega_{fj}}{P_s \Omega_{hk}} y + 1\right)^{-M} dy \end{aligned} \tag{34}$$

$$\begin{aligned} & \times \left(e^{-\left(\frac{y}{P_s \Omega_{hk}}\right)} \left[\left(\frac{P_s \Omega_{gk}}{P_s \Omega_{hk}} y + 1\right)^{-2} \left(\frac{P_s \Omega_{gk}}{P_s \Omega_{hk}}\right) \left(\frac{P_j \Omega_{fj}}{P_s \Omega_{hk}} y + 1\right)^{-M} \right. \right. \\ & + \left. \left(\frac{P_s \Omega_{gk}}{P_s \Omega_{hk}} y + 1\right)^{-1} M \left(\frac{P_j \Omega_{fj}}{P_s \Omega_{hk}} y + 1\right)^{-M-1} \left(\frac{P_j \Omega_{fj}}{P_s \Omega_{hk}}\right) \right. \\ & \left. \left. + \left(\frac{1}{P_s \Omega_{hk}}\right) \left(\frac{P_s \Omega_{gk}}{P_s \Omega_{hk}} y + 1\right)^{-1} \left(\frac{P_j \Omega_{fj}}{P_s \Omega_{hk}} y + 1\right)^{-M} \right] dy \right) \end{aligned} \tag{33}$$

By using the distributive property, (33) can be written as in (34). The first, second, and third integrals in (34) can be solved by using [20, Eq. (10, 11)] and [13, Eq. (13)] as in (35).

$$\begin{aligned} & \frac{P_s \Omega_{gk}}{\Gamma(2)\Gamma(M)} G_{1,0:1,1:1,1}^{1,0:1,1:1,1} \left(\begin{matrix} 1 & -1 & 1-M \\ - & 0 & 0 \end{matrix} \middle| P_s \Omega_{gk}, P_j \Omega_{fj} \right) \\ & + M \frac{P_j \Omega_{fj}}{\Gamma(M+1)} G_{1,0:1,1:1,1}^{1,0:1,1:1,1} \left(\begin{matrix} 1 & 0 & -M \\ - & 0 & 0 \end{matrix} \middle| P_s \Omega_{gk}, P_j \Omega_{fj} \right) \\ & + \frac{1}{\Gamma(M)} G_{1,0:1,1:1,1}^{1,0:1,1:1,1} \left(\begin{matrix} 1 & 0 & 1-M \\ - & 0 & 0 \end{matrix} \middle| P_s \Omega_{gk}, P_j \Omega_{fj} \right) \end{aligned} \tag{35}$$

The α term in [13, Eq. (13)] is set to 1. Utilizing the partial fraction decomposition technique, fourth integral term in (34) can be written as in (36).

$$\begin{aligned} & \int_0^\infty e^{-y\left(\frac{\gamma_{th}^{HD} \varphi^{-1}}{P_s \Omega_{hk}} + \frac{\gamma_{th}^{HD} \varphi^{-1}(2\varphi+1)}{P_s \Omega_{gk}} + \frac{1}{P_s \Omega_{hk}}\right)} \\ & \times \left[\sum_{i=1}^M \frac{A_i}{\left(\frac{P_j \Omega_{fj} \gamma_{th}^{HD}}{P_s \Omega_{gk}} y + 1\right)^i} + \frac{V}{\left(\frac{P_s \Omega_{gk}}{P_s \Omega_{hk}} y + 1\right)^2} \right. \\ & \left. + \sum_{l=1}^M \frac{C_l}{\left(\frac{P_j \Omega_{fj}}{P_s \Omega_{hk}} y + 1\right)^l} \right] dy \end{aligned} \tag{36}$$

$$\begin{aligned} A_i = & \lim_{y \rightarrow -\frac{P_s \Omega_{gk}}{\gamma_{th}^{HD} P_j \Omega_{fj}}} \frac{\partial^{M-i}}{(M-i)! \partial y^{M-i}} \left(\frac{P_j \Omega_{fj} \gamma_{th}^{HD}}{P_s \Omega_{gk}} y + 1 \right)^M [\Phi], \\ V = & \lim_{y \rightarrow -\frac{P_s \Omega_{gk}}{P_s \Omega_{hk}}} \frac{\partial}{\partial y} \left(\frac{P_s \Omega_{gk}}{P_s \Omega_{hk}} y + 1 \right)^2 [\Phi], \quad C_l = \\ & \lim_{y \rightarrow -\frac{P_s \Omega_{hk}}{P_j \Omega_{fj}}} \frac{\partial^{M-l}}{(M-l)! \partial y^{M-l}} \left(\frac{P_j \Omega_{fj}}{P_s \Omega_{hk}} y + 1 \right)^M [\Phi], \quad \text{and} \end{aligned}$$

$\Phi = \frac{1}{\left(\frac{P_j \Omega_{fj} \gamma_{th}^{HD}}{P_s \Omega_{gk}} y + 1\right)^M \left(\frac{P_s \Omega_{gk}}{P_s \Omega_{hk}} y + 1\right)^2 \left(\frac{P_j \Omega_{fj}}{P_s \Omega_{hk}} y + 1\right)^M}$. By using the distributed properties and [20, Eq. (10, 11)] and also [20, Eq. (21)] for solving the integral expression, (36) can be obtained as in (37).

$$\begin{aligned} & \left(\frac{\gamma_{th}^{HD} \varphi^{-1}}{P_s \Omega_{hk}} + \frac{\gamma_{th}^{HD} \varphi^{-1}(2\varphi+1)}{P_s \Omega_{gk}} + \frac{1}{P_s \Omega_{hk}} \right)^{-1} \sum_{i=1}^M \frac{A_i}{\Gamma(i)} \\ & \times G_{2,1}^{1,2} \left(\frac{\left(\frac{P_j \Omega_{fj} \gamma_{th}^{HD}}{P_s \Omega_{gk}}\right)}{\left(\frac{\gamma_{th}^{HD} \varphi^{-1}}{P_s \Omega_{hk}} + \frac{\gamma_{th}^{HD} \varphi^{-1}(2\varphi+1)}{P_s \Omega_{gk}} + \frac{1}{P_s \Omega_{hk}}\right)} \middle| \begin{matrix} 1-i & 0 \\ 0 & - \end{matrix} \right) \\ & + \left(\frac{\gamma_{th}^{HD} \varphi^{-1}}{P_s \Omega_{hk}} + \frac{\gamma_{th}^{HD} \varphi^{-1}(2\varphi+1)}{P_s \Omega_{gk}} + \frac{1}{P_s \Omega_{hk}} \right)^{-1} \frac{B}{\Gamma(2)} \\ & \times G_{2,1}^{1,2} \left(\frac{\left(\frac{P_s \Omega_{gk}}{P_s \Omega_{hk}}\right)}{\left(\frac{\gamma_{th}^{HD} \varphi^{-1}}{P_s \Omega_{hk}} + \frac{\gamma_{th}^{HD} \varphi^{-1}(2\varphi+1)}{P_s \Omega_{gk}} + \frac{1}{P_s \Omega_{hk}}\right)} \middle| \begin{matrix} -1 & 0 \\ 0 & - \end{matrix} \right) \\ & + \left(\frac{\gamma_{th}^{HD} \varphi^{-1}}{P_s \Omega_{hk}} + \frac{\gamma_{th}^{HD} \varphi^{-1}(2\varphi+1)}{P_s \Omega_{gk}} + \frac{1}{P_s \Omega_{hk}} \right)^{-1} \sum_{l=1}^M \frac{C_l}{\Gamma(l)} \\ & \times G_{2,1}^{1,2} \left(\frac{\left(\frac{P_j \Omega_{fj}}{P_s \Omega_{hk}}\right)}{\left(\frac{\gamma_{th}^{HD} \varphi^{-1}}{P_s \Omega_{hk}} + \frac{\gamma_{th}^{HD} \varphi^{-1}(2\varphi+1)}{P_s \Omega_{gk}} + \frac{1}{P_s \Omega_{hk}}\right)} \middle| \begin{matrix} 1-l & 0 \\ 0 & - \end{matrix} \right) \end{aligned} \tag{37}$$

Likewise, considering the same methodologies as in (37), the fifth and sixth integrals in (34) can be solved as in the fourth and seventh lines of (19). Please note that; $D_{aa} =$

$$\lim_{y \rightarrow -\frac{P_s \Omega_{gk}}{\gamma_{th}^{HD} P_J \Omega_{fj}}} \frac{\partial^{M-aa}}{(M-aa)! \partial y^{M-aa}} \left(\frac{P_J \Omega_{fj} \gamma_{th}^{HD}}{P_s \Omega_{gk}} y + 1 \right)^M [A^+],$$

$$E = \lim_{y \rightarrow -\frac{P_s \Omega_{hk}}{P_s \Omega_{gk}}} \frac{\partial}{\partial y} \left(\frac{P_s \Omega_{gk}}{P_s \Omega_{hk}} y + 1 \right) [A^+], \quad F_{bb} =$$

$$\lim_{y \rightarrow -\frac{P_s \Omega_{hk}}{P_J \Omega_{fj}}} \frac{\partial^{M+1-bb}}{(M+1-bb)! \partial y^{M+1-bb}} \left(\frac{P_J \Omega_{fj}}{P_s \Omega_{hk}} y + 1 \right)^{M+1} [A^+],$$

$$\text{and } A^+ = \frac{1}{\left(\frac{P_J \Omega_{fj} \gamma_{th}^{HD}}{P_s \Omega_{gk}} y + 1 \right)^M \left(\frac{P_s \Omega_{gk}}{P_s \Omega_{hk}} y + 1 \right) \left(\frac{P_J \Omega_{fj}}{P_s \Omega_{hk}} y + 1 \right)^{M+1}}.$$

$$G_{cc} = \lim_{y \rightarrow -\frac{P_s \Omega_{gk}}{\gamma_{th}^{HD} P_J \Omega_{fj}}} \frac{\partial^{M-cc}}{(M-cc)! \partial y^{M-cc}}$$

$$\times \left(\frac{P_J \Omega_{fj} \gamma_{th}^{HD}}{P_s \Omega_{gk}} y + 1 \right)^M [B^+], \quad H =$$

$$\lim_{y \rightarrow -\frac{P_s \Omega_{hk}}{P_s \Omega_{gk}}} \frac{\partial}{\partial y} \left(\frac{P_s \Omega_{gk}}{P_s \Omega_{hk}} y + 1 \right) [B^+], \quad I_{dd} =$$

$$\lim_{y \rightarrow -\frac{P_s \Omega_{hk}}{P_J \Omega_{fj}}} \frac{\partial^{M-dd}}{(M-dd)! \partial y^{M-dd}} \left(\frac{P_J \Omega_{fj}}{P_s \Omega_{hk}} y + 1 \right)^M [B^+], \quad \text{and}$$

$$B^+ = \frac{1}{\left(\frac{P_J \Omega_{fj} \gamma_{th}^{HD}}{P_s \Omega_{gk}} y + 1 \right)^M \left(\frac{P_s \Omega_{gk}}{P_s \Omega_{hk}} y + 1 \right) \left(\frac{P_J \Omega_{fj}}{P_s \Omega_{hk}} y + 1 \right)^M}.$$

Likewise, following the same procedures, Υ term in (22), can be obtained as in the second part of (19). Please note that, $J_{ee} =$

$$\lim_{y \rightarrow -\frac{P_s \Omega_{hk}}{\gamma_{th}^{HD} P_J \Omega_{fj}}} \frac{\partial^{M-ee}}{(M-ee)! \partial y^{M-ee}} \left(\frac{P_J \Omega_{fj} \gamma_{th}^{HD}}{P_s \Omega_{hk}} y + 1 \right)^M [C^+],$$

$$K = \lim_{y \rightarrow -\frac{P_s \Omega_{gk}}{P_s \Omega_{hk}}} \frac{\partial}{\partial y} \left(\frac{P_s \Omega_{hk}}{P_s \Omega_{gk}} y + 1 \right)^2 [C^+], \quad L_{ff} =$$

$$\lim_{y \rightarrow -\frac{P_s \Omega_{gk}}{P_J \Omega_{fj}}} \frac{\partial^{M-ff}}{(M-ff)! \partial y^{M-ff}} \left(\frac{P_J \Omega_{fj}}{P_s \Omega_{gk}} y + 1 \right)^M [C^+], \quad \text{and}$$

$$C^+ = \frac{1}{\left(\frac{P_J \Omega_{fj} \gamma_{th}^{HD}}{P_s \Omega_{hk}} y + 1 \right)^M \left(\frac{P_s \Omega_{hk}}{P_s \Omega_{gk}} y + 1 \right)^2 \left(\frac{P_J \Omega_{fj}}{P_s \Omega_{gk}} y + 1 \right)^M}.$$

$$M_{gg} = \lim_{y \rightarrow -\frac{P_s \Omega_{hk}}{\gamma_{th}^{HD} P_J \Omega_{fj}}} \frac{\partial^{M-gg}}{(M-gg)! \partial y^{M-gg}} \left(\frac{P_J \Omega_{fj} \gamma_{th}^{HD}}{P_s \Omega_{hk}} y + 1 \right)^M [D^+],$$

$$N^{***} = \lim_{y \rightarrow -\frac{P_s \Omega_{gk}}{P_s \Omega_{hk}}} \frac{\partial}{\partial y} \left(\frac{P_s \Omega_{hk}}{P_s \Omega_{gk}} y + 1 \right)^2 [D^+], \quad O_{hh} =$$

$$\lim_{y \rightarrow -\frac{P_s \Omega_{gk}}{P_J \Omega_{fj}}} \frac{\partial^{M+1-hh}}{(M+1-hh)! \partial y^{M+1-hh}} \left(\frac{P_J \Omega_{fj}}{P_s \Omega_{gk}} y + 1 \right)^{M+1} [D^+],$$

$$\text{and } D^+ = \frac{1}{\left(\frac{P_J \Omega_{fj} \gamma_{th}^{HD}}{P_s \Omega_{hk}} y + 1 \right)^M \left(\frac{P_s \Omega_{hk}}{P_s \Omega_{gk}} y + 1 \right)^2 \left(\frac{P_J \Omega_{fj}}{P_s \Omega_{gk}} y + 1 \right)^{M+1}}.$$

$$P_{ii} = \lim_{y \rightarrow -\frac{P_s \Omega_{hk}}{\gamma_{th}^{HD} P_J \Omega_{fj}}} \frac{\partial^{M-ii}}{(M-ii)! \partial y^{M-ii}}$$

$$\times \left(\frac{P_J \Omega_{fj} \gamma_{th}^{HD}}{P_s \Omega_{hk}} y + 1 \right)^M [E^+], \quad R =$$

$$\lim_{y \rightarrow -\frac{P_s \Omega_{gk}}{P_s \Omega_{hk}}} \frac{\partial}{\partial y} \left(\frac{P_s \Omega_{hk}}{P_s \Omega_{gk}} y + 1 \right) [E^+], \quad S_{jj} =$$

$$\lim_{y \rightarrow -\frac{P_s \Omega_{gk}}{P_J \Omega_{fj}}} \frac{\partial^{M-jj}}{(M-jj)! \partial y^{M-jj}} \left(\frac{P_J \Omega_{fj}}{P_s \Omega_{gk}} y + 1 \right)^M [E^+],$$

$$\text{and } E^+ = \frac{1}{\left(\frac{P_J \Omega_{fj} \gamma_{th}^{HD}}{P_s \Omega_{hk}} y + 1 \right)^M \left(\frac{P_s \Omega_{hk}}{P_s \Omega_{gk}} y + 1 \right) \left(\frac{P_J \Omega_{fj}}{P_s \Omega_{gk}} y + 1 \right)^M}.$$

PROOF OF PROPOSITION 2

Utilizing (16) and considering the same procedures as in (21), the $R_X^{FD} \approx \frac{\gamma_{xk}^{FD}}{\gamma_{xk,R}^{FD}} \leq \underbrace{2 \frac{R}{N}}_{\gamma_{th}^{FD}}$ can be obtained. Likewise,

$R_Y^{FD} \approx \frac{\gamma_{yk}^{FD}}{\gamma_{yk,R}^{FD}} \leq \underbrace{2 \frac{R}{N}}_{\gamma_{th}^{FD}}$ can be obtained. Utilizing these two

expressions in (18) and following the same procedures as in (22), following expressions can be obtained.

$$F_{R_{e2e}^{FD}}(\gamma_{th}^{FD}) = P_r(\min(R_X^{FD}, R_Y^{FD}) \leq R)$$

$$= 1 - \left(\underbrace{\int_0^\infty F_{\gamma_{xk}^{FD}}(\gamma_{th}^{FD} \gamma_{xk,R}^{FD}) f_{\gamma_{xk,R}^{FD}}(\gamma_{xk,R}^{FD}) d\gamma_{xk,R}^{FD}}_{\Psi} \right)$$

$$\times \left(\underbrace{\int_0^\infty F_{\gamma_{yk}^{FD}}(\gamma_{th}^{FD} \gamma_{yk,R}^{FD}) f_{\gamma_{yk,R}^{FD}}(\gamma_{yk,R}^{FD}) d\gamma_{yk,R}^{FD}}_{\zeta} \right) \quad (38)$$

Because of the intractable form of (13) and (14), these expressions can be upper-bounded by using $\frac{XY}{X+Y} \leq \min(X, Y)$ as in (39) and (40), respectively.

$$\gamma_{xk}^{FD} = \frac{\varphi \gamma_x \gamma_y}{\frac{\varphi \gamma_A + \varphi \gamma_B + \gamma_C + \varphi + 1}{\gamma_C + 1} (\gamma_C + 1)} = \varphi \frac{WZ}{W + Z}$$

$$\leq \gamma_{xk}^{FD(\text{up})} = \varphi \min(W, Z) \quad (39)$$

$$\gamma_{yk}^{FD} = \frac{\varphi \gamma_x \gamma_y}{\frac{\varphi \gamma_A + \varphi \gamma_B + \gamma_D + \varphi + 1}{\gamma_D + 1} (\gamma_D + 1)} = \varphi \frac{TU}{T + U}$$

$$\leq \gamma_{yk}^{FD(\text{up})} = \varphi \min(T, U) \quad (40)$$

where $W = \frac{\gamma_x}{\gamma_C + 1}$, $Z = \frac{\gamma_y}{(\varphi \gamma_A + \varphi \gamma_B + \gamma_C + \varphi + 1)}$, $T = \frac{\gamma_x}{\gamma_D + 1}$, $U = \frac{\gamma_y}{(\varphi \gamma_A + \varphi \gamma_B + \gamma_D + \varphi + 1)}$, $\gamma_B = \gamma_{c_k} + 1$, $\gamma_C = \gamma_{a_k} + 1$, and $\gamma_D = \gamma_{b_k} + 1$. Considering the same methodology as in (25), the CDF expression of (39) can be achieved as

$$\begin{aligned}
 F_{\gamma_{x_k}}^{\text{up}} &= \Pr(\varphi \min(W, Z) \leq \gamma_{th}^{\text{FD}}) \\
 &= \Pr\left(\varphi \min\left(\frac{\gamma_x}{\gamma_C + 1}, \frac{\gamma_y}{(\varphi\gamma_A + \varphi\gamma_B + \gamma_C + \varphi + 1)}\right) \leq \gamma_{th}^{\text{FD}}\right) \\
 &= 1 - \Pr\left(\gamma_x \geq \gamma_{th}^{\text{FD}} (\gamma_C + 1) \varphi^{-1}, \gamma_y \geq \gamma_{th}^{\text{FD}} \varphi^{-1} (\varphi\gamma_A + \varphi\gamma_B + \gamma_C + \varphi + 1)\right) \\
 &= 1 - (1 - F_{\gamma_x}(\gamma_{th}^{\text{FD}} (\gamma_C + 1) \varphi^{-1})) \\
 &\quad \times (1 - F_{\gamma_y}(\gamma_{th}^{\text{FD}} \varphi^{-1} (\varphi\gamma_A + \varphi\gamma_B + \gamma_C + \varphi + 1))) \\
 &= 1 - \mathbb{E}_{\gamma_J} \left[e^{-\gamma_{th}^{\text{FD}} \left(\frac{(\gamma_{a_k} + 2) \varphi^{-1}}{P_s \Omega_{h_k}} \right)} + \frac{(\gamma_J + \gamma_C + \varphi^{-1} \gamma_{a_k} + 2\varphi^{-1} + 3)}{P_s \Omega_{g_k}} \right] \Big| \gamma_{a_k}, \gamma_J, \gamma_C \\
 &= 1 - \left[e^{-\gamma_{th}^{\text{FD}} \left(\frac{2\varphi^{-1}}{P_s \Omega_{h_k}} + \frac{2\varphi^{-1} + 3}{P_s \Omega_{g_k}} \right)} \right. \\
 &\quad \times \int_0^\infty e^{-\gamma_J \left(\frac{\gamma_{th}^{\text{FD}}}{P_s \Omega_{g_k}} \right)} f_{\gamma_J}(\gamma_J) d\gamma_J \\
 &\quad \times \int_0^\infty e^{-\gamma_C \left(\frac{\gamma_{th}^{\text{FD}}}{P_s \Omega_{g_k}} \right)} f_{\gamma_C}(\gamma_C) d\gamma_C \\
 &\quad \left. \times \int_0^\infty e^{-\gamma_{a_k} \left(\frac{\gamma_{th}^{\text{FD}} \varphi^{-1}}{P_s \Omega_{h_k}} + \frac{\gamma_{th}^{\text{FD}} \varphi^{-1}}{P_s \Omega_{g_k}} \right)} f_{\gamma_{a_k}}(\gamma_{a_k}) d\gamma_{a_k} \right] \quad (41)
 \end{aligned}$$

Substituting $f_{\gamma_J}(\gamma)$, $f_{\gamma_C}(\gamma) = \frac{1}{P_r \Omega_c} e^{-\frac{\gamma}{P_r \Omega_c}}$ and $f_{\gamma_{a_k}}(\gamma) = \frac{1}{P_s \Omega_{a_k}} e^{-\frac{\gamma}{P_s \Omega_{a_k}}}$ [18], where $\Omega_c = \mathbb{E}[|c|^2]$ and $\Omega_{a_k} = \mathbb{E}[|a_k|^2]$, into (41) and solving the integral expressions by using [19, Eq. (3.310¹¹)] and [19, Eq. (3.351³)], the final result can be computed as

$$\begin{aligned}
 F_{\gamma_{x_k}}^{\text{FD}}(\gamma_{th}^{\text{FD}}) &= 1 - \left(\frac{P_j \Omega_{f_j} \gamma_{th}^{\text{FD}}}{P_s \Omega_{g_k}} + 1 \right)^{-M} \left(\frac{P_r \Omega_c}{P_s \Omega_{g_k}} \gamma_{th}^{\text{FD}} + 1 \right)^{-1} \\
 &\quad \times \left(\frac{\varphi^{-1} P_s \Omega_{a_k} \gamma_{th}^{\text{FD}}}{P_s \Omega_{h_k}} + \frac{\varphi^{-1} P_s \Omega_{a_k} \gamma_{th}^{\text{FD}}}{P_s \Omega_{g_k}} + 1 \right)^{-1} \\
 &\quad \times e^{-\gamma_{th}^{\text{FD}} \left(\frac{2\varphi^{-1}}{P_s \Omega_{h_k}} + \frac{2\varphi^{-1} + 3}{P_s \Omega_{g_k}} \right)} \quad (42)
 \end{aligned}$$

Likewise, considering the same methodologies as in (42), the $F_{\gamma_{y_k}}^{\text{FD}}(\gamma_{th}^{\text{FD}})$ can be obtained as

$$\begin{aligned}
 F_{\gamma_{y_k}}^{\text{FD}}(\gamma_{th}^{\text{FD}}) &= 1 - \left(\frac{P_j \Omega_{f_j} \gamma_{th}^{\text{FD}}}{P_s \Omega_{h_k}} + 1 \right)^{-M} \left(\frac{P_r \Omega_c}{P_s \Omega_{h_k}} \gamma_{th}^{\text{FD}} + 1 \right)^{-1} \\
 &\quad \times \left(\frac{\varphi^{-1} P_s \Omega_{b_k} \gamma_{th}^{\text{FD}}}{P_s \Omega_{g_k}} + \frac{\varphi^{-1} P_s \Omega_{b_k} \gamma_{th}^{\text{FD}}}{P_s \Omega_{h_k}} + 1 \right)^{-1} \\
 &\quad \times e^{-\gamma_{th}^{\text{FD}} \left(\frac{2\varphi^{-1}}{P_s \Omega_{g_k}} + \frac{2\varphi^{-1} + 3}{P_s \Omega_{h_k}} \right)} \quad (43)
 \end{aligned}$$

This subsection now focuses on the CDF derivation of LR expressions. By using (9) and (10) and also considering the similar methodologies as in (29), the LR expressions with respect to x_k and y_k can be obtained as in (44) and (45), respectively.

$$\begin{aligned}
 F_{\gamma_{x_k, R}}(\gamma_{th}^{\text{FD}}) &= 1 - \left(\frac{P_s \Omega_{g_k} \gamma_{th}^{\text{FD}}}{P_s \Omega_{h_k}} + 1 \right)^{-1} \left(\frac{P_j \Omega_{f_j} \gamma_{th}^{\text{FD}}}{P_s \Omega_{h_k}} + 1 \right)^{-M} \\
 &\quad \times \left(\frac{P_r \Omega_{c_k} \gamma_{th}^{\text{FD}}}{P_s \Omega_{h_k}} + 1 \right)^{-1} e^{-\left(\frac{\gamma_{th}^{\text{FD}}}{P_s \Omega_{h_k}} \right)} \quad (44)
 \end{aligned}$$

$$\begin{aligned}
 F_{\gamma_{y_k, R}}(\gamma_{th}^{\text{FD}}) &= 1 - \left(\frac{P_s \Omega_{h_k} \gamma_{th}^{\text{FD}}}{P_s \Omega_{g_k}} + 1 \right)^{-1} \left(\frac{P_j \Omega_{f_j} \gamma_{th}^{\text{FD}}}{P_s \Omega_{g_k}} + 1 \right)^{-M} \\
 &\quad \times \left(\frac{P_r \Omega_{c_k} \gamma_{th}^{\text{FD}}}{P_s \Omega_{g_k}} + 1 \right)^{-1} e^{-\left(\frac{\gamma_{th}^{\text{FD}}}{P_s \Omega_{g_k}} \right)} \quad (45)
 \end{aligned}$$

The derivative of (44) and (45) yields the $f_{\gamma_{x_k, R}}(\gamma_{th}^{\text{FD}})$ and $f_{\gamma_{y_k, R}}(\gamma_{th}^{\text{FD}})$ as in (46) and (47), respectively.

$$\begin{aligned}
 f_{\gamma_{x_k, R}}(\gamma_{th}^{\text{FD}}) &= e^{-\left(\frac{\gamma_{th}^{\text{FD}}}{P_s \Omega_{h_k}} \right)} \left[\left(\frac{P_s \Omega_{g_k} \gamma_{th}^{\text{FD}}}{P_s \Omega_{h_k}} + 1 \right)^{-2} \left(\frac{P_s \Omega_{g_k}}{P_s \Omega_{h_k}} \right) \left(\frac{P_j \Omega_{f_j} \gamma_{th}^{\text{FD}}}{P_s \Omega_{h_k}} + 1 \right)^{-M} \right. \\
 &\quad \times \left(\frac{P_r \Omega_{c_k} \gamma_{th}^{\text{FD}}}{P_s \Omega_{h_k}} + 1 \right)^{-1} + M \left(\frac{P_s \Omega_{g_k} \gamma_{th}^{\text{FD}}}{P_s \Omega_{h_k}} + 1 \right)^{-1} \left(\frac{P_j \Omega_{f_j} \gamma_{th}^{\text{FD}}}{P_s \Omega_{h_k}} + 1 \right)^{-M-1} \left(\frac{P_j \Omega_{f_j}}{P_s \Omega_{h_k}} \right) \\
 &\quad \times \left(\frac{P_r \Omega_{c_k} \gamma_{th}^{\text{FD}}}{P_s \Omega_{h_k}} + 1 \right)^{-1} + \left(\frac{P_s \Omega_{g_k} \gamma_{th}^{\text{FD}}}{P_s \Omega_{h_k}} + 1 \right)^{-1} \left(\frac{P_j \Omega_{f_j} \gamma_{th}^{\text{FD}}}{P_s \Omega_{h_k}} + 1 \right)^{-M} \\
 &\quad \times \left(\frac{P_r \Omega_{c_k}}{P_s \Omega_{h_k}} \right) \left(\frac{P_r \Omega_{c_k} \gamma_{th}^{\text{FD}}}{P_s \Omega_{h_k}} + 1 \right)^{-2} + \left(\frac{1}{P_s \Omega_{h_k}} \right) \left(\frac{P_s \Omega_{g_k} \gamma_{th}^{\text{FD}}}{P_s \Omega_{h_k}} + 1 \right)^{-1} \left(\frac{P_j \Omega_{f_j} \gamma_{th}^{\text{FD}}}{P_s \Omega_{h_k}} + 1 \right)^{-M} \\
 &\quad \left. \times \left(\frac{P_r \Omega_{c_k} \gamma_{th}^{\text{FD}}}{P_s \Omega_{h_k}} + 1 \right)^{-1} \right] \quad (46)
 \end{aligned}$$

$$\begin{aligned}
 f_{\gamma_{y_k, R}}(\gamma_{th}^{\text{FD}}) &= e^{-\left(\frac{\gamma_{th}^{\text{FD}}}{P_s \Omega_{g_k}} \right)} \left[\left(\frac{P_s \Omega_{h_k} \gamma_{th}^{\text{FD}}}{P_s \Omega_{g_k}} + 1 \right)^{-2} \left(\frac{P_s \Omega_{h_k}}{P_s \Omega_{g_k}} \right) \left(\frac{P_j \Omega_{f_j} \gamma_{th}^{\text{FD}}}{P_s \Omega_{g_k}} + 1 \right)^{-M} \right. \\
 &\quad \times \left(\frac{P_r \Omega_{c_k} \gamma_{th}^{\text{FD}}}{P_s \Omega_{g_k}} + 1 \right)^{-1} + M \left(\frac{P_s \Omega_{h_k} \gamma_{th}^{\text{FD}}}{P_s \Omega_{g_k}} + 1 \right)^{-1} \left(\frac{P_j \Omega_{f_j} \gamma_{th}^{\text{FD}}}{P_s \Omega_{g_k}} + 1 \right)^{-M-1} \left(\frac{P_j \Omega_{f_j}}{P_s \Omega_{g_k}} \right) \\
 &\quad \times \left(\frac{P_r \Omega_{c_k} \gamma_{th}^{\text{FD}}}{P_s \Omega_{g_k}} + 1 \right)^{-1} + \left(\frac{P_s \Omega_{h_k} \gamma_{th}^{\text{FD}}}{P_s \Omega_{g_k}} + 1 \right)^{-1} \left(\frac{P_j \Omega_{f_j} \gamma_{th}^{\text{FD}}}{P_s \Omega_{g_k}} + 1 \right)^{-M} \\
 &\quad \times \left(\frac{P_r \Omega_{c_k}}{P_s \Omega_{g_k}} \right) \left(\frac{P_r \Omega_{c_k} \gamma_{th}^{\text{FD}}}{P_s \Omega_{g_k}} + 1 \right)^{-2} + \left(\frac{1}{P_s \Omega_{g_k}} \right) \left(\frac{P_s \Omega_{h_k} \gamma_{th}^{\text{FD}}}{P_s \Omega_{g_k}} + 1 \right)^{-1} \left(\frac{P_j \Omega_{f_j} \gamma_{th}^{\text{FD}}}{P_s \Omega_{g_k}} + 1 \right)^{-M} \\
 &\quad \left. \times \left(\frac{P_r \Omega_{c_k} \gamma_{th}^{\text{FD}}}{P_s \Omega_{g_k}} + 1 \right)^{-1} \right] \quad (47)
 \end{aligned}$$

Substituting (42) and (46) into (38) and utilizing the distributive property, (48) can be obtained. Considering the partial fraction decomposition technique and also utilizing [20, Eq. (10,11)] and also [20, Eq. (21)] for solving the integral expression, first, second, third, and fourth integrals in (48) can be solved as in the first part of (20). Please note that following the same procedures the fifth integral expression in (48) can be solved as in (20). The other integral expressions, which are sixth, seventh, and eighth, in (48) can be solved by following the same procedures. In addition, the ζ term in (38) can also be obtained by following the same procedures as the Ψ term in (38). However, because of the space limitation these derivation details and the results are omitted. Please also

note that $A^* = \lim_{x \rightarrow -\frac{P_s \Omega_{h_k}}{P_s \Omega_{g_k}}} \frac{\partial}{\partial x} \left(\frac{P_s \Omega_{g_k}}{P_s \Omega_{h_k}} x + 1 \right)^2 [A^\phi]$, $B_{a_3}^* =$

$$\begin{aligned}
 \Psi = & \left(\frac{P_s \Omega_{gk}}{P_s \Omega_{hk}} \right) \int_0^\infty e^{-\left(\frac{x}{P_s \Omega_{hk}}\right)} \left(\frac{P_s \Omega_{gk}}{P_s \Omega_{hk}} x + 1 \right)^{-2} \left(\frac{P_j \Omega_{fj}}{P_s \Omega_{hk}} x + 1 \right)^{-M} \left(\frac{P_r \Omega_{ck}}{P_s \Omega_{hk}} x + 1 \right)^{-1} dx \\
 & + M \left(\frac{P_j \Omega_{fj}}{P_s \Omega_{hk}} \right) \int_0^\infty e^{-\left(\frac{x}{P_s \Omega_{hk}}\right)} \left(\frac{P_s \Omega_{gk}}{P_s \Omega_{hk}} x + 1 \right)^{-1} \left(\frac{P_j \Omega_{fj}}{P_s \Omega_{hk}} x + 1 \right)^{-M-1} \left(\frac{P_r \Omega_{ck}}{P_s \Omega_{hk}} x + 1 \right)^{-1} dx \\
 & + \left(\frac{P_r \Omega_{ck}}{P_s \Omega_{hk}} \right) \int_0^\infty e^{-\left(\frac{x}{P_s \Omega_{hk}}\right)} \left(\frac{P_s \Omega_{gk}}{P_s \Omega_{hk}} x + 1 \right)^{-1} \left(\frac{P_j \Omega_{fj}}{P_s \Omega_{hk}} x + 1 \right)^{-M} \left(\frac{P_r \Omega_{ck}}{P_s \Omega_{hk}} x + 1 \right)^{-2} dx \\
 & + \left(\frac{1}{P_s \Omega_h} \right) \int_0^\infty e^{-\left(\frac{x}{P_s \Omega_{hk}}\right)} \left(\frac{P_s \Omega_{gk}}{P_s \Omega_{hk}} x + 1 \right)^{-1} \left(\frac{P_j \Omega_{fj}}{P_s \Omega_{hk}} x + 1 \right)^{-M} \left(\frac{P_r \Omega_{ck}}{P_s \Omega_{hk}} x + 1 \right)^{-1} dx \\
 & - \left(\frac{P_s \Omega_{gk}}{P_s \Omega_{hk}} \right) \int_0^\infty e^{-x \left(\frac{2\varphi^{-1} \gamma_{th}^{FD}}{P_s \Omega_{hk}} + \frac{2\varphi^{-1} + 3}{P_s \Omega_{gk}} + \frac{\gamma_{th}^{FD}}{P_s \Omega_{hk}} \right)} \left(\frac{P_j \Omega_{fj} \gamma_{th}^{FD}}{P_s \Omega_{gk}} x + 1 \right)^{-M} \left(\frac{P_r \Omega_{ck} \gamma_{th}^{FD}}{P_s \Omega_{gk}} x + 1 \right)^{-1} \\
 & \times \left(\left(\frac{\varphi^{-1} P_s \Omega_{ak} P_s \Omega_{gk} \gamma_{th}^{FD} + \varphi^{-1} P_s \Omega_{ak} P_s \Omega_{hk} \gamma_{th}^{FD}}{P_s \Omega_{hk} P_s \Omega_{gk}} \right) x + 1 \right)^{-1} \left(\frac{P_s \Omega_{gk}}{P_s \Omega_{hk}} x + 1 \right)^{-2} \\
 & \times \left(\frac{P_j \Omega_{fj}}{P_s \Omega_{hk}} x + 1 \right)^{-M} \left(\frac{P_r \Omega_{ck}}{P_s \Omega_{hk}} x + 1 \right)^{-1} dx \\
 & - M \left(\frac{P_j \Omega_{fj}}{P_s \Omega_{hk}} \right) \int_0^\infty e^{-x \left(\frac{2\varphi^{-1} \gamma_{th}^{FD}}{P_s \Omega_{hk}} + \frac{2\varphi^{-1} + 3}{P_s \Omega_{gk}} + \frac{\gamma_{th}^{FD}}{P_s \Omega_{hk}} \right)} \left(\frac{P_j \Omega_{fj} \gamma_{th}^{FD}}{P_s \Omega_{gk}} x + 1 \right)^{-M} \left(\frac{P_r \Omega_{ck} \gamma_{th}^{FD}}{P_s \Omega_{gk}} x + 1 \right)^{-1} \\
 & \times \left(\left(\frac{\varphi^{-1} P_s \Omega_{ak} P_s \Omega_{gk} \gamma_{th}^{FD} + \varphi^{-1} P_s \Omega_{ak} P_s \Omega_{hk} \gamma_{th}^{FD}}{P_s \Omega_{hk} P_s \Omega_{gk}} \right) x + 1 \right)^{-1} \left(\frac{P_s \Omega_{gk}}{P_s \Omega_{hk}} x + 1 \right)^{-1} \\
 & \times \left(\frac{P_j \Omega_{fj}}{P_s \Omega_{hk}} x + 1 \right)^{-M-1} \left(\frac{P_r \Omega_{ck}}{P_s \Omega_{hk}} x + 1 \right)^{-1} dx \\
 & - \left(\frac{P_r \Omega_{ck}}{P_s \Omega_{hk}} \right) \int_0^\infty e^{-x \left(\frac{2\varphi^{-1} \gamma_{th}^{FD}}{P_s \Omega_{hk}} + \frac{2\varphi^{-1} + 3}{P_s \Omega_{gk}} + \frac{\gamma_{th}^{FD}}{P_s \Omega_{hk}} \right)} \left(\frac{P_j \Omega_{fj} \gamma_{th}^{FD}}{P_s \Omega_{gk}} x + 1 \right)^{-M} \left(\frac{P_r \Omega_{ck} \gamma_{th}^{FD}}{P_s \Omega_{gk}} x + 1 \right)^{-1} \\
 & \times \left(\left(\frac{\varphi^{-1} P_s \Omega_{ak} P_s \Omega_{gk} \gamma_{th}^{FD} + \varphi^{-1} P_s \Omega_{ak} P_s \Omega_{hk} \gamma_{th}^{FD}}{P_s \Omega_{hk} P_s \Omega_{gk}} \right) x + 1 \right)^{-1} \left(\frac{P_s \Omega_{gk}}{P_s \Omega_{hk}} x + 1 \right)^{-1} \\
 & \times \left(\frac{P_j \Omega_{fj}}{P_s \Omega_{hk}} x + 1 \right)^{-M} \left(\frac{P_r \Omega_{ck}}{P_s \Omega_{hk}} x + 1 \right)^{-2} dx \\
 & - \left(\frac{1}{P_s \Omega_h} \right) \int_0^\infty e^{-x \left(\frac{2\varphi^{-1} \gamma_{th}^{FD}}{P_s \Omega_{hk}} + \frac{2\varphi^{-1} + 3}{P_s \Omega_{gk}} + \frac{\gamma_{th}^{FD}}{P_s \Omega_{hk}} \right)} \left(\frac{P_j \Omega_{fj} \gamma_{th}^{FD}}{P_s \Omega_{gk}} x + 1 \right)^{-M} \left(\frac{P_r \Omega_{ck} \gamma_{th}^{FD}}{P_s \Omega_{gk}} x + 1 \right)^{-1} \\
 & \times \left(\left(\frac{\varphi^{-1} P_s \Omega_{ak} P_s \Omega_{gk} \gamma_{th}^{FD} + \varphi^{-1} P_s \Omega_{ak} P_s \Omega_{hk} \gamma_{th}^{FD}}{P_s \Omega_{hk} P_s \Omega_{gk}} \right) x + 1 \right)^{-1} \left(\frac{P_s \Omega_{gk}}{P_s \Omega_{hk}} x + 1 \right)^{-1} \\
 & \times \left(\frac{P_j \Omega_{fj}}{P_s \Omega_{hk}} x + 1 \right)^{-M} \left(\frac{P_r \Omega_{ck}}{P_s \Omega_{hk}} x + 1 \right)^{-1} dx
 \end{aligned} \tag{48}$$

$$\begin{aligned}
 \lim_{x \rightarrow -\frac{P_s \Omega_{hk}}{P_j \Omega_{fj}}} \frac{\partial^{M-a^3}}{(M-a^3)! \partial x^{M-a^3}} \left(\frac{P_j \Omega_{fj}}{P_s \Omega_{hk}} x + 1 \right)^M [A^\phi], & \quad \lim_{x \rightarrow -\frac{P_s \Omega_{hk}}{P_j \Omega_{fj}}} \frac{\partial^{M+1-b^3}}{(M+1-b^3)! \partial x^{M+1-b^3}} \left(\frac{P_j \Omega_{fj}}{P_s \Omega_{hk}} x + 1 \right)^{M+1} [B^\phi], \\
 C^* = \lim_{x \rightarrow -\frac{P_s \Omega_{hk}}{P_r \Omega_{ck}}} \frac{\partial}{\partial x} \left(\frac{P_r \Omega_{ck}}{P_s \Omega_{hk}} x + 1 \right) [A^\phi], & \quad \text{and} \quad F^* = \lim_{x \rightarrow -\frac{P_s \Omega_{hk}}{P_r \Omega_{ck}}} \frac{\partial}{\partial x} \left(\frac{P_r \Omega_{ck}}{P_s \Omega_{hk}} x + 1 \right) [B^\phi], \quad \text{and} \\
 A^\phi = \frac{1}{\left(\frac{P_s \Omega_{gk}}{P_s \Omega_{hk}} x + 1 \right)^2 \left(\frac{P_j \Omega_{fj}}{P_s \Omega_{hk}} x + 1 \right)^M \left(\frac{P_r \Omega_{ck}}{P_s \Omega_{hk}} x + 1 \right)}, & \quad B^\phi = \frac{1}{\left(\frac{P_s \Omega_{gk}}{P_s \Omega_{hk}} x + 1 \right) \left(\frac{P_j \Omega_{fj}}{P_s \Omega_{hk}} x + 1 \right)^{M+1} \left(\frac{P_r \Omega_{ck}}{P_s \Omega_{hk}} x + 1 \right)}. \\
 D^* = \lim_{x \rightarrow -\frac{P_s \Omega_{hk}}{P_s \Omega_{gk}}} \frac{\partial}{\partial x} \left(\frac{P_s \Omega_{gk}}{P_s \Omega_{hk}} x + 1 \right) [B^\phi], & \quad E_{b^3}^* = G^* = \lim_{x \rightarrow -\frac{P_s \Omega_{hk}}{P_s \Omega_{gk}}} \frac{\partial}{\partial x} \left(\frac{P_s \Omega_{gk}}{P_s \Omega_{hk}} x + 1 \right) [C^\phi], \quad H_{c^3}^* =
 \end{aligned}$$

$$\begin{aligned}
& \lim_{x \rightarrow -\frac{P_s \Omega_{h_k}}{P_j \Omega_{f_j}}} \frac{\partial^{M-c^3}}{(M-c^3)! \partial x^{M-c^3}} \left(\frac{P_j \Omega_{f_j}}{P_s \Omega_{h_k}} x + 1 \right)^M [C^\phi], \\
I^* &= \lim_{x \rightarrow -\frac{P_s \Omega_{h_k}}{P_r \Omega_{c_k}}} \frac{\partial}{\partial x} \left(\frac{P_r \Omega_{c_k}}{P_s \Omega_{h_k}} x + 1 \right)^2 [C^\phi], \quad \text{and} \\
C^\phi &= \frac{1}{\left(\frac{P_s \Omega_{g_k}}{P_s \Omega_{h_k}} x + 1 \right) \left(\frac{P_j \Omega_{f_j}}{P_s \Omega_{h_k}} x + 1 \right)^M \left(\frac{P_r \Omega_{c_k}}{P_s \Omega_{h_k}} x + 1 \right)^2}. \\
J^* &= \lim_{x \rightarrow -\frac{P_s \Omega_{h_k}}{P_s \Omega_{g_k}}} \frac{\partial}{\partial x} \left(\frac{P_s \Omega_{g_k}}{P_s \Omega_{h_k}} x + 1 \right) [D^\phi], \quad K_{d^3}^* = \\
& \lim_{x \rightarrow -\frac{P_s \Omega_{h_k}}{P_j \Omega_{f_j}}} \frac{\partial^{M-d^3}}{(M-d^3)! \partial x^{M-d^3}} \left(\frac{P_j \Omega_{f_j}}{P_s \Omega_{h_k}} x + 1 \right)^M [D^\phi], \\
L^* &= \lim_{x \rightarrow -\frac{P_s \Omega_{h_k}}{P_r \Omega_{c_k}}} \frac{\partial}{\partial x} \left(\frac{P_r \Omega_{c_k}}{P_s \Omega_{h_k}} x + 1 \right) [D^\phi], \quad \text{and} \\
D^\phi &= \frac{1}{\left(\frac{P_s \Omega_{g_k}}{P_s \Omega_{h_k}} x + 1 \right) \left(\frac{P_j \Omega_{f_j}}{P_s \Omega_{h_k}} x + 1 \right)^M \left(\frac{P_r \Omega_{c_k}}{P_s \Omega_{h_k}} x + 1 \right)}. \\
M^* &= \lim_{x \rightarrow -\frac{P_s \Omega_{g_k}}{P_j \Omega_{f_j} \gamma_{th}^{FD}}} \frac{\partial^{M-e^3}}{(M-e^3)! \partial x^{M-e^3}} \left(\frac{P_j \Omega_{f_j} \gamma_{th}^{FD}}{P_s \Omega_{g_k}} x + 1 \right) [E^\phi], \\
N^* &= \lim_{x \rightarrow -\frac{P_s \Omega_{g_k}}{P_r \Omega_{c_k} \gamma_{th}^{FD}}} \frac{\partial}{\partial x} \left(\frac{P_r \Omega_{c_k} \gamma_{th}^{FD}}{P_s \Omega_{g_k}} x + 1 \right) [E^\phi], \\
O^* &= \lim_{x \rightarrow -\left(\frac{\varphi^{-1} P_s \Omega_{a_k} P_s \Omega_{g_k} \gamma_{th}^{FD} + \varphi^{-1} P_s \Omega_{a_k} P_s \Omega_{h_k} \gamma_{th}^{FD}}{P_s \Omega_{h_k} P_s \Omega_{g_k}} \right)} \\
& \times \frac{\partial}{\partial x} \left(\left(\frac{\varphi^{-1} P_s \Omega_{a_k} P_s \Omega_{g_k} \gamma_{th}^{FD} + \varphi^{-1} P_s \Omega_{a_k} P_s \Omega_{h_k} \gamma_{th}^{FD}}{P_s \Omega_{h_k} P_s \Omega_{g_k}} \right) x + 1 \right) [E^\phi], \\
P^* &= \lim_{x \rightarrow -\frac{P_s \Omega_{h_k}}{P_s \Omega_{g_k}}} \frac{\partial}{\partial x} \left(\frac{P_s \Omega_{g_k}}{P_s \Omega_{h_k}} x + 1 \right)^2 [E^\phi], \quad R^* = \\
& \lim_{x \rightarrow -\frac{P_s \Omega_{h_k}}{P_j \Omega_{f_j}}} \frac{\partial^{M-f^3}}{(M-f^3)! \partial x^{M-f^3}} \left(\frac{P_j \Omega_{f_j}}{P_s \Omega_{h_k}} x + 1 \right)^M [E^\phi], \\
S^* &= \lim_{x \rightarrow -\frac{P_s \Omega_{h_k}}{P_r \Omega_{c_k}}} \frac{\partial}{\partial x} \left(\frac{P_r \Omega_{c_k}}{P_s \Omega_{h_k}} x + 1 \right) [E^\phi], \quad \text{and} \\
E^\phi &= \left[\frac{1}{\left(\frac{P_j \Omega_{f_j} \gamma_{th}^{FD}}{P_s \Omega_{g_k}} x + 1 \right)^M \left(\frac{P_r \Omega_{c_k} \gamma_{th}^{FD}}{P_s \Omega_{g_k}} x + 1 \right)} \right. \\
& \times \frac{1}{\left(\frac{\varphi^{-1} P_s \Omega_{a_k} P_s \Omega_{g_k} \gamma_{th}^{FD} + \varphi^{-1} P_s \Omega_{a_k} P_s \Omega_{h_k} \gamma_{th}^{FD}}{P_s \Omega_{h_k} P_s \Omega_{g_k}} \right) \left(\frac{P_s \Omega_{g_k}}{P_s \Omega_{h_k}} x + 1 \right)^2} \\
& \left. \times \frac{1}{\left(\frac{P_j \Omega_{f_j}}{P_s \Omega_{h_k}} x + 1 \right)^M \left(\frac{P_r \Omega_{c_k}}{P_s \Omega_{h_k}} x + 1 \right)} \right].
\end{aligned}$$

REFERENCES

- [1] R. Rivest, A. Shamir, and L. Adleman, "A method for obtaining digital signatures and public-key cryptosystems," *Commun. of the ACM*, vol. 21, pp. 120–126, 1978.
- [2] J. Daemen and V. Rijmen, "AES proposal: Rijndael," 1999.
- [3] A. D. Wyner, "The wire-tap channel," *Bell. Syst. Tech. J.*, vol. 54, no. 8, p. 13551387, 1975.
- [4] Z. Ding, Y. Liu, J. Choi, Q. Sun, M. Elkashlan, C. I. and H. V. Poor, "Application of non-orthogonal multiple access in LTE and 5G networks," *IEEE Commun. Magazine*, vol. 55, no. 2, pp. 185–191, February 2017.

- [5] C. Cai, Y. Cai, R. Wang, W. Yang, and W. Yang, "Resource allocation for physical layer security in cooperative OFDM networks," in *2015 Intern. Conf. on Wireless Commun. Signal Processing (WCSP)*, Oct 2015, pp. 1–5.
- [6] C. Jeong and I. M. Kim, "Optimal power allocation for secure multicarrier relay systems," *IEEE Trans. on Signal Process.*, vol. 59, no. 11, pp. 5428–5442, Nov 2011.
- [7] H. Zhang, H. Xing, J. Cheng, A. Nallanathan, and V. C. M. Leung, "Secure resource allocation for OFDMA two-way relay wireless sensor networks without and with cooperative jamming," *IEEE Trans. on Indust. Informatics*, vol. 12, no. 5, pp. 1714–1725, Oct 2016.
- [8] D. W. K. Ng, E. S. Lo, and R. Schober, "Secure resource allocation and scheduling for OFDMA decode-and-forward relay networks," *IEEE Trans. on Wireless Commun.*, vol. 10, no. 10, pp. 3528–3540, October 2011.
- [9] W. Aman, G. A. S. Sidhu, T. Jabeen, F. Gao, and S. Jin, "Enhancing physical layer security in dual-hop multiuser transmission," in *2016 IEEE Wireless Commun. and Networking Conf.*, April 2016, pp. 1–6.
- [10] C. Cai, Y. Cai, and W. Yang, "Secrecy rates for relay selection in OFDMA networks," in *2011 Third Intern. Conf. on Commun. and Mobile Comp.*, April 2011, pp. 158–160.
- [11] V. Ozduran, "Physical layer security of multi-user full-duplex one-way wireless relaying network," in *Advances in Wireless and Optical Communications (RTUWO'18)*, Riga, Latvia, 15–16 November 2018.
- [12] E. W. Weisstein, "Meijer g-function." *From MathWorld—A Wolfram Web Resource*. <http://mathworld.wolfram.com/MeijerG-Function.html>, accessed on 25 June 2019.
- [13] N. H. Mahmood, I. S. Ansari, P. Popovski, P. Mogensen, and K. A. Qaraqe, "Physical-layer security with full-duplex transceivers and multiuser receiver at eve," *IEEE Trans. on Commun.*, vol. 65, no. 10, pp. 4392–4405, Oct 2017.
- [14] E. Soleimani-Nasab, M. Matthaoui, M. Ardebilipour, and G. K. Karagiannidis, "Two-way AF relaying in the presence of co-channel interference," *IEEE Trans. on Commun.*, vol. 61, no. 8, pp. 3156–3169, August 2013.
- [15] J. Miranda, R. Abrishambaf, T. Gomes, P. Goncalves, J. Cabral, A. Tavares, and J. Monteiro, "Path loss exponent analysis in wireless sensor networks: Experimental evaluation," in *2013 11th IEEE International Conference on Industrial Informatics (INDIN)*, July 2013, pp. 54–58.
- [16] V. Ozduran, E. Soleimani-Nasab, and B. S. Yarman, "Opportunistic source-pair selection for multi-user two-way amplify-and-forward wireless relaying networks," *IET Commun.*, vol. 10, no. 16, pp. 2106–2118, 2016.
- [17] L. Jimnez Rodriguez, N. H. Tran, and T. Le-Ngoc, "Performance of full-duplex at relaying in the presence of residual self-interference," *IEEE Journal on Selected Areas in Commun.*, vol. 32, no. 9, pp. 1752–1764, Sep. 2014.
- [18] A. Papoulis and U. Pillai, *Probability, random variables and stochastic processes*, 4th ed. McGraw-Hill, 11 2001.
- [19] I. S. Gradshteyn and I. M. Ryzhik, *Tables of Integrals, Series and Products*. Elsevier Inc., 7th edition, 2007.
- [20] V. S. Adamchik and O. I. Marichev, *The algorithm for calculating integrals of hypergeometric type functions and its realization in REDUCE systems*. Proc. Conf. ISSAC'90, Tokyo, pp. 212224, 1990.



Volkan Ozduran graduated from department of Electronics at Soke Technical High School, Aydin, Turkey in 1997. He received his A.Sc. degree in Industrial Electronics, B.Sc., M.Sc. and Ph.D. degrees are in Electrical and Electronics Engineering from Istanbul University, Istanbul, Turkey in 2002, 2005, 2008 and 2015 respectively. During his Ph.D. studies he visited Stanford University, Stanford, CA,

USA department of Electrical Engineering, Space, Telecommunications, and Radioscience Laboratory, Dynamic Spectrum Management (DSM) Research group as a visiting student researcher between April 2012 and October 2012 under the supervision of Prof. Dr. John M. CIOFFI, the best known father of DSL. Prof. CIOFFI was his formal second advisor in his PhD studies. During his Ph.D. studies he also had some short visits to California Institute of Technology (CALTECH), Pasadena, CA, USA and Princeton University, Princeton, NJ, USA, department of Electrical Engineering in April 2013 and November 2014, respectively. His current research interests area more on cooperative communications, interference mitigation, massive MIMO and signal processing for wireless communications. He is an active Reviewer in various IEEE conferences and Transactions Journals

Design and Analysis of a Water Pumping System with Photovoltaic Source and Switched Reluctance Motor

Z. OMAÇ

Abstract— Solar energy is a clean energy and it is increasingly being used all over the world. In this study, a centrifugal water pump system driven by switched reluctance motor (SRM) has been designed with powered by a photovoltaic (PV) energy source. The voltage of the PV source has been increased by using a boost converter. The mathematical model of the system has been composed in the Matlab/Simulink and simulation results have been obtained. Proportional–integral–derivative (PID) controller has been used to control output voltage of the boost converter at 50 kHz switching frequency. The boost converter is controlled by an eight-bit PIC16F877A microcontroller. The electrical energy obtained by PV panels has been stored in batteries. Battery charge testers have been used to control the battery charge level. The speed and current control of SRM has been done by using DS1103 Ace kit. The values of phases currents have been measured by using hall sensors and transferred to the digital signal processor (DSP) by analog to digital converter inputs. The accuracy of simulation results has been proved by experimental results.

Index Terms— Solar Energy, Switched Reluctance Motor, Boost Converter, Photovoltaic energy (PV), Digital Signal Processor (DSP).

I. INTRODUCTION

AS A RESULT of increasing usage of the solar energy and developments in technology, photovoltaic (PV) pumping systems are put into operation [1]. PV pumping systems generally have a PV unit, a motor and a pump. Induction motors and direct current (DC) motors are mostly used in these systems [2].

Induction motors have a simple structure and they are also cheap. To run induction motors with minimum harmonics, they need complex alternating current (AC) power inverters. DC motors are very complicated and expensive motors and they have commutation segments and brushes. Therefore, DC motors have bigger maintenance problems than SRM. DC

motors have not only problem of limited size and speed but also arc problem. Switched reluctance motors (SRM) have advantages such as higher torque compared with the inertia, robust and reliable structure which are make them simple and cheap. Moreover, it has a simple power electronic converter and the ability to run at high efficiency and high speed [3]–[6].

This study displays the design of a water pumping system based on photovoltaic energy and switched reluctance motor. For increasing the voltage of PV panels, DC - DC boost converter has been used in the present study. All the system is modeled and analyzed by using MATLAB/Simulink software. Simulation results and experimental results are compared in this work to see the accuracy of the model developed. Additionally, it is targeted to contribute to the use of solar energy in countries that use solar energy widely.

II. DC-DC CONVERTERS


Because of the high stability and efficiency of DC - DC switching converter, it has been used in the fields of mobile communications, industrial applications, home appliances and so on. The analyses and design of the switch converter have already become the key points of the researches. There are two basic operation modes, which are classified as continuous conduction mode (CCM) and discontinuous conduction mode, on DC - DC converters [7].

Several studies have examined the direct current (DC) power distribution technology as a promising candidate for future power systems. However, the efficiency and reliability of DC power converters already used have not been comparable with those of AC transformers yet [4].

The most popular DC - DC converters of both non - isolated and isolated converters are classified as buck (step - down), boost (step - up) and buck - boost (step down - up) converters [7]. Buck converters decrease the input voltage where boost converters increase it. Buck - boost converters change the input voltage to a negative value. Since a boost converter is used in this study, it will be under our focus.

When a small change is made on a buck converter, a boost converter can be achieved. The boost converter is shown in Fig. 1. It is also known as “the step - up DC - DC converter” due to its voltage boosting function.

ZEKİ OMAÇ, is with Department of Electrical and Electronics Engineering Munzur University, Tunceli, Turkey,(e-mail: zomac@munzur.edu.tr).

 <https://orcid.org/0000-0002-9339-8243>

Manuscript received April 5, 2019; accepted July 1, 2019.
DOI: [10.17694/bajece.550031](https://doi.org/10.17694/bajece.550031)

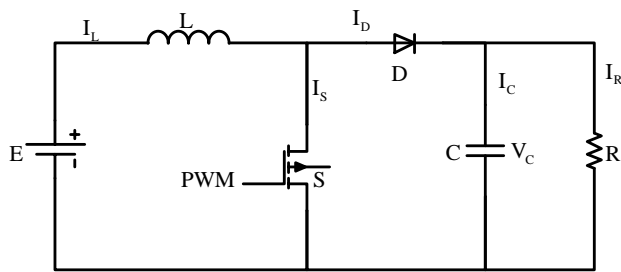


Fig. 1. The DC - DC boost converter circuit.

When the switch S is on, the inductor current is

$$\frac{di_L}{dt} = \frac{E}{L} \quad (1)$$

$$\frac{dV_C}{dt} = -\frac{V_C}{R.C} \quad (2)$$

Where E is DC input voltage, V_C is the DC output voltage, L is the inductance of inductor, i_L is inductor current, R is the load resistance, C is the capacitance and i_c is the capacitance current for DC-DC boost converter. When the switch S is off, the equation becomes

$$\frac{di_L}{dt} = \frac{E - V_C}{L} \quad (3)$$

$$i_C = i_L - \frac{V_C}{R} \quad (4)$$

The type of converter to be used is determined depending on the load. The power electronic components such as MOSFET, IGBT are strongly influenced by the component temperature in these converters [6]. In addition, manufacturer's tolerances in cell characteristics, environmental stresses and shadow problems may lead to mismatches of each PV module caused significant losses. DC - DC converters in series are used to solve these problems [7]. Switching loss is one of the prominent problems of converters. Because of switching losses and electromagnetic interference (EMI), switching frequency in hard - switched DC - DC converters cannot be significantly raised. To increase the efficiency and average power of DC - DC converter, soft - switching techniques, which can minimize the switching losses of the converters, should be applied. It is generally implemented by adding an active or passive snubber circuit [8]-[12].

III. MATHEMATICAL MODEL OF SRM

Variable Reluctance Motors (VRM) have this name since they have variable reluctance due to the change in the air gap with respect to the rotor position. Although the theory of variable reluctance motors was known for a long time, they have been begun to be used for adjustable speed applications since 1980s.

The term "switched reluctance motor" (SRM) is used to refer to both variable reluctance motor and its driver circuit together. SRM has several advantages such as the simple power electronic converter requirement, fault tolerance, high

efficiency and capability for very high-speed operations. In addition, due to their simple and robust structures, easy manufacturing and the possibility of exploiting power converts with a reduced number of switches, SRM can be a viable alternative to universal motors and AC machines. Furthermore, due to motor structure and converter, switched reluctance motor (SRM) drive has high application potential for electric vehicles (EV) within a wide speed range. Besides, asymmetric bridge converter is usually used in SRM among all SRM converters. In the literature, the features of the SRM are discussed widely and their advantages and disadvantages are investigated in three sections as motor, driver and control [13]- [15].

Linear working conditions that neither inductance changes with current, nor magnetic saturation occurs are assumed for mathematical model of SRM. Since the mutual inductances between the phases are too small, they are ignored. Fig. 2 shows the cross-sectional illustration of the SRM used to actuate the centrifugal pump.

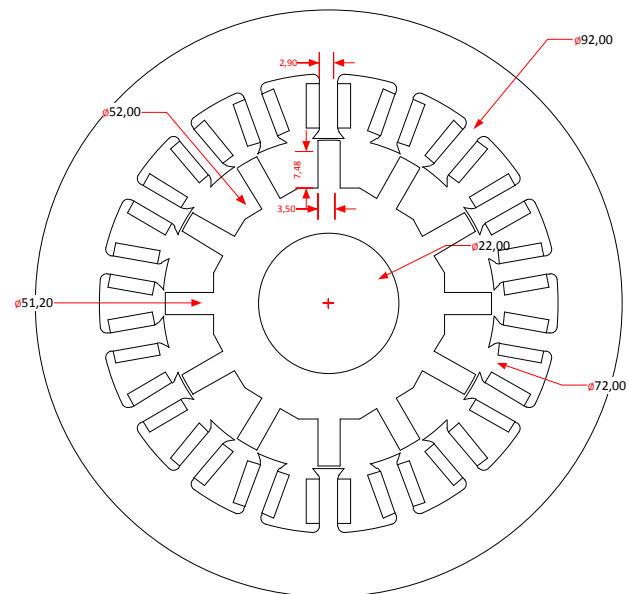


Fig. 2. Cross section of a switched reluctance motor driven water pumping system.

The phase winding voltage equation of SRM can be expressed as

$$V = Ri + \frac{d\psi(\theta, i)}{dt} \quad (5)$$

Where V is the phase voltage, i is the phase current, R is the phase resistance and ψ is the phase flux linkage. Flux linkage is a function of the rotor position and phase current. The phase winding voltage equation of SRM can be rewritten as

$$V = Ri + \frac{\partial \psi}{\partial i} \frac{di}{dt} + \frac{\partial \psi}{\partial \theta} \frac{d\theta}{dt} \quad (6)$$

and

$$\omega = \frac{d\theta}{dt} \quad (7)$$

Where θ is the rotor position, and ω is the angular speed of rotor. The relationship between the inductance (L) and the rotor position and phase current are given by Eq. (8);

$$L = \frac{\partial\psi}{\partial i} \quad (8)$$

The product of the self - inductance and the instantaneous phase current give the flux linkage in an active phase as

$$\psi = i \cdot L \quad (9)$$

Rearranging Equation (6) gives

$$V = Ri + L \frac{di}{dt} + i \frac{dL}{d\theta} \omega \quad (10)$$

The third term of the right side of Equation (10) is the induced back electromotive force (EMF):

$$E = i \frac{dL}{d\theta} \omega \quad (11)$$

The inductance L varies between maximum and minimum values. Maximum L_{max} and minimum inductance L_{min} take place when the rotor and stator poles axis are aligned and rotor and stator poles axis is unaligned, respectively.

The electromechanical torque (T) produced by the SRM is given by Equation (12),

$$T = \frac{1}{2} i^2 \frac{dL}{d\theta} \quad (12)$$

We can rewrite the whole torque equation (13) for the SRM.

$$T_e(\theta, i_a, i_b, i_c) = T_a(\theta, i_a) + T_b(\theta, i_b) + T_c(\theta, i_c) \quad (13)$$

The mechanical equation of an SRM can be defined as:

$$T_e = J \frac{d\omega}{dt} + B \frac{d\theta}{dt} + T_L \quad (14)$$

Where T_L , J , and B are the load torque, inertia, and damping coefficient, respectively. Substitution into Equation (7) gives

$$T_e = J \frac{d\omega}{dt} + B\omega + T_L \quad (15)$$

Equations (10) and (15) have the state equation form as shown below.

$$\frac{di}{dt} = \frac{1}{L} \left[V - \left(Ri + i \frac{dL}{d\theta} \omega \right) \right] \quad (16)$$

$$\frac{d\omega}{dt} = \frac{1}{J} [T_e - (B\omega + T_L)] \quad (17)$$

$$\frac{d\theta}{dt} = \omega \quad (18)$$

The torque is not unaffected by the polarity of phase current. To minimize ripples and to produce a smoother

torque, the current supplied by the converter must be a square wave.

In general, SRM drives can be designed as two different types as current - controlled and voltage - controlled. Each drive type has some advantages and disadvantages. Current - controlled drives are particularly suitable at low speeds. Therefore, the torque can be controlled with minimum ripple level in the constant torque region. Voltage - controlled drive is suitable for high - speed operation, but it is difficult to provide constant current at high speeds due to high back EMF. A good controller is expected to be able to operate at four quadrants, having low torque ripples, rapid response and good stability while it can start the motor at zero speed [13].

IV. CONTROL OF SRM

A good motor drive should have high efficiency and low cost. The construction of SRMs is simple and its manufacturing cost is low. The cost tends to increase as SR machines need auxiliary components, such as converters, rotor position sensors, current sensors, etc.

The triggering times of the switches of the drive circuit of an SRM depends on the position of the rotor. In order to control the current in the SRM phase windings, it is essential to know the rotor position. In SRM drives, rotor position information is essential for the stator phase commutation and advanced angle control. The rotor position is usually observed by position sensors.

Figure 3 consisting of the PV source, boost converter, SRM and centrifugal pump shows the block diagram of the overall system. Fig. 4 shows a converter configuration for a three phase SRM with two power switches per phase. The control unit generates gate signals regarding motor current, rotor position and motor operating mode (forward or reverse) for each switch.

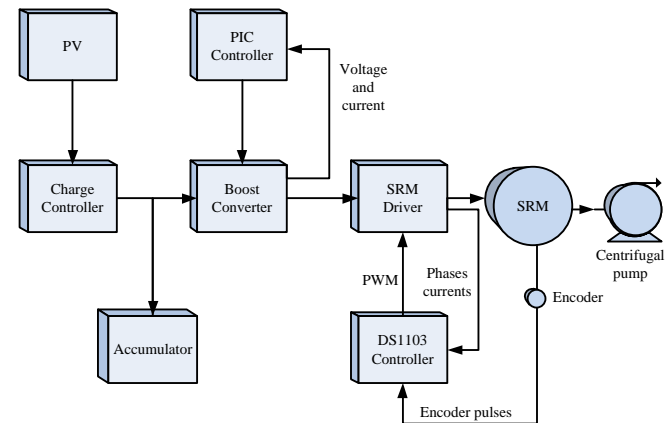


Fig. 3. The block diagram of the water pumping system with photovoltaic source and switched reluctance motor.

The average torque can be controlled by adjusting the current of the windings or by changing triggering angle. To minimize the variations in the torque, it is recommended to keep the triggering angle constant and to change the amplitude of the winding currents [14]. The average torque is the sum of

simultaneous pulses of electromagnetic torque produced by all phases. The machine produces discrete pulses of torque, but it is possible to produce a constant torque by overlapping phase inductance graphics partially.

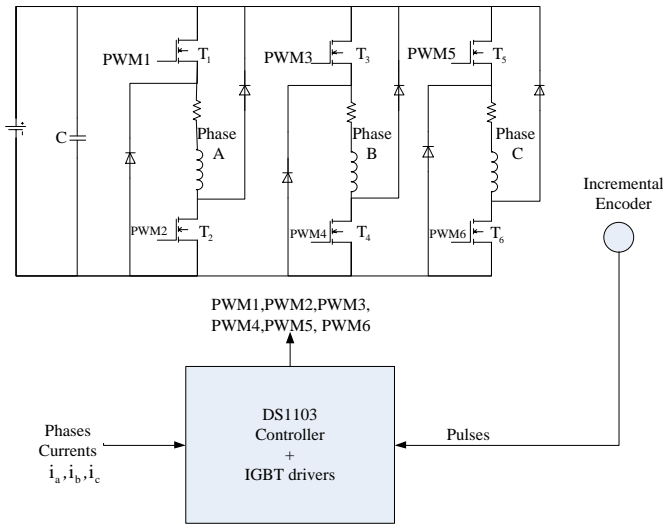


Fig. 4. Asymmetrical half-bridge converter and digital signal processor for SRM.

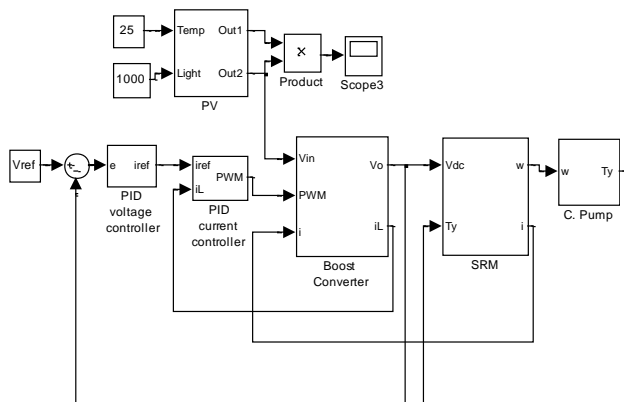


Fig. 5. Matlab/Simulink model of water pumping system with photovoltaic source and switched reluctance motor.

For positive torque generating, the pulses of phase current must coincide with a period of increasing inductance. Because of the presence of the inductor, the current cannot suddenly change. That's why forward voltage is applied at the beginning of the inductance curve with the positive slope to reach the maximum value of current on time. SRMs need a good commutation to decrease the phase current to zero before negative slope region of the inductance curve. Since the back EMF is lower than the line voltage under base speed, the torque is controlled with pulse width modulation (PWM). PWM current control is not possible above base speed because of high back EMF. The control of SRM speed is performed only by changing the triggering angles in the constant power region [13]. The control parameters above base speed are only the triggering angles. The linear model of SRM is simulated with Matlab/Simulink software. Block diagram of simulink

model of water pumping system with photovoltaic source and SRM is presented in Fig. 5.

The hardware of the experiment contains motor drive circuit of IGBTs, DSP and the sensors that measure current, voltage and speed. Processing of speed and current values and generation of appropriate pulse width modulation (PWM) constitute the software part of experimental study.

DSPs are used widely in motion control. Control of switched reluctance motors with DSP has become the most developed technique. Because of its digital processing capacity, DSPs are used to control all types of electrical motors. DSPs have the necessary features and hardware optimizations to be used directly for control. Some of these features are the shorter execution time for instructions and ability to make multiplication and other instructions in one machine cycle. High performance DSPs are used in the applications which require very fast execution of the control algorithm. In recent years, more than one system can be controlled at the same time with the help of very fast DSPs [15]. There are DSPs having similar features produced by various firms. In this work DS1103 Ace kit produced by Dspace has been used.

V. EXPERIMENTAL SETUP

Fig. 6 is the photograph of the PV unit used in the experiment set. Fig. 7, 8 and 9 are the photographs of other units of the system. The system consists of PV panels, batteries, fuse box, regulator, boost converter driver circuit and the pump. The code file used to operate the DS1103 can be run after the blocks are prepared with Matlab/Simulink and compiled. The file is optimized by the compiler after Matlab/Simulink simulation for faster execution. In this work, the program is prepared with Matlab/Simulink to control the SRM is transferred to the DSP.



Fig. 6. PV array.

Pumps can be defined as machines that convert mechanical energy to hydraulic energy. There are various types of pumps classified into mainly two groups as volumetric and centrifugal. Various types of pumps and motors are ready for use in the PV pump market. The most commonly used type is the centrifugal pump [17].

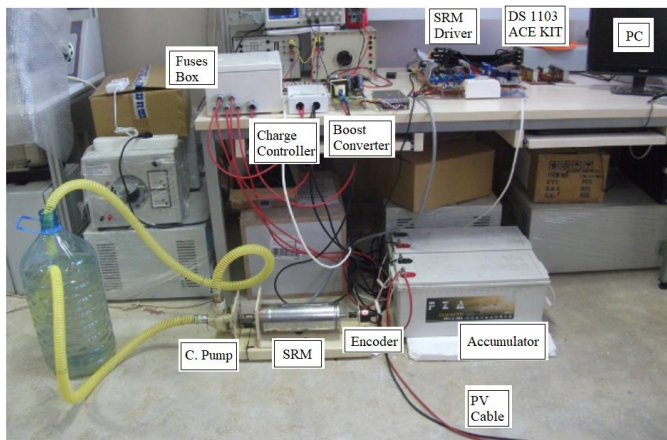


Fig. 7. Experiment set.

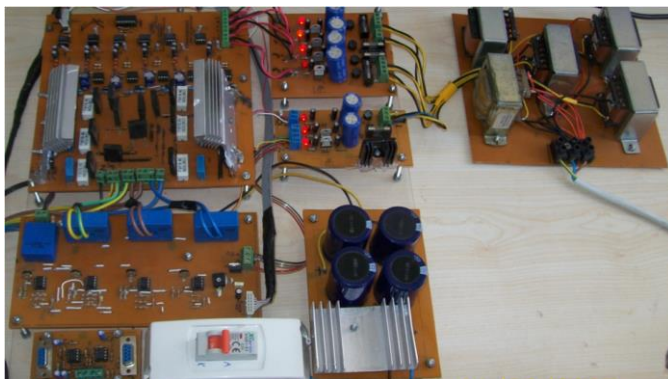


Fig. 8. The SRM driver.



Fig. 9. The photo of DC-DC boost converter.

Centrifugal pumps are preferred in low - height suction applications, especially if they are directly interfaced with the solar panels. In addition, these pumps are suitable for pumping high volumes of water and they comparably have high efficiency [16].

VI. SIMULATION AND EXPERIMENTAL RESULTS

Simulation parameters of SRM and boost converter are presented in Table I. The boost converter (Fig. 9) used to increase DC battery voltage (24 V) and SRM have been

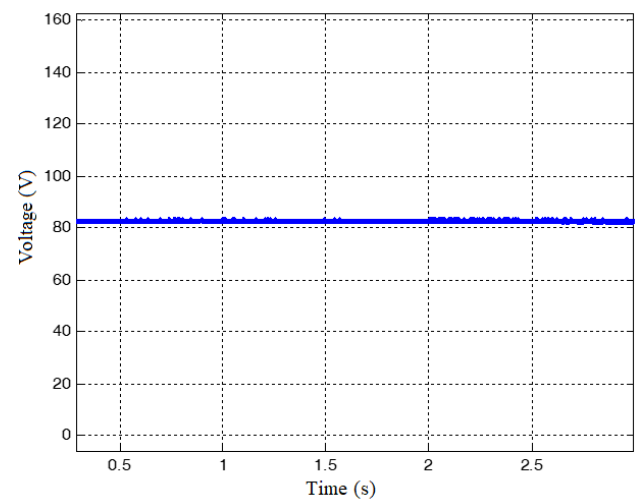


Fig. 10. Output voltage of the boost converter

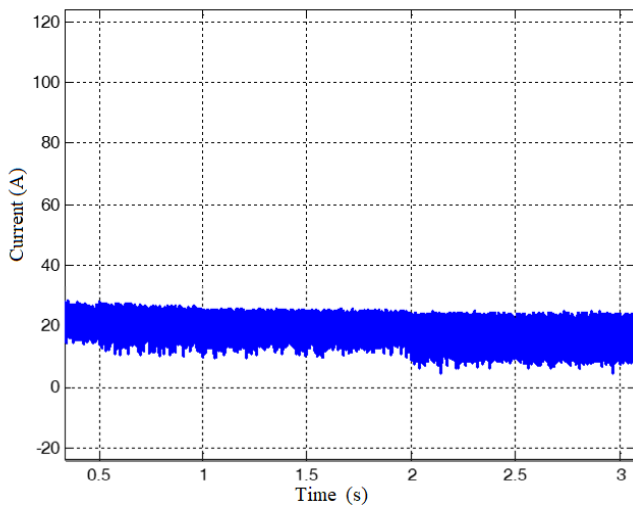
TABLE I
SIMULATION PARAMETERS OF SRM AND BOOST CONVERTER

Parameters	Values
Number of stator/rotor poles (N_s/N_r)	18/12
Rated power (P_n)	1.7 kW
Rated current (I_n)	6.5 A
Rated voltage (V_n)	300 V
A phase winding resistance (R)	2.6 Ω
Friction coefficient (B)	0.00018 Nm/rad/s
Moment of inertia (J)	0.000695 kgm ²
Aligned position inductance (L_{max})	7.29 mH
Unaligned position inductance (L_{min})	2.36 mH
Battery voltage	24 V
Boost converter inductance value (L)	200 μ H
Boost converter switching frequency	50 kHz
Boost converter capacitor value (C)	1000 μ F
SRM converter switching frequency	15 kHz
Proportionality coefficient (K_p)	30
Integral coefficient (K_i)	0.5
Derivative coefficient (K_d)	0.001

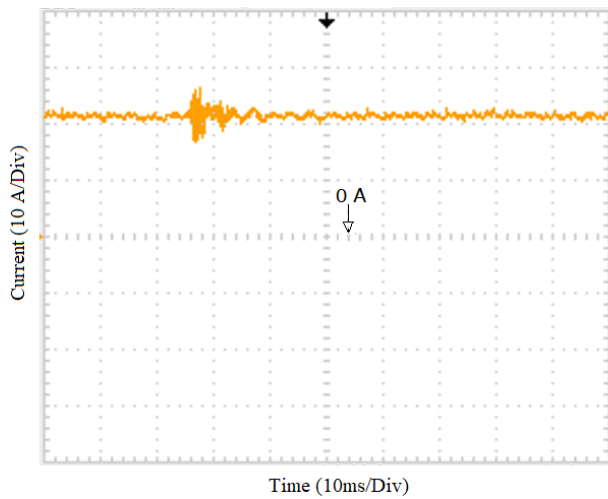
designed and simulated in Matlab/Simulink [17]. Then, bias and measurement circuits have been designed and connected. After tests and adjustments, the system has become ready to operate.

Boost converter has been designed later. Firstly, its circuit board has been manufactured. After that, the tests and measurements are started. In our experiment, the switching frequency of the boost converter is 50 kHz and the output voltage is regulated to the reference voltage of 80 V (Fig. 10). The switching frequency of the boost converter is observed by an oscilloscope. The four series - connected PV module that provide a rated output power of 600 W was used to supply motor. This PV module provides a rated output voltage of 80 V. Thus, the power loss of transmission line is reduced for higher current values, by increasing the voltage.

The connections and adjustments between PV panels and batteries has been done and recharge regulator has been used to control the charge level of batteries.

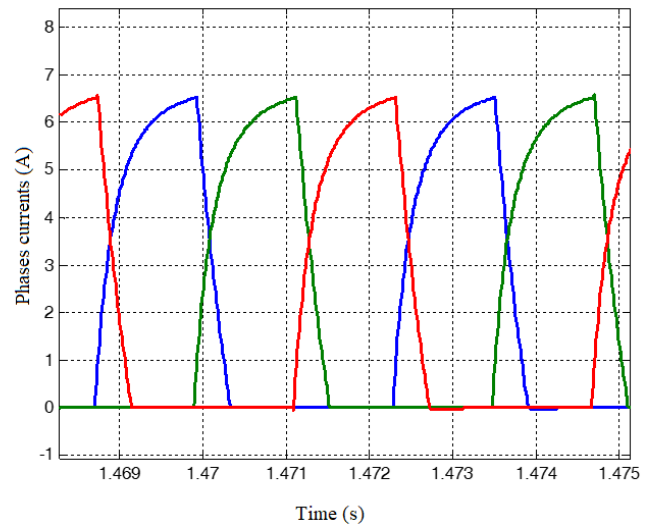


(a)

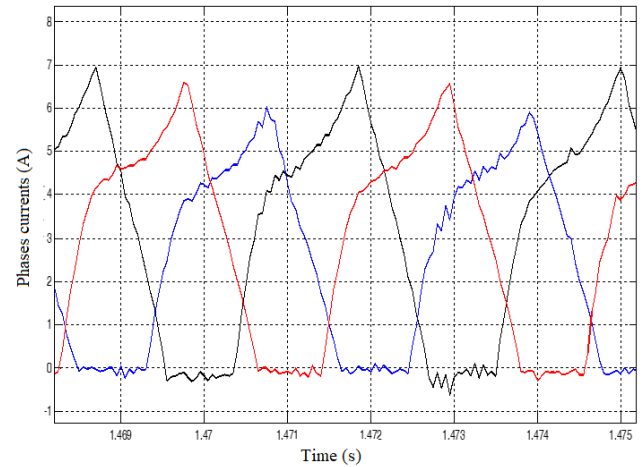


(b)

Fig. 11. Inductor current of the boost converter. (a) The simulation result, (b) The experimental result.



(a)



(b)

Fig. 13. Phases currents graphs. (a) The simulation results, (b) The experimental results.

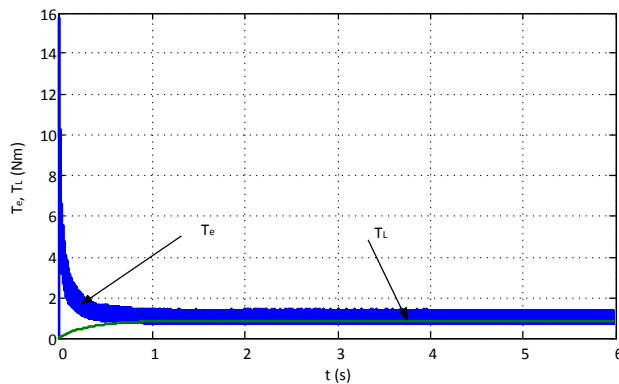


Fig.12. Simulation result of produced torque (T_e) by SRM and load torque (T_l)

A fuse box has been added for safe operation. Then, the system has been tested and the battery supply currents have been measured.

It has been observed that the battery charging current had been decreased from 6.5 A to zero. The variations of the boost converter output current values obtained by the simulation and by experimental are displayed in Fig. 11 (a) and (b), respectively. It is seen that the ripple level in the experimental values was less than that in simulation values. The fault in the adjustment of PID controller coefficient causes higher ripples in output current of the boost converter. The variation graphics of the torque produced by the SRM and the loading torque needed by the pump versus time are shown in Fig. 12. The torque needed by the centrifugal pump is proportional to the square of the speed. When the rotor speed reaches its constant value, the loading torque remains constant. It is shown in Fig. 13 (a) and (b) that the experimental results of current values are very much alike to the simulation results. The water flow rate reduces at lower speeds of the pump. This is expected for high speed centrifugal pumps because flow rate becomes quite high at the speed values near the rated speed of the pump. The

experimentally and simulation rotor speed graphs of SRM are shown in Fig. 14 (a) and (b).

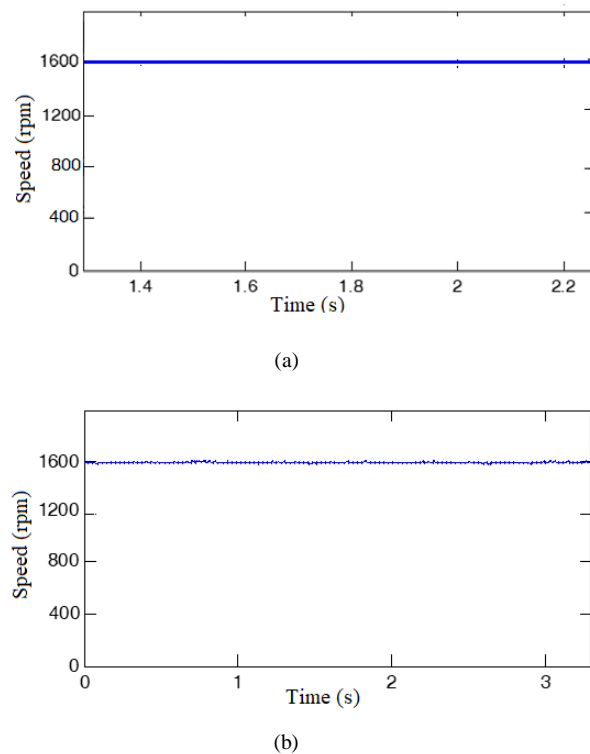


Fig. 14. Rotor speed graphs. (a) The simulation result, (b) The experimental result.

VII. CONCLUSIONS

In this work, an SRM-driven water pumping system which works with solar power has been designed and implemented. Electric energy is generated and stored in batteries by utilizing of solar energy which is an infinite source of energy. Low voltage level obtained from PVs has been increased to high voltage level required by SRM with DC-DC boost converter. It is utilized for turn on centrifugal pump by SRM due to its simple, robust structures stator and rotor without magnet and winding, low maintenance costs and high efficiency. The PV fed pumping system is simulated by using Matlab/Simulink software and simulation results are obtained. The experimental results are measured by hardware. Both experimental and simulation results are compared with each other. It is found that simulation results were very close to experimental results.

REFERENCES

- [1] A. K. Mishra and B. Singh, "Solar photovoltaic array dependent dual output converter-based water pumping using switched reluctance motor drive," *IEEE Trans. Ind. Appl.*, vol. 53, no. 6, pp. 5615–5623, Nov./Dec. 2017.
- [2] A. Mudlapur, V. V. Ramana, R. V. Damodaran, V. Balasubramanian, and S. Mishra, "Effect of partial shading on PV fed induction motor water pumping systems," *IEEE Trans. Energy Convers.*, vol. 34, no. 1, pp. 530–539, Mar. 2019.
- [3] Z. Omaç, "Fuzzy-logic-based robust speed control of switched reluctance motor for low and high speeds," *Turk J Elec Eng & Comp Sci*, vol. 27, no. 1, pp. 316–329, 2019.

- [4] Z. Omaç, M. Polat, E. Öksüztepe, M. Yıldırım, O. Yakut, H. Eren, M. Kaya, and H. Kürüm, "Design, analysis, and control of in-wheel switched reluctance motor for electric vehicles," *Electr. Eng.*, vol. 100, no. 2, pp. 865–876, 2018.
- [5] C. Gan, N. Jin, Q. Sun, W. Kong, Y. Hu, and L. M. Tolbert, "Multiport bidirectional SRM drives for solar-assisted hybrid electric bus powertrain with flexible driving and self-charging functions," *IEEE Trans. Power Electron.*, vol. 33, no. 10, pp. 8231–8245, Oct. 2018.
- [6] Y. Hu, C. Gan, W. Cao, Y. Fang, S. J. Finney, and J. Wu, "Solar PV-powered SRM drive for EVs with flexible energy control functions," *IEEE Trans. Ind. Appl.*, vol. 52, no. 4, pp. 3357–3366, Jul./Aug. 2016.
- [7] A. K. Mishra, B. Singh, "Design of solar-powered agriculture pump using new configuration of dual-output buck-boost converter," *IET Renew. Power Gener.*, vol. 12 no. 14, pp. 1640-1650, 2018.
- [8] V. Narayana, A. K. Mishra, and B. Singh, "Development of low-cost PV array-fed SRM drive-based water pumping system utilising CSC converter," *IET Power Electron.*, vol. 10, no. 2, pp. 156–168, Feb. 2017.
- [9] V. B. Koreboina, B. L. Narasimharaju, D. M. V. Kumar "Performance investigation of simplified PWM MPPT approach for direct PV-fed switched reluctance motor in water pumping system," *IET Electr. Power Appl.*, pp. 1–11, Jul. 2017.
- [10] A. K. Mishra, B. Singh, "Control of SRM drive for photovoltaic powered water pumping system," *IET Electr. Power Appl.*, vol. 11, no. 6, pp. 1055–1066, 2017.
- [11] B. Singh, A. K. Mishra, and R. Kumar, "Solar powered water pumping system employing switched reluctance motor drive," *IEEE Trans. Ind. Appl.*, vol. 52, no. 5, pp. 3949–3957, Sep./Oct., 2016.
- [12] B. C. Mecrow, J.W. Bennett, A. G. Jack, D. J. Atkinson, and A. J. Freeman, "Drive topologies for solar-powered aircraft," *IEEE Trans. Ind. Electron.*, vol. 57, no. 1, pp. 457–464, Jan. 2010.
- [13] R. Krishnan, *Switched Reluctance Motor Drives: Modeling, Simulation, Analysis, Design and Applications*. Boca Raton, FL, USA: CRC Press, Jun. 2001.
- [14] Z. Omaç, H. Kürüm, A. H. Selçuk, "Digital current control of a switched reluctance motor," *Int. J. Electr. and Power Eng.*, vol. 5, pp. 54-61, 2011.
- [15] Z. Omaç, H. Kürüm, A. H. Selçuk, "Design, analysis and control of a switched reluctance motor having 18/12 poles," *Firat U. J. Sci. Eng.* vol. 19, pp. 339-346, 2007.
- [16] M. A. Elgendy, B. Zahawi, D. J. Atkinson, "Comparison of directly connected and constant voltage controlled photovoltaic pumping systems," *IEEE Trans. Sust. Energy*, vol. 1, pp. 184-192, 2010.
- [17] Z. Omaç, A. Özel, H. Kürüm, "Modeling a switched reluctance motor-pump system directly fed from the photovoltaic battery using matlab simulink software," *Nat. Conf. on Electr. Electronics Eng. (ELECO 2012)*, 29 Nov.-1 Dec., Bursa, Turkey, pp. 807-810, 2012.

BIOGRAPHIES



ZEKİ OMAÇ was born in Elazığ, Turkey, in 1968. He received the B.S., M.S., and Ph.D. degrees from Fırat University, Elazığ, Turkey, in 1991, 1994, and 2006, respectively, all in electrical and electronics engineering.

Since 2009, he has been a Asst. Professor with the Department of Electrical and Electronics Engineering, Faculty of Engineering, Munzur University,

Tunceli, Turkey. His research interests include design, analysis and control of switched reluctance motor, induction motor, permanent magnet motor, and pure electrical vehicles.

Cryogenic DC Characteristics of Low Threshold Voltage (V_{TH}) n-channel MOSFETs

M. B. YELTEN


Abstract— Cryogenic electronics has grown in its widespread use for various technological applications. Particularly, CMOS devices and circuits are more frequently used in such systems due to their dominance in the electronics industry. At cryogenic temperatures, characteristics of CMOS devices vary, which should be characterized with measurements. In this paper, the changes in the electronic behavior of a low threshold voltage (V_{TH}) n-channel MOSFET (nMOSFET) are captured experimentally. The results are then compared with the measurements of a regular nMOSFET having the same channel width and length. It is shown that although the V_{TH} increase of both transistors is at the same amount, this value corresponds to a more significant percentage of the nominal threshold voltage for the low V_{TH} nMOSFET.

Index Terms— Cryogenic electronics, threshold voltage, low threshold voltage transistors, cryogenic measurements.

I. INTRODUCTION

CRYOGENIC systems, which can be defined as systems operating in the temperature regime below 100 K, have recently become prominent and widespread with increasingly more applications in the defense industry, space communications and research, novel computation architectures, and information storage systems. In the military, infrared cameras should have high precision detectors, for which the readout integrated circuits must have a very low noise figure. Such a performance is only possible when the operating temperatures are reduced down to the cryogenic range [1, 2].

Moreover, electronic equipment designed for space communications and research should accommodate the harsh conditions prevailing in space, where the ambient temperature can drop to -200 °C (80 K) [3-5]. As far as the novel computation architectures are concerned, quantum computing emerged as one of the most promising approaches, in which the probabilistic wave function of an electron defines the quantum state called qubit that replaces the bits in the traditional Boolean algebra. Qubits enable completely different algorithms with much higher computational efficiency to be. Nevertheless, qubits reach their operational state only when the temperature is cooled down to 15 – 20 mK [6]. Hence, peripheral electronic circuits that communicate with the qubits should be capable of operating at temperatures below 20K [7].

MUSTAFA BERKE YELTEN is with Department of Electronics and Communications in Istanbul Technical University, Istanbul, Turkey (e-mail: yeltenm@itu.edu.tr)  <https://orcid.org/0000-0001-7482-0536>

Manuscript received May 26, 2019; accepted July 5, 2019.
DOI: [10.17694/bajece.570215](https://doi.org/10.17694/bajece.570215)

Finally, the cryogenic regime has been shown to enhance the performance of memory systems where high-speed DRAM structures can be produced with better power efficiency [8, 9].

To design electronic circuits that will operate with high performance in cryogenic temperature range, devices, and components building such systems should be experimentally characterized. In this work, cryogenic characterization of low V_{TH} nMOSFETs, which are frequently used in low power circuit design, has been performed. The organization of the paper is arranged as follows. In Section II, the physical changes in the characteristics of a MOSFET at cryogenic temperatures are discussed. Subsequently, the test chip designed for the experimental analysis of the low V_{TH} MOSFETs will be described in Section III. In Section IV, measurement results encompassing $I_D - V_{DS}$ and $I_D - V_{GS}$ curves of both low and regular V_{TH} transistors are presented and discussed. Finally, conclusions will be drawn in Section V.

II. CHANGES IN MOSFET CHARACTERISTICS AT CRYOGENIC TEMPERATURES

As the temperature of a MOSFET is reduced, several of its physical properties are changed. The first of them is the charge carrier mobility. Scattering mechanisms determine how much the mobility is impaired at any temperature. Generally, at very low temperatures, the charge carriers have less kinetic energy; therefore, they stumble on the ionized impurities. Conversely, at high temperatures, due to increased energy of charge carriers and massive lattice vibration, more collisions occur, hence the mobility of the charge carriers comes down. The optimum temperature, at which the mobility is maximized, happens to be at much lower temperatures than the room temperature (300 K). Thus, the mobility of charge carriers increases significantly as the ambient temperature drops down to the cryogenic regime.

Another physical property that is being altered at cryogenic temperatures is the threshold voltage (V_{TH}). The typical equation for the MOSFET threshold voltage can be provided as follows [10]:

$$V_{TH} = V_{FB} - \frac{Q_I}{C_{ox}} - \frac{Q_D}{C_{ox}} + 2\phi_F, \quad (1)$$

In (1), the dominating term is the last one of the right side, which represents the Fermi potential of the substrate:

$$\phi_F = \frac{k_B T}{q_e} \ln \frac{N_A}{n_i} \quad (2)$$

Here, k_B is the Boltzmann constant, T is the temperature, q_e is the electronic charge, N_A is the substrate doping

concentration, and n_i is the intrinsic charge carrier concentration for the bulk material. n_i depends heavily on the temperature, and it severely drops at cryogenic temperatures. Therefore, the Fermi potential is increased significantly, and this leads to a rise in the nMOSFET V_{TH} .

The saturation velocity of charge carriers rises at cryogenic temperatures due to increasing mobility values. Furthermore, the drain-source resistance drops, since the conductivity of charge carriers grows, as long as complete ionization of dopant atoms can still be realized at that cryogenic temperature. However, impacts of these are minor in comparison to those of the changes in the charge carrier mobility and the device V_{TH} .

III. TEST CHIP FOR EXPERIMENTAL CHARACTERIZATION AND MEASUREMENT SETUP

In order to experimentally characterize the cryogenic properties of low V_{TH} nMOSFETs, a test chip has been fabricated that contains several types of transistors, including low V_{TH} nMOSFETs (Fig. 1) [11]. Here, four pads are assigned to every transistor corresponding each to one terminal of the transistor. In Fig. 2, the organization of the pads around the low V_{TH} MOSFET layout can be seen, which belongs to a commercial 180 nm device technology. The pads in Fig. 2 are used to apply DC voltages to the gate, source, bulk, and the drain, at which the drain current will be monitored.

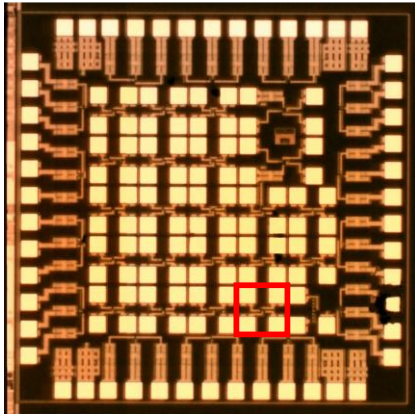


Fig.1. Chip micrograph of the fabricated test chip. The red rectangle shows the location of the low V_{TH} nMOSFET and the surrounding pads.

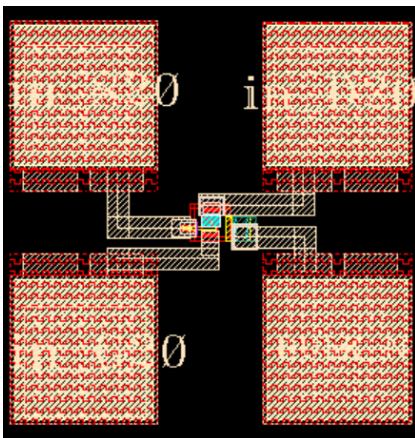


Fig.2. The layout of the low V_{TH} nMOSFET.

A low-cost cryogenic measurement setup has been

developed to experimentally characterize the fabricated test chip (Fig. 3). For this purpose, an MDC 441 Cryogenic Probing System has been employed, where a dewar containing liquid nitrogen (LN2) is connected through flexible metal pipes to the actual probe station. LN2 is directly passed underneath of the chuck, on which the bare die lies in intimate contact. In that regard, the die comes easily in thermal equilibrium with the boiling LN2 at $-196\text{ }^{\circ}\text{C}$ (77 K). The vaporized nitrogen is then dumped to outside in gas form. A stereo microscope with a long working distance is used to view and touch the pads of the transistors (Fig. 4a). Along with the probing station, the Agilent B1500A Semiconductor Parametric Analyzer is utilized to capture the $I-V$ characteristics of the transistors under test (Fig. 4b).

Overall, the test set-up that has been established in this work is cheaper since it only cools down the chuck rather than the entire volume around the chip. Nevertheless, the intimate contact is sufficient to ensure the right measurement temperature for the device under test, thereby rendering the set-up a practical alternative in comparison to more expensive cryostats and cryogenic probe stations.



Fig.3. Cryogenic probe station and the measurement test setup.

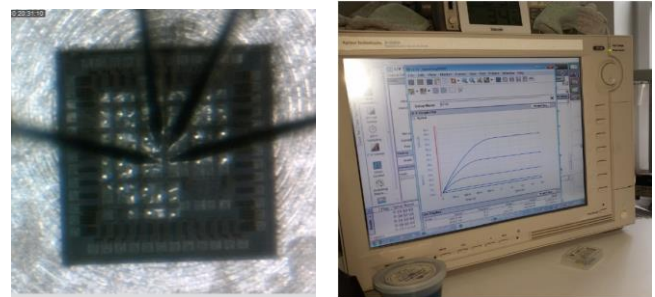


Fig.4. (Left) The test chip under stereo microscope, (right) Agilent B1500A used in the characterization of transistors under test.

IV. MEASUREMENT RESULTS AND DISCUSSION

The low V_{TH} nMOSFET characterized in this work has a channel length of 0.5 μm and a channel width of 35 μm with seven fingers. To better understand the $I - V$ characteristics of this device, a same-size regular nMOSFET is also experimentally analyzed, and the results acquired from both transistors are then compared.

First, the room temperature and cryogenic temperature characteristics of the low V_{TH} nMOSFET should be extracted. For this purpose, $I_D - V_{DS}$ and $I_D - V_{GS}$ curves have been captured at both 77 K and 300 K and depicted in Fig. 7 and Fig. 8, respectively. The changes in the I_D and V_{TH} of a regular and low V_{TH} nMOSFET have been analyzed numerically in Table I and Table II, respectively.

Fig. 7 clearly shows that at cryogenic temperatures, the I_D of low V_{TH} nMOSFETs sharply increases due to the rise in the mobility. In Table I, this change is noted to be by 50%. Through performing similar measurements on a regular nMOSFET, it is demonstrated that the rate of current increase is also around 50%. Thus, low V_{TH} nMOSFETs behave similarly to regular nMOSFETs as far as the drain current at cryogenic temperatures is concerned. Nevertheless, for the same gate and drain voltages applied, the drain current of low V_{TH} nMOSFETs is almost 50% higher due to the smaller device V_{TH} .

Fig. 8 shows that the threshold voltage is increased for a low V_{TH} nMOSFET at cryogenic temperatures in accordance with the theoretical expectations. V_{TH} is a key parameter and should remain low in order the circuit applications based on low V_{TH} characteristics of transistors can still be functional at cryogenic temperatures. Nevertheless, Table II indicates that the V_{TH} increase amounts are the same for both low V_{TH} and regular nMOSFETs, where the percentage change in the threshold voltage of low V_{TH} nMOSFETs reaches 75%. Therefore, circuit designers should be aware that the performance of designs based on low V_{TH} nMOSFETs would be significantly degraded at cryogenic temperatures due to this serious hike in the device V_{TH} . Even so, the threshold voltage of low V_{TH} nMOSFET is still around half of the regular transistors' V_{TH} .

Fig. 9 show the ensemble $I_D - V_{DS}$ characteristics of low V_{TH} nMOSFETs extracted experimentally from 11 different devices at both room and cryogenic temperatures. Results demonstrate that in the cryogenic regime, the variability of the $I_D - V_{DS}$ characteristics also goes up. Therefore, circuit designers should know that in addition to the changes in transistor parameters, the impact of variations would be more pronounced, as well. As a remedy, the designs should contain more room for random variations in the expense of performance cuts.

V. CONCLUSIONS

This paper describes the changes observed in the $I_D - V_{DS}$ and $I_D - V_{GS}$ characteristics of low V_{TH} nMOSFETs. In addition, the extracted characteristics have been interpreted with respect to the results acquired from the same-size regular nMOSFETs. Overall, it has been demonstrated that similar outcomes can be observed for both types of transistors, albeit low V_{TH}

nMOSFETs have a more dramatic increase in their V_{TH} values. This is a potentially significant issue as the performance of relevant circuits can be substantially degraded at cryogenic temperatures based on this change. Furthermore, the variability of $I_D - V_{DS}$ characteristics also increases in the cryogenic regime, which contributes to the burden of the previous problem. Hence, the designs should be generated such that the potential impact of such difficulties is properly accounted during circuit design (e.g., transistor sizing).

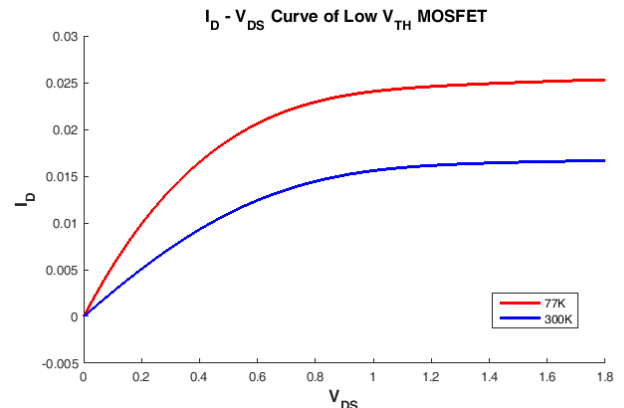


Fig.7. $I_D - V_{DS}$ characteristics of the low V_{TH} nMOSFET at 77 K and 300 K ($V_{GS} = 1.8$ V).

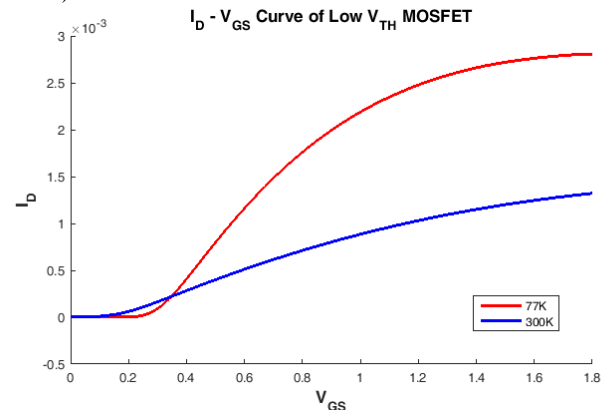


Fig.8. $I_D - V_{GS}$ characteristics of the low V_{TH} nMOSFET at 77 K and 300 K ($V_{DS} = 50$ mV).

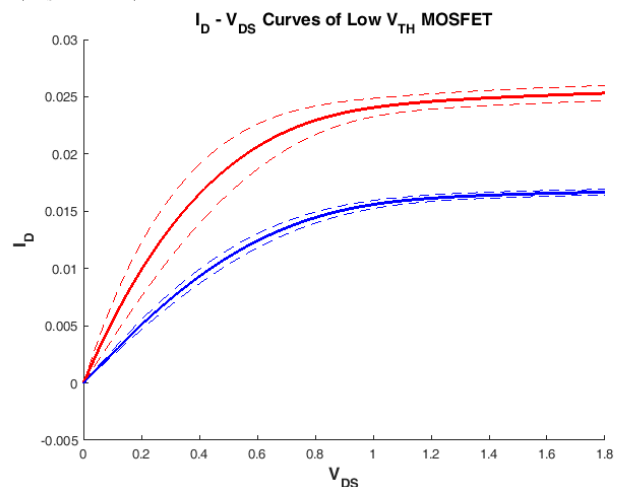


Fig.9. $I_D - V_{DS}$ characteristics of an ensemble of low V_{TH} nMOSFETs at 77 K and 300 K ($V_{GS} = 1.8$ V).

TABLE I.
Comparison of I_D values for regular and low V_{TH} nMOSFETs at room and cryogenic temperatures.

Transistor Type	Sizes (W x L)	I_D at room temperature	I_D at cryogenic temperature (LN2)	Difference	Increase
Low V_{TH} NMOS Transistor	35 μm x 0.5 μm	16.92 mA	25.31 mA	8.39 mA	%50
Regular V_{TH} NMOS Transistor	35 μm x 0.5 μm	11.2 mA	16.92 mA	5.72 mA	%51

TABLE II.
Comparison of V_{TH} values for regular and low V_{TH} nMOSFETs at room and cryogenic temperatures.

Transistor Type	Sizes (W x L)	V_{TH} at room temperature	V_{TH} at cryogenic temperature (LN2)	Difference	Increase
Low V_{TH} NMOS Transistor	35 μm x 0.5 μm	0.16 V	0.28 V	0.12 V	%75
Regular V_{TH} NMOS Transistor	35 μm x 0.5 μm	0.44 V	0.56 V	0.12 V	%27

ACKNOWLEDGMENT

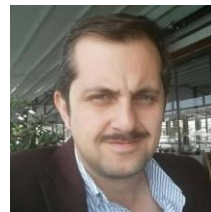
The author would like to express his gratitude to Aykut Kabaoğlu, for preparing the experimental results, Nergiz Şahin Solmaz, for her work in the test chip design, and Sadık İlik, for collecting the measurement outcomes. This work was sponsored by the Technological Research Council of Turkey under the project TÜBİTAK 1001 215E080.

REFERENCES

- [1] Shafique, A., Yazici, M., Kayahan, H., Ceylan, O., Gurbuz, Y., "Cryogenic Measurements of a Digital Pixel Readout Integrated Circuit for LWIR," Proc. SPIE 9451, Infrared Technology & Applications, XLI, 94510Y, 1 – 6, 2015.
- [2] Ceylan, O., Kayahan, H., Yazici, M., Baran, M.B., Gurbuz, Y., "Design and Realization of 144 x 7 TDI ROIC with Hybrid Integrated Test Structure", Proc. SPIE 8353, Infrared Technology & Applications, XXXVIII, 83531Q, 1 – 12, 2012.
- [3] Cressler, J.D. "Silicon-Germanium as an Enabling Technology for Extreme Environment Electronics," IEEE Transactions Device and Materials Reliability (TDMR), 10, 4, 437 – 448, 2010.
- [4] Woods, B. O., Mantooth H. A., Cressler, J. D., "SiGe HBT Compact Modeling for Extreme Temperatures," ISDRS, College Park, Maryland, ABD, 1 – 2, 2007.
- [5] Kabaoğlu, A., and Yelten, M. B., "A cryogenic modeling methodology of MOSFET IV characteristics in BSIM3", In IEEE 2017 14th International Conference on Synthesis, Modeling, Analysis and Simulation Methods and Applications to Circuit Design (SMACD), pp. 1-4, 2017.
- [6] Ladd, T.D., Jelezko, F., Laflamme, R., Nakamura, Y., Monroe, C., O'Brien, J.L., "Quantum Computers", Nature, vol. 464, 45 – 53, 2010.
- [7] Homulle, H., Visser, S., Patra, B., Ferrari, G., Prati, E., Almudéver, C.G., Bertels, K., Sebastiano, F., Charbon, E., 2016. "CryoCMOS hardware technology a classical infrastructure for a scalable quantum computer"

- [8] Ware, F., Gopalakrishnan, L., Linstadt, E., McKee, S. A., Vogelsang, T., "Do Superconducting Processors Really Need Cryogenic Memories? The Case for Cold DRAM", In ACM Proceedings of the International Symposium on Memory Systems, pp. 183-188, October 2017.
- [9] Tannu, S. S., Carmean, D. M., & Qureshi, M. K., "Cryogenic-DRAM based memory system for scalable quantum computers: a feasibility study," In Proceedings of the ACM International Symposium on Memory Systems, pp. 189-195, October 2017.
- [10] Streetman, B. and Banerjee, S., 2016, "Solid State Electronic Devices," Pearson Education, Global 7th edition, Essex, İngiltere.
- [11] Kabaoğlu, A., Solmaz, N. Ş., İlik, S., Uzun Y., and Yelten, M. B. "Statistical MOSFET Modeling Methodology for Cryogenic Conditions," in IEEE Transactions on Electron Devices, vol. 66, no. 1, pp. 66-72, Jan. 2019.

BIOGRAPHY



MUSTAFA BERKE YELTEN was born in Istanbul, Turkey, in 1982. He received his B.Sc. degree in electrical engineering (with high honor) from Boğaziçi University, Istanbul, in 2006, the M.Sc. and the Ph.D. degrees in electrical engineering from North Carolina State University, Raleigh, in 2008 and 2011, respectively. He worked as a quality-reliability research engineer in Intel Cooperation between 2011 and 2015. Since 2015,

he is an Assistant Professor at Istanbul Technical University Electronics and Communications Engineering Department. His research interests include the design, optimization, simulation, and modeling of nanoscale transistors as well as analog/mixed-signal/RF integrated circuits with emphasis on variability and reliability analyses.

Publication Ethics

The journal publishes original papers in the extensive field of Electrical-electronics and Computer engineering. To that end, it is essential that all who participate in producing the journal conduct themselves as authors, reviewers, editors, and publishers in accord with the highest level of professional ethics and standards. Plagiarism or self-plagiarism constitutes unethical scientific behavior and is never acceptable.

By submitting a manuscript to this journal, each author explicitly confirms that the manuscript meets the highest ethical standards for authors and coauthors

The undersigned hereby assign(s) to *Balkan Journal of Electrical & Computer Engineering* (BAJECE) copyright ownership in the above Paper, effective if and when the Paper is accepted for publication by BAJECE and to the extent transferable under applicable national law. This assignment gives BAJECE the right to register copyright to the Paper in its name as claimant and to publish the Paper in any print or electronic medium.

Authors, or their employers in the case of works made for hire, retain the following rights:

1. All proprietary rights other than copyright, including patent rights.
2. The right to make and distribute copies of the Paper for internal purposes.
3. The right to use the material for lecture or classroom purposes.
4. The right to prepare derivative publications based on the Paper, including books or book chapters, journal papers, and magazine articles, provided that publication of a derivative work occurs subsequent to the official date of publication by BAJECE.
5. The right to post an author-prepared version or an official version (preferred version) of the published paper on an internal or external server controlled exclusively by the author/employer, provided that (a) such posting is noncommercial in nature and the paper is made available to users without charge; (b) a copyright notice and full citation appear with the paper, and (c) a link to BAJECE's official online version of the abstract is provided using the DOI (Document Object Identifier) link.



ISSN: 2147- 284X
Year: July 2019
Volume: 7
Issue: 3

CONTENTS

S.Turkdogan; Design and Impl. of a Cost Effective Quartz Crystal Microbalance System for Monitoring Small Changes on any Surface...	213-217
E. Yanmaz Adam; Leveraging Connectivity for Coverage in Drone Networks for Target Detection,	218-225
O. Yaman&Y. Bicen; An Internet of Things (IoT) based Monitoring System for Oil-immersed Transformers,.....	226-234
M. U. Khan; Mobile Robot Navigation Using Reinforcement Learning in Unknown Environments,	235-244
M. Cansiz; Radio Frequency Energy Harvesting with Different Antennas and Output Powers,	245-249
M. S. Cengiz; Effects of Luminaire Angle on Illumination Performance in Tunnel Lighting,	250-256
L.A.Ajao et all; Design of a Secure Tracking Automobile System for Oil and Gas Distribution using Telematics and Blockchain Tech,....	257-268
M.E.Başoğlu; Analyzes of Flyback DC-DC Converter for Submodule Level Maximum Power Point Tracking in Off-grid Photovoltaic S,....	269-275
B. B. Alagoz, G. Kavuran, A. Ates, C. Yeroglu and H. Alisoy; Multi-loop Model Reference Adaptive PID Control for Fault-Tolerance,....	276-285
B. Reis, S.B. Kaya, O.K.Sahingoz; A Clustering Approach for Intrusion Detection with Big Data Processing on Parallel Computing Plat,....	286-293
Y.Kaya, D.Avcı, M.Gedikpınar; Comparing of K-Means, K-Medodis and Fuzzy C Means Cluster Method for Analog Modulation Rec,....	294-299
M. R. Çorapsız, H. Kahveci and M. F. Çorapsız; Analysis and Suppressing Speed Fluctuations in Brushless DC Motors,	300-310
T.Tuncer, Y.Sönmez; A Novel Data Hiding Method based on Edge Detection and 2k Correction with High Payload and High Visual Qua,....	311-318
M.R. Tur; The Impact of Emerging Renewable Energy on Capacity Mechanisms in Power Systems and Expert Opinion,	319-325
O. Çiçek, S. Kurnaz; LabVIEW Based a Software System:Quantitative Determination of Main Electronic Parameters for Schottky Jnc S,....	326-331
A. Karafil and H. Ozbay; Power Control of Single Phase Active Rectifier,.....	332-336
M.A.Arserim, C.Haydaroğlu, H.Acar, A.Uçar; Forming and Co-simulation of Square and Triangular Waveforms by Using Sys Gen,....	337-341
V. Ozduran; Physical Layer Security of Multi-user Half/Full-Duplex Wireless Two-Way Relaying Network,....	342-354
Z. Omaç; Design and Analysis of a Water Pumping System with Photovoltaic Source and Switched Reluctance Motor,	355-361
M. B. Yelten; Cryogenic DC Characteristics of Low Threshold Voltage (VTH) n-channel MOSFETs,.....	362-365

BALKAN JOURNAL OF ELECTRICAL & COMPUTER ENGINEERING

(An International Peer Reviewed, Indexed and Open Access Journal)

Contact

Batman University
Department of Electrical-Electronics Engineering
Bati Raman Campus Batman-Turkey

Web: <http://dergipark.gov.tr/bajece>
<http://www.bajece.com>
e-mail: bajece@hotmail.com

